STRUCTURAL HEALTH MONITORING OF ATTRIDGE DRIVE OVERPASS

A thesis submitted to the
College of Graduate Studies and Research
in Partial Fulfillment of the requirements
for the Degree of Masters of Science
in the Department of Civil and Geological Engineering
University of Saskatchewan
Saskatoon

By
Abu Bakkar Siddique

PERMISSION TO USE

In presenting this thesis in partial fulfillment of the requirements for a Postgraduate degree from the University of Saskatchewan, I agree that the Libraries of this University may make it freely available for inspection. I further agree that permission for copying this thesis in any manner, in whole or in part, for scholarly purposes may be granted by the professors who supervised my thesis work or, in their absence, by the Head of the Department or the Dean of the College in which my thesis work was done. It is understood that any copying or publication or use of this thesis or parts thereof for financial gain shall not be allowed without my written permission. It is also understood that due recognition shall be given to me and to the University of Saskatchewan in any scholarly use which may be made of any material in my thesis. Requests for permission to copy or to make other use of material in this thesis in whole or part should be addressed to:

Head of the Department of Civil and Geological Engineering
University of Saskatchewan
57 Campus Drive
Saskatoon, Saskatchewan, S7N 5A9

ABSTRACT

Vibration-based damage detection (VBDD) comprises a family of non-destructive testing methods in which changes to dynamic characteristics are used to track the condition of a structure. Although VBDD methods have been successfully applied to various mechanical systems and to simple beam-like structures, significant challenges remain in extending this technology to complex, spatially distributed structures such as bridges.

In the present study, numerical simulations using a calibrated finite element model were used to investigate the use of VBDD methods to detect small-scale damage on a two-span, integral abutment overpass structure located in Saskatoon, Saskatchewan. The small scale damage was defined in this study as the removal of a concrete element from the top surface of the bridge deck, resembling the spalled clear cover of concrete deck of the overpass. Five different VBDD techniques were evaluated, including the Change in Mode Shape, Change in Flexibility, Change in Mode Shape Curvature, Change in Uniform Flexibility Curvature and Damage index methods. In addition, the influence of the size of damage, the orientation of damage geometry, sensor spacing (3 m, 5 m and 7.5 m), the approach used for mode shape normalization, and uncertainty in the measured mode shapes was investigated.

It was found that localized damage could be reliably detected and located if the sensors were located within 3 m of the damage (the distance between adjacent girders) and if uncertainty in the mode shapes was attenuated through the use of a sufficient number of repeated trials. Furthermore, studies using a limited sensor installation that could be achieved without interrupting the flow of traffic indicated that small scale

damage could be detected and potentially located using sensors that are placed well away from the damaged area, provided uncertainty in mode shape was attenuated.

ACKNOWLEDGEMENTS

First I would like to recall the mercy of Allah (God) who has blessed me with patience to overcome all the odds throughout this research work.

My profound appreciation goes to my supervisors: Professor Leon Wegner and Professor Bruce Sparling for their guidance, mentorship and suggestions. Their patience and expertise helped me to keep my journey in the right track towards the completion of this research work.

I also owe appreciation to my Advisory Committee members: Professor M. Hosain, Professor M. Boulfiza, and Professor G. Putz for their suggestions.

I acknowledge the financial support of ISIS Canada Network of Centres of Excellence and the logistic support of the City of Saskatoon.

The technical support of Mr. Dale Pavier and Mr. Alan Duffy, Structural Laboratory Technicians, is also appreciated. Mr. Dale Pavier has braved severe winter weather to perform the field tests.

Special thanks are due to my wife for her painstaking efforts in helping me to create all the plots and format the whole thesis. Without her sacrifices for last three years, it would have been very challenging for me to continue this research work.

DEDICATION

This thesis is dedicated to:

SRITI,
B. RASHID
and K. RASHID

TABLE OF CONTENTS

LIST OF TABLES

LIST OF FIGURES

LIST OF SYMBOLS

C	=	Summation of the squared value of modal amplitude elements
c	=	Damping of a system
E	=	Modulus of Elasticity
F	=	Flexibility matrix
$\mathbf{F}^*$	=	Flexibility matrix of a damaged system
F_{ij}	=	Element of flexibility matrix at the i^{th} row and j^{th} column.
$\boldsymbol{f}$	=	Uniform load flexibility
$\boldsymbol{f''}$	=	Uniform load flexibility curvature
$\boldsymbol{f}_j$	=	Uniform load flexibility at j^{th} location
G	=	Modulus of rigidity
$H(\omega)$	=	Dynamic amplification function
I	=	Identity matrix
$I_{\Delta\phi}$	=	Resultant intensity of mode shape changes
K	=	Stiffness matrix
K_t	=	Translational stiffness of pile/backfill soil
K_θ	=	Rotational stiffness of pile
k	=	Stiffness of a system
M	=	Mass matrix
m	=	Mass

m_i	=	Lumped mass at i^{th} node
p_o	=	Amplitude of varying loading force
$\mathbf{q}$	=	Eigenvector
$S_x(\omega)$	=	Spectral density function
t	=	Varying time
x	=	Displacement
$\dot{x}$	=	Velocity
$\ddot{x}$	=	Acceleration
$x_i(t)$	=	Time varying displacement at i^{th} node
x_n	=	Instantaneous measured acceleration at the instant t_n
y_n	=	Conditioned (modified) acceleration reading at the time instant t_n
$\mathbf{Z}_j$	=	Normalized damage index
β_j	=	Damage index at j^{th} node for multiple modes.
β_{ji}	=	Damage index at the location of j^{th} node for i^{th} mode shape
$\bar{\delta}_j$	=	Maximum absolute value of a column of change in flexibility matrix.
ζ	=	Damping Ratio
λ	=	Eigenvalue
μ_β	=	Mean value of damage indices
ρ	=	Density of material

ρ_{bottom}	=	Density of concrete of bottom layer of deck
ρ_{median}	=	Density of concrete at median
ρ_{middle}	=	Density of concrete of middle layer of deck
ρ_{top}	=	Density of concrete of top layer of deck
σ_{β}	=	Standard deviation of damage indices
υ	=	Poisson's ratio of concrete element
ω	=	Excitation frequency of the time varying force
ω_i	=	i^{th} natural frequency of the system
ω_i^*	=	i^{th} natural frequency of the damaged system
ω_o	=	Natural frequency of the system
$\boldsymbol{\phi}^{t_1}$	=	Mode shape vector at temperature range of t_1
$\boldsymbol{\phi}^{t_2}$	=	Mode shape vector at temperature range of t_2
$\boldsymbol{\phi}_i$	=	i^{th} vibration mode shape vector
$\boldsymbol{\phi}_i^*$	=	i^{th} vibration mode shape vector of damaged induced structure.
$\boldsymbol{\phi}_i^{''}$	=	Curvature of mode shape vector
$\phi_i^{''}(x)$	=	Curvature of mode shape function at i^{th} mode.
$\boldsymbol{\phi}_i^{''*}$	=	Curvature of damaged mode shape vector
$\phi_i^{''}(x)$	=	Curvature of damaged mode shape function at i^{th} mode.
ϕ_{ji}	=	Modal amplitude at point j to the i^{th} mode.
$\phi_{ji}^{''}$	=	Curvature at point j to the i^{th} mode shape.

$\boldsymbol{\phi}_i^T$	=	Transpose of mode shape vector at i^{th} mode.
$\boldsymbol{\phi}_{Ti}$	=	Modal amplitude vector of temperature range i
$\boldsymbol{\phi}_{To}$	=	Modal amplitude vector of temperature range 20°C to 26°C
Φ_H	=	Phase Angle

LIST OF ABBREVIATIONS

ADINA	Automatic Dynamic Incremental Nonlinear Analysis: A finite element software
ANAS	Averaged normalized acceleration spectra
CMIF	Complex mode identification function
dB	Decibels
DC	Direct current
dof	Degree of freedom
FE	Finite element
FFT	Fast Fourier transform
LDT	Linear displacement transducers
LDV	Laser doppler vibrometry
MAC	Modal assurance criteria
NCD	Non-destructive crack detection
NDE	Non-destructive evaluation
PRD	Percent relative difference
RMS	Root mean square
SDOF	Single degree of freedom
SHM	Structural health monitoring
VBDD	Vibration based damage detection
3-D	Three Dimensional

CHAPTER 1. INTRODUCTION

1.1 BACKGROUND

The Government of Canada, in cooperation with other levels of government and private sector organizations, has invested in the development of the infrastructure of Canada since the early days of Confederation. The rationale behind the basic infrastructure development is its pivotal role on the health of the national economy, as well as on the well being and quality of life of all Canadians (Mirza et al. 2003). One of the most important components of the transportation infrastructure is the bridge network, which has attracted huge investment, not only in Canada, but all over North America, due to its significance to commerce, economic vitality and personal mobility. In the United States, the catastrophic collapse in 1967 of the U.S. Highway 35 Silver Bridge connecting Point Pleasant in West Virginia and Kanauga in Ohio, led to the development of a nationwide policy for the 'Safety of bridge structures and inspection' in 1971 (Phares et al. 2005). Since then, most major bridge structures in North America have been monitored on a regular basis. However, in Saskatchewan, many smaller bridges have never been inspected (Brownlee 2007).

New materials and complex structural systems with relatively short track records are increasingly used in the construction, rehabilitation and repair of bridges. Public agencies are recognizing the need for increased vigilance with respect to monitoring the condition of the infrastructure under their management. In view of the fact that visual inspections alone have been found to be remarkably unreliable (FHWA Rep. 2001), other monitoring and condition assessment techniques are being considered.

Numerous local, non-destructive evaluation (NDE) techniques are currently available, including those that rely on half-cell potential, radiography, ultrasonics, liquid penetrants, magnetic particles, eddy currents, and acoustic emission (Kobayashi 1993). The main advantage of local NDE methods as a group lies in the fact that they can be used to detect, locate, and/or characterize defects with relatively good precision. However, they are generally capable of interrogating only small areas at a time, so that the inspection of a large structure can be costly and time consuming. In addition, the region to be inspected must be accessible.

The disadvantages of NDE methods for inspecting large and complex structures has led to continuing research on developing alternative methods for Structural Health Monitoring (SHM). One class of SHM techniques, collectively referred to as global methods, makes use of changes in the overall response characteristics of a structure to indicate the presence and nature of damage. Common global approaches include static field tests (Jenkins et al. 1997, Bakht and Csagoly 1980), semi-static field tests (Schulz et al. 1995), and vibration-based methods (Doebling et al. 1996). By assessing the entire structure simultaneously, these procedures can be performed in a relatively short period of time and are not limited to the consideration of accessible components. In many cases, they can also be adapted for remote monitoring applications.

Vibration Based Damage Detection (VBDD) is based on the premise that changes in stiffness, mass or energy dissipation properties of a structure due to damage will lead to changes in the dynamic properties of the structure. Damage can then be assessed by measuring the changes in dynamic properties. The immense potential

economic benefits, along with the associated significant technical and practical challenges, have inspired researchers to explore its possibilities.

The well established use of acoustic methods by potters to detect cracks in their products may be the earliest successful implementation of VBDD, even though this has been practiced as more of an art than a science. To date, VBDD methods have been successfully introduced to rotating machinery; Farrar and Duffey (1999) and Sohn et al. (2003) mentioned the successful transition of VBDD used on rotating machinery from a research phase to industrial use. West (1982, 1984), Hunt et al. (1990), and Grygier et al. (1994) reported on the application of VBDD methods to aerospace systems. Stubbs and Osegueda (1990) and Zhou et al. (2004) describe the successful implementation of VBDD methods to simply supported beams in controlled, laboratory environments. Over the last decade, a number of studies have also been undertaken applying VBDD methods to bridges (Toksoy and Aktan 1994; Farrar et al. 1994; Jauregui and Farrar 1996; Zhang and Aktan 1998; Peeters 2000; Catbas and Aktan 2002; Ventura et al. 2002; Kim and Stubbs 2003). All of these studies, in general, focused on a few, relatively severe damage cases and have reported some successes in identifying, locating and occasionally estimating the severity of damage. However, in contrast to simple mechanical systems, some of the common characteristics of civil engineering structures identified by most researchers such as the large size, uncertainties in effective material properties, support conditions, and connectivity of components, and variability in loading and environmental conditions introduce complications to the successful implementation of VBDD.

Despite the challenges, the development of reliable VBDD methods holds the potential for great benefit and cost savings to infrastructure owners. It is therefore important that their capabilities and limitations be explored more fully. The application of VBDD methods to a real structure, considering small-scale damage, limitations in potential sensor locations, and the challenges related to field conditions has not yet been fully explored. The present study was therefore designed and performed to address these practical implementation issues.

A research programme investigating the application of VBDD techniques to bridge structures was started in 2000 and is still in progress at University of Saskatchewan. Zhou et al. (2004, 2007) reported some early successes of the application of VBDD techniques on simple structures (i.e., a prestressed girder and a single span, simply supported bridge deck) in a well-controlled laboratory environment. Structural Health Monitoring of the Attridge Drive Overpass was undertaken to extend this investigation scheme to a more complex and spatially distributed structure.

In the present study, the Attridge Drive Overpass, located in Saskatoon, Canada, was monitored intermittently at a variety of different temperatures over a period of almost two years. This study is a part of the project for investigating the application of VBDD to bridges. The measured responses were used to identify its dynamic properties, notably natural frequencies and mode shapes, along with the level of uncertainty associated with these field measurements. The effect of temperature changes on natural frequencies and mode shapes was also investigated.

1.2 OBJECTIVES

The primary objective of this thesis was to investigate the use of VBDD methods to detect and locate small scale damage on the deck of an actual bridge structure. Specific sub-objectives included the following:

1. To establish the baseline dynamic characteristics (natural frequencies and mode shapes) of the Attridge Drive Overpass;
2. To ascertain the influence of temperature changes on the dynamic properties of the Attridge Drive Overpass;
3. To determine the measurement uncertainty associated with natural frequencies and mode shapes; and
4. To determine the ability of several currently available VBDD techniques to identify the presence and location of damage on the bridge deck, considering the influence of the following variables:
    i. the location of damage;
    ii. the size (severity) of damage;
    iii. the number and distribution of measurements locations; and
    iv. measurement uncertainty.

The results of the study represent a contribution toward the establishment of practical guidelines for VBDD implementation.

1.3 METHODOLOGY

The Attridge Drive Overpass, a recently built structure (2001) located in Saskatoon, Canada, was chosen as the subject of the study. Descriptions of structural features of the Attridge Drive Overpass are given in Chapter 3 and Chapter 5. The

methodology for the study featured two components: field measurements and numerical modelling. The components were executed in a coordinated, parallel fashion. The methodology of the present project is delineated in a flow diagram shown in Figure 1-1.

The field measurements consisted of dynamic testing of the overpass under ambient traffic loading. Data processing was then carried out to identify the natural frequencies and mode shapes of the overpass. Time histories of vibration measurements were recorded, and data processing, as described in Chapter 3, was employed to extract the required dynamic properties. Data collected under a wide variety of ambient weather conditions were used to assess the effects of temperature changes on the dynamic properties of the structure.

The numerical modelling component consisted of creating a finite element (FE) model of the overpass and calibrating the model to the real structure using the measured dynamic properties. This calibrated model was then used as the reference model for subsequent studies. The FE model was used to simulate the dynamic response of the structure as various damage states were induced. Mode shapes generated from both the undamaged and damaged models were used to investigate VBDD techniques by comparing the mode shapes before and after damage. Five different VBDD methods were investigated in this study: the change in mode shape, change in mode shape curvature, change in flexibility, change in uniform flexibility curvature and damage index methods. It is noteworthy that all of these VBDD methods are non-model based; in other words, the methods do not require an FE model to be used in practice. However, a FE model was used in this study to extend the scope of the investigation beyond what could be accomplished in the field program (for example, the real structure could not be

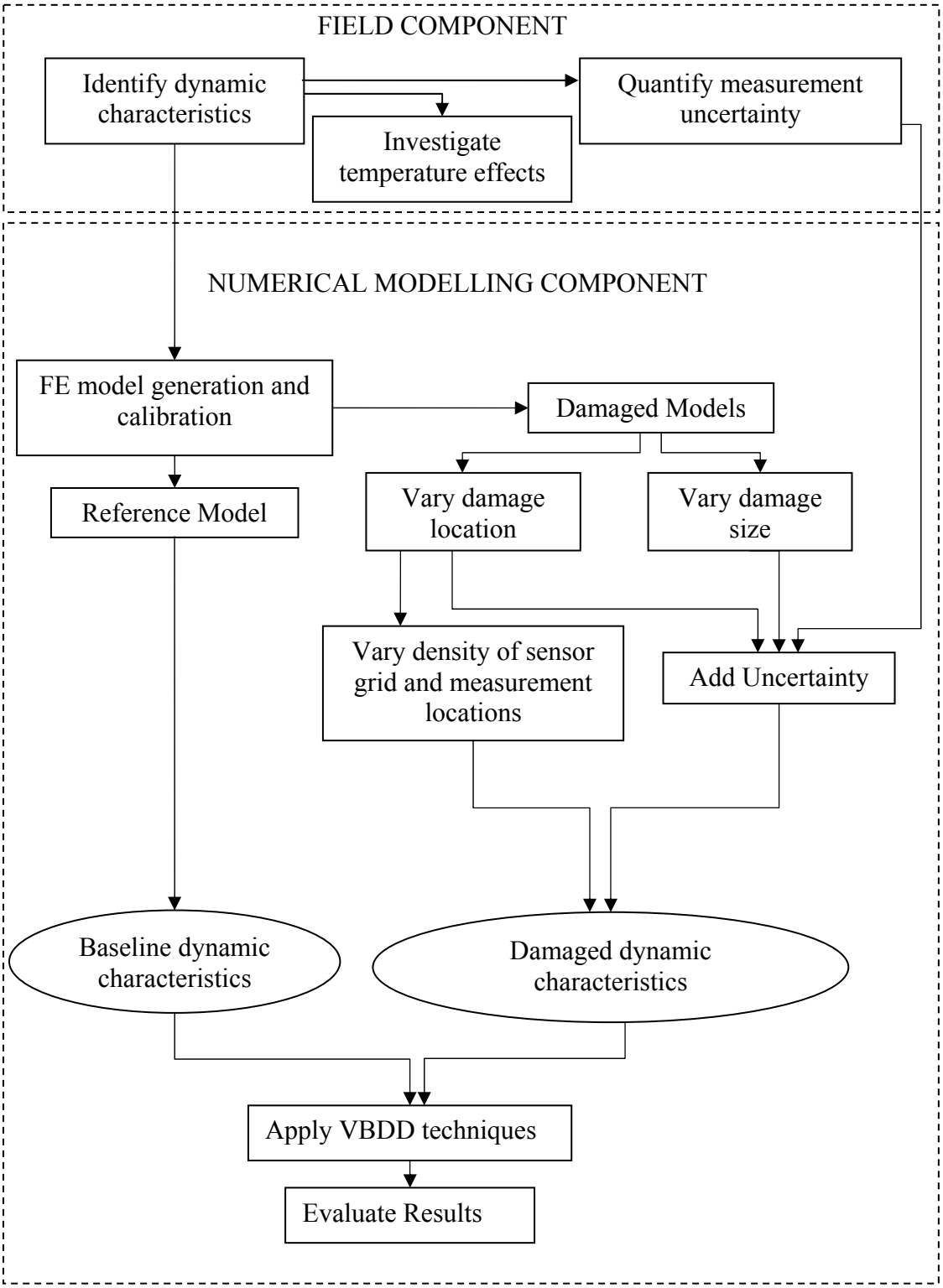

Figure 1-1. Flow diagram of the components of the study.

damaged). Uncertainty in the mode shape measurements was also simulated in the FE models and its influence on the performance of the VBDD methods was investigated.

1.4 THESIS LAYOUT

The thesis is organized in nine chapters, with additional information provided in the appendices. A chapter by chapter overview is given below, accompanied by an information flow diagram in Figure 1-2.

In Chapter 1, an overview presenting the background and establishing the need for Structural Health Monitoring were presented. In addition, the objectives and methodology of the present study were outlined.

The theoretical background and a summary of the VBDD techniques applied in this thesis are presented in Chapter 2, along with a review of the literature related to the application of these techniques.

The field component of this study is described in Chapter 3, which contains a description of the overpass structure, instrumentation, experimental program and data processing. A conceptual description of data conditioning and processing methods are also provided in this chapter.

The experimental results and discussion are presented in Chapter 4. Effects of temperature changes on the dynamic properties of the overpass structure, and uncertainties in the dynamic property measurements are discussed in this chapter.

Details of the finite element (FE) modelling procedures, as well as the calibration of the model to the field measurements, are provided in Chapter 5.

The results of the numerical investigation (using the FE model) are discussed in Chapter 6, 7 and 8. The performance of VBDD methods under ideal conditions is

discussed, as well as under the influence of the practical challenges associated with the more realistic operating conditions outlined in the objectives.

The conclusions and recommendations are given in Chapter 9.

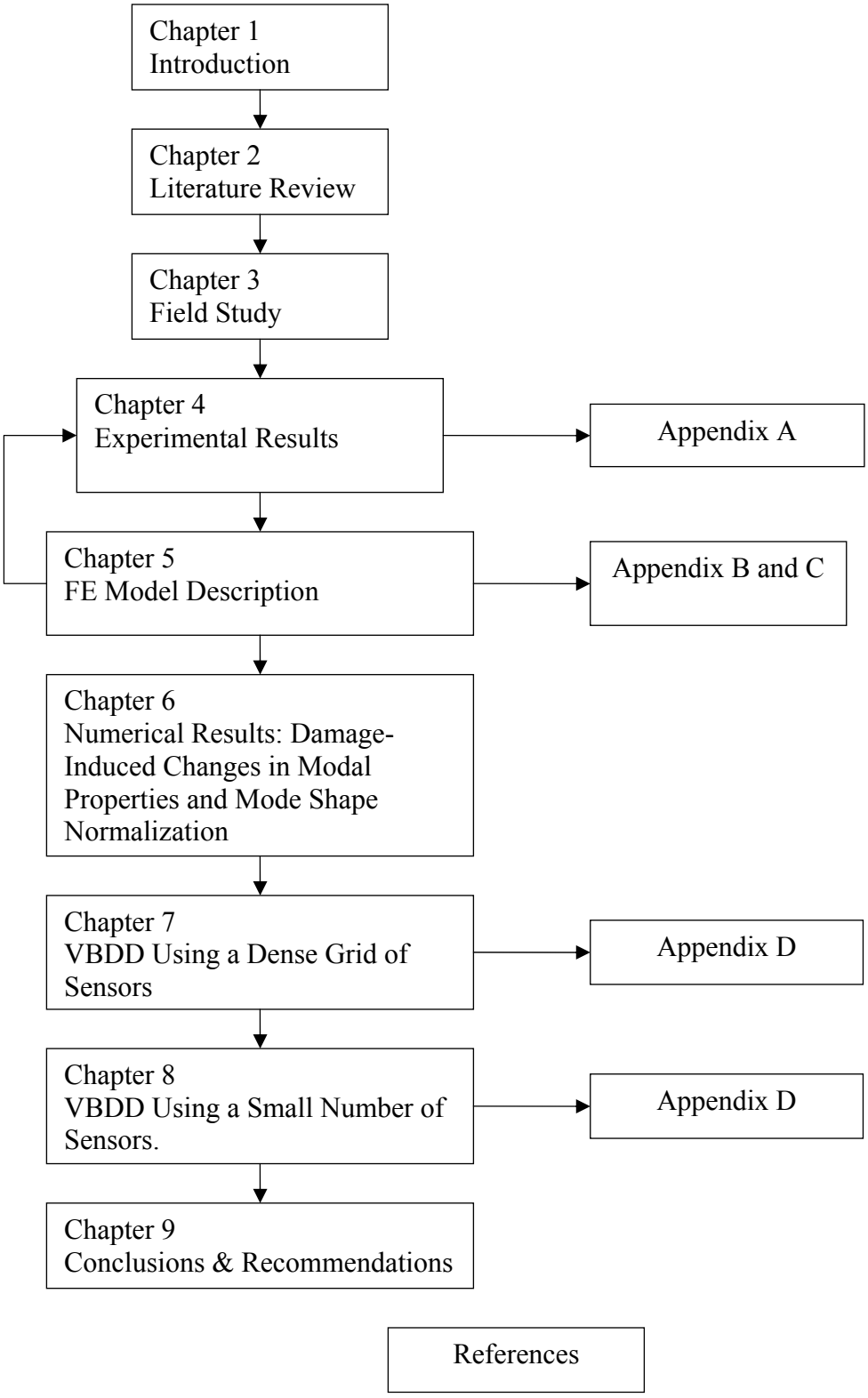

Figure 1-2. Information flow diagram for the thesis.

CHAPTER 2. LITERATURE REVIEW

2.1 OVERVIEW

The very first step in Vibration Based Damage Detection (VBDD) is the system identification of a structure. In simple terms, system identification refers to the extraction of the modal properties of a structure. A brief background on modal properties, notably natural frequencies and mode shapes is provided in Section 2.2. The methodology applied to extract the modal properties from the measured vibration responses of the Attridge Drive Overpass is delineated in Section 2.3.

Vibration Based Damage Detection for civil engineering structures is still in a developmental stage. To date, researchers have proposed different VBDD methods and indices. Section 2.4 covers a brief background on VBDD indices. A concise summary of research works on the application of VBDD methods is provided in Section 2.4.2.

2.2 MODAL PROPERTIES OF STRUCTURES

In general, a structure vibrates in response to a dynamic load with magnitudes that vary with time. The response (displacement, acceleration, etc.) of a structure to a time-varying load is also time-varying in nature. In contrast to a static load case, where an imposed load is resisted by the stiffness, a dynamic load on a structure is resisted by the stiffness, inertia (the product of moving mass and acceleration of the structure) and damping forces. In general, the damping in civil engineering structures is relatively small in comparison to mechanical systems.

The vibration of any real structure consists of a series of vibration modes. Each vibration mode has a unique resonance (natural) frequency and mode shape. If a lightly

damped structure hypothetically vibrates freely in one of its natural frequencies, the inertia force exerted on the structure will be balanced by the stiffness and damping forces. The deflected shape of the structure in that hypothetical case is the mode shape pertaining to that natural frequency. However, the deflected shape of a structure in real conditions typically consists of a combination of different mode shapes.

The mathematical solution of the dynamic equilibrium equations of a structural system leads to an eigenvalue problem, which can be expressed mathematically as

$$([\mathbf{A}] - \lambda[\mathbf{I}])\{\mathbf{q}\} = \{0\} \ , \tag{2.1}$$

where **A** is a square matrix of order N (the number of system degrees of freedom), **I** is the identity matrix of the same order as **A**, λ is a system eigenvalue and **q** is the corresponding eigenvector of order N. The solution for an eigenvector is not unique; only the relative magnitudes of its elements may be determined.

A simple three degrees of freedom system featuring a cantilever beam with discretised lumped masses is shown in Figure 2-1, in which m_i and $x_i\ (t)$ are the lumped

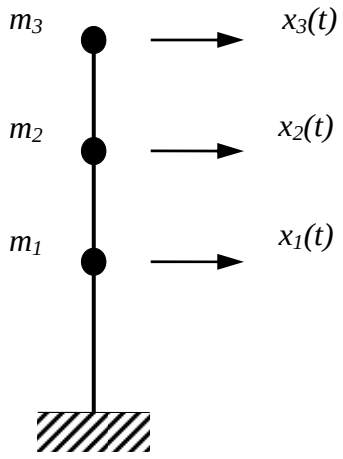

Figure 2-1. A simple three degree of freedom system (a cantilever beam with discretised lumped masses, m_1, m_2, m_3).

masses and time-varying displacements at node i, respectively, where i = 1,2,3. The equations of motion can be expressed as

$$[\mathbf{M}]\{\ddot{\mathbf{x}}\} + [\mathbf{K}]\{\mathbf{x}\} = \{0\} \ . \tag{2.2}$$

Assuming harmonic motion, Equation 2.2 can be modified to the following eigenvalue problem

$$([\mathbf{K}] - \omega_i^2[\mathbf{M}])\{\boldsymbol{\phi}\}_i = \{0\} \ , \tag{2.3}$$

where $\omega_i = i^{th}$ natural frequency (rad/s), i.e., the frequency at which the structure will vibrate freely (without external excitation) if disturbed from a state of rest. Also, $\{\boldsymbol{\phi}\}_i$ = i^{th} vibration mode shape, which gives the relative amplitudes of vibration at each degree of freedom. The absolute amplitudes of vibration are indeterminate, depending on the initial conditions. It is noteworthy that ω_i and $\boldsymbol{\phi}_i$ are the properties of a structure which are independent of loading type.

2.3 EXTRACTING MODAL PROPERTIES FROM FIELD MEASUREMENTS

Ambient vibration was used as the sole excitation source in the field study described in this thesis. In this context, ambient vibration is taken to mean vibration induced by wind and traffic. Therefore, the input force is not controlled and can not be measured. For these conditions, the following methods are commonly cited in the literature as methods to extract the dynamic properties from a measured ambient vibration response:

a) Peak Picking Method (Bendat and Piersol 1993);

b) Averaged Normalized Power Spectral Densities (Felber 1993);

c) Complex Mode Indication Function (CMIF) methods (Shih et al. 1988, Brickner et al. 2000);

d) Stochastic-Subspace Identification Method (Peeters and DeRoeck 2000);

As the peak picking method is the simplest and most widely used method among those listed above, it was selected for use in this study. The method is named after the very key step of selecting the resonant frequencies and modal response from the peaks in a Fourier response spectrum. A brief overview of the theoretical basis for the peak picking method is described below; more detailed discussions have been published by others (Clough and Penzien 1975).

The equation of dynamic equilibrium for a single degree of freedom (SDOF) dynamic system such as that shown in Figure 2-2 is commonly presented as

$$m\ddot{x} + c\dot{x} + kx = p(t)\,, \tag{2.4}$$

where $\ddot{x}$, $\dot{x}$, $x, m, c, k, p(t)$ are the acceleration, velocity, displacement, mass, damping, stiffness and time-varying load, respectively.

For a harmonic load of the form

$$p(t) = p_o \sin(\omega t)\,, \tag{2.5}$$

where p_o is the force amplitude, ω is the forcing frequency, and t is the elapsed time, the displacement response of the system can be described by the following expression

$$x(t) = x_{st} H(\omega) \sin(\omega t + \Phi_H) = \frac{p_o}{k} H(\omega) \sin(\omega t + \Phi_H)\,, \tag{2.6}$$

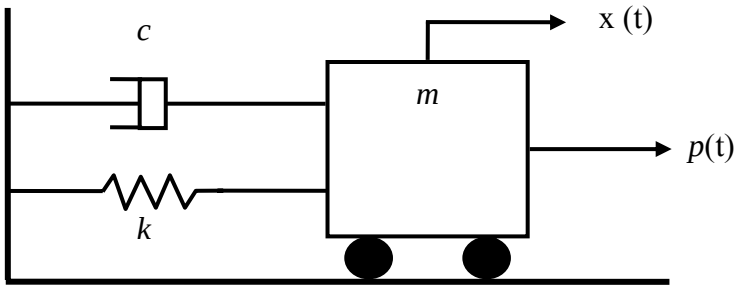

Figure 2-2. Simplified single degree of freedom system.

in which x_{st} is the displacement due to a static force of magnitude p_o, and Φ_H is the phase angle by which the response lags the load. The dynamic amplification $H(\omega)$ can be written as

$$H(\omega) = \frac{1}{\sqrt{\left[1-\left(\frac{\omega}{\omega_o}\right)^2\right]^2 + \left[2\zeta\left(\frac{\omega}{\omega_o}\right)\right]^2}}, \tag{2.7}$$

in which

$$\zeta = \frac{c}{2m\omega_o} \; and \; \omega_o = \sqrt{\frac{k}{m}}, \tag{2.8}$$

where ω, ω_o, and ζ are the excitation frequency of the force, the natural frequency of the system, and the damping ratio of the system expressed as a fraction of critical damping, respectively.

The dynamic amplification $H(\omega)$ for different damping ratios is plotted in Figure 2-3. It can be seen that $H(\omega)$ reaches a peak very near the so-called resonant condition, when $\approx \omega_o$. For lightly damped structures such as bridges, this peak value of $H(\omega)$ may reach 25 or higher, demonstrating that the dynamic response to harmonic loading with frequencies near the natural frequencies of the system will be much larger than that due to loading at non-resonant frequencies.

For a multi-degree of freedom system excited by ambient loading, which is typically random in nature and features a broad band of frequency content, the response time history will generally have the form shown in Figure 2-4 (a). This response can be represented in the frequency domain by a power spectral density function $S_x(\omega)$, or power spectrum, such as those shown in Figure 2-4 (b) and (c), which indicates how the energy of the response is distributed with frequency.

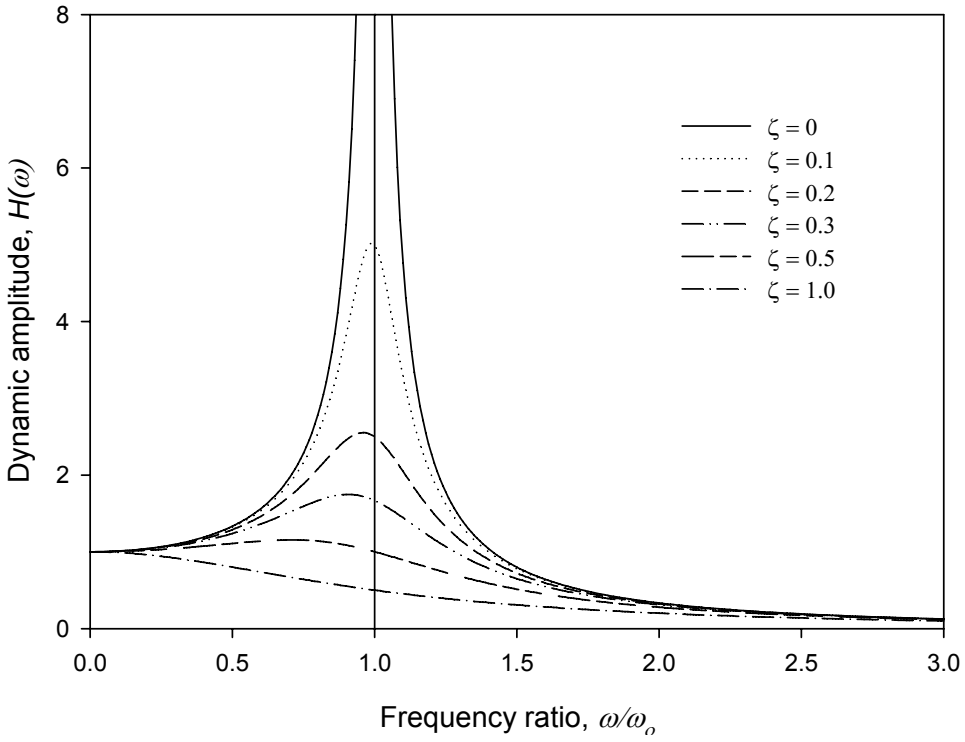

Figure 2-3. Variation of dynamic amplification with frequency.

Conceptually, natural frequencies and their corresponding modal response amplitudes can be identified by locating resonant peaks in the response spectrum, which are caused by the large dynamic amplification in these regions, as discussed above. In practice, however, these resonant peaks must be differentiated from non-resonant peaks arising as a result of natural variation in the frequency content of the excitation, measurement noise (errors), and signal processing approximations. Fortunately, these non-resonant peaks tend to be random in nature and can therefore be attenuated by averaging the response spectra from more than one event. Since the resonant (modal) response tends to appear consistently in all events, the averaging process tends to reinforce these desired peaks while diminishing the extraneous random variations.

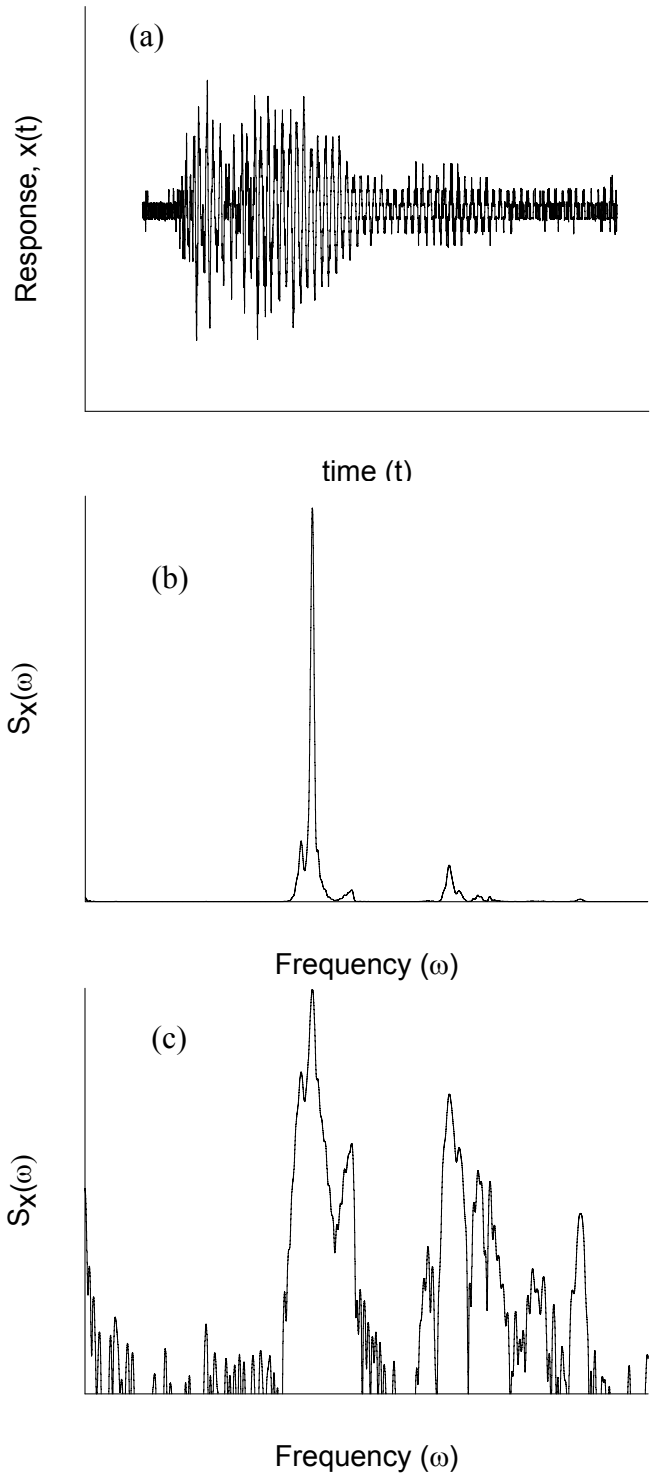

Figure 2-4. Response to ambient loading: (a) response time history; (b) power spectrum; and (c) power spectrum in semi-log scale showing lower energy content.

Once the natural frequencies have been identified, the relative amplitudes of the resonant response peaks at each measurement location can be used to construct the vibration mode shapes corresponding to each natural frequency.

Further details on the specific procedures used to extract modal properties from the measured field data are provided in Sections 3.4.5 and 3.4.6.

2.4 DAMAGE DETECTION

2.4.1 Overview

In a broad sense, "damage" implies a change in the performance of any system relative to some previously existing desired level of performance. Intrinsic in this definition of damage is the existence of a desired level of performance which serves as a reference point to define the state of damage. In a structural system, damage could be in the form of deformation in geometry, lack of integrity in connectivity among structural components, deteriorated material properties and changes in boundary conditions. Damage can occur suddenly due to an earthquake or an impact force. Damage can also be a slow paced, incremental degradation process due to corrosions or fatigue (Farrar and Doebling 1997).

Damage can be classified as linear or non-linear based on the structural response to loads after the structure has been damaged. A linear elastic structure will remain linear after experiencing linear damage. On the other hand, a linear elastic structure will behave non-linearly after experiencing non-linear damage. Loose connections in steel structures and fatigue cracks in concrete are examples of non-linear damage (Doebling et al. 1998). Pearson et al. (2001) reported that a non-linearity in the damage (crack in the concrete) had relatively insignificant effects on damage identification. Including

non-linearity when modelling damage is far more complex and time consuming than modelling linear damage. To simplify the numerical modelling and emphasize the focus on other salient damage detection issues, linear damage was considered in the present study.

A systematic approach is usually adopted to monitor the ongoing condition of a structure. This approach typically involves data acquisition, the extraction of damage sensitive parameters for the structure, the use of an appropriate damage detection method, and inferring the severity of damage. Data acquisition encompasses a broad field ranging from localized visual inspections to global vibration response measurements. For the vibration based damage detection methods, the vibration response of the structure is used to detect the damage. The systematic approach mentioned above is commonly referred as 'Structural Health Monitoring' in the literature.

Rytter (1993) has proposed four tiers of damage identification, defined as follows:

- Level I: Determination of the presence of damage;
- Level II: Determination of the presence and location of damage;
- Level III: Determination of the presence, location and severity of damage; and
- Level IV: Determination of the presence, location, severity and the remaining service life of the structure.

VBDD methods developed to date can be applied to field data without the use of a numerical model for Level I and Level II damage detection. Field data with the aid of a trained numerical model can theoretically make it possible to carry out Level III and

Level IV damage detection (Doebling et al. 1996, Sohn et al. 2003). The damage identification levels proposed by Rytter (1993) are followed in this study when explaining the results of the damage detection investigation.

2.4.2 Vibration Based Damage Detection (VBDD)

2.4.2.1 Overview

The dynamic properties of a structure including its natural frequencies, mode shapes and damping properties, depend on the stiffness of a structure, as well as its mass. Any form of structural damage which changes the structural stiffness in turn changes the dynamic properties of the structure. As a result, damage can be detected by tracing the changes in the dynamic properties over time.

The dynamic properties are usually extracted from the measured vibration response of a structure. The excitation source used to induce a dynamic response could be either forced vibration or ambient vibration. Forced vibration can be applied using a mechanical shaker, step relaxation, or hammer impact. On the other hand, normal traffic when the bridge is in use and wind are the usual sources of ambient excitation. Ambient excitation is more attractive for the development of remote SHM schemes, as well as for the evaluation of dynamic properties during actual operating condition.

The vibration response is commonly measured in terms of strains, displacements or accelerations. Conventional electric resistance strain gauges or fibre optic sensors are typically used for strain measurements. Todd et al. (2000) developed a high resolution, low noise strain sensing system using fibre-optic Bragg Grating sensors. Kim and Paik (1997) found that Fabry-Perot fibre-optic sensors were also capable of high resolution dynamic measurements.

Displacements can be measured by Laser Doppler Vibrometry (LDV) or linear displacement transducers (LDT). Zak et al. (1999) used LDV to measure the displacements of a composite plate in response to impulse excitation while investigating the dynamic response. Zimmerman (1999) investigated the dynamic response of a vertical stabilizer using scanning Laser Vibrometry. The vertical stabilizer assembly was intended for use in space applications. Accelerometers are commonly used to measure acceleration. Farrar et al. (1994) and Wegner et al. (2004) used accelerometers to investigate the dynamic response of bridge structures. In the present study, the Attridge Drive Overpass was monitored primarily using accelerometers. Strain gauges were also installed; however, due to the presence of significant noise in the strain gauge data, only accelerometer readings were used for subsequent investigations.

2.4.2.2 Vibration-Based Damage Detection Indices

The underlying premise of the VBDD methods proposed to date is that changes in the dynamic properties can be used to identify damage or deterioration in the structure. A number of quantitative parameters have been developed based on changes in modal characteristics; damage can be identified and located based on the spatial variation of these parameters.

As mentioned, numerous VBDD damage indices have been proposed, all related in some manner to changes in modal parameters. Detailed reviews of these have been provided by Doebling et al. (1996, 1998). In summary, proposed indices include those that rely on shifts in natural frequencies (Cawley and Adams 1979; Salawu 1997; Peeters 2000), direct changes to mode shapes (Fox 1992; Srinivasan and Kot 1992; Salawu and Williams 1994); changes to mode shape curvatures (Pandey et al. 1991;

Zhang and Aktan 1995), changes to measurement-derived flexibility or stiffness matrices (Pandey and Biswas 1994; Zimmerman and Kaouk 1994), changes to modal strain energy (Kim and Stubbs 1995, 2003), updates to numerical models to match the measured response of the damaged structure (Hajela and Soeiro 1990; Beck and Katafygiotis 1992a and 1992b; Casas and Aparicio 1994; Hu et al. 2001), and neural network-based methods (Wu et al. 1992; Masri et al. 1996). The five VBDD techniques employed in this study are described below.

Change in Mode Shape Method

The most straightforward of the methods investigated was one which simply considered the difference between the damaged and undamaged mode shapes. Since damage is expected to cause a localized decrease in stiffness, the greatest change in mode shape amplitude is expected to occur at the location of damage. For the i^{th} vibration mode, if the damaged and undamaged mode shape amplitudes are denoted by $\boldsymbol{\phi}_i^*$ and $\boldsymbol{\phi}_i$, respectively, the change in mode shape $\Delta\boldsymbol{\phi}_i$ caused by damage is simply defined as:

$$\Delta\boldsymbol{\phi}_i = \boldsymbol{\phi}_i^* - \boldsymbol{\phi}_i \ . \tag{2.9}$$

The location associated with the largest absolute value in the vector $\Delta\boldsymbol{\phi}_i$ would then represent the most likely location of damage. For the present study, only fundamental mode shapes were considered (i.e., $i = 1$). Since the scale of mode shapes is arbitrary by definition, the mode shapes $\boldsymbol{\phi}_i^*$ and $\boldsymbol{\phi}_i$ must be normalized to a suitable, common basis to allow for meaningful comparisons. Various mode shape normalization schemes, and their effect on VBDD, are discussed in Section 6.4.

Change in Mode Shape Curvature Method

Since the curvature of a beam in response to a given loading state is directly proportional to the inverse of its flexural stiffness, a localized reduction in stiffness caused by damage will produce an increase in curvature at that location. Pandey et al. (1991) demonstrated that an increase in the curvature of mode shapes can be a good indicator and locator of damage for beam-like structures.

Given the normalized damaged and undamaged mode shapes, $\boldsymbol{\phi}_i^*$ and $\boldsymbol{\phi}_i$, the corresponding mode shape curvature vectors may be denoted by $\boldsymbol{\phi}_i^{"*}$ and $\boldsymbol{\phi}_i^{"}$, where the double prime notation signifies the second spatial derivative. In that case, the change in mode shape curvature associated with damage is calculated by

$$\Delta\boldsymbol{\phi}_i^{"} = \left|\boldsymbol{\phi}_i^{"*}\right| - \left|\boldsymbol{\phi}_i^{"}\right| , \tag{2.10}$$

where the evaluation of absolute values is carried out on individual elements of the vectors $\boldsymbol{\phi}_i^{"*}$ and $\boldsymbol{\phi}_i^{"}$. Large positive peaks within $\Delta\boldsymbol{\phi}_i^{"}$ are then indicative of the location of damage. If multiple modes are used, the sum of differences in curvature may be employed as a damage indicator, as expressed by

$$\Delta\boldsymbol{\phi}_i^{"} = \sum_{i=1}^{n} \Delta\boldsymbol{\phi}_i^{"} , \tag{2.11}$$

where n is the number of modes considered. If not measured directly, mode shape curvature vectors may be computed using the central difference approximation for the second derivative,

$$\phi_{ji}^{"} = \frac{\phi_{(j+1)i} - 2\phi_{ji} + \phi_{(j-1)i}}{h^2}, \tag{2.12}$$

here ϕ''_{ji} is the curvature at point *j* corresponding to the i^{th} mode (i.e., the j^{th} element of the vector $\boldsymbol{\phi}_i''$), ϕ_{ji} is the displacement at point *j* corresponding to the i^{th} mode (i.e., the j^{th} element of the vector $\boldsymbol{\phi}_i$), and *h* is the average distance between discrete points in $\boldsymbol{\phi}_i$.

Change in Flexibility Method

The flexibility matrix, **F**, of a structure in its undamaged and damaged states may be estimated from a few of the lower vibration modes, as follows (Pandey and Biswas 1994):

$$\mathbf{F} \approx \sum_{i=1}^{n} \frac{1}{\omega_i^2} \boldsymbol{\phi}_i \boldsymbol{\phi}_i{}^T \text{ and}$$

$$\mathbf{F}^* \approx \sum_{i=1}^{n} \frac{1}{\omega_i^{*2}} \boldsymbol{\phi}_i{}^* \boldsymbol{\phi}_i{}^{*T} \quad , \tag{2.13}$$

where ω_i is the angular frequency of the i^{th} mode. The change in flexibility caused by damage can be obtained from the difference between the respective matrices, i.e.

$$\Delta\mathbf{F} = \mathbf{F}^* - \mathbf{F} \quad , \tag{2.14}$$

where $\Delta\mathbf{F}$ is the change in flexibility matrix. For the j^{th} column of this matrix, the parameter $\bar{\delta}_j$ may be defined as the maximum absolute value of the elements in that column, or

$$\bar{\delta}_j = \max\left|\Delta F_{ij}\right| \quad i = 1 \ldots m \tag{2.15}$$

where ΔF_{ij} are elements of $\Delta\mathbf{F}$, and m is the number of points at which the mode shape is defined. The parameter $\bar{\delta}_j$ is then a measure of the change of flexibility at point *j* and the largest value of $\bar{\delta}_j$ is assumed to be indicative of the location where the change in physical properties (i.e., damage) is located.

Damage Index Method

For a structure that can be represented as a beam, Stubbs and Kim (1995) derived a damage index based on the change in modal strain energy at location *j* for the i^{th} mode as follows:

$$\beta_{ji} = \frac{\left(\int_a^b \left[\phi_i^{"*}(x)\right]^2 dx + \int_o^L \left[\phi_i^{"*}(x)\right]^2 dx\right)}{\left(\int_a^b \left[\phi_i^{"}(x)\right]^2 dx + \int_o^L \left[\phi_i^{"}(x)\right]^2 dx\right)} \times \frac{\int_o^L \left[\phi_i^{"}(x)\right]^2 dx}{\int_o^L \left[\phi_i^{"*}(x)\right]^2 dx} = \frac{NUM_{ji}}{DEN_{ji}} \qquad (2.16)$$

where $\phi_i^{"}(x)$ and $\phi_i^{"*}(x)$ are continuous mode shape curvature functions for the i^{th} mode in terms of distance *x* along the beam, corresponding to the undamaged and damaged structures, respectively. These are based on the second derivatives of continuous displacement mode shape functions $\phi_i(x)$ and $\phi_i^{*}(x)$. In addition, *L* is the length of the beam, and *a* and *b* are the limits of a segment of the beam over which the extent of damage is being evaluated. In discrete form, assuming that the spacing between points in the mode shape vectors is uniform, calculation of the damage index is carried out using the relationship:

$$\beta_{ji} = \frac{\left(\phi_{ji}^{"\,*}\right)^2 + \sum_{k=1}^{m}\left(\phi_{ki}^{"\,*}\right)^2}{\left(\phi_{ji}^{"}\right)^2 + \sum_{k=1}^{m}\left(\phi_{ki}^{"}\right)^2} \times \frac{\sum_{k=1}^{m}\left(\phi_{ki}^{"}\right)^2}{\sum_{k=1}^{m}\left(\phi_{ki}^{"\,*}\right)^2} = \frac{NUM_{ji}}{DEN_{ji}} \; . \qquad (2.17)$$

If more than one mode is used, a single index for each location, *j*, is formed by

$$\beta_j = \frac{\sum_{i=1}^{n} NUM_{ji}}{\sum_{i=1}^{n} DEN_{ji}} \; . \qquad (2.18)$$

Assuming that the set of damage indices for the structure represents a sample population of a normally distributed random variable, a normalized damage indicator may be calculated as follows:

$$\mathbf{Z}_j = \frac{(\boldsymbol{\beta}_j - \mu_\beta)}{\sigma_\beta} \,, \tag{2.19}$$

where μ_β and σ_β are the mean and standard deviation of damage indices, respectively. Damage indices falling two or more standard deviations from the mean (i.e. $Z_j \geq 2$)) are defined as being indicative of a possible damage location.

Change in Uniform Flexibility Curvature Method

The j^{th} column of the flexibility matrix **F**, calculated by Equation 2.13, corresponds to the deflected shape assumed by the structure when a unit load is applied at the j^{th} degree of freedom. The sum of all columns of the flexibility matrix, therefore, represents the deflected shape if a unit load is applied at each degree of freedom simultaneously. This shape is referred to as the uniform load flexibility, and is represented here by the vector $\boldsymbol{f}$.

Zhang and Aktan (1995) indicated that the change in curvature of the uniform load flexibility surface caused by damage could be used to determine the location of the damage. Elements of the uniform flexibility curvature vector,$\boldsymbol{f}''$, may be calculated from $\boldsymbol{f}$, again using the central difference approximation

$$f_j'' = \frac{f_{j+1} - 2f_j + f_{j-1}}{h^2} \,, \tag{2.20}$$

where h is the average distance between measurement locations. For the current study, the change in curvature at location j was evaluated as

$$\Delta f_j'' = \left|f_j''^*\right| - \left|f_j''\right| \,, \tag{2.21}$$

where the asterisk indicates the damaged state. The largest positive value of $\Delta f_j''$ was taken to be indicative of the location of damage. In the present study, it was assumed that curvature changes were random samples of a normal distribution. The curvature

changes were converted to a sample of 'Zero' mean and 'Unit' standard deviation by using an equation similar to Equation 2.19, where μ and σs are the mean and standard deviation of $\Delta \boldsymbol{f}''$, respectively.

2.5 LITERATURE REVIEW RELATED TO THE APPLICATION OF VBDD METHODS.

A comprehensive review of the studies on damage detection methods based on modal properties was performed by Doebling et al. (1996) and Sohn et al. (2003). A condensed summary of the literature relevant to the current study is presented below, divided into different sections based on the type of structure.

2.5.1 Application of VBDD to Offshore Structures

Modal property-based damage detection for offshore structures was investigated by oil industries in the early 1970's and 1980's. Vandiver (1975, 1977), Begg et al. (1976), and Loland and Dodds (1976) reported that changes in natural frequencies could potentially be used to detect damage in offshore structures. Wojnarowski et al. (1977) numerically examined the effects of different parameters on the natural frequency. They found that foundation properties, among other parameters such as marine growth, entrained water inside the members, corrosion, change in deck loads and failed members, caused the maximum changes on the natural frequencies.

Duggan et al. (1980) and Kenley and Dodds (1980) suggested the corresponding mode shape be associated with the natural frequencies being observed to improve the accuracy of damage detection using natural frequency changes. Based on the monitoring program of the Alpha Forties platform owned by British Petroleum, Whittome and Dodds (1983) reported that changes in natural frequencies due to structural damage were

greater than the changes in natural frequencies experienced by the undamaged platform over time.

Nataraja (1983) monitored three offshore platforms in the North Sea over a two-year period and concluded that monitoring changes in the deck mass is required to distinguish structural damage. Another observation by the same author is that damage localization is not possible; however, only global changes in the structure could be detected using measured acceleration.

All of the above mentioned research concluded that the natural frequencies of offshore platforms changed as a result of structural damage. However, substantial changes in mass due to marine growth and variation in the amount of fluid in the fluid tank, as well as equipment noise made the natural frequency monitoring process quite challenging.

2.5.2 Application of VBDD on Rotating Machinery

To date, VBDD techniques have been applied most successfully to rotating machinery (Shives and Mertaugh 1986, Farrar and Duffey 1999). A non-model based vibration pattern recognition in either the time or frequency domain coupled with a previously developed database of signature vibration patterns is usually used to identify damage in rotating machinery. Condition monitoring of rotating machinery is now used in industrial settings, and commercial packages are available to apply this method systematically to rotating machinery.

2.5.3 Application of VBDD on Simple Structures

VBDD has also been applied successfully to simple beam structures in controlled laboratory conditions (Stubbs and Osegueda 1990 and Zhou et al. 2004).

Stubbs and Oseguenda (1990) performed a model-based VBDD investigation using a series of aluminium cantilevered beams (25 mm x 12.7 mm x 1000 mm). A sensitivity-based matrix update method was used to identify and locate damage, where the structural mass, stiffness and damping matrices were updated based on the optimization of an error function of matrix perturbations. Damage was induced by reducing the cross sectional dimensions of the beam and impact excitation was used to induce vibrations. It was reported that damage cases were located accurately, except for an occasional false positive and false negative indication of damage.

Zhou et al. (2004) reported the successful application of VBDD methods for a simply supported, 12.2 m long, prestressed concrete girder with a cross-section of 1216 mm x 508 mm in a well controlled laboratory environment. Forced white noise excitation was used while natural frequencies were identified. Mode shapes were then inferred from measured acceleration amplitudes excited by forced harmonic excitation at resonant frequencies. Damage detection algorithms were applied using mode shapes that were interpolated between measurement points using a cubic spline function. It was found that small-scale damage could be successfully located using five different non-model based VBDD methods. A similar investigation was performed on a half-scale, two-girder, slab-on-girder bridge deck, with similarly successful results (Zhou et al. 2007).

Poudel et al. (2005) reported the use of a high speed (2000 frames /second) digital video camera to extract modal properties. VBDD was investigated using a simply supported prismatic steel beam featuring a rectangular cross section (15.24 cm x 0.635 cm). Damage was inflicted by 2 saw-cuts having depths of 2.5 cm and 2.2 cm,

respectively. Vibration time series were then inferred from the captured images. Pictures were captured at a rate of 1000 frames/s for 1 second. A new edge detection algorithm (image processing) at the sub-pixel level was developed to improve the resolution in image processing. It was reported that the high speed digital video camera was able to acquire an intensive high resolution vibration response in a more cost effective manner than the conventional contact based sensors. Natural frequencies, mode shapes and damping ratios were extracted from the synthesised time series. A second-order complex Gaussian transformation was applied to the mode shape difference function (between pristine and damaged state) to locate damage. Predications of damage location were reported to have a very good agreement with the inflicted damage locations.

2.5.4 Application of VBDD on Bridge

Salane et al. (1981) reported the possibility of using bridge stiffness calculated from experimentally determined mode shape and mechanical impedance plots to detect fatigue cracks on a bridge girder. They investigated the dynamic properties of a highway bridge with three spans excited by an electro-hydraulic actuator.

Biswas et al. (1990) reported on an investigation involving the dynamic response of a two-span composite highway bridge excited by a shaker. A fatigue crack was induced by removing a set of bolts at a splice connection on a girder. Changes in the frequency response function and small but consistent drops in natural frequencies were noticed due to the presence of the simulated crack.

Tang and Leu (1991) examined the frequency shifts due to the presence of damage in a defective prestressed concrete girder bridge. The bridge was excited by the step relaxation method. It was reported that changes in mode shape may have more

potential than frequency shifts to detect damage, since frequency shifts on an order of 0.01 Hz must be detected to identify damage.

Zhang and Aktan (1995) performed an investigation of VBDD using a calibrated FE model of a three-span highway bridge with a concrete deck on steel stringers located close to Cincinnati in Ohio. Modal characteristics of the bridge were inferred using forced vibration (impact) to calibrate the model. Damage was simulated on one of the steel stringers at midpoint of the middle span by changing the stiffness of a single beam element. The uniform flexibility curvature method was found to be capable of detecting damage, while changes in mode shapes and natural frequencies were insensitive to the presence of damage.

Farrar et al. (1994) performed a test using the I-40 bridge over the Rio Grande in Albuquerque, NM. The bridge superstructure consisted of a concrete deck supported by two steel plate girders. Four levels of damage were introduced by torch cuts on the web and flange of a girder, located in the mid span region, close to the seat of a floor beam. The bridge was excited by a hydraulic shaker and accelerometers were used to measure the vibration responses. Two sets of accelerometer spacings (4.87 m for a refined set and 6.2 m for a coarse set) were used to increase the accuracy in detecting damage locations. It was reported that resonant frequencies for the first two modes dropped by 7.6 and 4.4 percent, respectively, after the final level of damage was induced. Changes in natural frequencies were not noticed for the other levels of damage. The mode shapes after damage had been induced were compared with the initial mode shapes using the modal assurance criteria (MAC) (Ewins. 2000). Significant changes were observed for the final level of damage only. The damage index, mode shape curvature, change in flexibility,

change in uniform flexibility curvature and change in stiffness methods were also investigated to study the efficiency of these methods. The change in mode shape curvature and damage index methods proved capable of locating all levels of damage using both the coarse and refined sensor spacings. The change in stiffness method, on the other hand, was capable of locating all levels of damage using the coarse sensor distribution, while surprisingly it could only locate higher levels of damage using the refined sensor distribution. The other three methods investigated were typically capable of locating higher levels of damage using both sensor distributions.

Wang et al. (1997) investigated the damage index method using a simple span bridge supported by plate girders. Damage index values were assumed to be normally distributed, and were normalized to a mean value of zero and standard deviation of unity. Damage was induced on the flanges of girders and excitation was provided by impact hammer. Mode shapes were inferred from measured accelerations. The normalized damage index was found to be effective in detecting damage for severe damage cases.

Stubbs et al. (1999) investigated the damage index method to estimate the presence and severity of damage. Vibration testing on a four lane highway bridge (using 26 measurement locations on the deck and 4 locations on a column) that crossed I-40 was performed to measure the natural frequencies and mode shapes for the five lowest modes of that structure. An FE model that served as a base line (pristine condition) reference for the bridge was also generated using information from as-built drawings of the bridge. The location and severity of damage were estimated by comparing the mode

shapes of the real structure and FE model. The estimated damage was compared to cracking patterns found during a visual inspection; a good correlation was reported.

Maeck and De Roeck (1999) investigated damage detection on a pre-stressed concrete bridge in Switzerland. The structure was a three span bridge featuring three post-tensioned box cell girders, where damage was induced as concrete spalling, anchor head failure, tendon rupture and support settlement. The direct stiffness method was employed to detect and locate damage. Stiffness was calculated using measured mode shapes and natural frequencies. It was reported that presence of damage could be detected by tracing changes in the dynamic stiffness. The magnitude of stiffness change was small when the damage was on the end spans, leading to difficulties in predicting the damage location.

Choi and Kwon (2000) performed a numerical study on a railway (truss) bridge built in 1940. An FE model was developed using information from the design drawings. Measured static and dynamic data were used to update the stiffness of elements and support conditions of the structure, altered due to aging effects. Eight damage cases were induced by reducing the stiffness of eight different truss members. Two neural networks were developed and trained using numerically generated data. The bridge was divided into two areas demarcated by the midpoint of the bridge to narrow down the general damage locations into two. The first neural network was designed to identify where the damage was located with respect to the midpoint of the bridge, while the second neural network was designed to identify which truss member among selected eight members was damaged. It was reported that the two step neural network successfully located all the damage cases.

Pearson et al. (2001) reported on an experiment using a quarter-scale simply supported concrete bridge deck with a span of 4.8 m featuring Tee-beam construction. Accelerometers at seven different locations were set up to measure the vibration response while the bridge deck was excited by an instrumented hammer. A commercial modal analysis software package (Doebling et al. 1997) was used to extract the natural frequencies and mode shapes. Modal analysis of the bridge deck was performed while different levels of damage were induced on the bridge, as well as with the bridge deck in pristine condition. Damage in the form of cracking was induced by applying four point bending loads. Changes in modal properties for higher modes (mode 3 and above) were observed to be sensitive to damage, while the changes were not significant due to similar levels of damage for lower modes. It was also observed that inducing damage could either change the order of vibration modes or produce an entirely new vibration mode. As a result, it was recommended that natural frequencies related to similar mode shape patterns be compared while damage detection methods were applied. The effects of the non-linear behaviour of concrete (after inducing damage) on the dynamic properties, measured by calculating the so-called normalized reciprocity, were reported to be relatively insignificant for damage detection.

Kim and Stubbs (2003) introduced an algorithm for a non-destructive crack detection (NCD) scheme to identify, locate and quantify the severity of damage. The presence of damage was determined using statistical-pattern-recognition of normalized damage indices. A modified damage index that differed from that of Kim et al. (1995) was employed in this study. The severity of damage (cracking) was determined using natural frequency perturbations. A bridge on Highway 40 over the Rio Grande River,

NM, featuring a concrete deck, steel beams (stringers, floor beams and plate girders) was tested to evaluate the NCD scheme. Four damage cases were induced on the plate girders at approximately midpoint of the mid span. The first damage case was a torch cut on the web centered at mid height. The cut on the web was extended down to the bottom flange for the second damage case. The third damage case consisted of damage case 2 plus a torch cut on the bottom flange that started from the edge and extended halfway on both sides of the web. For the fourth damage case, damage case 3 was augmented with a complete cut in the bottom flange. Damage localization was reported to be successful with a localization error of 0.23%, i.e. the distance between predicted damage and inflicted damage was approximately 0.3 m. However, a false positive indication of damage was apparent in the south barrier wall, except for the case of the fourth level of damage. It was also reported that the severity of damage was estimated with a higher level confidence for damage cases 2 and 4. The percentage error in crack size estimation varied from 3.6% to 23.8%, where the severity of damage case 3 was determined with the lowest agreement with the actual damage scenario.

Galvín and Domínguez (2007) reported on the dynamic characterization of the Barqueta Bridge over the Guadalquivir River in Seville, Spain. The iconic bridge was a cable stayed bridge deck (box shaped deck consisting of concrete slab and steel beams), where cables were supported by a steel arch spanning over 168 m. The bridge was tested while excited by ambient traffic and accelerations were measured using nine accelerometers. Four methods were employed to extract modal properties from the measured vibration response to the bridge: a) Peak picking method (Bendat and Piersol 1993); b) Averaged Normalized Power Spectral Densities (Felber 1993); c) Enhanced

Frequency Domain Decomposition (Brincker et al. 2001); and Stochastic Subspace Identification (Peeters 2000). Natural frequencies for the first 10 modes were identified using the four methods and were found to be very close to each other, as well as to those obtained from an FE model. The effects of ambient temperature changes within a range of 10°C on natural frequencies were reported to be insignificant. The damping ratio was found to increase significantly (by approximately 200%) when half of the length of bridge deck was occupied with traffic. Comparing the mode shapes extracted at two times separated by an interval of 1 year using the Damage Index method, it was determined that the structure had no damage during this time interval. A simpler laboratory model made of steel was also used to evaluate the accuracy of the Damage Index method for locating damage. Damage location was detected with an error smaller than 3%.

Zhang (2007) reported on the use of data normalization and a probability-based statistical diagnosis tool to circumvent the effects of field uncertainties. A time series analysis, as suggested by Sohn and Farrar (2001), was performed to extract damage features for both the damaged and pristine conditions. The probability that the damage indicating parameter of the damaged structure exceeded the same damage indicating parameter for that structure in pristine condition was defined as the statistical index of structural novelty. A FE model of a three span continuous steel girder bridge was developed to create the time series response of vibration. Gaussian white noise was used to introduce noise in the measured time series. It was reported that induced noise (with signal to noise ratios of 10 dB and 20 dB) did not impair the performance of the statistical diagnosis tool (when used) with data normalization in localizing damage. A

dense grid of sensors was suggested for use with the above mentioned scheme, to increase the accuracy of damage identification.

2.5.5 Effects of Ambient Temperature on Natural Frequencies of the Structure

The effects of ambient temperature changes on the natural frequencies of bridges have been observed by many researchers. These effects often mask the effects of a severe damage case. A brief review of temperature effects on modal properties of a structure is given below.

Askegaard and Mossing (1988) reported a 10% variation in the natural frequencies of a three span foot bridge over a one year period. Roberts and Pearson (1998) found a range of 3%–4% variation in the natural frequencies of a nine span bridge over a one year period. Farrar et al. (1997) reported an approximately 5% variation in the natural frequencies of the Alamosa Canyon bridge due to temperature fluctuations over a period of 24 hours. Rohrmann et al. (2000) found a 10% variation in natural frequencies over a period of one year for a seven span bridge in Berlin.

Peeters et al. (2000, 2001) monitored the Z-24 overpass in Switzerland over a period of one year at different temperatures and reported a variation of 14%-18 % in natural frequencies. Figure 2-5 shows the variation in measured natural frequencies with temperature for the Z-24 overpass. The white line superimposed on the data shows the general trend of changes in natural frequency with temperature. In their study, the variation of natural frequencies with temperature could be roughly approximated as a bi-

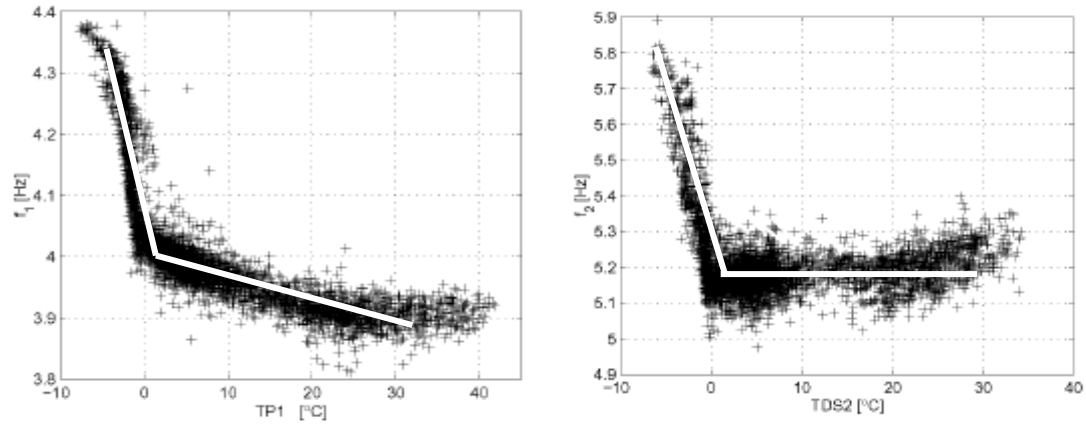

Figure 2-5. Natural frequency vs. temperature for the Z-24 overpass (reproduced from Peeters et al. (2000)).

linear plot having a knee at 0˚C, a fact that was attributed primarily to increases in the elastic modulus of the asphalt pavement at temperatures below 0°C.

Ni et al. (2005) reported a variation of 0.2% - 1.52% in natural frequencies due to temperature changes for the Ting Kau Bridge in Hong Kong over a one year period. It was also mentioned that the effects of temperature may mask the effects of damage on natural frequencies.

Xia et al. (2006) observed the variation in natural frequencies of an experimental reinforced concrete slab for different levels of ambient relative humidity (15% - 80%) and temperature (10ºC - 40ºC). Natural frequencies related to bending modes were reported to decrease by 0.13% - 0.23% for every 1ºC increase in temperature, while a 0.03% decrease in natural frequencies was observed per 1% increase in relative humidity. Changes in modal properties related to torsional modes were found to be significantly different from those related to bending modes.

Kim et al. (2007) performed vibration tests over a temperature range of 0ºC to 30ºC using a model of a stainless steel plate-girder bridge in a controlled, laboratory

environment. A variation in natural frequencies of 6.3% to 17% was observed over this temperature range, while the maximum change in natural frequencies due to inflicted damage was 5.6 %. The most severe damage case induced in this study was a complete cut in the bottom flange.

2.5.6 Summary

In summary, the following trends were observed from previous studies:

- VBDD has become an industrial tool to monitor rotating machinery. However, VBDD is still in the research phase for civil engineering structures. Civil engineering structures are quite different and more complex than rotating machinery in terms of non-homogeneity of material properties, uncertainty in the connectivity of different components, their larger size and exposure to different ambient environments. On the other hand, measurement of the vibration response and extraction of the modal features of a complex civil engineering structure is more economical and may be performed more quickly than conventional health monitoring methods. Therefore the economic potential, as well as the many challenges, have made VBDD a very active area of research recently.
- VBDD for offshore platforms based on natural frequency shifts was very challenging due to significant changes in mass over time due to marine growth and changes in fluid levels in tanks.
- Research on simple structural components such as beams have successfully demonstrated the potential of VBDD, leading researchers to investigate more complex structures like bridges. In addition, the monitoring of bridge structures on a regular basis is mandatory in many jurisdictions.

- Natural frequencies appear to be relatively insensitive to small-scale damage, but are influenced more strongly by temperature variations.
- VBDD methods based on mode shape changes (or some derivative thereof) have been successfully applied to various bridge structures.
- Non contact-based vibration sensing methods, such as image processing, exhibit potential to become a faster and more economical option in acquiring intensive and high resolution vibration response data.
- Statistical pattern recognition techniques, coupled with efficient data management, also show promise for damage detection using the vibration response in changing ambient environments.

CHAPTER 3. DESCRIPTION OF EXPERIMENTAL STUDY

3.1 BACKGROUND ON THE ATTRIDGE DRIVE OVERPASS

The Attridge Drive Overpass is located at the interchange of Attridge Drive and Circle Drive in Saskatoon, Saskatchewan, Canada (Figures 3-1 and 3-2). It was constructed in 2001 and features six lanes, two uneven spans (38.7 m and 30.6 m), and a skewed alignment of approximately 16° relative to the abutments. The conventional

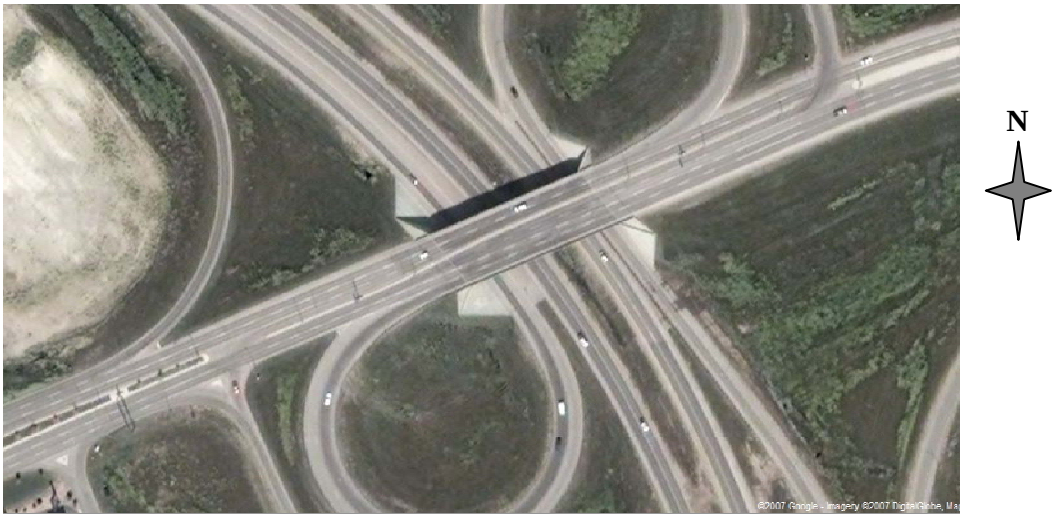

Figure 3-1. Arial view of the Attridge Drive Overpass (Source: Google Maps).

Figure 3-2. Side view of Attridge Drive Overpass, viewed from the north.

composite superstructure is composed of a reinforced concrete deck and nine steel girders, with a total width of 27 m.

To eliminate potential corrosion problems associated with expansion joints, the overpass features integral abutment construction in which the bridge deck and girders are made continuous with the abutment walls. Thermal expansion is then accommodated by frame action achieved primarily through flexure of the slender abutment walls and pile supports. The abutments are supported by 6 piles on each side.

3.2 INSTRUMENTATION OF THE BRIDGE

For this study, the primary instrumentation consisted of six accelerometers (model JTF/F 482-03, Sensotec Inc., Ohio and model EpiSensor FBA ES-U, Kinemetrics Inc., California), each configured for a maximum range of 0.5 g and precision of 0.00025 g. The accelerometers were calibrated before each experimental setup as per the manufacturer's specifications. The accelerometers were fixed to the bridge deck using either putty during summer or ice when the temperatures were below freezing. Prior to installation of the accelerometers, the bridge surface was cleaned to obtain intimate contact at the base of the instrument. The base was then levelled to ensure horizontal positioning. In the summer, accelerometers were placed directly on the bridge deck, approximately 12 inches away from the face of the barrier wall. During the winter months, on the other hand, they were placed on the barrier wall to avoid any accumulated snow.

As shown on Figure 3-3, one reference accelerometer remained at a fixed location, while the remaining five sensors were moved successively to each of the four bridge quadrants, designated as South West, South East, North West and North East. In

each of the four quadrants, the five mobile accelerometers were mounted at 5.0 m intervals longitudinally, with the first accelerometer located 5.0 m from the centre-line of the abutment wall in that quadrant.

Because the bridge was in service during testing, the accelerometers were only installed off the driving lanes, either close to, or on top of the barrier walls, as discussed previously. The accelerometers were connected to a 32-channel data acquisition system (DAQ Card 6036 E, National Instruments SCXI), which, in turn, was controlled by a personal computer.

In addition to the accelerometers, a total of 51 conventional electrical 350-ohm strain gauges with a 6 mm gauge length were permanently installed at the locations indicated on Figure 3-3. At each of these 17 locations, three strain gauges were mounted on the web of the steel girder, aligned vertically to enable the determination of the girder

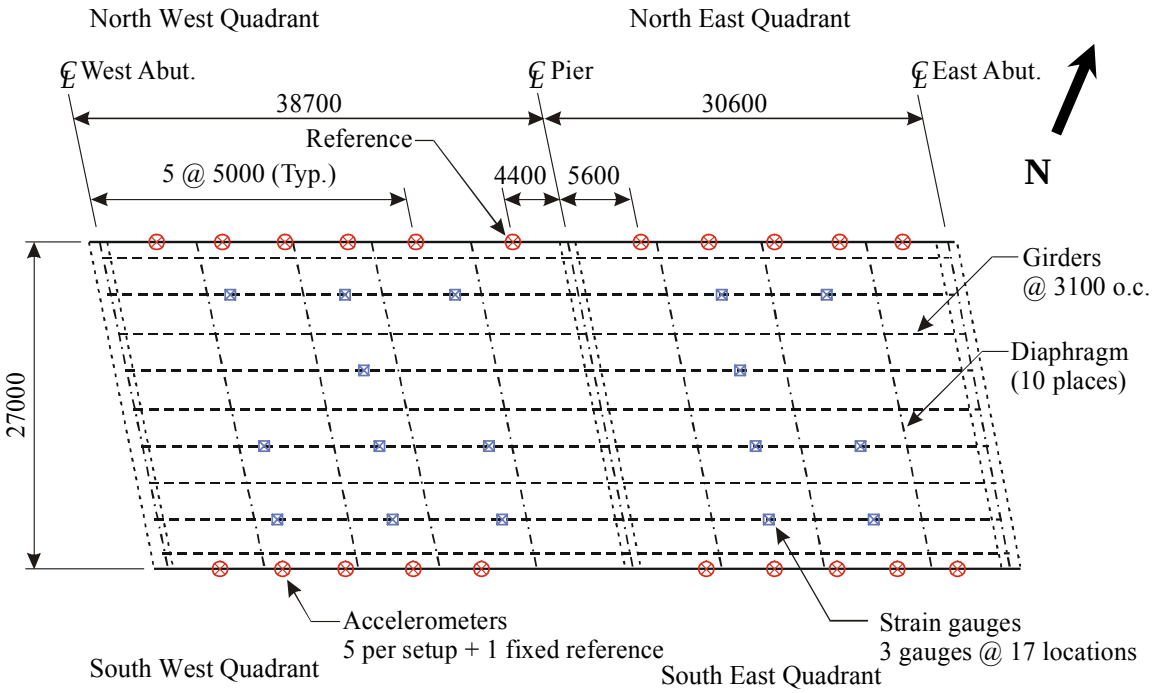

Figure 3-3. Plan View of the bridge deck, showing a schematic layout of the accelerometers and strain gauges (dimensions in mm).

curvature at that point. Strain gauge data were not considered in this study due to the low signal to noise ratios observed in the readings from these sensors.

3.3 FIELD TESTING

The overpass was monitored on four different dates throughout the study, at different ambient temperatures ranging from -12°C to 40°C. Ambient temperature conditions, as well as the number of data sets obtained on each occasion, are given in Table 3-1. The temperature of the top surface of the bridge deck was measured intermittently during the testing periods, which typically had duration of approximately 6 hours. The ambient air temperature was also measured periodically below the bridge. During the testing periods, the bridge deck temperature (top surface of the bridge deck as well as below the bridge) varied over the ranges indicated in Table 3-1.

Dynamic excitation for the vibration measurements on the overpass was provided solely by ambient traffic. Typically, excitation due to large trucks or fully occupied buses was considered for further analysis since these generated the largest signal levels. The traffic lane closest to the accelerometers was closed during the testing

Table 3-1. Summary of data sets acquired.

Temperature range	Number of Data Sets by Quadrant for each sensor location			
	South West Side	South East Side	North West Side	North East Side
-12°C to -5° C	17	11	12	12
-9°C to -7°C	14	21	22	8
20°C to 26°C	9	9	22	12
30°C to 40°C	12	15	N/A	2

period to permit safe movement of technical personnel. This lane closure created a bottle neck at the entrance of the overpass, which ultimately reduced the speed of vehicles in these lanes during testing; therefore, the bridge likely experienced lower amplitude excitation than normal due to these reduced traffic speeds.

Time series response data were acquired initially for a period of 30 seconds at a sampling rate of 150 samples per second. The vibration of the overpass generated by a heavy vehicle decayed within a very short period of time after the vehicle had crossed. It was observed that the decaying portion of vibration (damped free vibration) of the overpass was influenced by the presence of other vehicles if the data measurement period was 30 seconds. To reduce the influence of this interference, a shorter period (10 seconds) was subsequently selected to acquire the response data. A higher sampling rate (300 samples per second) was used to increase the number of discrete data points in the new shorter record. The data were recorded using LabView™ software (LabView 2000) and stored digitally on a personal computer.

3.4 DATA PROCESSING

As detailed in the following sections, the data conditioning used in the natural frequency extraction phase included the removal of static components and signal drift, normalization to attenuate the influence of load event intensity, and filtering to improve the clarity of resulting response spectra.

Modal properties of the overpass were inferred from acceleration spectra. Acceleration spectra were derived from acceleration time series using Fast Fourier Transform (FFT); details of the modal property extraction are described in Sections 3.4.5 and 3.4.6.

Prior to performing the FFT, acceleration time series were subjected to several data processing steps to improve the quality of the signals for subsequent analyses. Natural frequencies were then inferred from averaged frequency domain representations of the acceleration. The flow chart in Figure 3-4 gives an overview of these processes. For the mode shape extraction phase, a similar data conditioning process (see Figure 3-5) was used, except that normalization to account for loading intensity was not performed, since response spectra were subsequently normalized by that of the reference accelerometer.

3.4.1 Removal of the DC-component

For a structure vibrating in place, the acceleration time history must oscillate about a mean value of zero. Depending on the instrumentation settings, though, the accelerometer readings may contain a constant (DC) offset. If a signal does contain a DC-component, it will show up as a spurious peak at 0.0 Hz on spectral plots generated by the FFT analysis; in addition, the non-physical static offset will contaminate subsequent deflection calculations. To avoid this problem, DC-components were removed from the raw time series data before performing a Fast Fourier Transform. This was done by subtracting the time-averaged mean value of the acceleration from the original time series of each data set (Ramirez 1985). For example, an acceleration time series with an obvious DC offset is illustrated in Figure 3-6.

3.4.2 Data Conditioning Using High Pass Filter

A high pass digital filter was used to remove any slowly varying drift that may have appeared in the acceleration signal. For this purpose, the following first order,

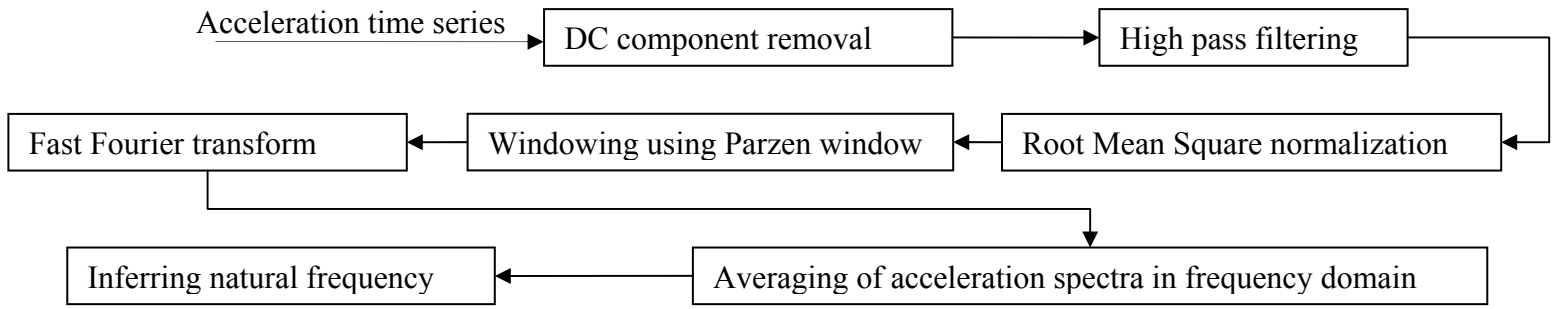

Figure 3-4. Flow chart of data conditioning processes to extract natural frequency.

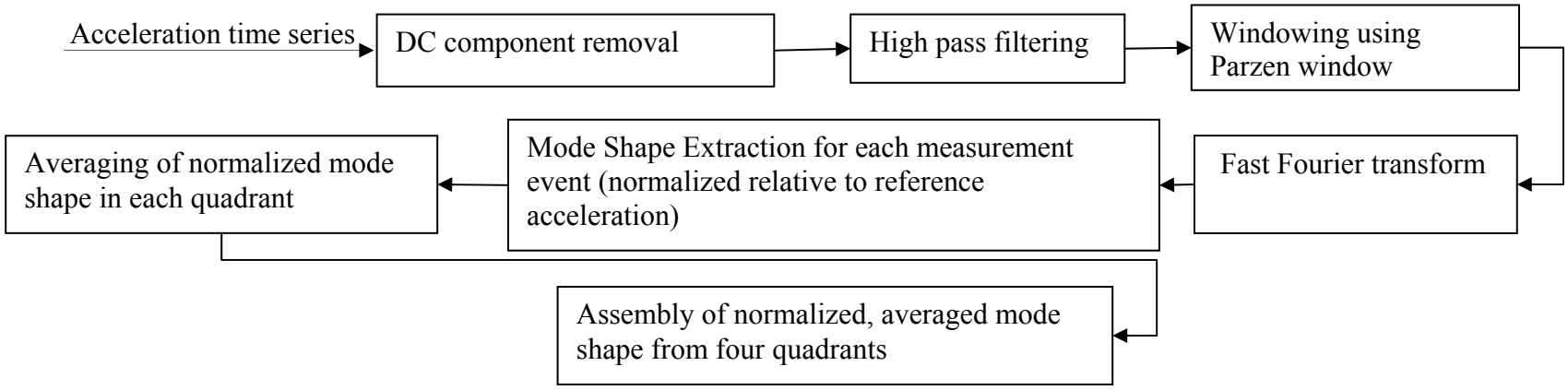

Figure 3-5. Flow chart of data conditioning processes to extract mode shape.

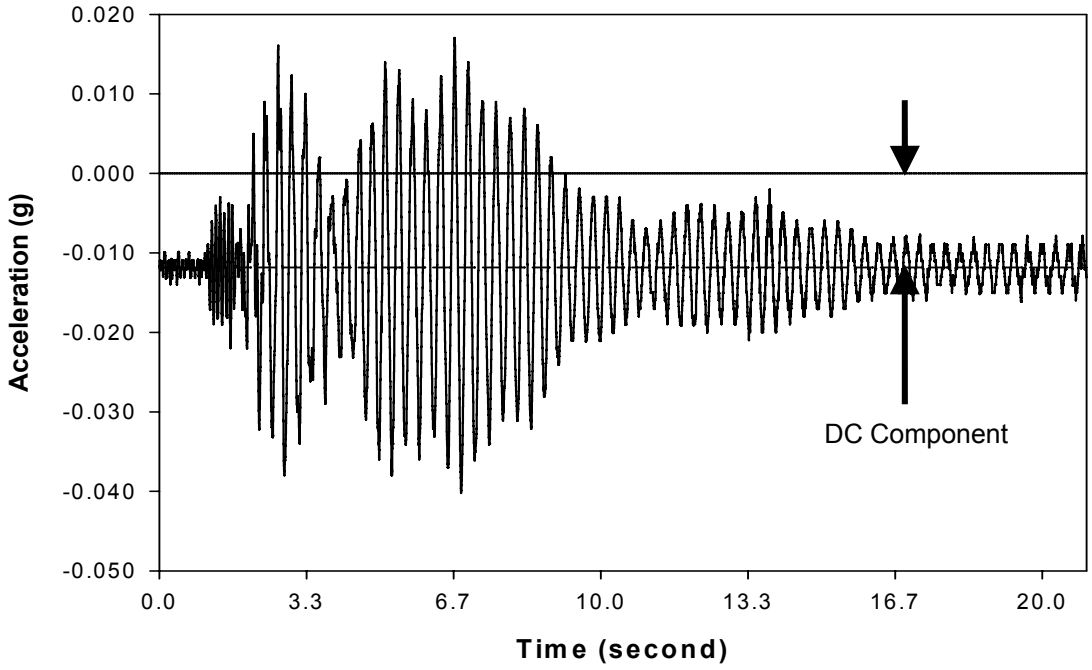

Figure 3-6. Acceleration time series prior to removal of DC component.

recursive, high pass digital filter was used to condition the acceleration data:

$$y_n = 0.999y_{n-1} + x_n - x_{n-1} \tag{3.1}$$

where x_n is the instantaneous measured acceleration at the instant t_n, x_{n-1} is the instantaneous measured acceleration at the previous instant t_{n-1} and y_n is the conditioned (modified) acceleration reading at the same time instant. It is a recursive process because the previously conditioned output of acceleration for the previous time step y_{n-1} is used to condition the output acceleration y_n at time the instant t_n.

The term 'high pass' filter means that only higher frequency components are allowed to pass through the filter. The order of a digital filter is the largest count of previous input or output samples used in the recursive process. For the filter used in this study, only one previous time step was considered, producing a first order filter.

3.4.3 Root Mean Square Normalization

Natural frequencies were extracted from averaged acceleration spectra. Since the spectral amplitude from different loading events and accelerometer locations could vary drastically depending on vehicle size, speed, and number of vehicles, it was necessary to scale all the data sets to a common base to facilitate the identification of the natural frequencies. To accomplish this, the time series signals were normalized by their respective root mean square (RMS) values, the square of which are proportional to the energy represented by the signal. In the case of an acceleration wave form, the energy depends on the on the intensity of the traffic excitation.

The RMS value of a data set is the square root of the mean-squared value of the variable in that set. In mathematical form, the RMS is expressed as

$$\mathrm{RMS}(X) = \sqrt{\frac{\sum_{i=1}^{n} {x_i}^2}{n}}\ , \tag{3.2}$$

where $x_{i,}$ in this case, is the acceleration at the i^{th} discrete point in time, and n is the number of samples contained in each data set. Note that, prior to normalization, the time history x_t had been made into a zero-mean process, as described in Section 3.4.1, and the high-pass filter applied, as described in Secion 3.4.2.

3.4.4 Window Functions

An assumption inherent in the Fourier transform is that the process in question is periodic, repeating itself identically in every period. Non-periodic processes containing discontinuities at either end of the period will introduce spurious frequency components into the resulting spectrum, causing a blurring, or "leakage" of the frequency domain representation of the response away from the true frequency components into adjacent frequency "bins" (see Figure 3-7). Window functions are therefore applied to the

original time series data before applying the FFT to ensure smooth, zero amplitude transitions at the both ends of the segment of data being analysed. A more detailed discussion on window functions and their effects is given in Ramirez (1985).

A Parzen window function was selected for this work because it appeared to give the best resolution in the spectral peaks. On the other hand, a window function reduces the energy in the original signal, leading to a possible reduction in precision in the resulting spectrum due to numerical rounding errors. However, root mean square normalization prior to windowing, as described in Section 3.4.3 increases the signal magnitudes that helped to increase the precision in the resulting spectrum.

3.4.5 Extraction of Natural Frequencies

Local maxima in the output spectra for any location occur at frequencies where either the excitation spectra features a peak or at the natural resonant frequencies of the system, where dynamic amplification effects are most prominent. Peaks at non-resonant frequencies are typically random in nature and, thus, will tend to an average value of zero over several data sets. Therefore, these non-resonant peaks can be attenuated by averaging the spectra produced by several data sets of measured acceleration.

In the present study, acceleration spectra for each sensor location and load event were averaged for each temperature range to produce smoothed curves suitable for natural frequency extraction. The number of data sets used to average the acceleration spectra were the available data sets for each sensor location within each quadrant in each temperature range, as shown in Table 3-1.

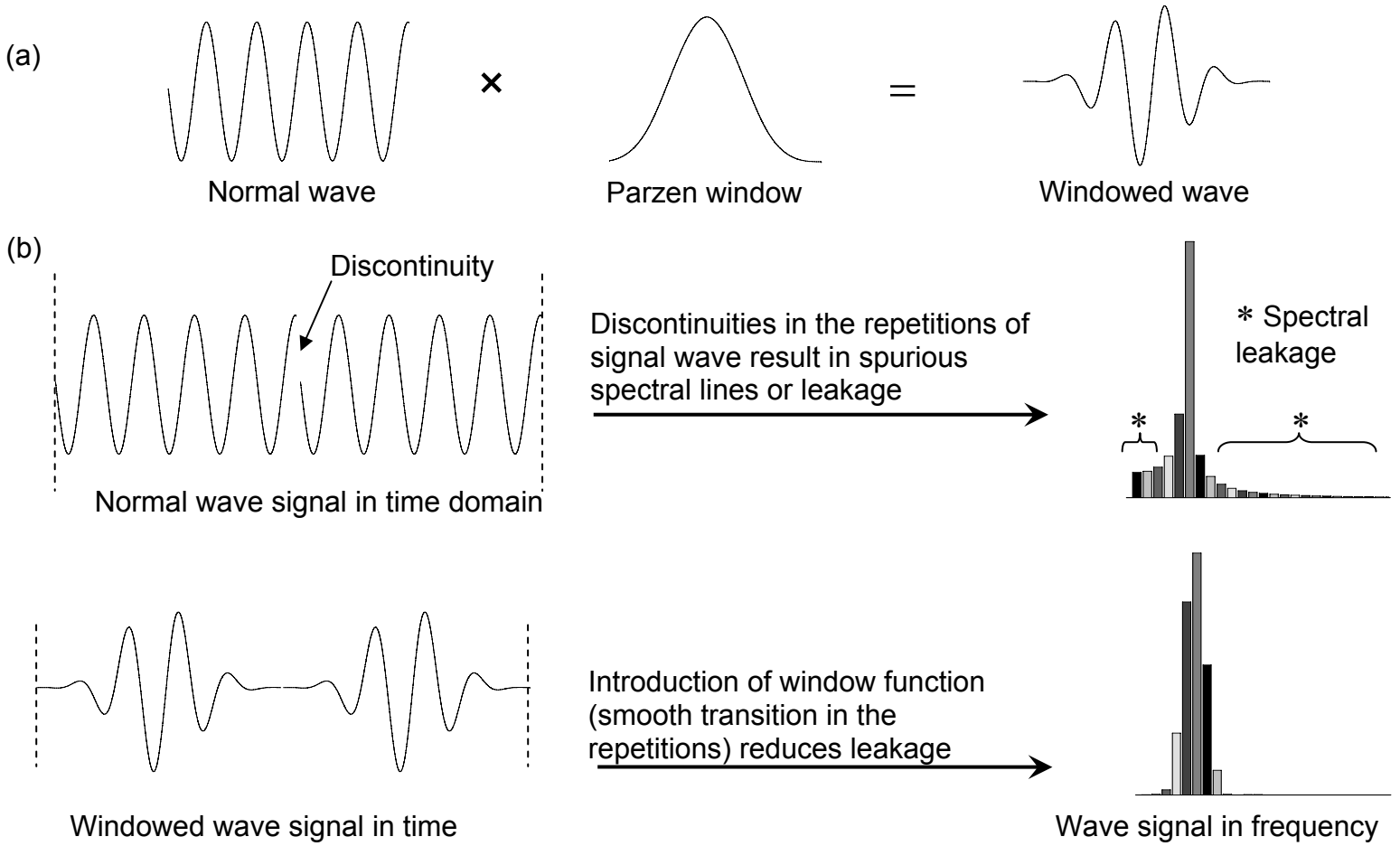

Figure 3-7. The application of window functions: (a) transforming the time series; and (b) the effects of windowing on the resulting spectrum.

Figures 3-8 and 3-9 show typical plots of the averaged acceleration spectra in each quadrant for the temperature range of 20°C to 26°C. Each plot contains the average spectra of all sensor locations in the given quadrant, as well as of the reference sensor, to facilitate the comparison of peaks in the spectra. The number of data sets used to average the acceleration spectra for the north–west, north–east, south–west and south–east quadrants were 22, 12, 9 and 9, respectively. Since the average acceleration spectra for five sensor locations are plotted in each figure, there are 20 (5 sensor locations per quadrant x 4 quadrants) averaged acceleration spectra available in the temperature range of 20°C — 26°C to compare for natural frequency identification. Resonant frequencies with a higher rate of occurrence among all averaged spectra in a particular temperature range were then taken to be the natural frequencies of the overpass in that temperature range.

For example, Figure 3-8 (a) shows the first three distinctive peaks in the average spectra corresponded to frequencies of 3.085 Hz, 3.26 Hz, and 3.81 Hz, respectively. In addition, these peaks are consistent for all five sensor locations. Similarly, frequencies for the first three peaks could also be identified in Figure 3-8(b) and Figure 3-9 (a) and (b). Table 3-2 summarizes the natural frequencies corresponding to first three peaks in the temperature range of 20°C — 26°C.

The most commonly observed frequency values at the first three peaks were then selected as the best estimate of the system natural frequencies. From Table 3-2, it is evident that the best estimate of first three natural frequencies would be the average value for all four quadrants, or 3.076Hz, 3.26 Hz and 3.81 Hz, respectively. Figures 3-8 and 3-9 also show the presence of fourth, fifth and higher peaks. However, since they

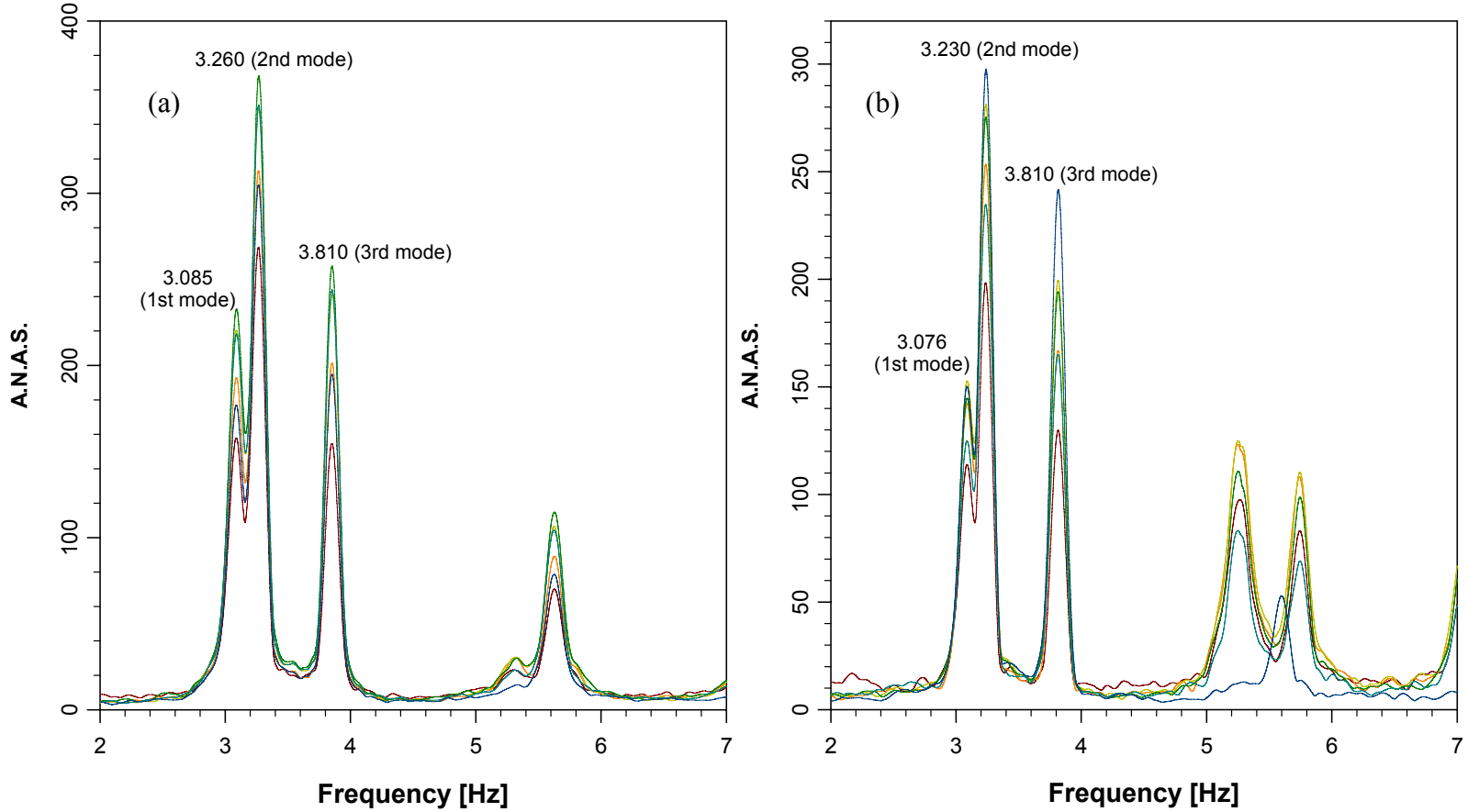

Figure 3-8. Averaged normalized acceleration spectra from six accelerometers (each line represents a single accelerometer) in the temperature range 20°C — 26°C showing spectral peaks in: (a) the north–west quadrant; and (b) the north–east quadrant.

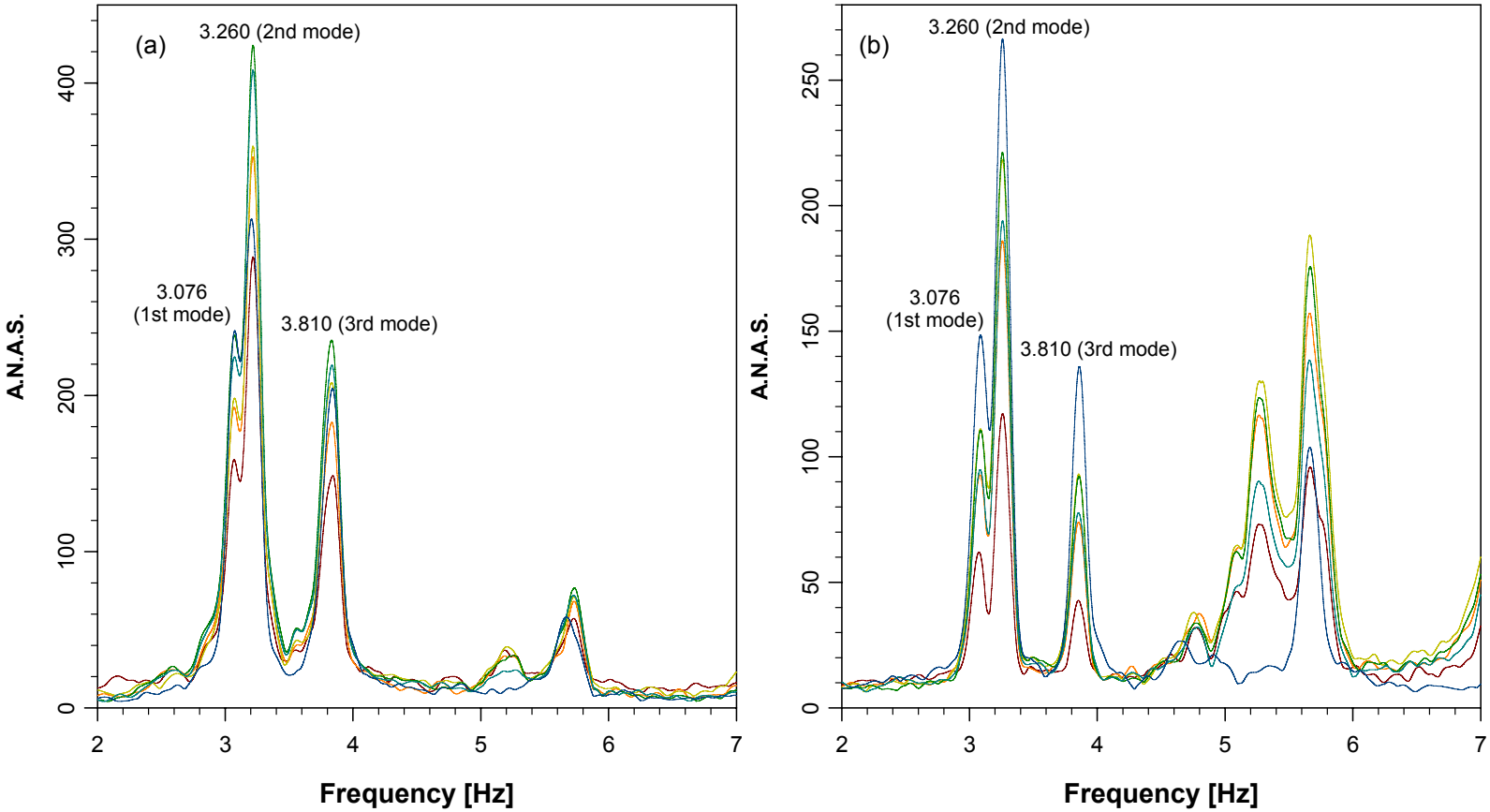

Figure 3-9. Averaged normalized acceleration spectra from six accelerometers (each line represents a single accelerometer) in the temperature range 20°C — 26°C showing spectral peaks in: (a) the south–west quadrant; and (b) the south–east quadrant.

Table 3-2. Frequencies (Hz) corresponding to first three peaks (20°C — 26°C).

	Frequency in Hz (Number of average spectra)			
	North–West Quadrant	North–East Quadrant	South–West Quadrant	South–East Quadrant
First peak	3.085 (5)	3.076 (5)	3.076 (5)	3.076 (5)
Second Peak	3.26 (5)	3.23 (5)	3.26 (5)	3.26 (5)
Third Peak	3.81 (5)	3.81 (5)	3.81 (5)	3.81 (5)

were not consistent for all sensor locations, they were not considered in subsequent analyses.

Natural frequencies in other temperature ranges were obtained following the same methodology as mentioned above. Plots of averaged spectra, along with tabulated data for the frequencies corresponding to first three spectral peaks for other three temperature ranges are given in Appendix A.

3.4.6 Mode Shape Extraction

A flow chart of the data conditioning processes for mode shape extraction was shown in Figure 3-5. Once the natural frequencies were identified as mentioned in Section 3.4.5, mode shapes for each quadrant were assembled by extracting corresponding modal amplitudes at the identified natural frequencies from the original accelerometer spectra (without RMS normalization). In order to assemble the mode shape for the whole system from various loading events and accelerometer configurations, modal amplitudes for individual accelerometers from specific events were normalized by the corresponding reference accelerometer amplitude for that event. The phase angle for each event (computed as part of the FFT analysis) at each sensor location was compared with the phase angle of the reference sensor for the same event

to identify the relative sign of modal amplitude with respect to reference sensor (the phase angle was either near-zero if the acceleration reading had the same sign as the reference acceleration or near 180° if it had the opposite sign). The average mode shapes at the first three natural frequencies for all sets of data were then assumed to be the mode shapes corresponding to a specific temperature range in subsequent discussions.

The standard deviation of normalized mode shape amplitudes at individual sensor locations was defined as the uncertainty in these field measurements. Thus, the uncertainty in mode shape measurements at each sensor location was calculated as

$$\text{Uncertainty} = \sqrt{\frac{\sum\left(\phi_{ij} - \bar{\phi}_i\right)^2}{h^2}}\ , \tag{3.3}$$

where ϕ_{ij} is the modal amplitude of the j^{th} measurement event at the i^{th} sensor location, and n is the total number of measurement events, and $\bar{\phi}_i$ is the mean modal amplitude at the i^{th} location.

CHAPTER 4. EXPERIMENTAL RESULTS

4.1 BACKGROUND

In this chapter, the natural frequencies and mode shapes extracted from the acceleration data acquired on the Attridge Drive Overpass are presented. Since the ambient temperature varied over the period during which the field measurements were taken, the influence of temperature on natural frequencies is also presented in this chapter. In addition, due to the influence of a number of factors, the mode shapes varied from one trial to the next. As described in Chapter 3, this variation was quantified by calculating the standard deviation of the normalized modal amplitude at each sensor location, thereby providing a measure of the reliability of the measured mode shape data.

4.2 NATURAL FREQUENCIES

Natural frequencies were identified by observing the peaks on the plots of the averaged and normalized acceleration spectra, which were obtained as described in Chapter 3. As mentioned previously, the dynamic response of the overpass was monitored at ambient temperatures ranging from -12°C to 40°C.

The natural frequencies obtained for the lowest three vibration modes at different ambient temperatures are presented in Table 4-1 and illustrated in Figure 4-1. It should be recalled that temperatures were measured periodically over a six hour test period; during that period, the ambient conditions varied over the ranges indicated in Table 4-1.

Since the reported natural frequencies were derived from averaged spectra of

Table 4-1. Experimental natural frequencies.

	Natural Frequencies (Hz)		
Temperature range	1st Mode	2nd Mode	3rd Mode
-12°C to -5°C	3.35	3.68	4.36
-9°C to -7°C	3.3	3.57	4.30
20°C to 26°C	3.07	3.26	3.81
30°C to 40°C	3.07	3.23	3.80
% Change[a]	8.4%	12.2%	12.8%

[a] % Change of natural frequencies over the total temperature range at each mode, relative to those in the lowest temperature range.

loading events occurring throughout the test period, only averaged natural frequencies were available; the variation of frequencies within individual testing periods was not investigated.

4.3 INFLUENCE OF TEMPERATURE ON NATURAL FREQUENCIES

It is evident from Table 4-1 that there is an inverse relationship between the temperature and natural frequencies; i.e., natural frequencies were observed to decrease with rising temperature. Figure 4-1 shows the trend more comprehensively.

It is observed that the natural frequencies increase rapidly with decreasing temperature at lower temperatures (it is impossible to pinpoint the breakpoint due to scarcity of data), while much less variation is seen at higher temperatures (above 20°C). This same phenomenon was also broadly observed by Peeters et al. (2000), a study that was presented briefly in Chapter 2. In that study, it was found that the relation between natural frequency and temperature could be approximated, in a general sense, as a bilinear plot having a knee at 0°C (see Figure 2-5), a fact that was attributed primarily to increases in the elastic modulus of the asphalt pavement at temperatures below 0°C. In the present study, the lack of data between -7°C and 20°C makes it impossible to

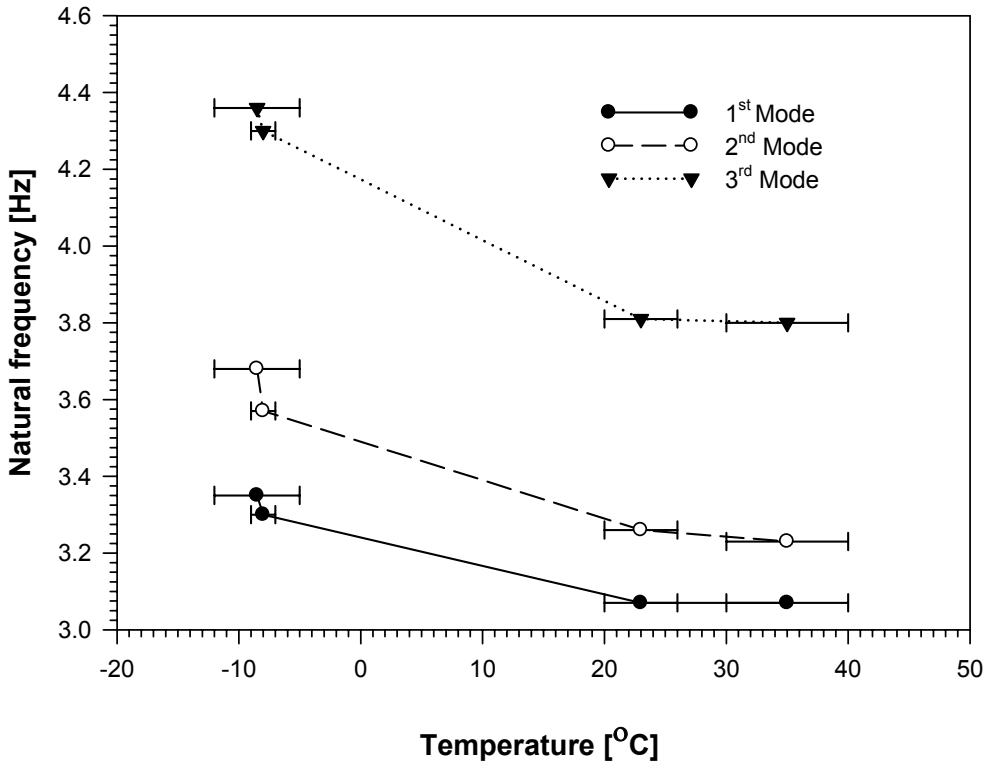

Figure 4-1. Natural frequency vs. temperature for the Attridge Drive Overpass.

confirm that a similar transition occurs at the freezing point for the Attridge Drive Overpass, although such a trend could be reasonably anticipated based on the findings of Peeters et al. (2000).

The natural frequencies for the first, second and third vibration modes of the Attridge Drive overpass were seen to decrease by 8.3%, 12.2% and 12.8%, respectively, over the temperature range considered, suggesting perhaps that higher modes may be more sensitive to temperature effects. As described in Section 2.3, some other authors have also reported natural frequency changes due to temperature and environmental effects. Reported variations range from 3 to 18% over time periods ranging from 24 hours to one year.

4.4 MODE SHAPES

As described in Section 3.4.6, mode shapes derived from each event were assembled from the acceleration spectra from individual sensors, using corresponding data from the reference acceleration to normalize resonant response peaks in the individual spectra to a common basis. Averaged mode shapes for all the events in a temperature range were taken as the representative mode shape for that particular temperature range, assuming that the deviation of a mode shape representing a single event from the average mode shape was random in nature.

Figures 4-2 and 4-3 show the mode shapes at different temperature ranges. Mode shapes shown here were unit-norm normalized as described in Section 5.3, so that they could be compared both to each other and to numerically obtained mode shapes described in subsequent sections. As mentioned in Chapter 3, mode shapes were measured along the two outside edges of the bridge, leading to an apparent similarity between the first and third modes. As demonstrated in numerically generated mode shapes in Chapter 5, however, the first mode was seen to be a pure bending mode, with minimal variation across the width of the bridge between the two edges, whereas the third mode was found to include both bending and torsion components, generating both lateral and longitudinal variations in the mode shape.

In Figure 4-3(d,e,f) , mode shapes shown for the temperature range of 30°C to 40°C are not complete. Due to erroneous data, measurements for the northwest quadrant were not obtained. The abrupt jump in the northeast quadrant at 44.3 meters from the west abutment wall is also obviously erroneous. However, mode shapes on the south side for this temperature range are thought to be reliable. A comparison of measured

mode shapes in the temperature range of 20°C to 26°C to the mode shapes generated numerically is given in Section 5.3.

4.5 COMPARISON OF MODE SHAPE AT DIFFERENT TEMPERATURES

A quantitative comparison between mode shapes can be made using the modal assurance criteria (MAC) (Ewins. 2000), defined as

$$\mathrm{MAC} = \frac{\left[\sum_{j=1}^{n}(\phi^{t_1})_j(\phi^{t_2})_j\right]^2}{\left[\sum_{j=1}^{n}(\phi^{t_1})_j(\phi^{t_1})_j\right]\left[\sum_{j=1}^{n}(\phi^{t_2})_j(\phi^{t_2})_j\right]}, \tag{4.1}$$

in which $\phi^{t_1}$and ϕ^{t_2} are the two mode shape vectors, in this case corresponding to two different temperature ranges t_1 and t_2, the subscript j indicates an element in the vectors (corresponding to a particular sensor location), and n represents the number of points at which the two mode shapes are compared. A MAC value of 1.0 would indicate that the two mode shapes are perfectly correlated at the measurement points, while a value of zero would indicate that they are orthogonal.

To investigate the effects of temperature on mode shapes, MAC values were calculated using Equation 4.1 to compare the mode shape derived at a given temperature range to that found at the reference temperature range of 20°C to 26°C. Mode shapes in the north and south side were compared separately. There were no sensors at locations 20 m and 44.5 m from the west abutment wall for the temperature ranges of -9°C to -7°C and -12°C to -5°C. Therefore, a cubic spline curve was fitted to the mode shape data to interpolate the modal amplitude at locations 20 m and 44.5 m from the west abutment wall for the temperature ranges of -9°C to -7°C and -12°C to -5°C, so that

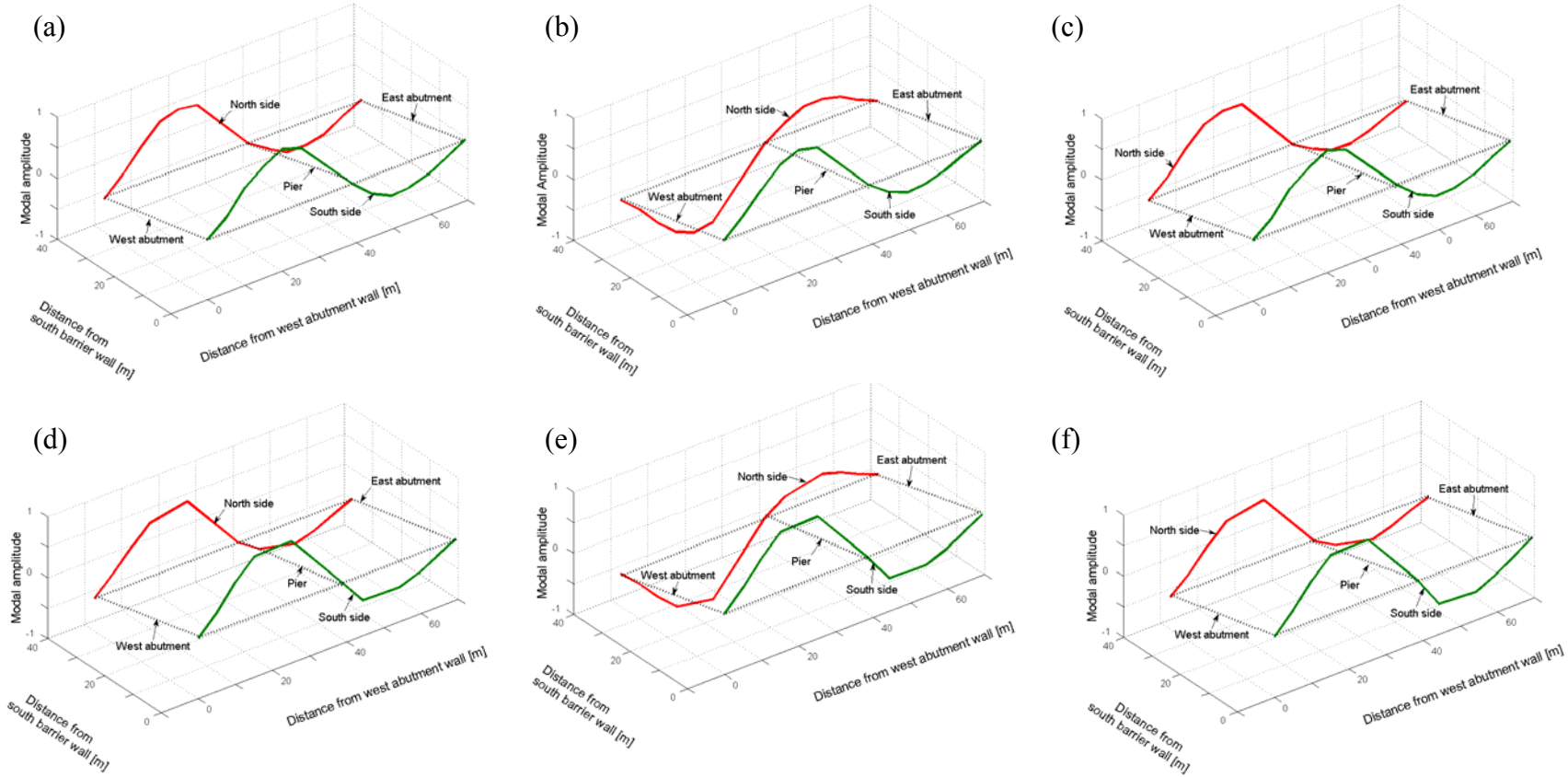

Figure 4-2. Measured mode shapes in the temperature range of 20°C to 26°C: (a) 1st mode; (b) 2nd mode; (c) 3rd mode, and in the temperature range of -12°C to -5°C: (d) 1st mode; (e) 2nd mode; (f) 3rd mode.

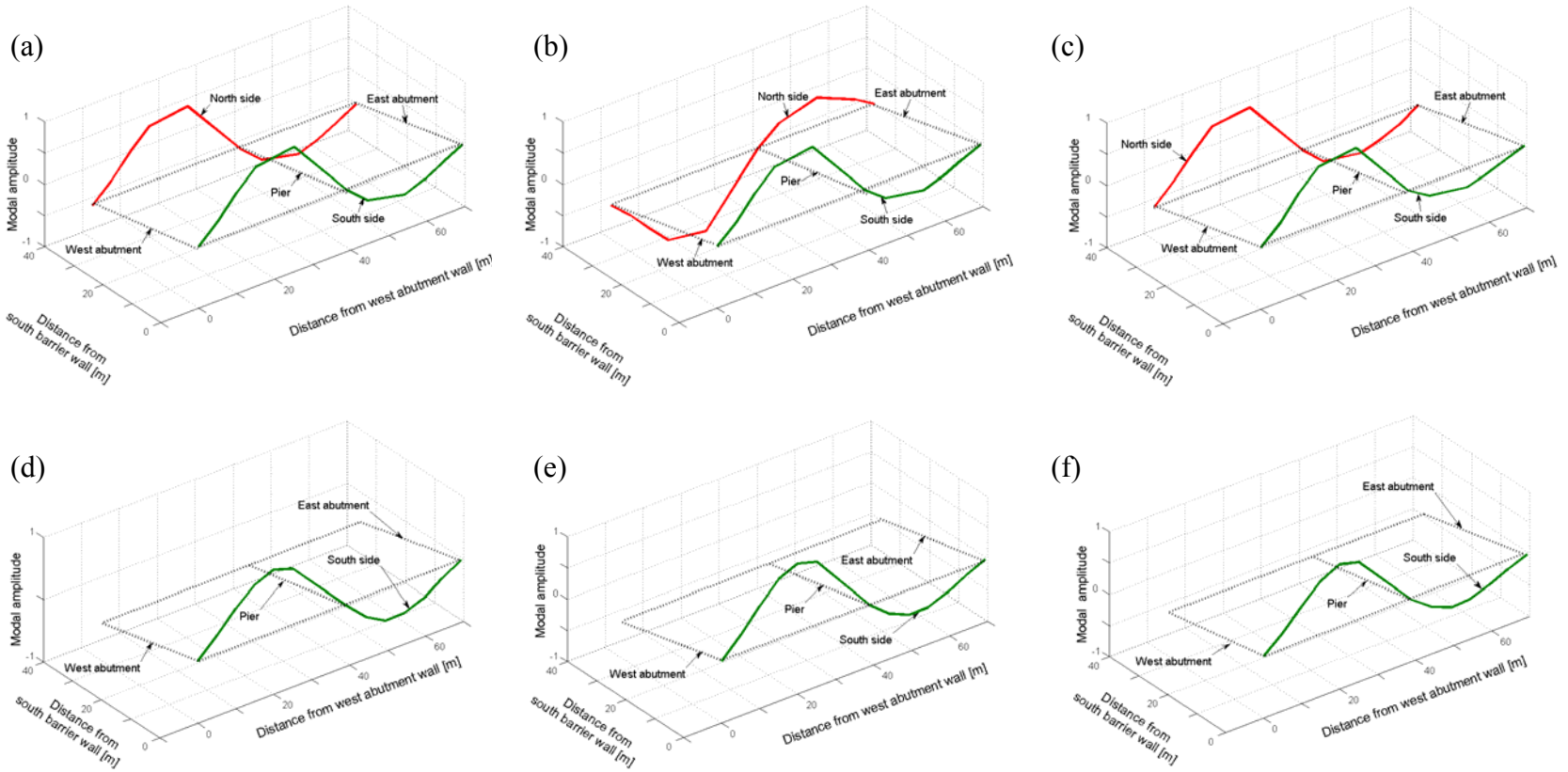

Figure 4-3. Measured mode shapes in the temperature range of -9°C to -7°C: (a) 1st mode; (b) 2nd mode; (c) 3rd mode, and in the temperature range of 30°C to 40°C: (d) 1st mode; (e) 2nd mode; (f) 3rd mode.

mode shapes for these two temperature ranges could be compared with the mode shapes in the other two temperature ranges. Averaged mode shapes (in all temperature ranges) used for subsequent comparisons were normalized by the modal amplitude of a sensor located 20 m away from the west abutment. Results of this comparison are given in Table 4-2. Mode shapes at different temperatures appear to be very similar, based on the MAC values presented in Table 4-2, even though there are changes in natural frequencies.

As an alternative method of comparing the mode shapes, the difference between the mode shape in a given temperature range and the mode shape in the temperature range of 20°C to 26°C was calculated by

$$\Delta\phi_T = \frac{\phi_{Ti} - \phi_{To}}{|\phi_{To}|_{\max}} \times 100, \tag{4.2}$$

where $\Delta\phi_T$, ϕ_{Ti} and ϕ_{To} represent the vector of percentage change in mode shape between two temperature ranges, mode shape vector in temperature range *i*, and mode shape vector in the temperature range of 20°C to 26°C, respectively. The term $|\phi_{To}|_{\max}$ represents the absolute maximum value of the ϕ_{To} vector.

Table 4-2. Modal Assurance Criteria (MAC) of the mode shapes at a given temperature range compared with those in the 20°C - 26°C range.

Temperature Range	1st Mode Shape		2nd Mode Shape		3rd Mode Shape	
	North Side	South Side	North Side	South Side	North Side	South Side
-12°C to -5°C	0.9970	0.9966	0.9981	0.9859	0.9989	0.9873
-9°C to -7°C	0.9974	0.9981	0.9976	0.9995	0.9920	0.9824
20°C to 26°C	1	1	1	1	1	1
30°C to 40°C	N/A	0.9970	N/A	0.9997	N/A	0.9958

Figure 4-4 shows the percentage change in mode shape relative to that in the 20°C to 26°C temperature range; this data is also summarised in Tables 4-3 to 4-5.

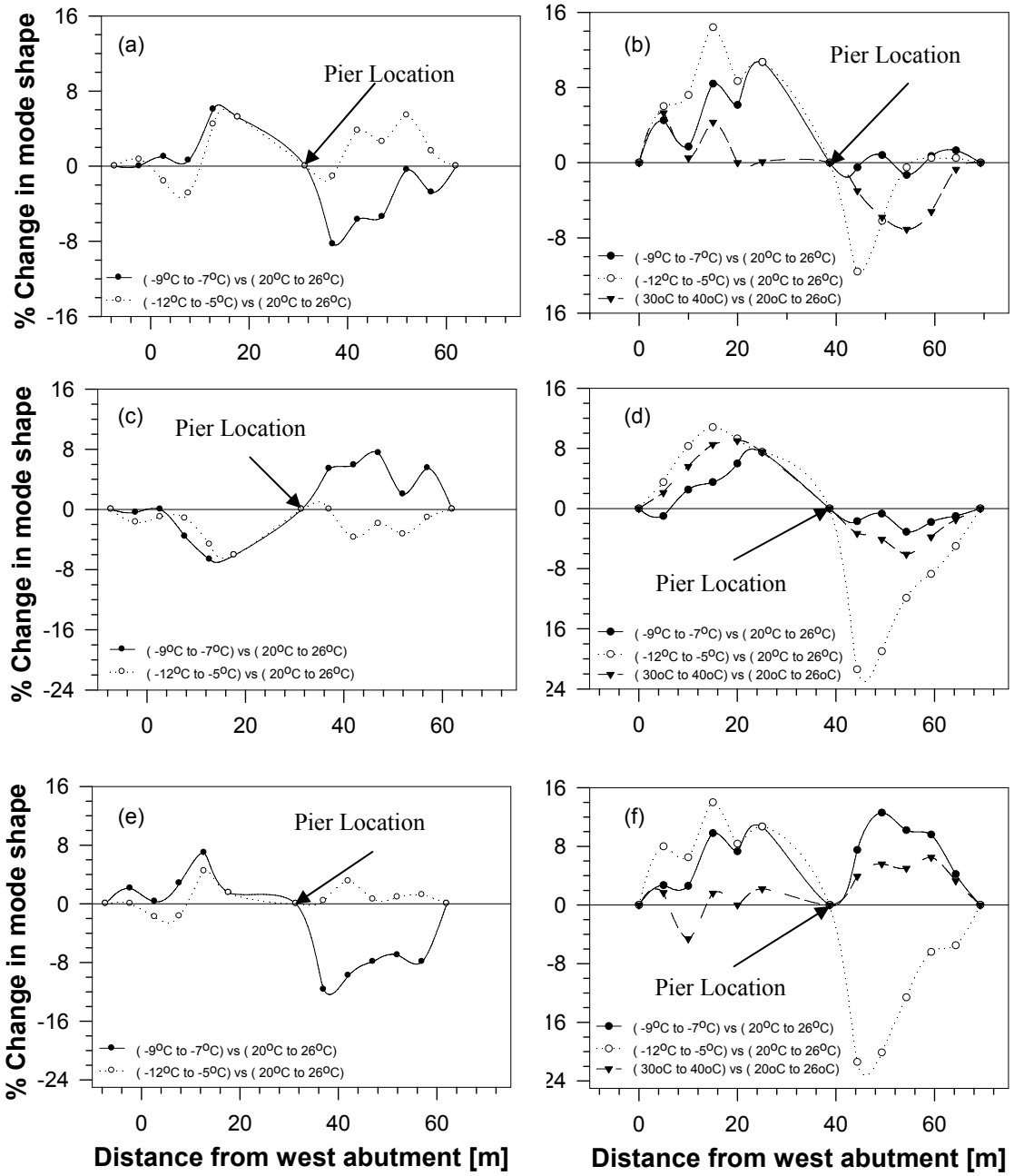

Figure 4-4. Comparison of mode shapes by percentage change with respect to the mode shape in the temperature range of 20°C to 26°C: (a) 1st mode shape in north side; (b) 1st mode shape on south side; (c) 2nd mode shape on north side; (d) 2nd mode shape on south side; (e) 3rd mode shape on north side; and (e) 3rd mode shape on south side.

Although measured mode shapes for all temperature ranges appear to be nearly identical from the MAC values in Table 4-2, there are differences among the mode shapes measured at various temperature ranges, as shown in Figure 4-4. Generally, mode shapes measured on the south side changed more significantly than those on the north side (see Figure 4-4 and Table 4-3 through Table 4-5). The first and second mode shapes in the temperature range of -9°C to -7°C are exceptions to this observation, where differences in mode shapes were higher on the north side. The MAC values listed in Table 4-2 show a similar general trend, having relatively lower values on the south side except for the first and second mode shapes in the temperature range of -9°C to -7°C.

The percentage change in mode shape shown in Figure 4-4 appears to have no general trend, in contrast to the natural frequency changes shown in Figure 4-1. However, change in mode shapes in the temperature range of -12°C to -5°C exhibit maximum changes on the south side, while maximum changes in the temperature range

Table 4-3. Comparison of 1st mode shape by percentage difference.

Temperature Range	Distance from west abutment wall (m)									
	5	10	15	20	25	44.3	49.3	54.3	59.3	64.3
	North Side (% Difference)									
-12°C to -5°C	0.7	1.6	2.9	4.4	5.2	1.1	3.8	2.6	5.4	1.6
-9°C to -7°C	0.0	1.0	0.6	6.0	5.2	8.3	5. 8	5.4	0.4	2.8
20°C to 26°C	0.0	0.0	0.0	0.0	0.0	0.0	0.0	0.0	0.0	0.0
30°C to 40°C	N/A	N/A	N/A	N/A	N/A	N/A	N/A	N/A	N/A	N/A
	South Side (% Difference)									
-12°C to -5°C	6	7.2	14.4	8.7	10.7	11.6	6.2	0.5	0.5	0.5
-9°C to -7°C	4.5	1.7	8.4	6.1	10.7	0.5	0.8	1.3	0.7	1.3
20°C to 26°C	0.0	0.0	0.0	0.0	0.0	0.0	0.0	0.0	0.0	0.0
30°C to 40°C	5.3	0.5	4.3	0.0	0.1	3.0	5.8	7.1	5.2	0.7

Table 4-4. Comparison of 2nd mode shape by percentage difference.

Temperature Range	Distance from west abutment wall (m)									
	5	10	15	20	25	44.3	49.3	54.3	59.3	64.3
	North Side (% Difference)									
-12°C to -5°C	1.7	1.0	1.2	4.7	6.1	0.0	3.7	1.9	3.3	1.1
-9°C to -7°C	0.4	0.0	3.6	6.7	6.1	5.4	5.9	7.5	2.0	5.5
20°C to 26°C	0.0	0.0	0.0	0.0	0.0	0.0	0.0	0.0	0.0	0.0
30°C to 40°C	N/A	N/A	N/A	N/A	N/A	N/A	N/A	N/A	N/A	N/A
	South Side (% Difference)									
-12°C to -5°C	3.5	8.3	10.8	9.3	7.5	21.4	19	11.9	8.7	5.0
-9°C to -7°C	1.0	2.5	3.5	6.0	7.5	1.7	0.7	3.1	1.8	1.0
20°C to 26°C	0.0	0.0	0.0	0.0	0.0	0.0	0.0	0.0	0.0	0.0
30°C to 40°C	2.1	5.6	8.5	9.0	7.5	3.3	4.1	6.1	3.8	1.5

Table 4-5. Comparison of 3rd mode shape by percentage difference.

Temperature Range	Distance from west abutment wall (m)									
	5.0	10	15	20	25	44.3	49.3	54.3	59.3	64.3
	North Side (% Difference)									
-12°C to -5°C	0.0	1.8	1.7	4.5	1.5	0.4	3.1	0.6	0.9	1.2
-9°C to -7°C	2.1	0.3	2.8	7.0	1.5	11.7	9.8	7.9	7.0	7.9
20°C to 26°C	0.0	0.0	0.0	0.0	0.0	0.0	0.0	0.0	0.0	0.0
30°C to 40°C	N/A	N/A	N/A	N/A	N/A	N/A	N/A	N/A	N/A	N/A
	South Side (% Difference)									
-12°C to -5°C	8.0	6.5	14	8.4	10.7	21.4	20.1	12.6	6.4	5.5
-9°C to -7°C	2.7	2.6	9.8	7.3	10.7	7.5	12.6	10.2	9.6	4.2
20°C to 26°C	0.0	0.0	0.0	0.0	0.0	0.0	0.0	0.0	0.0	0.0
30°C to 40°C	1.7	4.6	1.6	0.0	2.2	3.9	5.6	5.0	6.5	3.3

of -9°C to -7°C occur on the north side.

The average percentage change in mode shape over a given bridge side and temperature range is plotted against corresponding MAC values in Figure 4-5. Irrespective of some sporadic data, a general trend can be observed in which the percentage change in mode shape decreases as the MAC value increases.

4.6 LEVEL OF UNCERTAINTY IN MEASURED MODE SHAPES

As in all experimental studies, mode shape measurements in the current study were measured with some degree of uncertainty. In practice, inaccuracies are introduced into the mode shape measurements through a number of sources, including instrumentation error, signal noise from nearby electrical fields, analog-to-digital discretisation error and signal processing routines (i.e. analog and digital filters, windowing functions, FFT's, etc.). In addition, the random nature of ambient traffic excitation adds considerable uncertainty into the interpretation of dynamic response results.

In order to quantify the uncertainty, the standard deviation and coefficient of

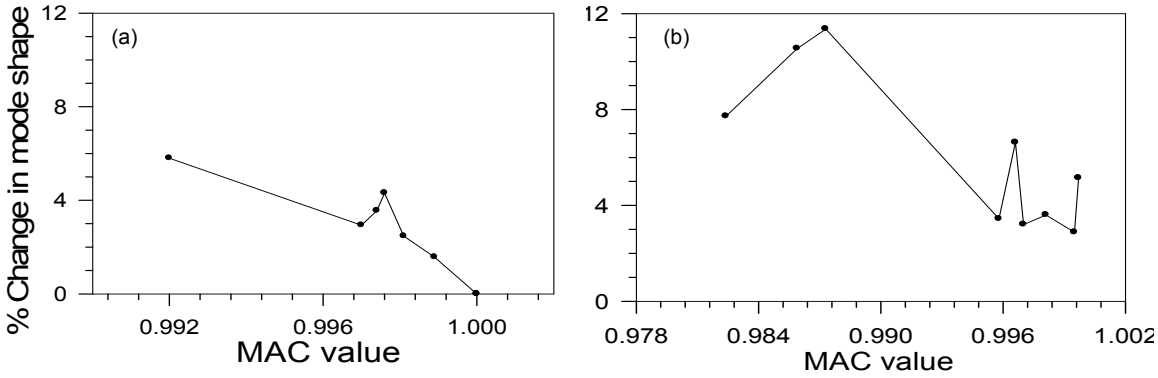

Figure 4-5. Comparison of percentage in mode shape with MAC value on (a) the north side and (b) the south side.

variation of the modal amplitudes for all data sets at a given sensor location were calculated, all of which had been normalized by the corresponding value from the reference sensor. The computed standard deviation values were then used as input for the subsequent numerical investigation of the influence of uncertainty on damage detection; in addition, coefficients of variation derived from these results were used to provide an indication of the level of uncertainty relative to modal amplitudes.

The average value, standard deviation and coefficient of variation of modal amplitudes at each sensor location for the temperature range of 20°C to 26°C are given in Table 4-6. Also, Figure 4-6 provides a graphical illustration of the variation in the first mode for this temperature range. Standard deviations and coefficients of variation of modal amplitudes for the other temperature ranges are given in Appendix A.

As seen in Table 4-6, the level of uncertainty at different sensor locations, expressed in terms of the coefficient of variation, varied from 1.6% to 17.8%, for the temperature range of 20°C to 26°C. The range of variation in the level of uncertainty was even broader (from 0.8 % to 32.8 %) when all the temperature ranges were considered. A summary of this variation in the level of uncertainty for the first three mode shapes and all the temperature ranges is given in Table 4-7. It was observed that median and mean values differed somewhat for the first mode, while those for second and third modes were very close. In general, the second mode was found to exhibit less variation in the average deviation values compared to the first and third modes. The average deviation was defined as

$$\text{Average deviation} = \frac{1}{\text{n}}\sum_{i=1}^{n}|x_i - \bar{x}|, \tag{4.3}$$

where x_i is the coefficient of variation at a specific sensor location, $\bar{x}$ is the mean coefficient of variation for all sensors and n is the number of sensors considered.

The influence of uncertainty in mode shape measurements was investigated numerically (in Chapters 7 and 8) using a calibrated finite element model. The average standard deviation of measured modal amplitudes in all sensor locations and for the first mode in the temperature range of 20°C to 26°C was used to represent field uncertainties in this numerical study. To provide a common basis for defining the uncertainty, the

Table 4-6. Uncertainty in the first three measured mode shapes in the temperature range of 20°C to 26°C.

			Sensor Location from West abutment (m)									
			5	10	15	20	25	44.3	49.3	54.3	59.3	64.3
1st Mode Shape	South Side	Avg	0.43	0.83	1.20	1.37	1.28	0.43	0.65	0.62	0.48	0.24
		SD	0.02	0.02	0.04	0.05	0.03	0.04	0.05	0.05	0.03	0.03
		COV (%)	4.6	2.2	3.0	3.7	2.1	9.4	7. 0	7.7	6.6	9.8
	North Side	Avg	0.50	1.11	1.63	1.80	1.70	0.41	0.70	0.71	0.59	0.28
		SD	0.03	0.06	0.10	0.09	0.07	0.04	0.07	0.04	0.06	0.05
		COV (%)	6.4	5.2	6.3	4.9	4.0	9.0	9.7	5.8	9.4	17.8
2nd Mode Shape	South Side	Avg	0.56	1.23	1.79	2.04	1.87	0.51	0.76	0.71	0.53	0.24
		SD	0.02	0.04	0.06	0.07	0.07	0.04	0.06	0.06	0.02	0.01
		COV (%)	2.7	2.9	3.4	3.6	3.6	6.9	7.4	8.4	3.3	4.6
	North Side	Avg	0.46	1.04	1.50	1.71	1.64	0.39	0.65	0.66	0.52	0.23
		SD	0.03	0.04	0.05	0.08	0.05	0.04	0.05	0.07	0.04	0.03
		COV (%)	7.0	4.0	3.0	4.8	2.9	10.7	7.1	10.6	7.2	13.8
3rd Mode Shape	South Side	Avg	0.34	0.88	1.21	1.44	1.29	0.42	0.61	0.59	0.43	0.20
		SD	0.01	0.01	0.03	0.02	0.03	0.04	0.04	0.03	0.03	0.03
		COV (%)	4.0	1.6	2.5	1.7	2.1	9.6	7.0	5.4	5.8	13.6
	North Side	Avg	0.43	1.02	1.49	1.70	1.64	0.35	0.57	0.58	0.43	0.20
		SD	0.03	0.04	0.04	0.07	0.05	0.02	0.04	0.03	0.02	0.01
		COV (%)	6.6	3.5	2.7	4.1	3.1	6.5	6.1	4.8	4.0	5.9

Avg = Average; SD= Standard Deviation; COV= Coefficient of Variation. The numbers of trials for the southwest, south east, northwest and northeast quadrant were respectively 9,9,22, and 12.

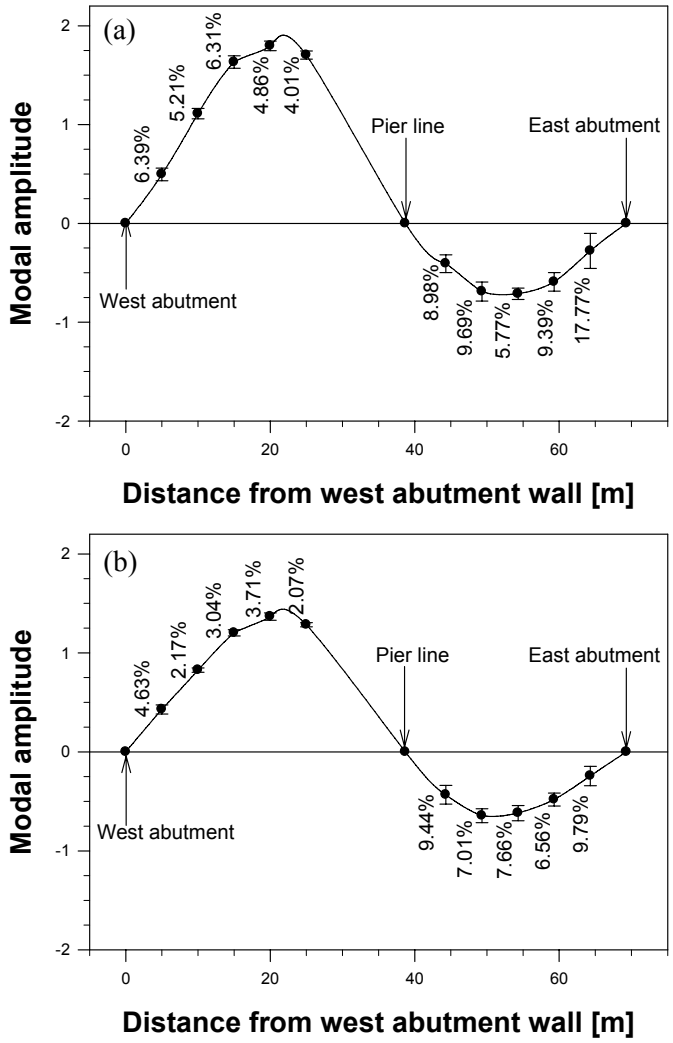

Figure 4-6. Mode shape variability at individual sensor locations for the first mode (20°C - 26°C): (a) the north side of the bridge; and (b) the south side of the bridge.

Table 4-7. Comparison of coefficients of variation of the first three mode shapes for all the temperature ranges.

Mode shape	Maximum value	Minimum value	Mean	Median	Average deviation
First	30.2	0.84	11.0	9.0	6.2
Second	23.1	0.85	8.8	8.8	3.8
Third	32.8	0.16	8.9	7.4	4.5

average standard deviation in the numerical study was normalized by dividing it by the mean modal amplitude of a specified reference location, selected as 20 meters from west abutment wall on the north side of the bridge. On this basis, the average and normalized average standard deviation for the first mode shape in the temperature range of 20°C to 26°C were 0.047 and 0.0261, respectively. Further details of the numerical investigation on uncertainty are given in Chapter 6 and in Appendix D.

CHAPTER 5. DESCRIPTION OF NUMERICAL STUDY

5.1 OVERVIEW

A linear elastic finite element (FE) model of the overpass was generated using the commercial package ADINA (2002). The purpose of the model was to simulate the dynamic response of the bridge as damage was induced, since this could not be carried out experimentally.

Information on dimensions and material properties were taken from the design drawings of the Attridge Drive Overpass. All structural features were modelled to closely match their actual behaviour and geometry.

The model was first calibrated to closely match the measured dynamic properties of the physical system. The natural frequencies and mode shapes derived from eigenvalue analyses of the calibrated model in different damage conditions were then used to evaluate the ability of VBDD techniques to detect and locate the damage on the structure.

An isometric view of the FE model is shown in Figure 5-1. The entire model comprised 6071 elements, 7570 nodes and 23882 degrees of freedom. Details of the model, its calibration, and damage scenarios investigated are described in the following sections.

5.2 DESCRIPTION OF NUMERICAL MODEL

A variety of finite element types (3D solid, shell and beam elements) were used to model the bridge structure. Details of how the different structural components were modelled to reproduce realistic structural attributes are described in the following

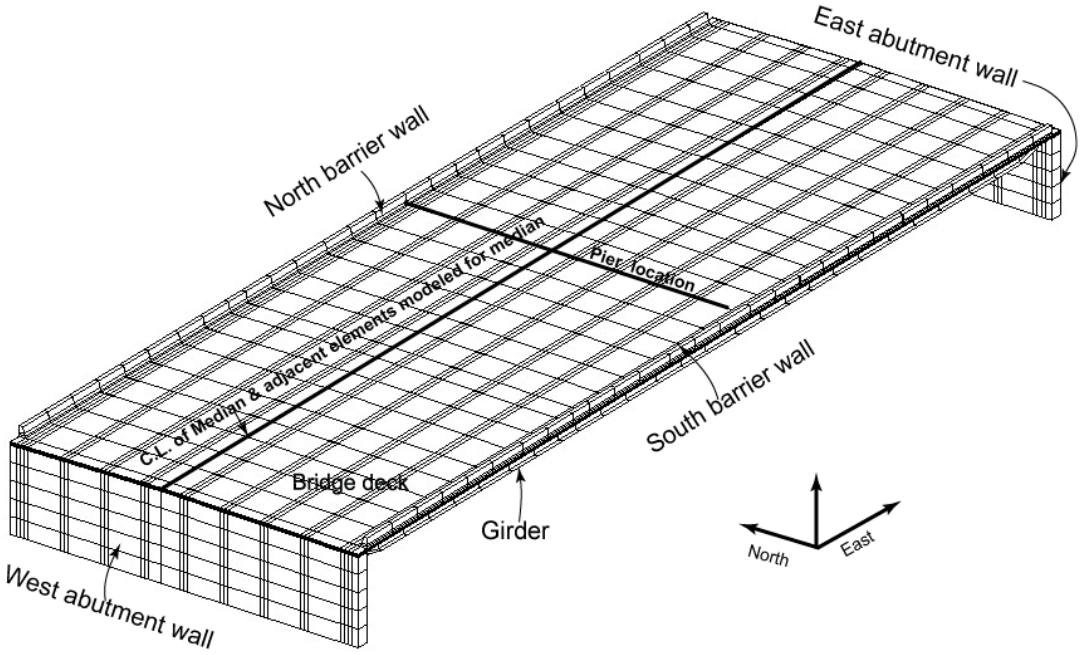

Figure 5-1. Finite element model of the Attridge Drive Overpass.

sections. Assumed properties for the bridge elements are summarized in Table 5-1. The various components are described in detail in the following sections.

5.2.1 Bridge Deck

The concrete bridge deck was modelled using 8-node, 3-dimensional isoparametric solid elements, which have three translational degrees of freedom (dof) at each node. The deck was descretised into three vertical layers, each of which featured 29 elements longitudinally and 31 elements transversely. The top layer was made 50 mm deep to represent the concrete cover over the top layer of reinforcing steel, while the remaining two layers were 75 mm and 100 mm deep, respectively. The asphalt concrete wearing surface and the median were modelled as distributed masses by increasing the density of the top deck layer; as such, they were assumed not to contribute to the stiffness of the bridge deck. Since the average thickness of the asphalt wearing surface is

Table 5-1. Material properties of different structural elements of the calibrated FE model.

Structural Element	Finite Element Type	Material	Material Properties
Bridge deck	8-node 3-D solid brick element	concrete	$^{*}E_1 = 13.0$ GPa; $E_2 = 4.10$ GPa; $E_3 = 13.0$ GPa $^{\wedge}\upsilon_{12} = 0.25$; $\upsilon_{23} = 0.20$; $\upsilon_{13} = 0.21$ $^{\$}G_{12} = 5.2$ GPa; $G_{13} = 5.4$ GPa; $G_{23} = 1.7$ GPa $^{\wedge}\rho_{top} = 6540$ kg/m^3 ; $\rho_{median} = 8778$ kg/m^3 $\rho_{middle} = \rho_{bottom} = 2400$ kg/m^3
Barrier walls & abutments	8-node 3-D solid brick element	concrete	$^{\$}E=26$ GPa; $^{\wedge}\upsilon = 0.2$; $^{\wedge}\rho=2400$ kg/m^3
Girders and pier diaphragm	4-node shell element	steel	$^{\$}E=200$ GPa; $^{\wedge}\upsilon = 0.3$; $^{\wedge}\rho=7800$ kg/m^3
Truss Diaphragms	truss element & beam element	steel	$^{\$}E=200$ GPa; $^{\wedge}\upsilon = 0.3$; $^{\wedge}\rho=7800$ kg/m^3
Pile supports	spring elements		$^{!}K_t = 4.46$ N/m $^{!}K_\theta = 90$ N.m/rad.
Backfill pressure	spring elements		$^{!}K_t = 4.5 \times 10^6$ N/m

*Direction 1 = Along the length of the overpass.
Direction 2 = Along the width of the overpass.
Direction 3 = Along the vertical direction of the overpass.
$^{!}$ K_t = Translational stiffness; K_θ = Rotational stiffness.
$^{\$}$ E = Young's modulus of elasticity; G =Modulus of rigidity.
$^{\wedge}\upsilon$ = Poisson's ratio; $^{\wedge}\rho$ = Density.

90 mm, the equivalent modified density used for the top layer element was 6540 $\frac{kg}{m^3}$ (i.e., 50 mm deep concrete at 2400 $\frac{kg}{m^3}$ plus 90 mm deep asphalt concrete at 2300 $\frac{kg}{m^3}$). Similarly, the modified density for top layer elements below the median was taken to be 8778 $\frac{kg}{m^3}$ (i.e., 50 mm deep by 1000 mm wide concrete deck , 225 mm deep by 336 mm wide concrete barrier, both at 2400 $\frac{kg}{m^3}$, plus 90 mm deep by 664 mm wide asphalt

concrete at 2300 $\frac{kg}{m^3}$). The nominal density of concrete for the remainder of the deck was taken as 2400 $\frac{kg}{m^3}$.

5.2.2 Barrier Walls and Abutments

The barrier walls and abutments were also modelled using 8-node 3-dimensional isoparametric solid elements. The effect of the barrier walls in terms of the added mass and stiffness was therefore included by modelling the barrier walls as 3D solid elements with similar properties to the actual barriers. To avoid overestimating the stiffening effect of the barrier walls, which were constructed in a segmental fashion, a small gap was included between adjacent barrier wall segments on the FE model at a longitudinal spacing of 3 m, close to the actual segmental length of 3.2 m (See Figure 5-2 a). The barrier walls were discretised into three vertical layers of varying thickness to model their actual shape.

The abutment walls were discretised into a grid featuring 31 elements transversely and 9 elements vertically (6 elements plus 3 elements having similar depth to those in the bridge deck as shown in Figure 5-2 b). While the wing walls adjacent to the abutment walls were not modelled explicitly, their effect was simulated by applying translational fixity to all degrees of freedom at appropriate nodes located at the bottom corner of the abutment walls. Wing walls of Attridge Drive Overpass were not monolithically connected to the abutment walls; rather they were connected by mechanical fastener at points, intended only to provide support to wing walls. However, the pile supports of wing walls and mechanical fasteners combined to act as a support providing translational fixity to the bottom corners of the abutment wall.

5.2.3 Girders and Diaphragms

The nine welded wide flange steel girders, as well as the beam diaphragm members located along the pier line, were modelled using 4-node, isoparametric shell elements, which have six degrees of freedom at each node (three translational and three

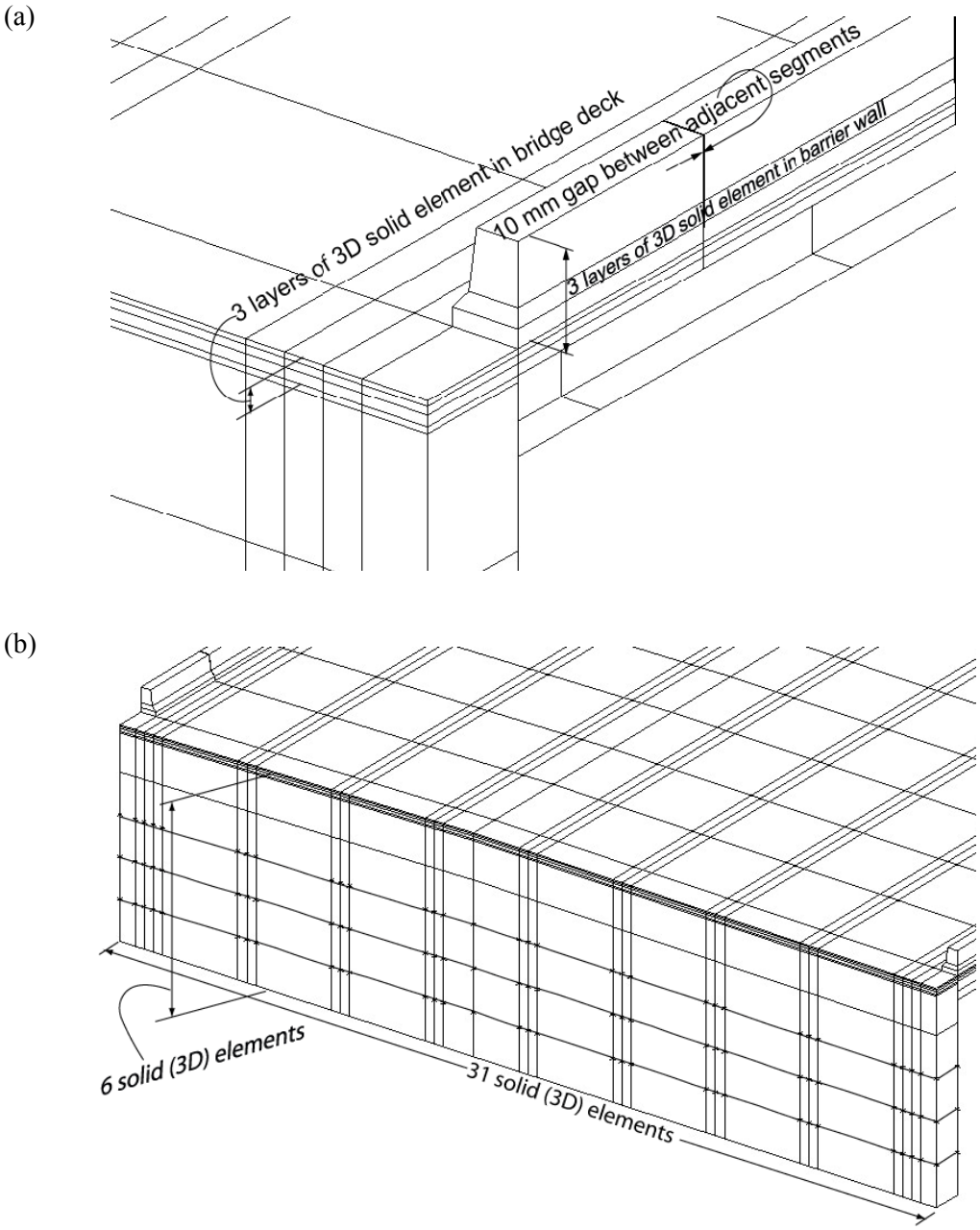

Figure 5-2. Partial view of bridge components, as defined in the finite element model: (a) barrier walls, and (b) west abutment.

rotational). Figure 5-3 shows a partial view of the girders, pier diaphragm and truss diaphragms as defined geometrically in the finite element model. In this figure, shell elements were made transparent for a clear view of the structural arrangement.

On the actual overpass structure, the top flange of a steel girder is connected to the concrete deck using shear studs to achieve composite behaviour at the material interface. In the numerical model, it was assumed that the shear studs prevented relative displacements along the faying surfaces between the steel girders and concrete deck in both the horizontal and vertical directions. This was achieved in the finite element model by imposing compatibility constraints between translational degrees of freedom in the horizontal and vertical directions at the nodes on the top surface of the girder and the deck's bottom surface. Figure 5-4 shows a schematic diagram illustrating the restraint conditions at the connecting nodes.

To avoid numerical errors resulting from the co-location of the top surface of the girders and the bottom surface of the deck, a fictitious 5 mm gap was introduced in

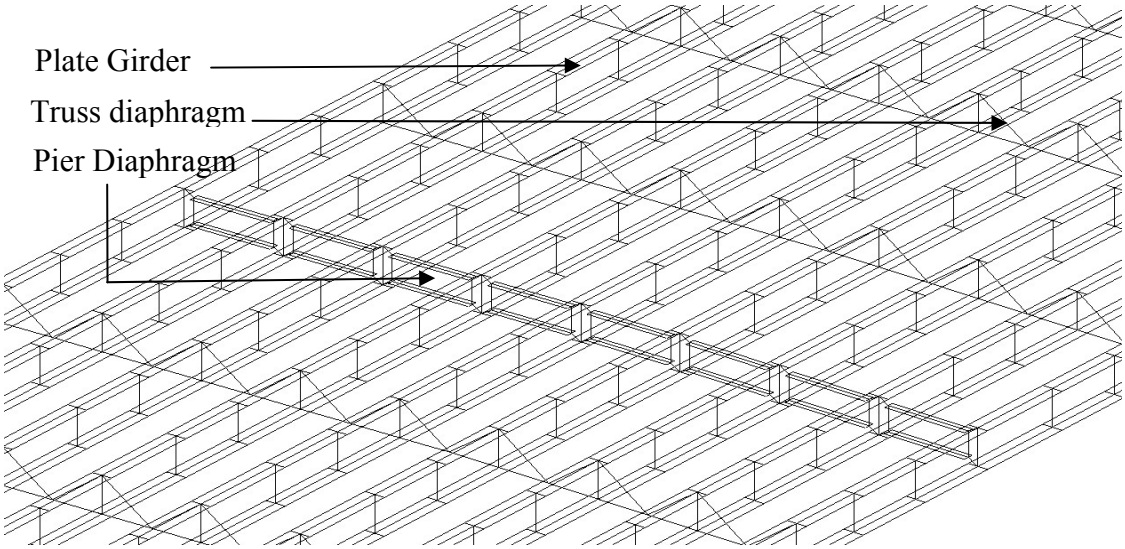

Figure 5-3. Girders and diaphragms as defined geometrically in the finite element model.

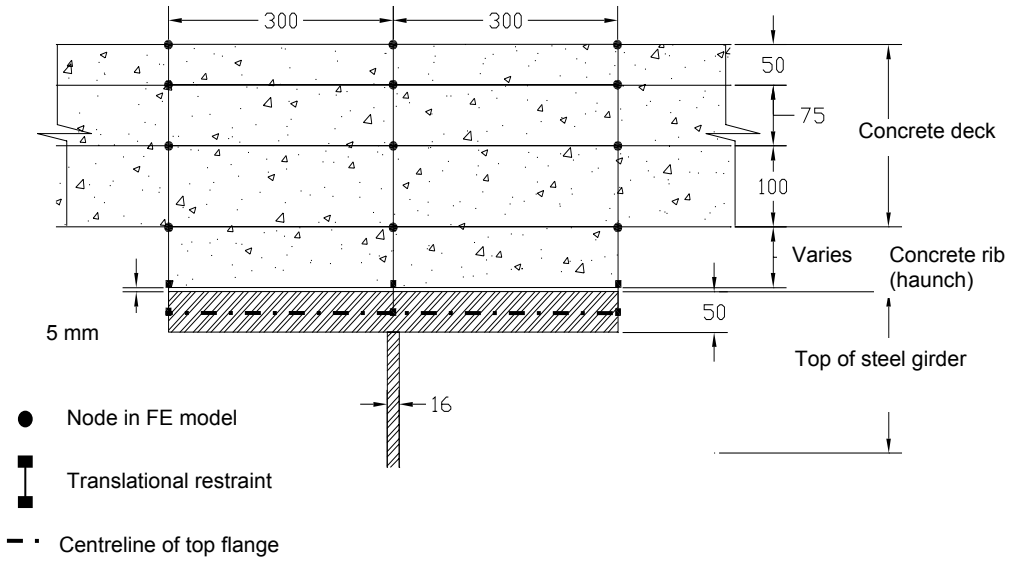

Figure 5-4. Constraint between a girder's top flange and the bottom of concrete deck (all dimensions are in mm).

the model (see Figure 5-4). To keep the total depth of composite beam as close as the original structure, this fictitious gap was minimized as much as possible.

The welded beam diaphragms (a wide flange section) along the pier line were modelled in segments, with one segment placed between each pair of adjacent girders, both ends of which were connected rigidly to the web of the steel girder. Shell elements similar to those used for the steel girders were used to model the beam diaphragms, as well as the rigid connection between the webs of diaphragm segments and the steel girders. However, to reproduce existing conditions in the actual structure, beam diaphragm elements were not connected to concrete deck.

On the actual overpass structure, the girders are embedded into the abutment walls, a condition which is known as integral abutment construction. In the FE model, elements used for the girders and abutment walls were not compatible in terms of the degrees of freedoms at the respective nodes (the girders were modelled with shell

elements featuring 6 degrees of freedom per node, while the abutment walls were modelled with 3D solid elements featuring 3 degrees of freedom per node). To deal with this situation, ADINA features transition nodes to make the interface between the shell nodes and 3-D solid nodes possible. In effect, the rotation of a shell node at the interface is determined from the translational degrees of freedom of the top and bottom nodes of the 3-D solid elements at the interface.

Translations for a shell node were obtained by linear interpolation of the translations at the top and bottom nodes of the 3-D solid element, while rotations were computed based on the slope of the line connecting the displaced top and bottom joints on the solid element. Figure 5-5 illustrates the translation relationships.

Members of the truss diaphragms in the actual structure are made of double–angle sections and connected to the webs of steel girders. In the FE model, the bottom chord of the truss diaphragm was represented as a beam element featuring six degrees of freedom at each node in order to provide rotational stability with respect to out of plane motion, which was achieved by imposing continuity between the two bottom chord members at the truss node located midway between adjacent girders. Figure 5-6 shows the finite elements used to model the truss diaphragm. The beams were modelled using

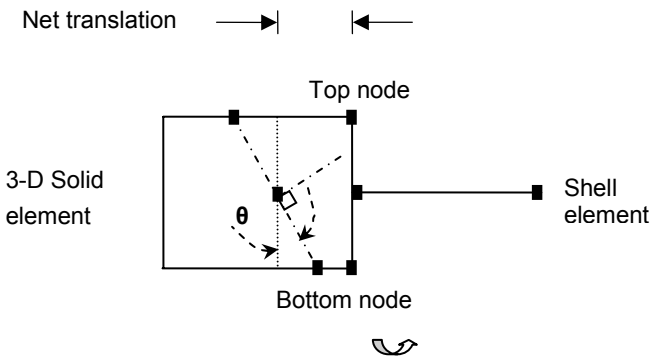

Figure 5-5. Transition nodes between shell and 3-D solid elements.

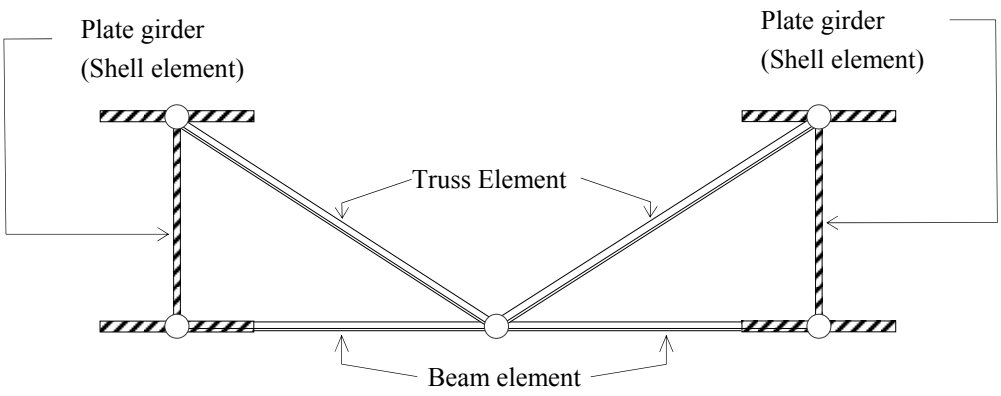

Figure 5-6. Truss diaphragm as assumed for FE model (not drawn to scale).

2–node Hermitian beam elements with a constant cross-section and six degrees of freedom at each node. Diagonals in the truss diaphragms were modelled using truss elements featuring three translational degrees of freedom at each node. For simplicity, an equivalent rectangular area having bending stiffness about the strong and weak axes similar to that of double-angle section was used to define the cross-sectional properties of the beam and truss elements.

5.2.4 Boundary Conditions

The actual bridge structure is supported by piles located below both the abutment walls and the pier at mid span. The steel girders are then supported by the central pier in such a manner that the girders are restrained from lateral and vertical movement but are free to rotate in their own longitudinal plane and to translate in the longitudinal direction of the bridge. This support condition was achieved in the FE model by applying lateral and vertical translational fixidity to the three nodes on the bottom surface of each girder directly above the central pier location. However, translational degrees of freedom in the longitudinal direction of the bridge structure, as

well as all rotational degrees of freedom at the support node on the pier, were free to move in the FE model.

The piles supporting the abutment walls were modelled using both translational and rotational spring elements. Translational spring elements were oriented along both of the horizontal axes (longitudinal and lateral), while rotational spring elements were also defined about both the horizontal axes. The stiffness of the spring elements was determined by considering the flexural rigidity of the piles, assuming them to be fixed at an appropriate depth below grade. The total rotational and translational stiffness of six piles below each abutment wall were equally distributed to along the nodes along the bottom face of each abutment wall. Spring elements representing piles in the FE model are shown in Figure 5-7. Details of spring stiffness estimation for pile supports are explained in Appendix B. Backfill soil resistance exerted on the abutment walls was represented in the FE model by using horizontal spring elements; backfill soil stiffness calculations are also explained in Appendix B.

5.3 CALIBRATION AND CORRELATION

Numerical modelling inevitably involves some degree of theoretical approximation of complex structural behaviours. To account for differences between the initial model and the actual structure, the model was calibrated to the measured dynamic properties of the actual bridge, obtained in the temperature range of 20°C to 26°C. The calibration was achieved primarily by adjusting the stiffness of the concrete deck elements. It was found that the stiffness of the springs used to represent the piles and backfill soil did not have a significant effect on the computed modal properties of the overpass; therefore, foundation stiffness properties were not adjusted in the model

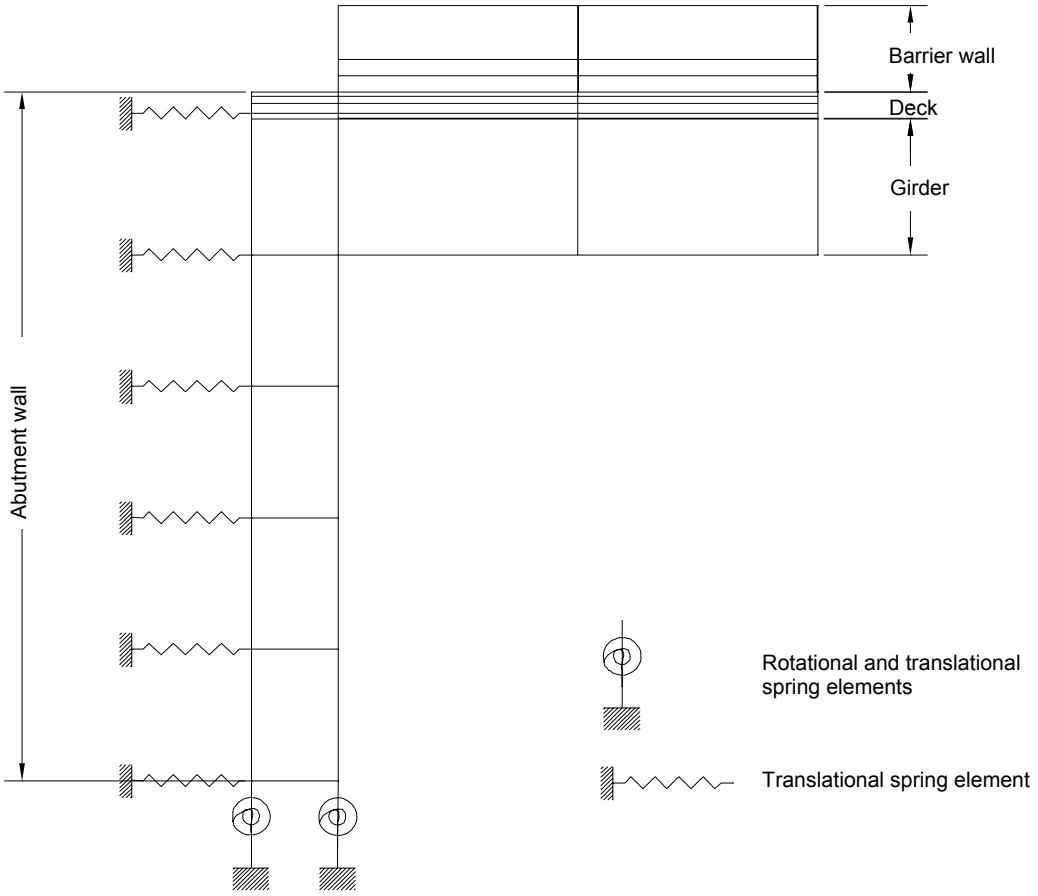

Figure 5-7. Partial side view of bridge abutment wall showing foundation spring elements in the FE model.

calibration exercise.

To model the existence of flexural cracking in the bridge deck in an approximate fashion without resorting to nonlinear analyses, the elastic modulus of the concrete making up the deck elements was adjusted independently in the longitudinal and lateral directions, with care taken to ensure that the resulting flexural rigidity was not reduced below values representative of a fully cracked deck cross section. An elastic–orthotropic material model was used to model the bridge deck, in which Poisson's ratio values were adjusted to make sure that the stress-strain constitutive matrix of the FE model was

positive definite. Resulting modulus of rigidity values for a given direction were then calculated on the basis of the modulus of elasticity and Poisson's ratio for that direction.

Calculations to determine the minimum stiffness of a fully cracked elastic section are given in Appendix C. Material properties used for different structural elements of the calibrated model are given in Table 5-1.

The natural frequencies and mode shapes of the structural system were calculated numerically by performing an eigenvalue analysis of the FE model. The first three natural frequencies and mode shapes obtained in the experimental study were used to calibrate the FE model, since only first three modes were obtained with a high level of confidence from the experimental data. Higher modes were either not prominent in the data, or were not consistently found in all test records.

Since the experimental mode shapes were measured only in the vertical directions on the deck, only vertical elements of the eigenvectors from nodes on the top surface of the deck were considered when defining numerical mode shapes.

The lowest three natural frequencies obtained from both the experimental results in the temperature range of 20°C to 26°C and the calibrated FE model are presented in Table 5-2. It can be seen that excellent agreement was achieved, with a maximum difference of 0.31% found between predicted and measured values.

Table 5-2. Comparison of experimental and numerical natural frequencies.

Source	1st Mode	2nd Mode	3rd Mode
FE Model (Hz)	3.070	3.269	3.817
Experimental (Hz)	3.076	3.259	3.809
Difference (%)	0.19%	0.31%	0.21%

The first three mode shapes generated from the FE model are shown in Figure 5-8. Due to restrictions on possible sensor locations during normal bridge operation, however, experimental mode shapes could be defined only along the two outside edges of the bridge. The vertical components of the experimental and numerical mode shapes along these two edges are presented in Figure 5-8(b), again suggesting consistently close agreement between the numerical model and the prototype.

A more quantitative comparison between mode shapes can be made using the modal assurance criteria (MAC) value as described in Equation 4.1. In this case, symbols $\boldsymbol{\phi}^{t_1}$ and $\boldsymbol{\phi}^{t_2}$ are the corresponding numerical and experimental mode shape vectors, respectively. It should be recalled that a MAC value of 1.0 would indicate that the experimental and numerical mode shapes were perfectly correlated at the

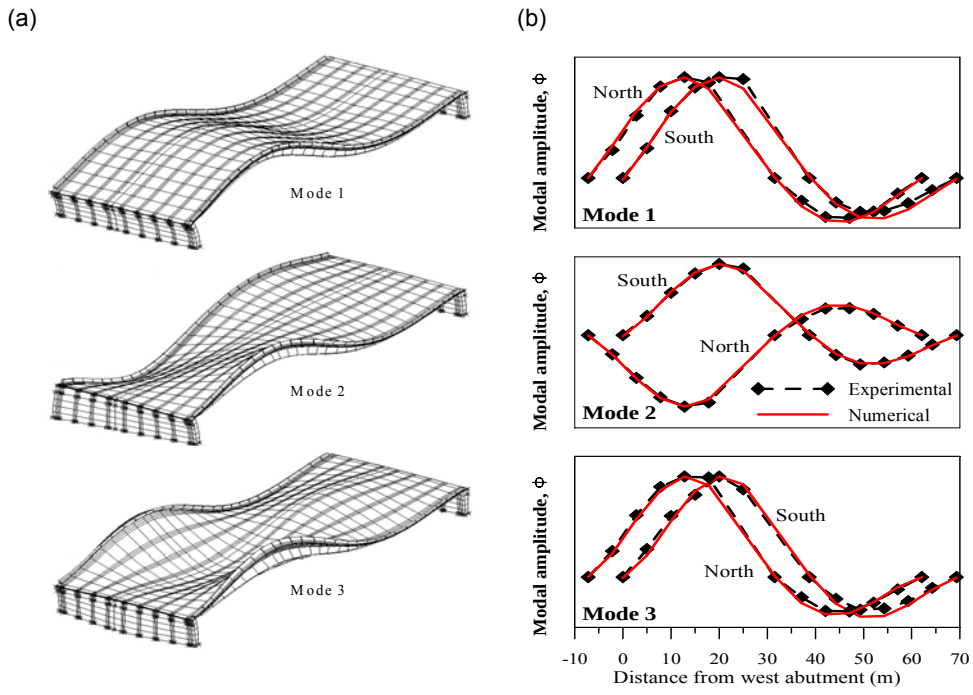

Figure 5-8. Numerical and experimental mode shapes: (a) numerical mode shapes, and (b) experimental and numerical mode shapes along the north and south barrier walls.

measurement points, while a value of zero would indicate that they were orthogonal (i.e. no consistent correlation).

MAC values comparing the experimental and numerical mode shapes along the north and south edges of the bridge are presented in Table 5-3 for the lowest three vibration modes. Since the FE node points did not, in general, correspond to sensor locations on the physical system, numerical modal displacements at the sensor locations were estimated by fitting a cubic spline curve to the FE generated mode shapes. Both the numerical and experimental mode shapes were normalized before applying Equation 4.1. For this purpose, the modal amplitude at an interpolated node, 20 m away from the west abutment was used to normalize the numerical mode shape of each side separately. Similarly, experimental mode shapes along each side of the bridge were also normalized using the modal amplitude of a sensor located 20 m away from the west abutment.

As demonstrated in Table 5-3, MAC values for all three modes considered exceeded 0.99 along both sides of the bridge, indicating excellent agreement between the measured and numerical mode shapes.

Based on these calibration results, the FE model was shown to have similar dynamic characteristics to those of the actual structure, at least in the lower modes of

Table 5-3. Comparisons of numerically and experimentally derived mode shapes based on MAC values.

	1st Mode	2nd Mode	3rd Mode
North side of bridge	0.9972	0.9980	0.9964
South side of bridge	0.9938	0.9989	0.9975

vibration. Although not conclusive proof of the model's veracity, the calibration exercise provided some measure of confidence in subsequent VBDD simulations.

5.4 SIMULATED DAMAGE SCENARIOS

Two series of simulated damage were induced on the numerical model by removing selected elements from the bridge deck. In the first damage series, a single element was removed at a time from the top layer (50mm deep) of the bridge deck at different locations to simulate small-scale, localized deterioration in the top concrete cover. Such damage could result, for example, from mechanical wearing of the top deck surface or due to corrosion-induced spalling of the top cover. As illustrated in Figure 5-9, all damage cases (R1C1 through R16C15) were confined to the south-west quadrant of the bridge deck and featured horizontal dimensions ranging in extent from 0.3m to 3m, depending on the size of the particular element removed. Here, the grid location of the damage has been specified by its transverse (R1 – R16) and longitudinal (C1 – C15) coordinates, as defined on Figure 5-9.

A total of 133 different damage states were investigated in this series, with a few of these representing duplicate cases used as part of separate investigations. Descriptions of the damage states, including damage size and location, are illustrated in Figure 5-9 and described in Table 5-4 and Table 5-5. In subsequent discussions, damage state R10C9 (approximately at the centre of the quadrant) was used in most cases to portray the different aspects related to the VBDD parameters, while damage states from R10C1 through R10C15 (15 damage cases) were used to investigate the influence of sensor

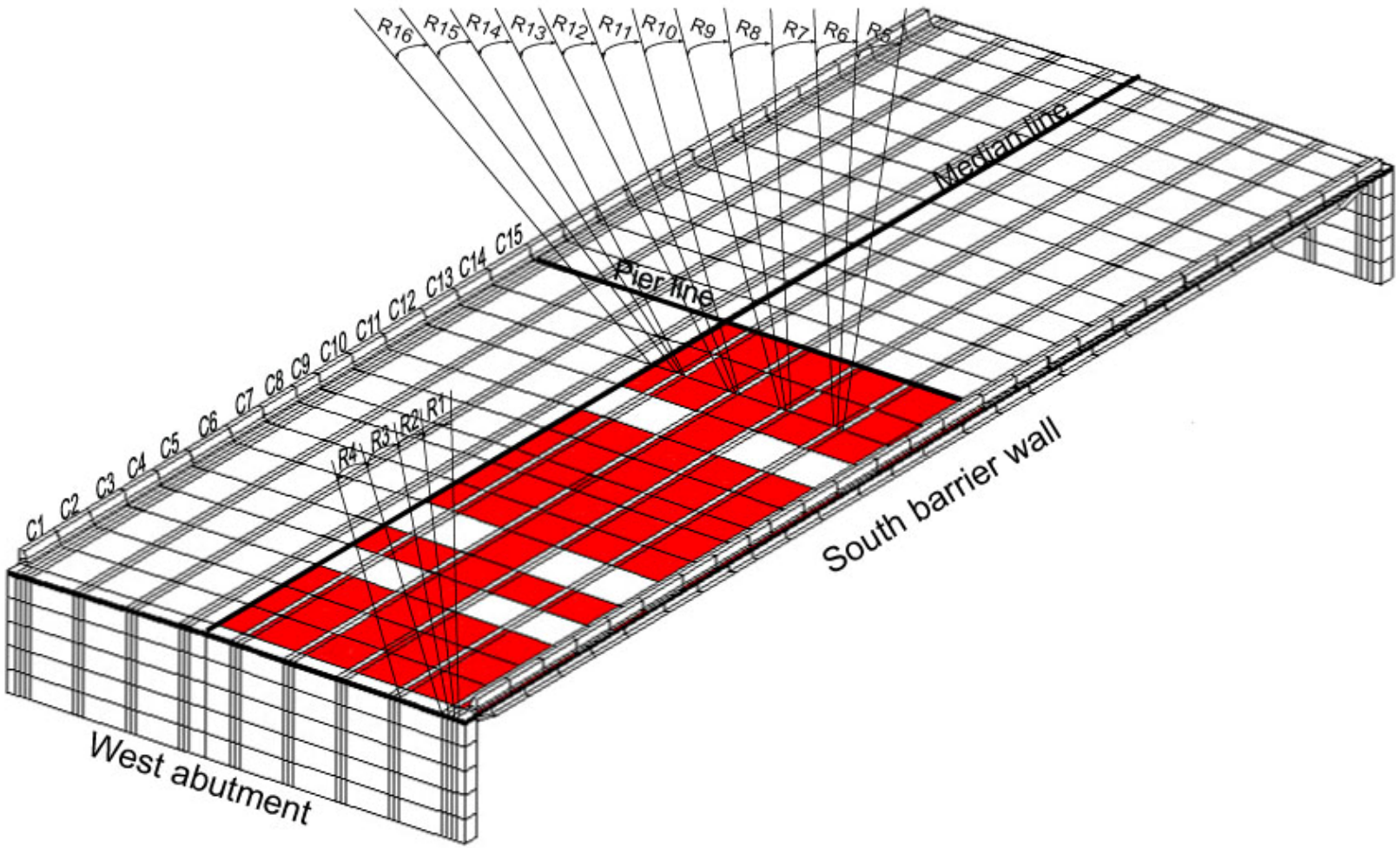

Figure 5-9. Locations of damage cases R1C1 through R16C15 (see Tables 5.4 and 5.5).

Table 5-4. Locations of damage states R1C1 through R16C15.

Distance of 1st end from south barrier wall (m)	Distance of 1st end from west abutment (m)															Distance of 2nd end from south barrier wall (m)
	0.76	3.26	5.76	8.31	10.81	13.31	16.31	18.81	21.31	23.01	25.51	28.01	31.01	33.51	36.01	
0.5	R1C1	R1C2	R1C3	–	R1C5	–	R1C7	R1C8	R1C9	R1C10	R1C11	–	R1C13	R1C14	R1C15	0.8
0.8	R2C1	R2C2	–	–	–	–	–	–	–	–	–	–	–	–	–	1.1
1.1	–	–	–	–	–	–	–	–	–	–	–	–	–	R3C14	–	1.4
1.4	R4C1	R4C2	R4C3	–	R4C5	–	R4C7	R4C8	R4C9	R4C10	R4C11	–	R4C13	R4C14	R4C15	3.9
3.9	R5C1	R5C2	R5C3	–	R5C5	–	R5C7	R5C8	R5C9	R5C10	R5C11	–	R5C13	–	R5C15	4.2
4.2	–	–	–	–	–	–	–	–	–	–	–	–	–	R6C14	–	4.5
4.5	R7C1	R7C2	R7C3	–	R7C5	–	R7C7	R7C8	R7C9	R7C10	R7C11	–	R7C13	R7C14	R7C15	7.0
7.0	R8C1	R8C2	R8C3	–	R8C5	–	R8C7	R8C8	R8C9	R8C10	R8C11	–	R8C13	–	R8C15	7.3
7.3	–	R9C2	–	–	–	–	–	–	–	–	–	–	–	R9C14	–	7.6
7.6	R10C1	R10C2	R10C3	R10C4	R10C5	R10C6	R10C7	R10C8	R10C9	R10C10	R10C11	R10C12	R10C13	R10C14	R10C15	10.1
10.1	R11C1	–	R11C3	R11C4	R11C5	R11C6	R11C7	R11C8	R11C9	R11C10	R11C11	R11C12	R11C13	–	R11C15	10.4
10.4	–	–	–	–	–	–	–	–	R12C9	–	–	–	–	R12C14	–	10.7
10.7	R13C1	R13C2	R13C3	–	R13C5	–	R13C7	R13C8	R13C9	R13C10	R13C11	–	R13C13	R13C14	R13C15	13.2
13.2	R14C1	R14C2	R14C3	–	R14C5	–	R14C7	R14C8	R14C9	R14C10	R14C11	–	R14C13	–	R14C15	13.5
13.5	–	–	–	–	–	–	–	–	–	–	–	–	–	R15C14	–	13.8
13.8	R16C1	R16C2	R16C3	–	R16C5	–	R16C7	R16C8	R16C9	R16C10	R16C11	–	R16C13	R16C14	R16C15	15.3
	3.26	5.76	8.31	10.81	13.31	16.31	18.81	21.31	23.01	25.51	28.01	31.01	33.51	36.01	39.01	
Distance of 2nd end from west abutment (m)																

Table 5-5. Sizes of damage states R1C1 through R16C15.

Width of damage (m)	Length of damage (m)														
	2.5	2.5	2.6	2.5	2.5	3	2.5	2.5	1.7	2.5	2.5	3.0	2.5	2.5	3.0
0.3	R1C1	R1C2	R1C3	–	R1C5	–	R1C7	R1C8	R1C9	R1C10	R1C11	–	R1C13	R1C14	R1C15
0.3	R2C1	R2C2	–	–	–	–	–	–	–	–	–	–	–	–	–
0.3	–	–	–	–	–	–	–	–	–	–	–	–	–	R3C14	–
2.5	R4C1	R4C2	R4C3	–	R4C5	–	R4C7	R4C8	R4C9	R4C10	R4C11	–	R4C13	R4C14	R4C15
0.3	R5C1	R5C2	R5C3	–	R5C5	–	R5C7	R5C8	R5C9	R5C10	R5C11	–	R5C13	–	R5C15
0.3	–	–	–	–	–	–	–	–	–	–	–	–	–	R6C14	–
2.5	R7C1	R7C2	R7C3	–	R7C5	–	R7C7	R7C8	R7C9	R7C10	R7C11	–	R7C13	R7C14	R7C15
0.3	R8C1	R8C2	R8C3	–	R8C5	–	R8C7	R8C8	R8C9	R8C10	R8C11	–	R8C13	–	R8C15
0.3	–	R9C2	–	–	–	–	–	–	–	–	–	–	–	R9C14	–
2.5	R10C1	R10C2	R10C3	R10C4	R10C5	R10C6	R10C7	R10C8	R10C9	R10C10	R10C11	R10C12	R10C13	R10C14	R10C15
0.3	R11C1	–	R11C3	R11C4	R11C5	R11C6	R11C7	R11C8	R11C9	R11C10	R11C11	R11C12	R11C13	–	R11C15
0.3	–	–	–	–	–	–	–	–	R12C9	–	–	–	–	R12C14	–
2.5	R13C1	R13C2	R13C3	–	R13C5	–	R13C7	R13C8	R13C9	R13C10	R13C11	–	R13C13	R13C14	R13C15
0.3	R14C1	R14C2	R14C3	–	R14C5	–	R14C7	R14C8	R14C9	R14C10	R14C11	–	R14C13	–	R14C15
0.3	–	–	–	–	–	–	–	–	–	–	–	–	–	R15C14	–
1.5	R16C1	R16C2	R16C3	–	R16C5	–	R16C7	R16C8	R16C9	R16C10	R16C11	–	R16C13	R16C14	R16C15

spacing on the ability of the VBDD techniques to detect and localize damage.

The second series of damage states consisted of 7 damage cases, in which the dimensions of the damage were varied to investigate the effects of damage size on the VBDD parameters. In this phase of the investigation, damage states S_1 through S_3 were defined such that they had similar plan areas, but the depth of damage varied from 50 mm to 225 mm, as the damage case subscript number increased (i.e. S_1, S_2, or S_3). A similar pattern of variation in depth was followed for damage states (S_4, S_5) and (S_6, S_7). Damage states S_1 through S_7 are illustrated in Figure 5-10, while their dimensions are given in Table 5-6. Damage states S_1 through S_7 are shown in an elevated position with the partial view of finite elements of the bridge deck in the background to illustrate the relative sizes of damage states.

The second series of damage states was further divided into three subgroups to systematically investigate the effect of damage size on VBDD parameters. In the first subgroup, damage states S_1 through S_3 were included to investigate the effect of damage depth on VBDD parameters, while the plan area of the damage was fixed. The second subgroup consisted of damage states S_1, S_4 and S_6, in which depth and width of damage were fixed while length was varied in an ascending fashion from S_1 through S_6. The third subgroup (damage states S_3, S_5 and S_7) had similar variations in the dimensions of damage in second subgroup, except that the damage was deeper than it was for the second subgroup.

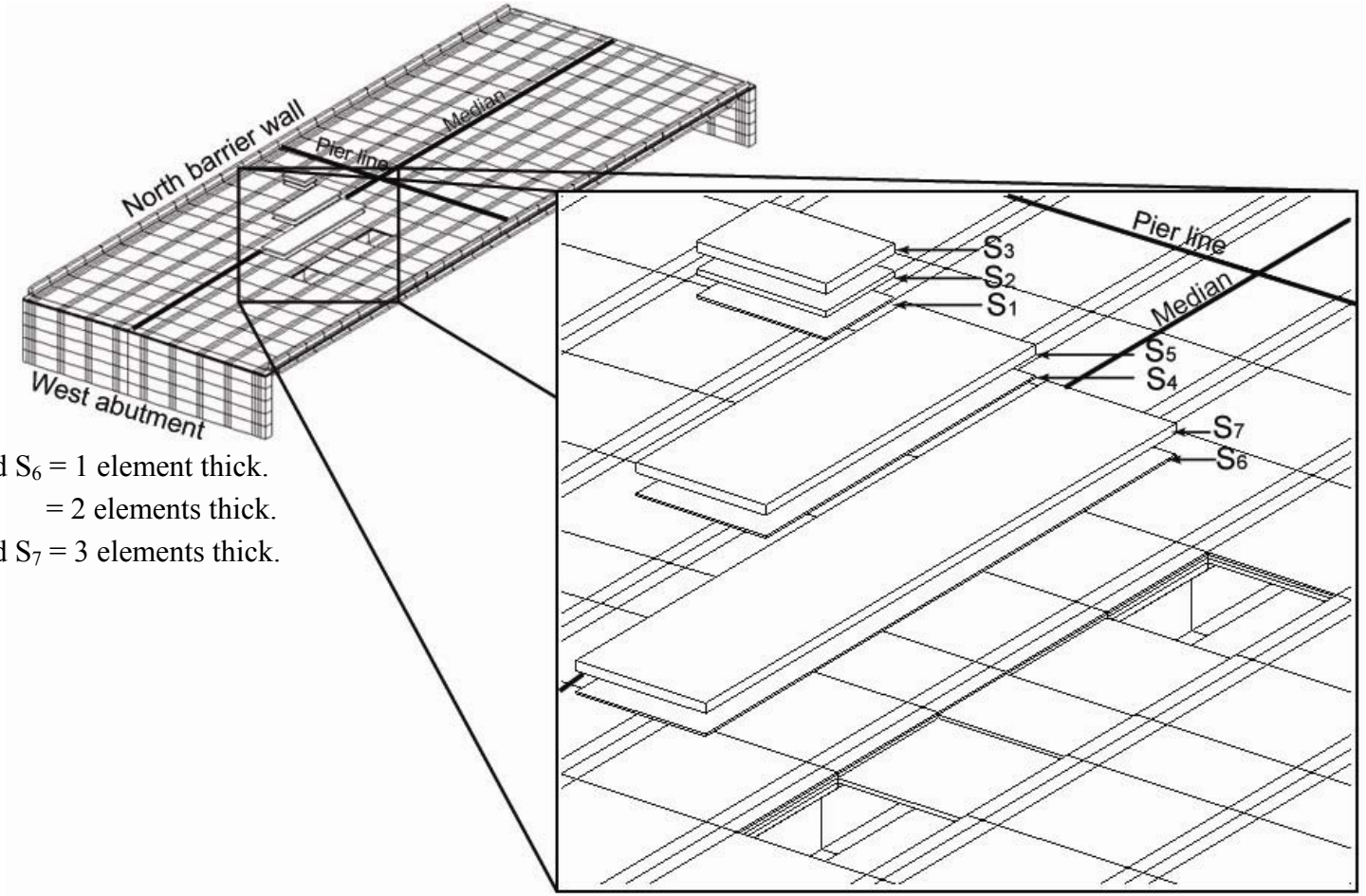

S_1, S_4 and S_6 = 1 element thick.
S_2 = 2 elements thick.
S_3, S_5 and S_7 = 3 elements thick.

Figure 5-10. Locations of damage states S_1 through S_7 showing their locations on the bridge deck and their relative sizes.

Table 5-6. Damage cases with their corresponding sizes and aspect ratios for the second series.

Damage Case	Distance from west edge to west abutment (m)	Distance from east edge to west abutment (m)	Distance from south edge to south barrier wall (m)	Distance from north edge to south barrier wall (m)	Size (m×m×m)	Aspect ratio (length: width: depth)
S_1	21.3058	23.0058	7.6	10.1	1.7×2.5×0.05	0.68:1:0.02
S_2	21.3058	23.0058	7.6	10.1	1.7×2.5×0.125	0.68:1:0.05
S_3	21.3058	23.0058	7.6	10.1	1.7×2.5×0.225	0.68:1:0.09
S_4	18.8058	25.5058	7.6	10.1	6.7×2.5×0.05	2.68:1:0.02
S_5	18.8058	25.5058	7.6	10.1	6.7×2.5×0.225	2.68:1:0.09
S_6	16.3058	28.0058	7.6	10.1	11.7×2.5×0.05	4.68:1:0.02
S_7	16.3058	28.0058	7.6	10.1	11.7×2.5×0.225	4.68:1:0.09

CHAPTER 6. NUMERICAL RESULTS: DAMAGE-INDUCED CHANGES IN MODAL PROPERTIES AND MODE SHAPE NORMALIZATION

6.1 OVERVIEW

A finite element model of the Attridge Drive Overpass, calibrated to field measured dynamic properties, was used to investigate the changes of dynamic properties (i.e., natural frequencies and mode shapes) due to simulated damage states. A description of damage states referred to in the subsequent sections was given in Section 5.4 of Chapter 5. Results regarding changes in natural frequencies are presented in Section 6.2. A brief introduction to mode shape changes is presented in Section 6.3; more detailed results using the VBDD parameters discussed in Section 2.4.2.2 are provided in subsequent chapters. It was found that methods used to normalize the mode shapes had a significant effect on the resulting VBDD parameters when used for damage detection. Therefore, a study of various normalization procedures using the FE model is presented in Section 6.4.

6.2 DAMAGE-INDUCED CHANGES IN NATURAL FREQUENCY

The damage scenarios considered in this numerical study failed to produce significant changes in the lowest three natural frequencies of the system. In fact, the order of magnitude of damage-induced frequency changes was limited to the fourth decimal place (i.e., 10^{-4} Hz). Contrasting this with the much larger range of temperature-induced variations in natural frequency presented in Section 4.2, it becomes apparent that natural frequencies, by themselves, are unlikely to provide a reliable indicator of

damage. Similar conclusions have been reached by others (e.g., Alampalli 1998), although Peeters et al. (2001) suggested that damage-induced changes to natural frequencies could be distinguished from environmental effects through the use of continuous monitoring and suitable pattern recognition algorithms.

6.3 DAMAGE-INDUCED CHANGES IN MODE SHAPE

Relatively small scale damage to the bridge deck of the FE model, as described in Section 5.4, were found to cause changes in the mode shapes. As an example, consider Figure 6-1, in which the first mode shape along the south barrier wall and a

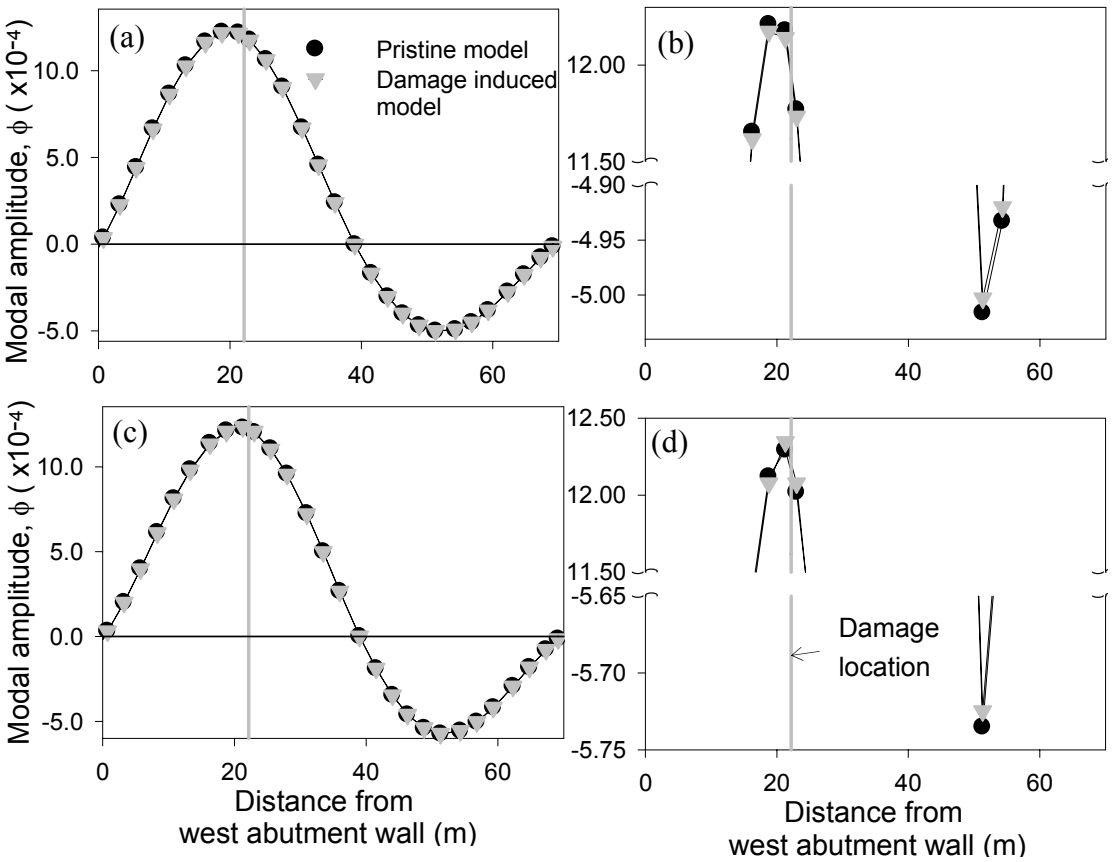

Figure 6-1. First numerical mode shape before and after damage case S_3 was induced in the calibrated FE model: (a) along south barrier wall; (b) locally enlarged plot along south barrier wall; (c) along north edge of damage; and (d) locally enlarged plot along north edge of damage.

sensor line adjacent to the damage are shown before and after damage case S_3 was induced. For this figure, modal amplitudes were taken directly from the vertical components of the eigenvectors at the corresponding nodes of the FE model without normalization. Figure 6-1 shows that damage case S_3 induced almost imperceptible changes in mode shape over the entire length of the bridge on the sensor lines shown, except perhaps where, maximum changes occurred approximately at the mid point of both spans. The magnitudes of change in mode shape ($5x10^{-6}$) were small compared to the magnitude of the mode shape itself ($1.23x10^{-3}$). However, VBDD parameters considered in this study successfully utilized these relatively small magnitude changes to identify the location of damage.

The five VBDD parameters (see Section 2.4.2.2) considered in the present study were all based on the use of the mode shape in some form. It was observed in the course of this study that the method used in the normalization of the mode shapes influenced the performance of the five VBDD parameters in detecting damage, as did the relative distance of sensors from the location of damage and the size of damage. A numerical study on mode shape normalization is described in the following section. The effects of different normalization methods on the VBDD parameters are also described and illustrated in Chapters 7 and 8.

The relative distance of the sensors from the damage location was observed to be pivotal in localizing the damage (Level II damage detection). The use of a dense grid of sensors is described in Chapter 7 to investigate the efficiency of five VBDD parameters for Level II damage detection. In practice, a substantial amount of work is involved during the placement of a dense grid of sensors. It also hinders the traffic flow if sensors

are placed on top of the bridge deck. Therefore, the use of VBDD parameters when sensors are placed in easily accessible locations where traffic will not be interrupted was also investigated. The variation of VBDD parameters for different damage states using a limited number of measurement locations is presented in Chapter 8.

6.4 NORMALIZATION OF MODE SHAPE

By definition, the elements of a mode shape vector or eigenvector are only defined relative to each other; their absolute magnitudes are indeterminate. In order to identify changes to mode shapes caused by damage, it is advantageous to scale the undamaged and damaged mode shapes to be as similar as possible, in a general sense. Therefore, a suitable normalization procedure was required for this study. Normalization procedures used in this study are presented below.

6.4.1 Unit-Norm Normalization

One common normalization procedure, known as mass orthonormalization, requires mode shapes to satisfy the following relationship:

$$\boldsymbol{\phi}_n^T \mathbf{M} \boldsymbol{\phi}_n = 1 \ , \tag{6.1}$$

where $\boldsymbol{\phi}_n$ denotes the normalized eigenvector and **M** is the mass matrix (Humar 1990). For a structure in which the mass is uniformly distributed among the nodes, the mass matrix will be $m\mathbf{I}$, in which m is the uniform lumped mass at each node and **I** is an identity matrix. In this case, the mass orthonormalization expression for the undamaged mode shape can be simplified as follows:

$$\boldsymbol{\phi}_n \mathbf{M} \boldsymbol{\phi} = \boldsymbol{\phi}^T m \mathrm{I} \boldsymbol{\phi} = m \boldsymbol{\phi}^T \boldsymbol{\phi} = mC \ , \tag{6.2}$$

where

$$C = \boldsymbol{\phi}^T \boldsymbol{\phi} \ . \tag{6.3}$$

Since it can be reasonably assumed that the mass is, in fact, distributed quite evenly throughout the bridge structure, even after sustaining small-scale damage, the expression for the damaged mode shape can be written as

$$\boldsymbol{\phi}^{*T}\mathbf{M}\boldsymbol{\phi}^{*} = mC^{*} \ , \tag{6.4}$$

where the superscript $*$ denotes the damaged eigenvector. In practice, it is very challenging to ascertain m for a real structure. To avoid the need for m in the current study, the damaged and undamaged mode shapes were normalized by dividing them by $\sqrt{C}$ and $\sqrt{C^{*}}$, respectively. Thus,

$$\boldsymbol{\phi}_n = \frac{\boldsymbol{\phi}}{\sqrt{C}} \tag{6.5}$$

$$\text{and } \boldsymbol{\phi}_n{}^{*} = \frac{\boldsymbol{\phi}^{*}}{\sqrt{C^{*}}} \ . \tag{6.6}$$

The mode shape vectors resulting from this procedure, referred to as unit-norm normalization, differ from that obtained by mass orthonormalization (assuming a uniform mass distribution) by a factor of m.

6.4.2 Optimum Normalization

As mentioned above, the goal of normalization is to scale the damaged and undamaged mode shape vectors to be as similar as possible, in an averaged sense, in order to maximize localized differences caused by damage and, thereby, to improve the likelihood of successfully identifying the presence and location of the damage. While unit-norm normalization is easy to implement, it was not known whether this procedure would minimize the average differences between damaged and undamaged mode shape vectors. Therefore, a study was undertaken to determine the optimal scaling factor for the mode shape vectors and to compare the optimal factor to that resulting from the unit-norm normalization procedure.

Assuming that different scaling factors are used for damaged and undamaged mode shape vectors, the difference between the two vectors, $\boldsymbol{\Delta}$, may be expressed as

$$\Delta = a\boldsymbol{\phi}^* - b\boldsymbol{\phi} \ , \tag{6.7}$$

where a and b are the scaling factors applied to the damaged and undamaged mode shape vectors, respectively. Recognizing that the ratio of the two scaling factors is unique, but that the factors themselves are not, Equation 6.7 was divided through by b to obtain

$$\Delta = \frac{a}{b}\boldsymbol{\phi}^* - \boldsymbol{\phi} \ . \tag{6.8}$$

This may also be thought of as using a unit scaling factor for the undamaged mode shape and scaling the damaged mode shape by a factor of $\frac{a}{b}$ to make it as similar as possible to the undamaged one.

The optimal scaling factor ratio, $\left(\frac{a}{b}\right)_{opt}$, was found by using a least-squares regression technique implemented within MATLAB®, to minimize the sum of squares of the differences between the mode shape vector elements. Mathematically, the following expression was minimized:

$$\sum_{i=1}^{n}\left(\frac{a}{b}\phi_i^* - \phi_i\right)^2 \ , \tag{6.9}$$

where n corresponds to the number of elements in the vector, and the ϕ_i is the i^{th} element in the vector. For the unit-norm normalized vectors, the corresponding sum of the squares is

$$\sum_{i=1}^{n}\left(\sqrt{\frac{C}{C^*}}\phi_i^* - \phi_i\right)^2 \ . \tag{6.10}$$

Thus, the unit-norm scaling factor ratio may be compared to the optimal scaling ratio by means of a percent relative difference (PRD) as follows:

$$PRD = \left(\frac{\left(\frac{a}{b}\right)_{opt} - \sqrt{\frac{C}{C^*}}}{\sqrt{\frac{C}{C^*}}} \right) \times 100 \ . \tag{6.11}$$

The optimal scaling factor ratio was found to vary with the size and location of damage. Another factor that was observed to influence the optimal scaling factor was the size of the subset of mode shape data that was included in the mode shape vectors when performing the normalization, as described in the subsequent sentences. For the work of this thesis, only modal amplitudes at the vertical degrees of freedom on the top surface of the bridge deck were used to define mode shapes. In addition, only the fundamental mode shape of the calibrated FE model was used for the normalization investigation.

Two general options were considered for normalizing the mode shapes: either data from vertical degrees of freedom located along the barrier walls and median were used to perform the normalization in a single calculation (i.e. a single scaling factor was defined for the entire bridge deck based on modal amplitudes along the barrier walls and median), or separate scaling factors were used for different regions of the deck, thus normalizing the mode shape in a piecewise fashion by considering subsets of the data corresponding to individual regions. The former option was chosen for study since that data (along the barrier walls and median) was the largest common subset of modal amplitudes used in all investigations in both Chapters 7 and 8. The choice of subsets used to define the mode shape vectors was found to exert a large influence on both the optimal scaling factor ratio and the unit-norm scaling factor. In subsequent sections, two alternative approaches were employed: (1) "3-line normalization," in which data at vertical degrees of freedom located along the barrier walls and median were used, and

(2) "single line normalization," in which the subset of data used for piecewise normalization consisted of modal amplitudes along individual longitudinal lines spanning the length of the bridge deck. Subsets of modal amplitude data along individual transverse lines were also studied for single line normalization. However, it was found by visual observation that single line normalization along individual transverse lines exhibited a level of precision in damage detection similar to 3-line normalization; consequently, this approach is not included in subsequent discussions.

A total of 13 different damage scenarios (see Section 5.4 for a description of the damage), as indicated on Figure 6-2, were investigated in the normalization study. For all damage scenarios, damage was confined to the top 50 mm layer of concrete in the deck. The optimum scaling factor ratio was determined along 30 individual simulated longitudinal sensor lines as indicated on Figure 6-2. Therefore there were 30 optimum scaling factor ratios, as well as 30 unit-norm scaling factors for single line normalization

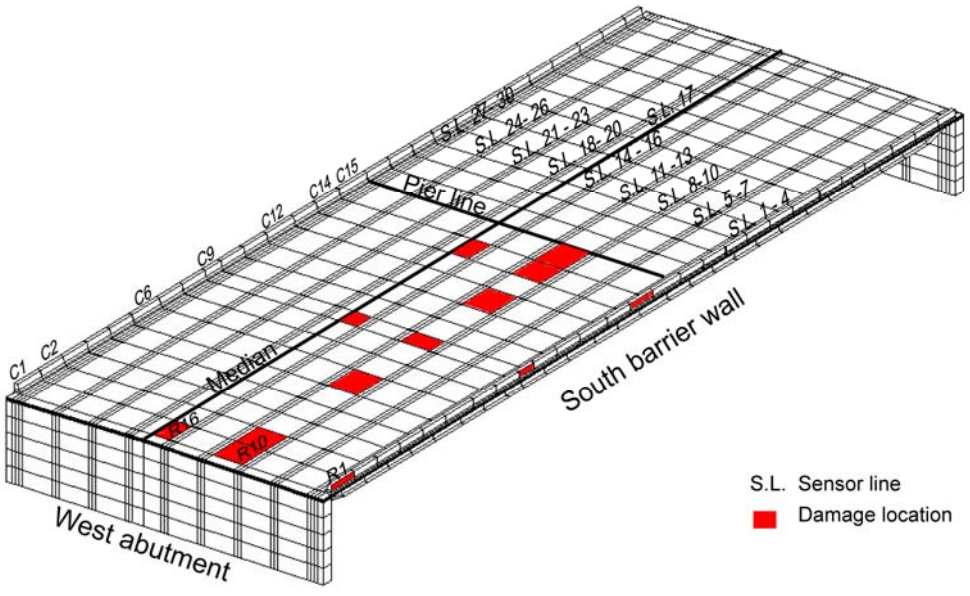

Figure 6-2. Damage locations and sensor lines used to determine optimal normalization.

pertinent to each damage case. On the other hand, there was a single factor for 3-line normalization for each damage case.

PRD values (as defined by Eq. 6.11) along four selected sensor lines for both single line and 3-line normalization for all 13 damage cases are illustrated in Figure 6-3; here, a log scale was used for the vertical axis to illustrate the small PRD values that were representative of single line normalization. Corresponding PRD values are also listed in Table 6-1. Results along four sensor lines are illustrated here as they encompass all the salient features noted from this investigation. It is evident that the PRD value

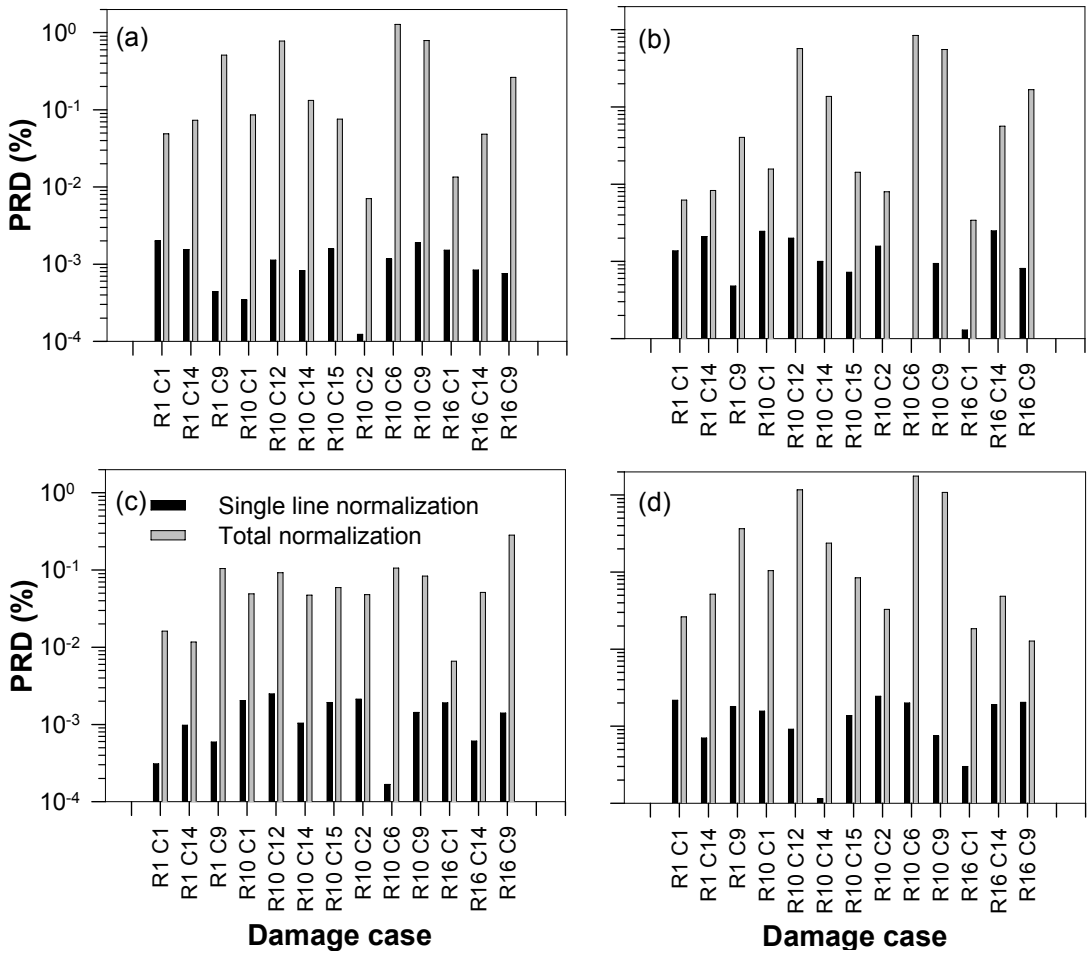

Figure 6-3. Comparison of PRD values for both single line and 3-line normalization: (a) sensor line 1; (b) sensor line11; (c) sensor line 17; and (d) sensor line 30.

Table 6-1. PRD values of damage cases on selected sensor lines.

Damage Case	Sensor line 1		Sensor line 11		Sensor line 17		Sensor line 30	
	Single line (%)	3-line (%)	Single line (%)	3-line (%)	Single line (%)	3-line (%)	Single line (%)	3-line (%)
R1 C1	0.00200	0.04879	0.00137	0.00621	0.00031	0.01621	0.00217	0.02621
R1 C14	0.00154	0.07330	0.00209	0.00830	0.00098	0.01170	0.00070	0.05170
R1 C9	0.00044	0.51047	0.00048	0.04045	0.00059	0.10456	0.00180	0.36457
R10 C1	0.00034	0.08569	0.00246	0.01567	0.00204	0.04935	0.00157	0.10437
R10 C12	0.00113	0.77840	0.00200	0.57297	0.00250	0.09198	0.00091	1.17063
R10 C14	0.00082	0.13218	0.00100	0.13719	0.00104	0.04713	0.00011	0.23805
R10 C15	0.00157	0.07572	0.00073	0.01432	0.00193	0.05934	0.00137	0.08435
R10 C2	0.00012	0.00706	0.00158	0.00794	0.00213	0.04796	0.00244	0.03295
R10 C6	0.00117	1.27944	0.00008	0.84309	0.00017	0.10580	0.00200	1.76501
R10 C9	0.00190	0.79028	0.00094	0.55473	0.00143	0.08363	0.00075	1.08410
R16 C1	0.00152	0.01341	0.00013	0.00341	0.00190	0.00659	0.00030	0.01841
R16 C14	0.00084	0.04858	0.00248	0.05644	0.00061	0.05144	0.00190	0.04858
R16 C9	0.00075	0.26316	0.00081	0.16756	0.00141	0.28275	0.00204	0.01274
Maximum	0.00200	1.27944	0.00248	0.84309	0.00250	0.28275	0.00244	1.76501
Minimum	0.00012	0.00706	0.00008	0.00341	0.00017	0.00659	0.00011	0.01274
Mean	0.00109	0.31588	0.00124	0.18679	0.00131	0.07373	0.00139	0.38475

changes as the damage case, sensor line, or normalization procedure changes. However, the PRD of single line normalization along any given sensor line for all damage cases is much smaller than that of the 3-line normalization. For single line normalization, the average PRD was approximately 0.00126%, indicating that unit-norm normalization produced near optimal scaling of the mode shapes. When 3-line normalization was performed, the average PRD was approximately 0.35% on the barrier walls and approximately 0.13% on the intermediate sensor lines in between barrier walls, indicating that unit-norm normalization using 3-line normalization was further from optimal than that using single line normalization, but that it was still very close to optimal. However, based on this measure, single line normalization appeared to increase

the performance level (i.e. sensitivity) of VBDD methods for Level II damage detection, as presented in subsequent sections. Also, since unit-norm normalization was found to be near optimal for all cases considered, it was adopted for the remainder of the work described in this thesis.

Unit-norm normalization was applied to the mode shapes of both the damaged induced and pristine finite element models before evaluating changes in mode shape and other VBDD parameters. As mentioned above, unit-norm normalization is based on the premise that the mass is distributed among nodes in a fairly uniform manner. Since the nodes on the bridge deck (FE model) were not evenly spaced, though, modal amplitudes at uniform intervals were estimated by fitting a cubic spline curve to the FE generated mode shapes along individual longitudinal lines (sensor line), as shown in Figure 6-2. A uniform spacing of 1 m between two successive simulated modal amplitudes was maintained in this study for investigating VBDD techniques. Both the mode shapes derived from the damaged and pristine FE models were interpolated to generate evenly spaced modal amplitudes prior to applying unit-norm normalization.

CHAPTER 7. VBDD USING A DENSE GRID OF SENSORS

7.1 OVERVIEW

Precision in damage detection using VBDD parameters based on mode shapes is believed to depend largely on the accuracy of mode shape definition. Mode shape definition, in turn, depends on the sensor spacing, uncertainty in field measurements and proximity of sensor placement to the damage location. Increasing the density of the grid of sensors will increase the likelihood that a sensor will be located close to the damage location.

The spatial distributions of the five VBDD parameters discussed in Section 2.4.2.2 vary as the location and size of damage changes. The effects of damage location and size on the spatial variations of the five parameters calculated for the Attridge Drive Overpass are presented in Sections 7.2 and 7.3, respectively. A numerical study was also performed to investigate the effects of sensor spacing on the VBDD parameters. Results of that study are presented in Section 7.4. Uncertainty in mode shape measurements is also known to affect the effectiveness of the VBDD parameters in detecting damage. The influence of uncertainty in mode shape measurements on the resulting VBDD parameters when using a dense grid of sensors is presented in Section 7.5.

7.2 SPATIAL CHARACTERISTICS OF VBDD PARAMETERS

In this section, the spatial distributions over the surface of the bridge deck of the five VBDD parameters described in Section 2.4.2.2 are presented, with a focus on ascertaining their ability to reveal the presence (Level I) and location (Level II) of damage. Two representative damage cases (R10C1 and R10C9) of nearly similar size

were selected to simplify the discussion and avoid repetition. As indicated in Section 5.4, damage case R10C9 was located in the middle region of the south-west quadrant of the deck (approximately 22 m east of the west abutment wall and 9 m north of the south barrier wall) and featured a missing deck element 1.7 m long x 2.5 m wide x 50 mm deep. Damage case R10C1 was located adjacent to the west abutment wall (approximately 0.76 m east of the west abutment wall and 7.6 m north of the south barrier wall). In this damage case, a 2.5 m long x 2.5 m wide x 50 mm deep element was removed to simulate damage on the bridge deck. The spatial distribution of the VBDD parameters over the entire deck surface, as well as distributions along four longitudinal lines spanning the entire length of the bridge deck (a line bordering the north edge of damage, lines along north and south barrier walls, and a line along the central median), were plotted for each damage case. Only the fundamental mode shape was used in this study; in addition, both the single line and 3-line unit-norm normalization procedures were applied for each damage case to compare the effectiveness of the respective normalization procedures.

7.2.1 Spatial Characteristics of Change in Mode Shape

Spatial distributions of the change in mode shape using single line and 3-line normalization for damage case R10C9 are shown in Figure 7-1 (a) and (c), respectively. The changes in mode shape at the location of damage is distinctive and prominent, clearly identifying the damage location when single line normalization is used, even though significant mode shape changes are seen over the entire bridge deck. On the other hand, the spatial distribution of changes in mode shape using 3-line normalization

also exhibits a distinctive hump at the location of damage, but the magnitude of changes in other locations overshadows the distinctive indication at the damage location.

Figure 7-1 (b) and (d) show the distributions of the change in mode shape along the barrier walls, median and a longitudinal line immediately adjacent to the north edge of damage location, when mode shapes were normalized using the single line and 3-line

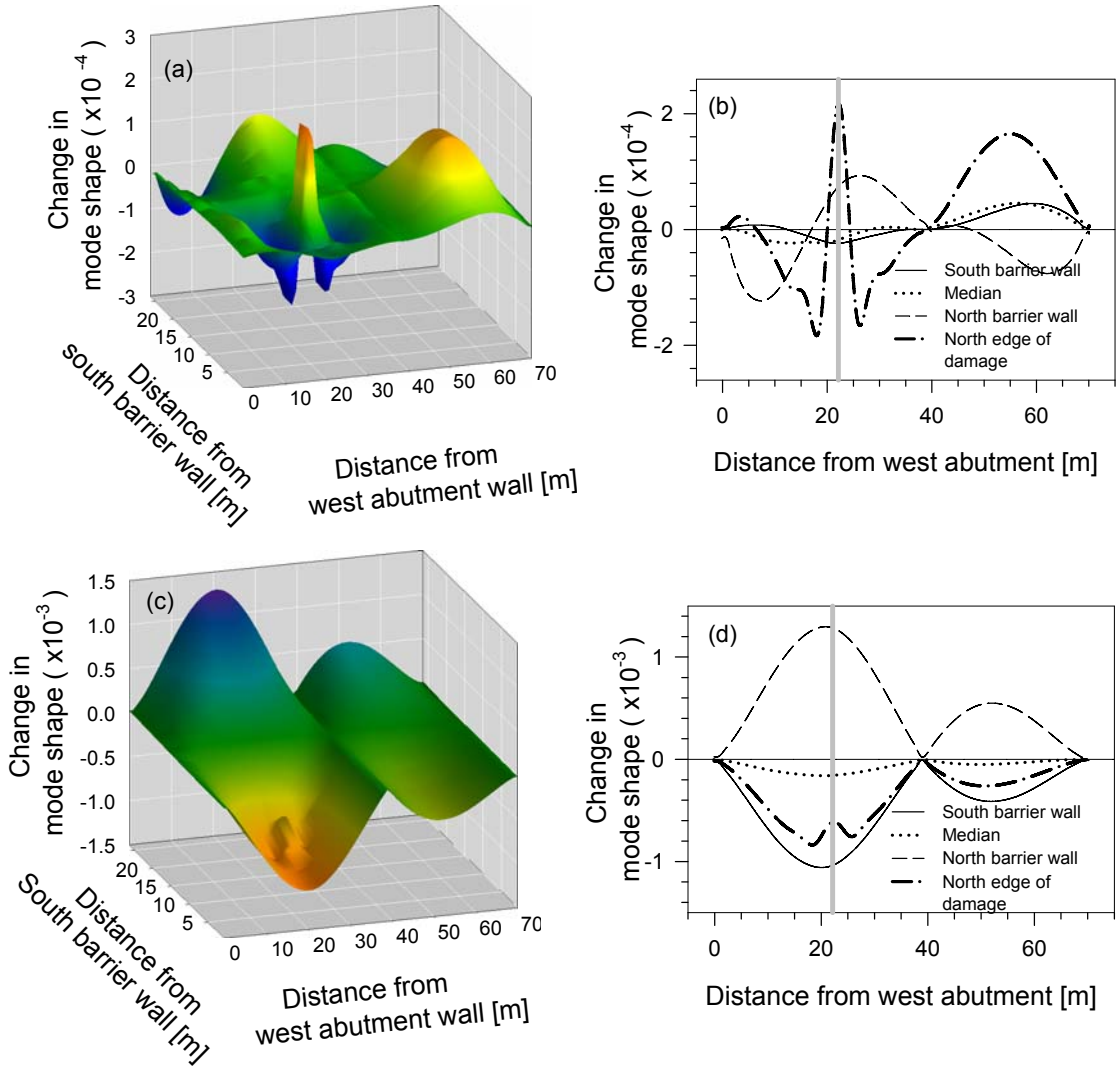

Figure 7-1. Distributions of change in mode shape for damage case R10C9: (a) spatial distribution for single line normalization; (b) longitudinal distribution along selected lines for single line normalization; (c) spatial distribution for 3-line normalization; and (d) longitudinal distribution along selected lines for 3-line normalization.

normalization procedures, respectively. When 3-line normalization was used, a small hump centred at the damage location on the longitudinal distribution plot close to the north edge of damage (as seen in Figure 7-1 d) indicates the location of damage. However, the hump is not seen in the changes in mode shape on barrier walls. The longitudinal distribution of the change in mode shape along the line adjacent to the north edge of damage using single line normalization, on the other hand, shows a distinctive peak, relatively higher in magnitude, centred at the damage location (see Figure 7-1 b). In this plot, a broad peak of nearly the same magnitude as that at the damage location was also observed over the east span; due to the distinctive narrow peak at the damage location, however, it did not add any ambiguity to interpreting the change in mode shape parameter in Level II damage detection in this case. Another observation is that the magnitudes of mode shape changes using single line normalization were smaller than those for 3-line normalization, which implies that there was a closer fit between the damaged and baseline mode shape when the single line normalization was used.

Similarly, for damage case R10C1, single line normalization created a distinctive peak at the damage location (see Figure 7-2 a and b), even though the pattern of that peak differs considerably from that observed for damage case R10C9. The location of damage, being signified by a single negative peak whose magnitude is lower than the subsequent positive peak located just to the east of the damage, was not immediately obvious on the plot of change in mode shape along the north edge of the damage. This characteristic negative peak, though, was noted for all damage cases located near abutment or pier supports, providing a means for uniquely locating the damage despite the apparent ambiguity. Change in mode shape values at the location of

damage are also relatively higher than those at any other location on the bridge deck. On the other hand, a small negative hump followed by a small positive hump (see Figure 7-2 c and d) is seen just east of the location of damage on the plot of change in mode shape along the north edge of the damage, when 3-line normalization was used. However, relatively higher values at other locations on the bridge deck overshadow the distinctive changes at the location of damage for this case.

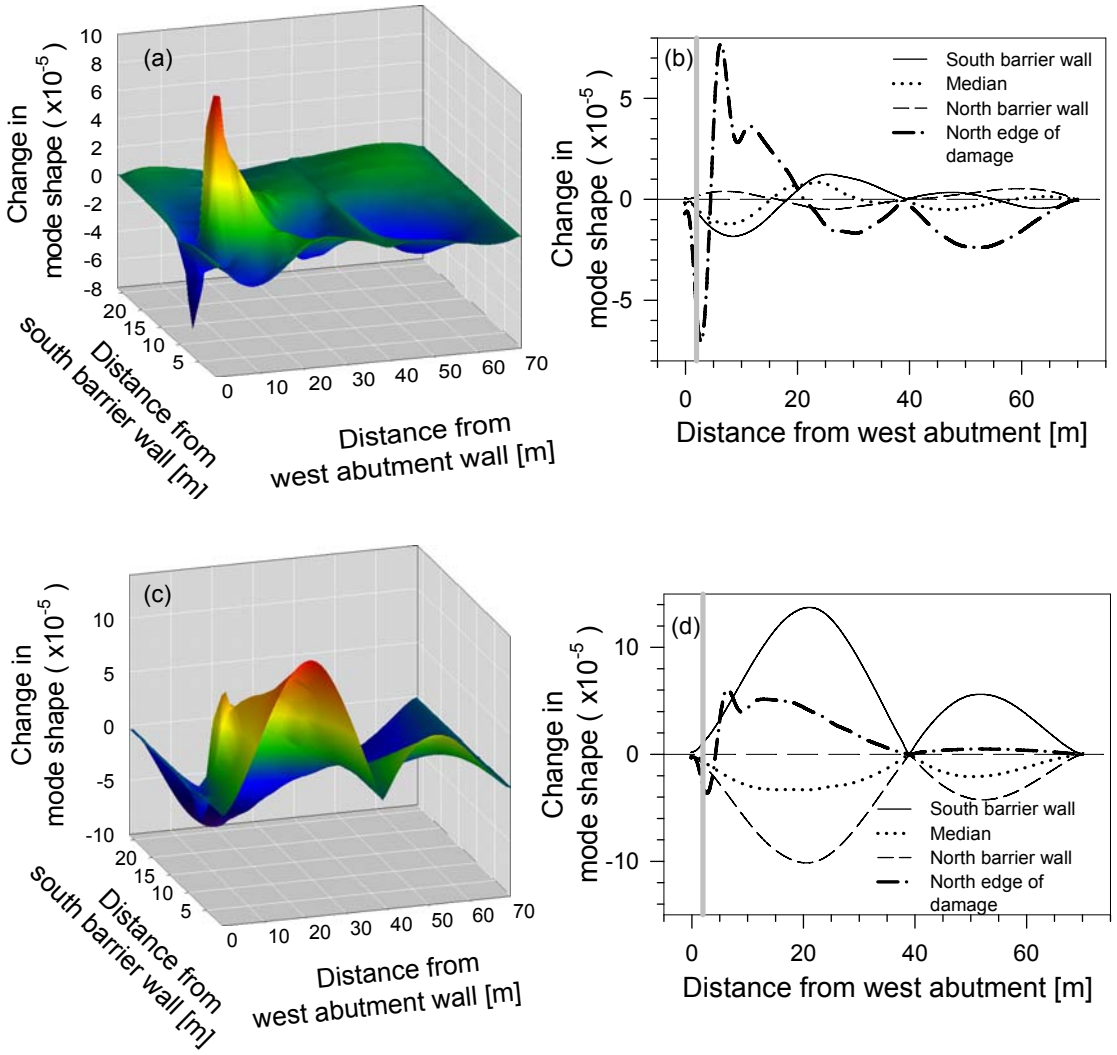

Figure 7-2. Change in mode shape for damage case R10C1: (a) spatial distribution for single line normalization; (b) longitudinal distribution along selected lines for single line normalization; (c) spatial distribution for 3-line normalization; and (d) longitudinal distribution along selected lines for 3-line normalization.

As a result of these observations, single line normalization appears to be more effective than 3-line normalization to produce a distinctive indication of the location of damage (Level II detection) when change in mode shape is used as the damage detection parameters. Change in mode shape values for both damage cases using single line normalization along the more distant barrier walls were considerably lower in magnitude than those along adjacent sensor lines and lacked any distinct peaks that may provide a direct indication of the damage location. However, the presence of measurable changes in mode shape even along these distant sensor lines may allow the presence of damage to be detected (Level I detection), if not precisely located (Level II detection). Furthermore, study of other damage cases suggests that characteristic patterns of mode shape changes using 3-line normalization, even along sensor lines located far from the actual damage, may provide some indication as to the general region where the damage is located on the bridge deck. This aspect is discussed in Chapter 8.

7.2.2 Spatial Characteristics of Change in Flexibility

Spatial characteristics of the change in flexibility parameter for damage case R10C9, using both single line and 3-line normalization, are presented in Figure 7-3 (a) and (c). The spatial plot using single line normalization features three successive, prominent and distinguished peaks (see Figure 7-3 a) at the location of missing elements and a broad peak on the south-east quadrant. There are also changes in flexibility over the entire bridge deck due to the presence of the induced damage R10C9; however, the magnitude and pattern of the change in flexibility at the location of missing elements is sufficiently unique to identify the location of damage (Level II). The distributions of change in flexibility along selected longitudinal lines (barrier walls, median and a sensor

line close to the north edge of damage) show the peaks at the damage location more clearly (Figure 7-3 b). Using 3-line normalization, on the other hand, causes relatively higher changes in the VBDD parameter in regions close to the edges of bridge deck

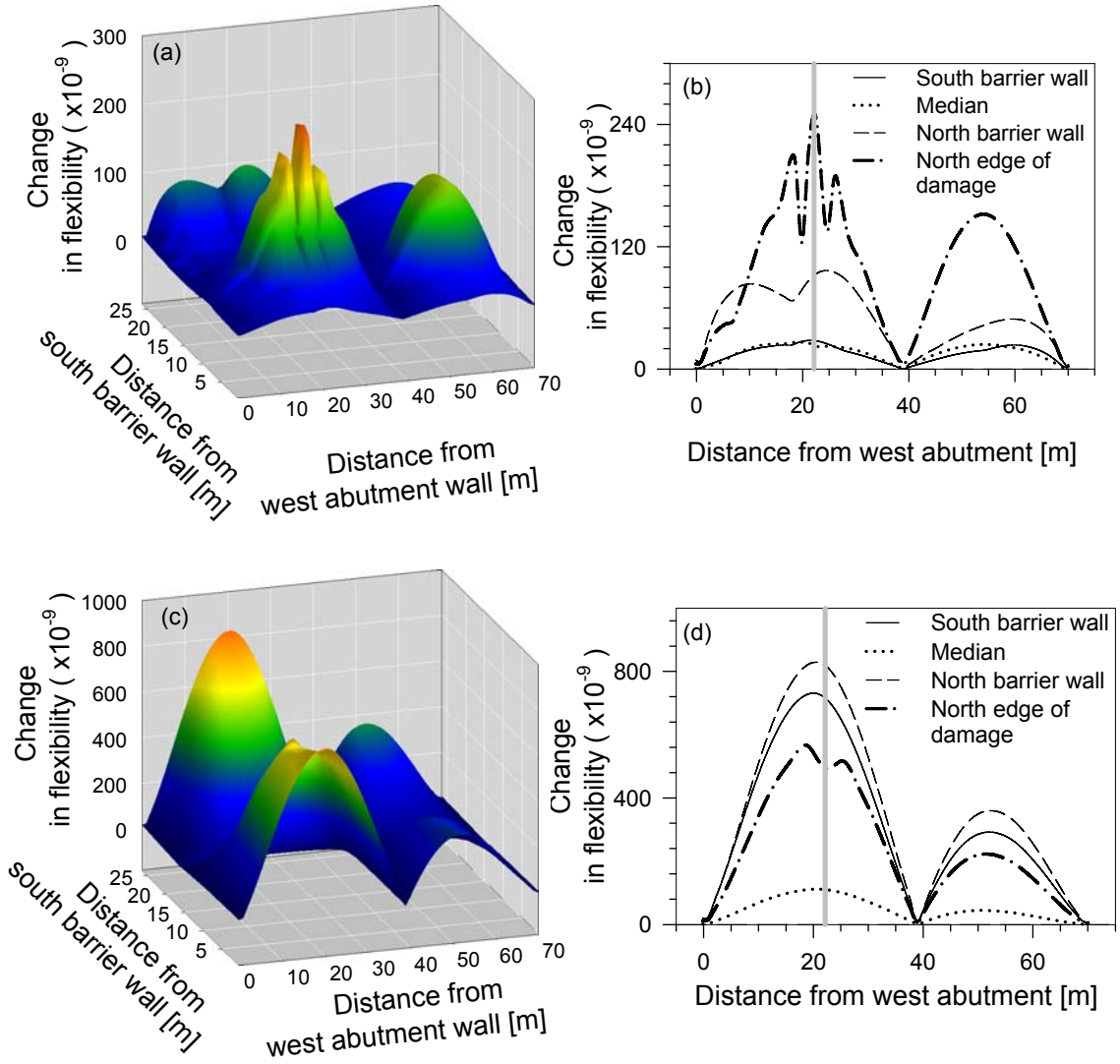

Figure 7-3. Change of flexibility for damage case R10C9: (a) spatial distribution for single line normalization; (b) longitudinal distribution along selected lines for single line normalization; (c) spatial distribution for 3-line normalization; and (d) longitudinal distribution along selected lines for 3-line normalization.

compared to that at the location of damage (Figure 7-3 c), making damage localization more difficult. A minor depression at the location of damage (see Figure 7-3 d) is observed in the plot along the longitudinal line close to the north edge of the damage; however, the magnitude of this change is too small to discern in comparison to that at other locations on the bridge deck.

Similarly, spatial plots of change in flexibility using single line normalization for damage case R10C1 (see Figure 7-4 a and b) show two successive peaks at the location of damage, even though the location of damage cannot be identified with a high level certainty. The peaks at the location of damage for damage case R10C1 differ from those for damage case R10C9. However, this pattern of peaks was found to be common when the damage was located immediately adjacent to the west abutment wall. As was the case for damage case R10C9, 3-line normalization causes higher magnitudes of the change in flexibility parameter along the barrier walls (see Figure 7-4 c). As seen in Figure 7-4 d, when 3-line normalization was used, the change in flexibility distribution plot along a longitudinal line adjacent to the damage features a small positive hump preceded by a small negative hump adjacent to, and east of, the location of damage, providing an indication of the approximate location of damage, even though the peaks are not as prominent as that exhibited when single line normalization was used. In addition, the magnitude of the change in flexibility in regions more distant from the damage (i.e. barrier walls) overshadowed the peak at the location of damage.

It was clear that single line normalization increased the discernability of the location of damage when the change in flexibility parameter was used. As with the change in mode shape, change in flexibility using single line normalization exhibited

relatively lower magnitudes along more distant sensor lines compared with those near the damage. On the other hand, 3-line normalization, increased the magnitude of change in flexibility values in regions more distant from damage, which may be beneficial for Level I damage detection, even when a small number of sensors are used.

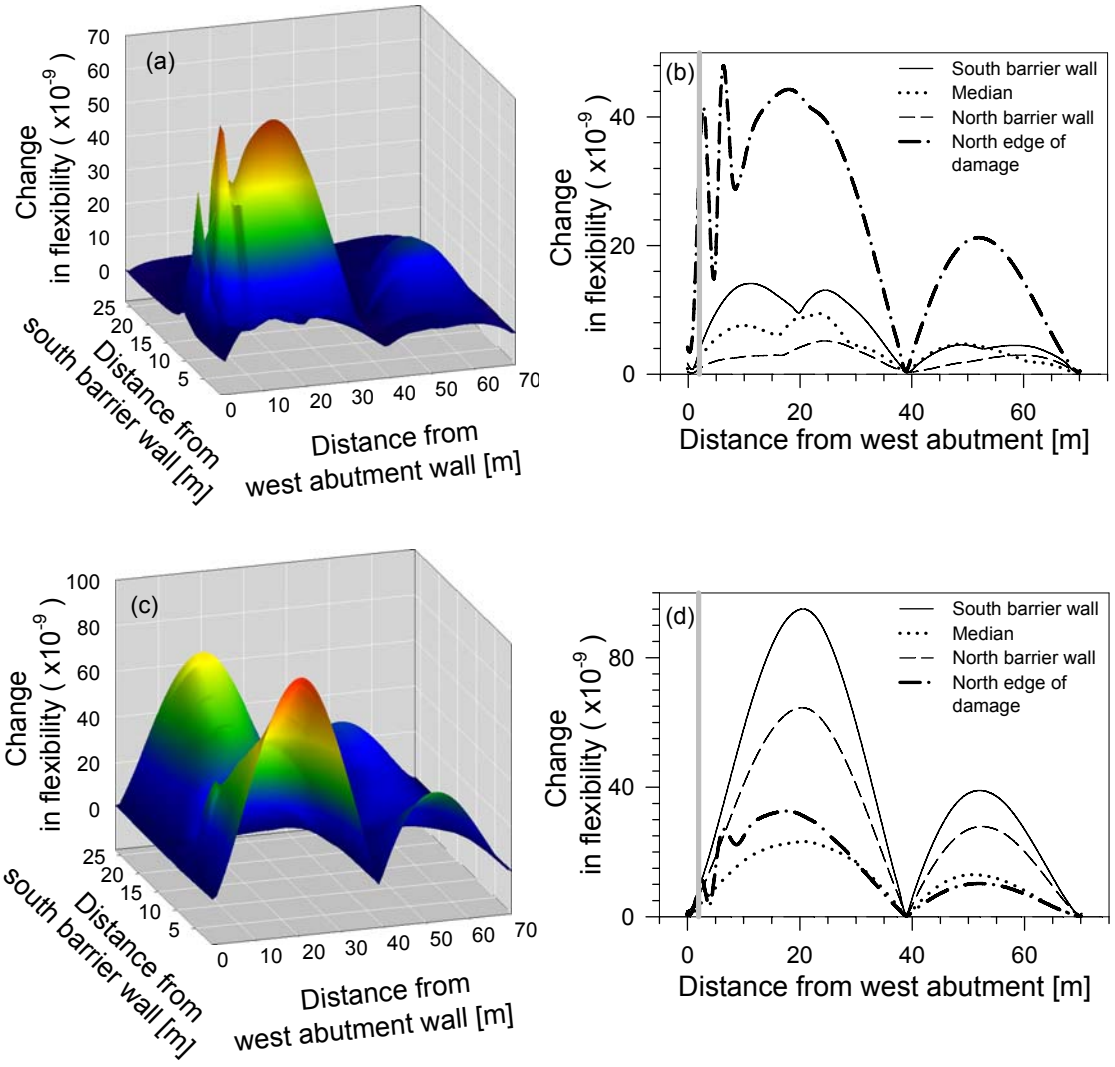

Figure 7-4. Distributions of change in flexibility for damage case R10C1: (a) spatial distribution for single line normalization; (b) longitudinal distribution along selected lines for single line normalization; (c) spatial distribution for 3-line normalization; and (d) longitudinal distribution along selected lines for 3-line normalization.

7.2.3 Spatial Characteristics of Change in Mode Shape Curvature, Change in Uniform Flexibility Curvature and Damage Index

Spatial distributions of the change in mode shape curvature, damage index and change in uniform flexibility curvature for damage case R10C9, using both single line normalization and 3-line normalization, are presented in Figure 7-5 a and c, Figure 7-6 a and c, and Figure 7-7 a and c, respectively. These three methods produced a similar characteristic pattern of peaks at the location of damage for both single line and 3-line normalization. This pattern features a positive peak centred at the damage location accompanied by an adjacent negative peaks on each side. Changes in VBDD parameters in regions more distant from the damage location are generally too small to identify visually. However, depending on the procedure used for normalization and the particular VBDD parameter, the magnitude of VBDD parameter in regions distant from the damage location varies significantly. None of the three methods exhibited any visually identifiable changes in distant regions when single line normalization was used. 3-line normalization, on the other hand, induced visually identifiable changes in parameters for change in mode shape curvature and change in uniform flexibility curvature along barrier walls. This is seen in Figure 7-5 d and Figure 7-7 d). The damage index method did not exhibit any visually identifiable changes in the distant regions, irrespective of normalization procedure.

The spatial distribution for these three VBDD parameters for damage case R10C1 are shown on Figures 7-8, 7-9, and 7-10. The distributions are similar to those for damage case R10C9, except that the pattern of characteristic peaks at the damage location differs. For damage case R10C1, a positive peak is apparent at the location of damage followed by a negative peak on the east side only. This pattern was common to

all damage cases located immediate adjacent to the west abutment wall. The damage index method, similar to observations for damage case R10C9, did not exhibit any visually identifiable changes in parameters in regions distant from damage, irrespective of the normalization procedure used. The change in mode shape curvature and change in

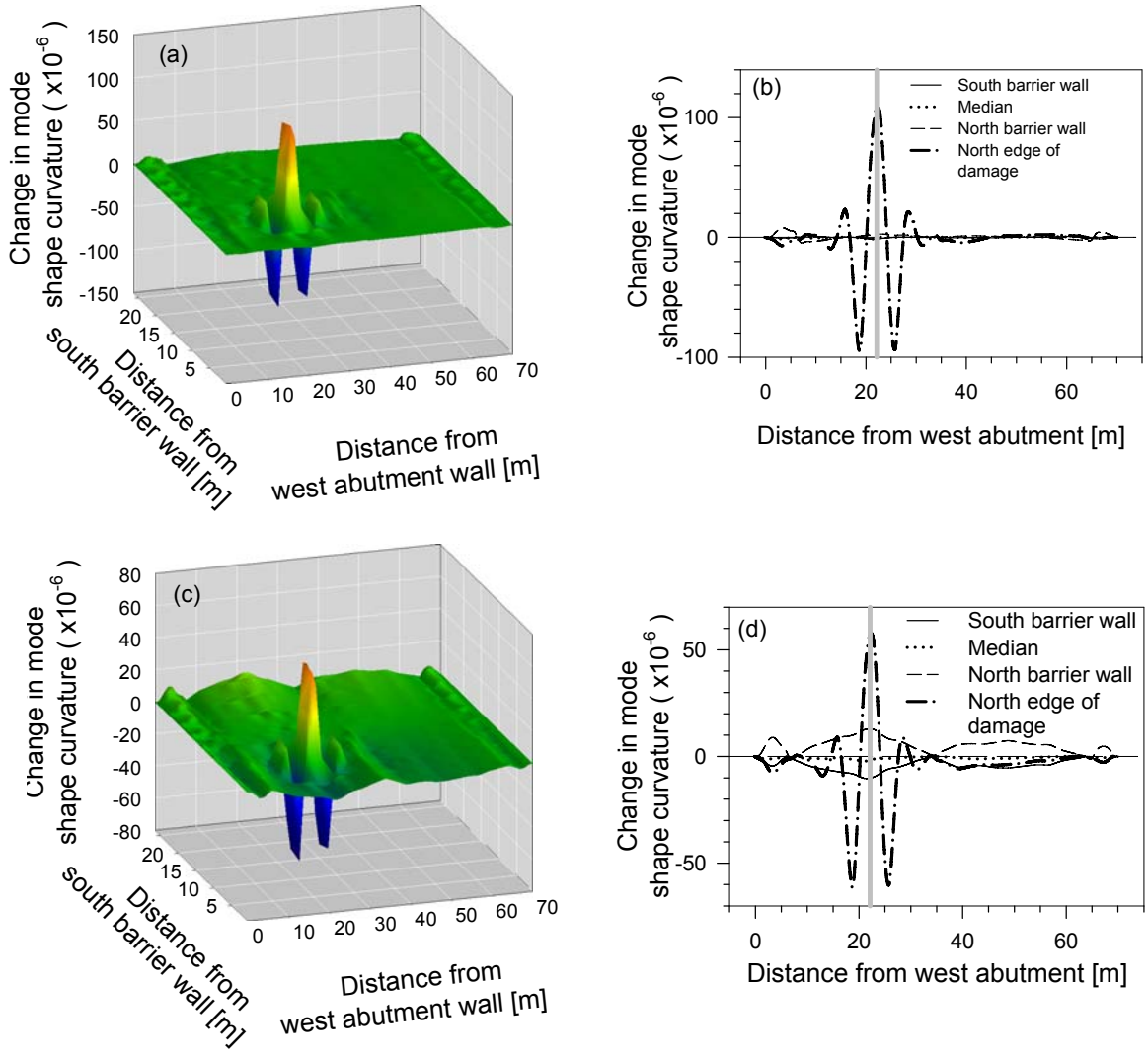

Figure 7-5. Change in mode shape curvature for damage case R10C9: (a) spatial distribution for single line normalization; (b) longitudinal distribution along selected lines for single line normalization; (c) spatial distribution for 3-line normalization; and (d) longitudinal distribution along selected lines for 3-line normalization.

uniform flexibility curvature methods only produced visually identifiable changes along barrier walls when 3-line normalization was used.

In summary, all five methods could successfully locate the simulated damage (Level II), which was indicated by large, distinct peaks in the damage parameter plots at the location of the missing element. This was done using only the fundamental mode

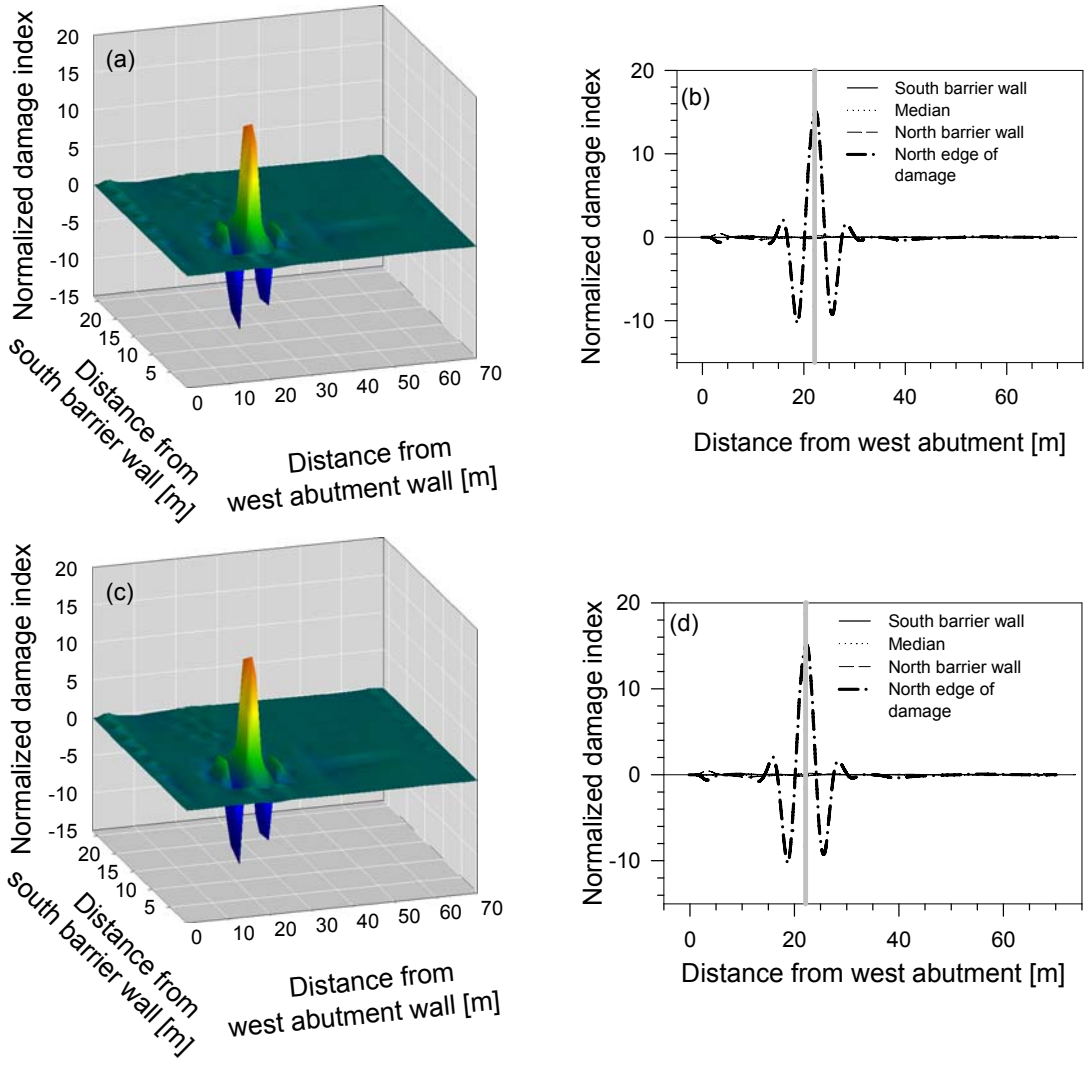

Figure 7-6. Distributions of damage index for damage case R10C9: (a) spatial distribution for single line normalization; (b) longitudinal distribution along selected lines for single line normalization; (c) spatial distribution for 3-line normalization; and (d) longitudinal distribution along selected lines for 3-line normalization.

shape normalized using the unit-norm, single line normalization procedure. Results from this numerical study suggests that small-scale damage can be accurately located on the bridge deck using any of the five VBDD methods considered in this study, providing that a sufficient number of sensors are used and located in close proximity to the

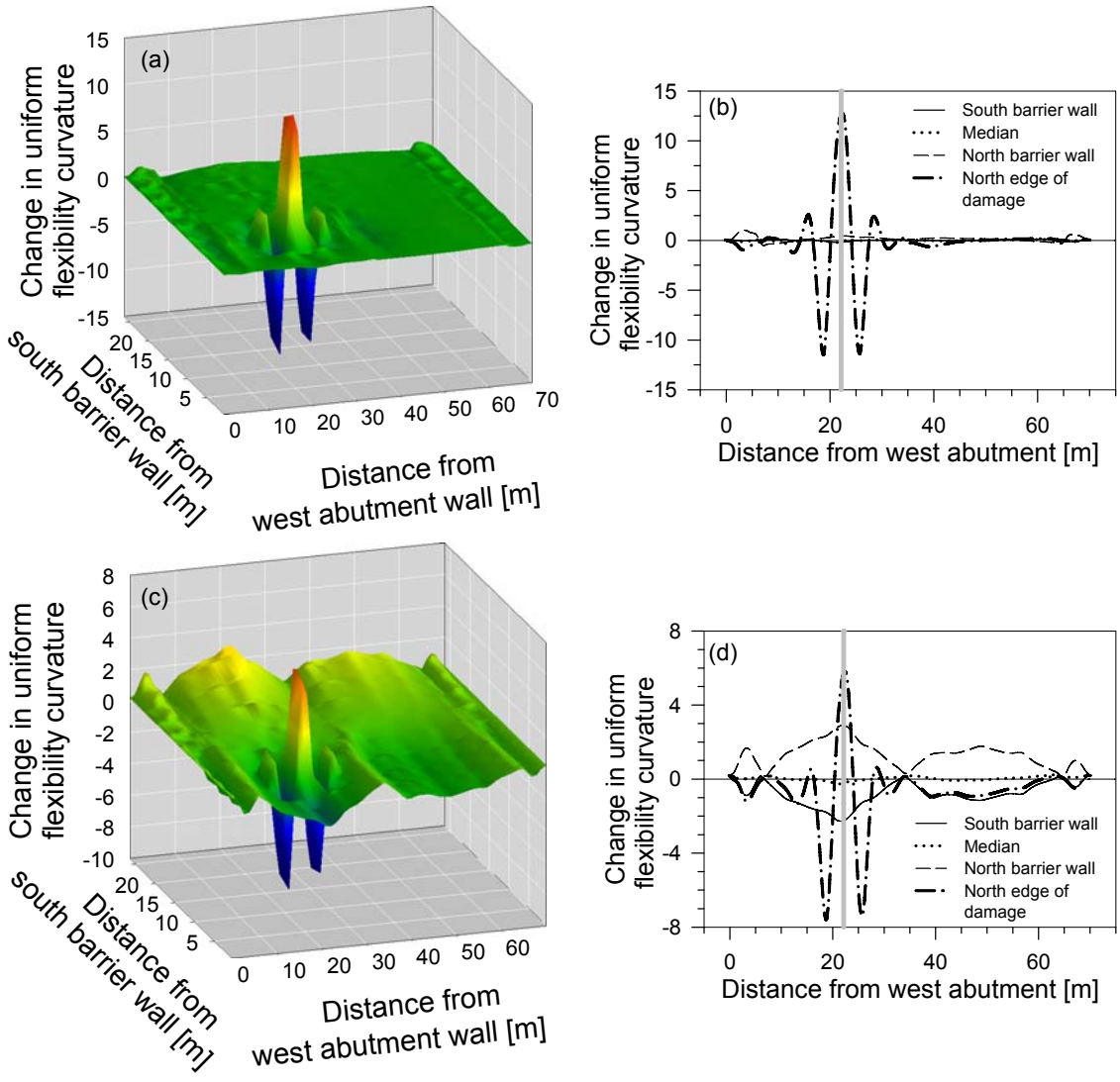

Figure 7-7. Distributions of uniform flexibility curvature for damage case R10C9: (a) spatial distribution for single line normalization; (b) longitudinal distribution along selected lines for single line normalization; (c) spatial distribution for 3-line normalization; and (d) longitudinal distribution along selected lines for 3-line normalization.

damaged areas (for example, within one girder spacing laterally). If those conditions are satisfied, the change in mode shape curvature, damage index and change in uniform flexibility curvature methods appear to provide the most reliable and unambiguous indication of the damage location, particularly for damage occurring near supports. If

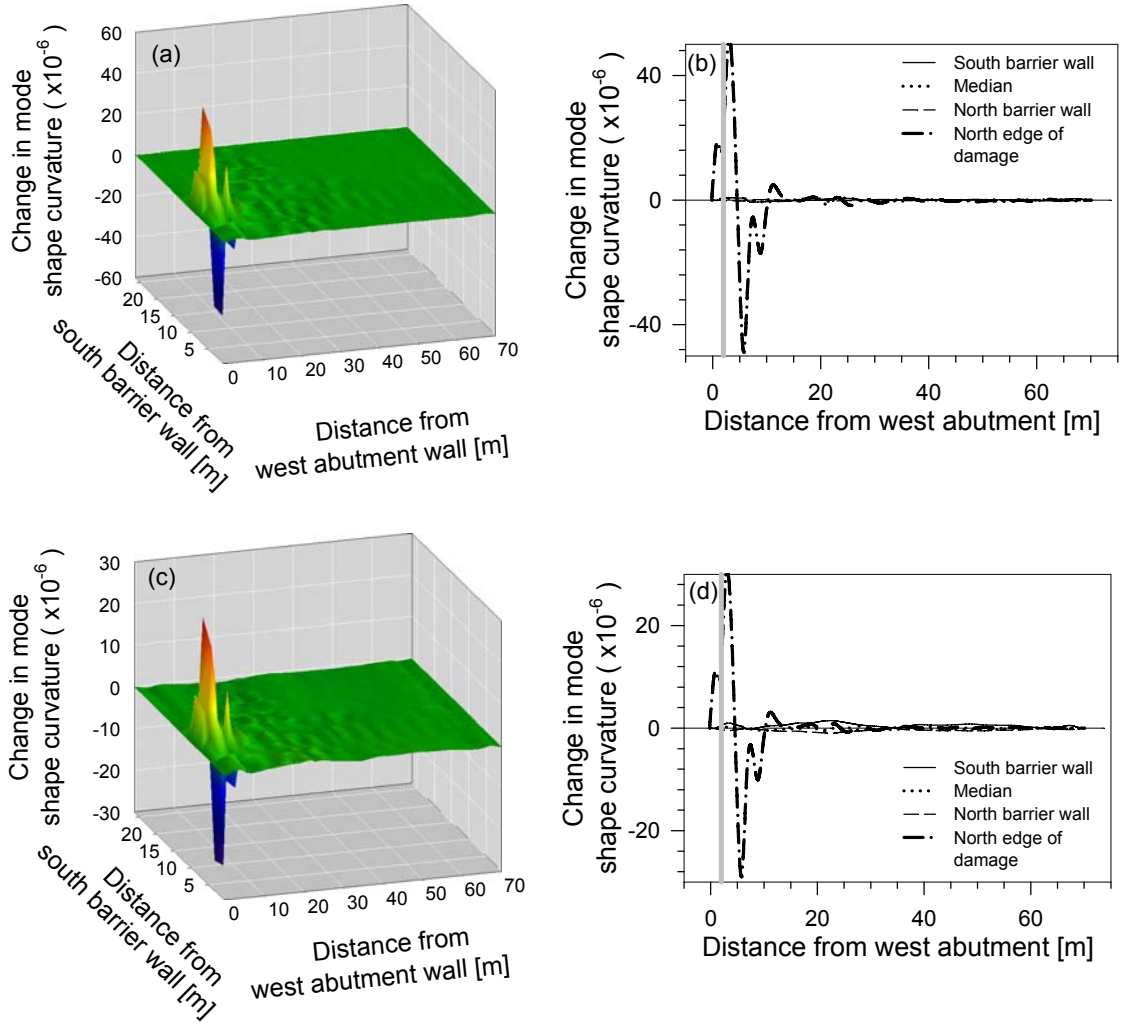

Figure 7-8. Distributions of change in mode shape curvature for damage case R10C1: (a) spatial distribution for single line normalization; (b) longitudinal distribution along selected lines for single line normalization; (c) spatial distribution for 3-line normalization; and (d) longitudinal distribution along selected lines for 3-line normalization.

the location of the sensors is restricted due to operational considerations, however, these three methods will not provide any indication of either the presence or location of damage cases located any appreciable distance away from the sensors. The change in mode shape and change in flexibility methods, though, may permit Level I damage

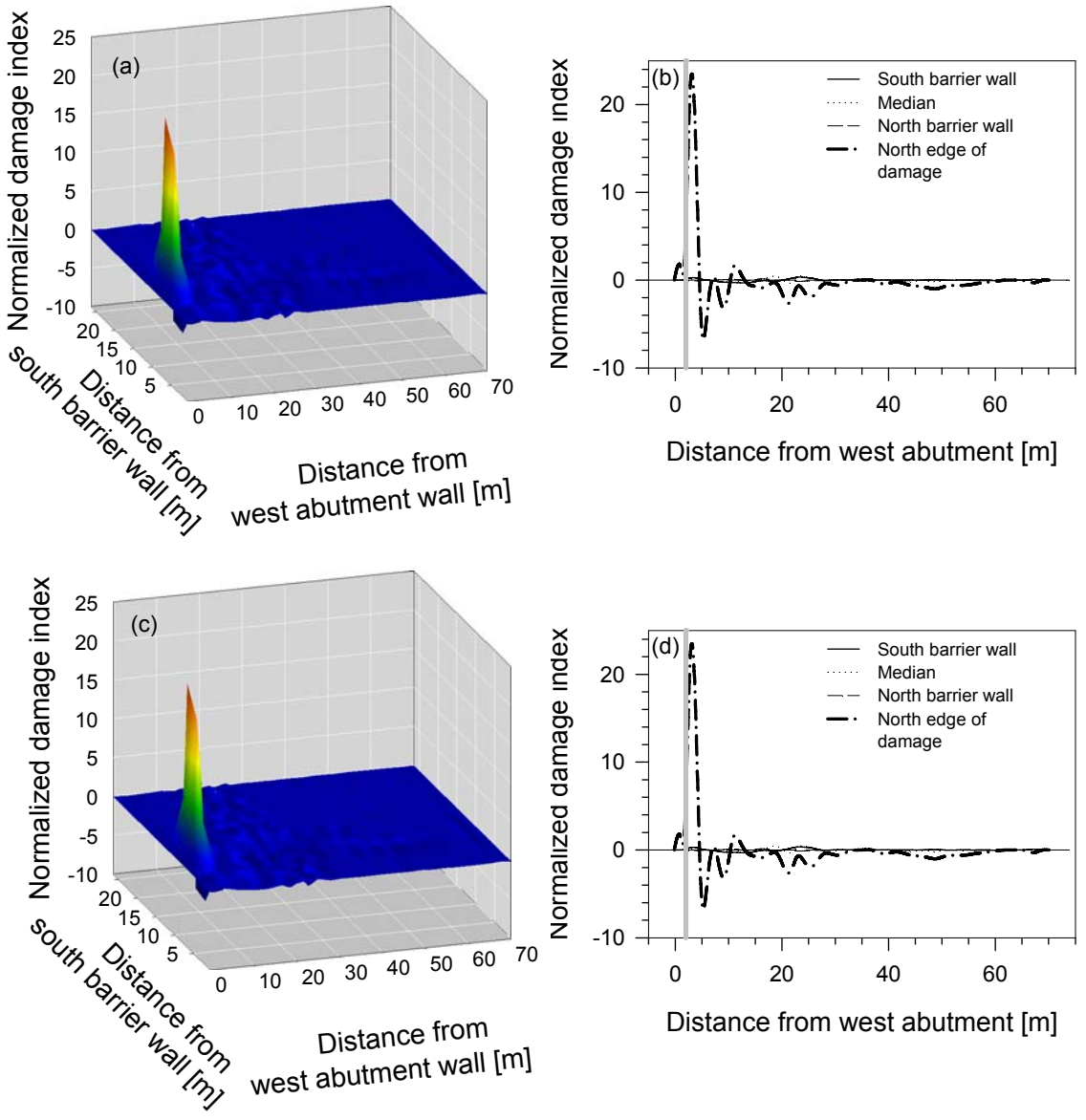

Figure 7-9. Distributions of normalized damage index for damage case R10C1: (a) spatial distribution for single line normalization; (b) longitudinal distribution along selected lines for single line normalization; (c) spatial distribution for 3-line normalization; and (d) longitudinal distribution along selected lines for 3-line normalization.

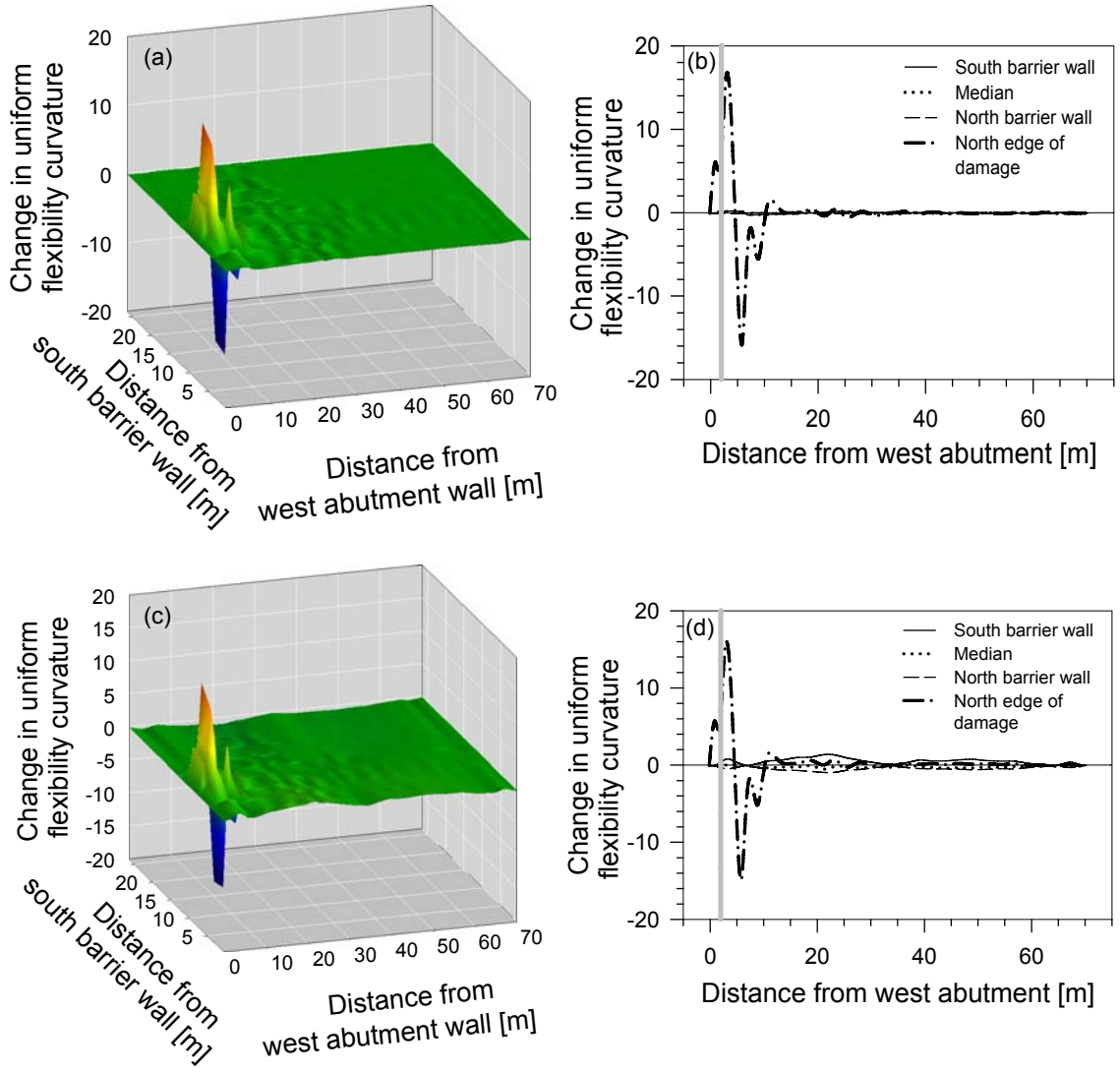

Figure 7-10. Change in uniform flexibility curvature for damage case R10C1: (a) spatial distribution for single line normalization; (b) longitudinal distribution along selected lines for single line normalization; (c) spatial distribution for 3-line normalization; and (d) longitudinal distribution along selected lines for 3-line normalization.

detection (i.e. detecting the presence of damage), as well as some indication of the general locale of the damage, even if the sensors are more distant from the damaged areas.

7.3 EFFECTS OF DAMAGE SIZE ON VBDD PARAMETERS

The results presented in Section 7.2 showed that both Level I and Level II damage detection could be performed effectively for small scale damage on the bridge deck of the Attridge Drive Overpass using the five VBDD parameters studied, provided a dense grid of sensors and single line unit-norm normalization was used. Damage states presented in that section were of approximately similar size at two different locations.

To identify the impact of damage size on the VBDD parameters, damage cases S_1 to S_7 were introduced in the finite element model. As was indicated in Table 5.4 and Figure 5.8, damage size was varied from 1.7 m × 2.5 m × 0.05 m to 11.7 m × 2.5 m × 0.225 m. The aspect ratio was used to provide a non-dimensional indication of damage size, in which the width ratio was set to a value of unity, while the Length to Depth ratio varied. Damage cases were divided into three groups: a) S_1, S_2 and S_3; b) S_1, S_4 and S_6; and c) S_3, S_5 and S_7. In the first group, the depth of damage increased incrementally while the plan dimensions remained constant. In the second and third groups, the length of damage increased while the width and depth remained constant. However, the depth of damage in the third group was larger than that for second group.

As indicated in Section 7.2, VBBD parameters indicated the location of damage unambiguously along a longitudinal line spanning the entire bridge length and passing adjacent to the damage location, as long as mode shapes were normalized using the single line, unit-norm normalization procedure. To demonstrate the effects of damage size on VBDD parameters, the profiles of the parameters obtained using mode shapes that were unit-norm, single line normalized are shown in the following sections along selected longitudinal lines, all of which span the entire bridge length. The first plot of each set of figures contains the profile along a line adjacent to the north edge of the

damage, where peaks in the VBDD parameters are most prominent, thereby offering potential for both Level I and Level II damage detection. The other three plots provide parameter variations along the barrier walls and median, which are more distant from the damage location. The longitudinal extent of the damage location on each plot is shown by a single shaded line.

7.3.1 Effect of Damage Size on the VBDD Parameters for Change in Mode Shape

Effects of damage size on the change in mode shape are shown in Figure 7-11 through Figure 7-13. Influence of changing damage depth was investigated by focusing on Group 1, where the depth of damage increases from 50 mm to 225 mm while keeping the plan dimensions constant (plan aspect ratio = 0.68:1). In all three damage cases, the actual location of damage was indicated by a distinct positive peak flanked by a negative peak on each side (see Figure 7-11 a) on a sensor line near the damage location. However, as the depth of damage decreased, the magnitude of the peak also decreased. In regions farther from the damage location, the change in mode shape magnitude was less sensitive to the depth of damage than it was in regions closer to the damage location. The magnitude of change in mode shape along the north barrier wall appears to be less sensitive to the depth of damage in comparison to that on south barrier wall and median. It is noteworthy that the north barrier wall was the farthest possible longitudinal sensor line from the damage location. However, the magnitude of the change in mode shape is clearly sensitive to different damage depths even in regions relatively distant from the damage.

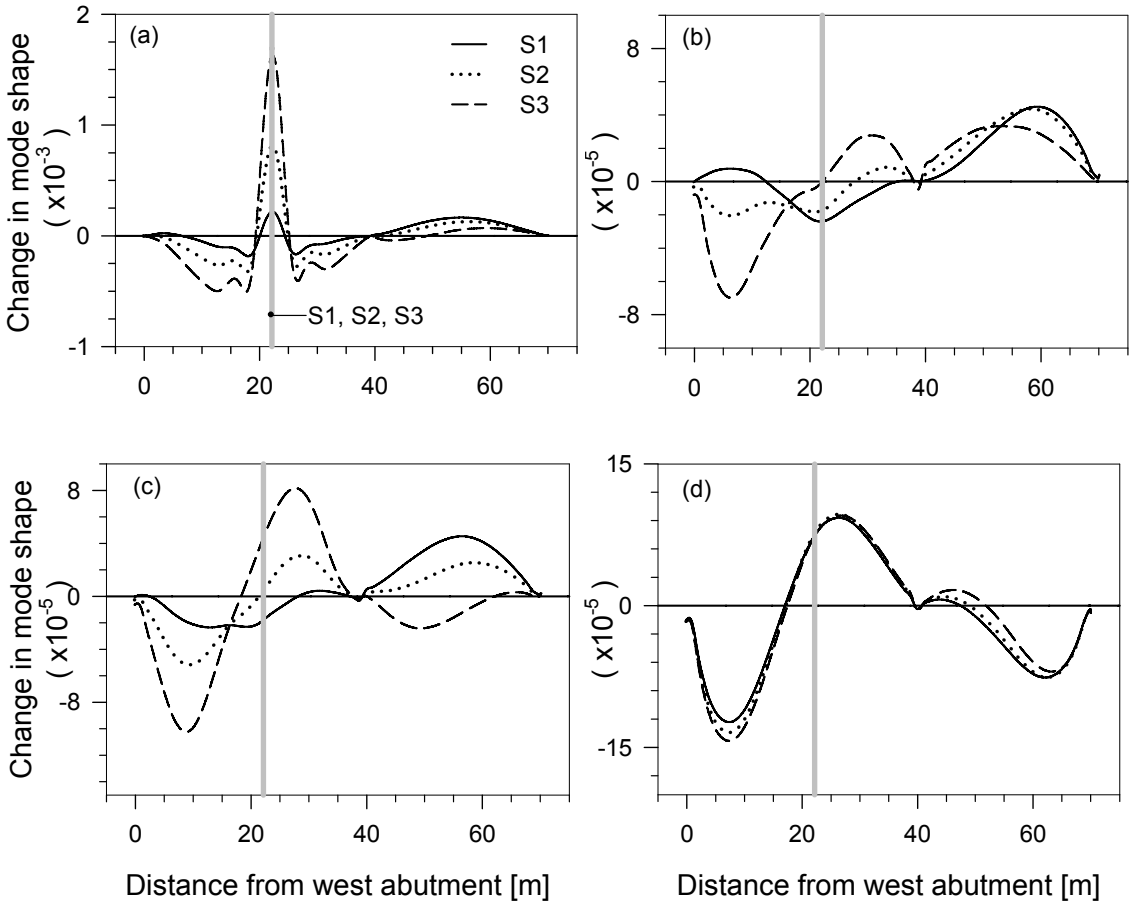

Figure 7-11. Change in mode shape distribution along longitudinal lines for damage cases S_1, S_2, S_3: (a) north edge of damage; (b) south barrier wall; (c) median; and (d) north barrier wall.

Next, the influence of changing the length of damage with a constant depth was considered. This was achieved by considering the second (S_1, S_4 and S_6) and third (S_3, S_5 and S_7) groups of damage cases, where damage depths were 0.05 m and 0.225 m, respectively, and the damage length increased from 1.7 m to 11.7 m. Aspect ratios of the plan area for the second and third groups of damage were, 0.68:1, 2.68:1 and 4.68:1.

Results for the second group of damage cases are shown in Figure 7-12. As shown in Figure 7-12 a, as the damage length increased in a direction parallel to the

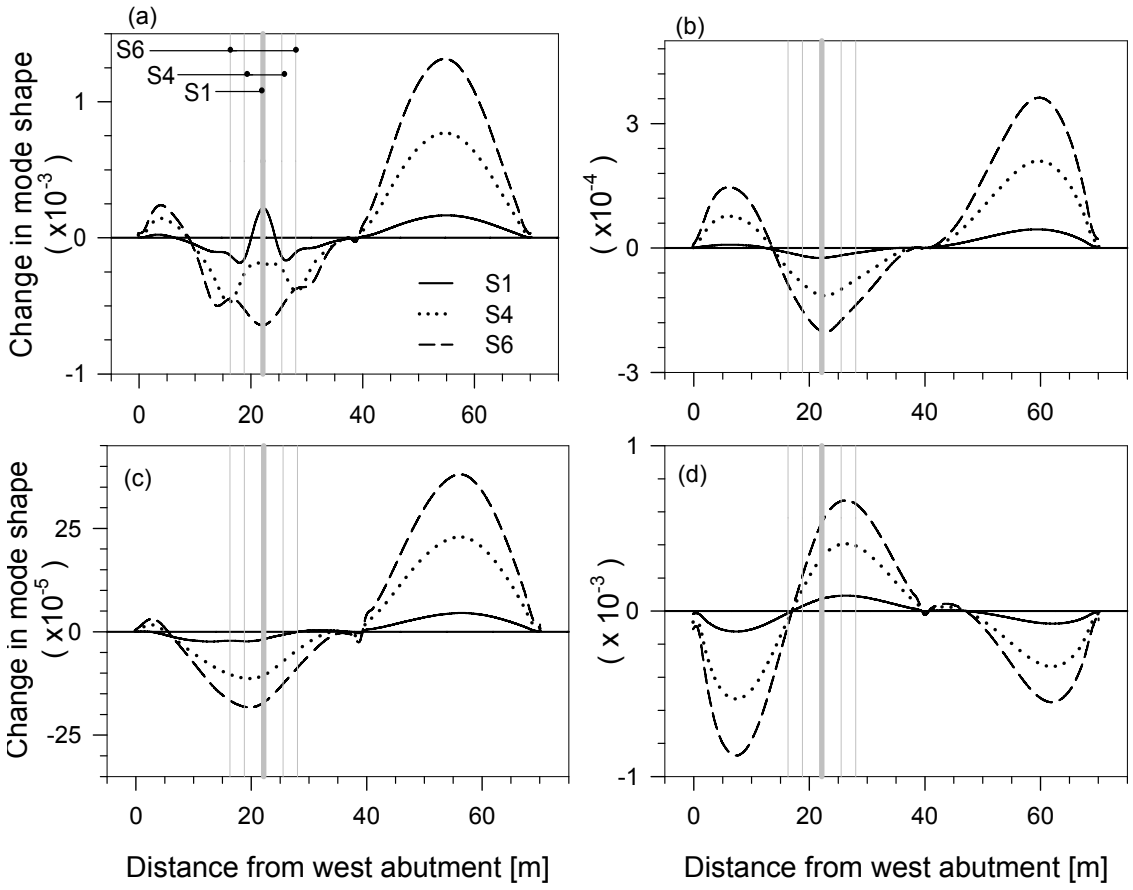

Figure 7-12. Change in mode shape distribution along longitudinal lines for damage cases S_1, S_4, S_6: (a) north edge of damage; (b) south barrier wall; (c) median; and (d) north barrier wall.

sensor lines, the peak in the vicinity of damage became less distinctive, and the distributions became dominated by a broad positive hump over the adjacent non-damaged span. The magnitude of change in mode shape in the distant regions (Figure 7-12 b, c and d) increased as the aspect ratio of the damage increased. Even along the north barrier wall, the farthest possible longitudinal sensor line from the damage location, the change in mode shape exhibited an almost equal sensitivity to the changing length of damage as was exhibited along the median and south barrier wall.

A similar trend for the change in mode shape was also observed for the third group of damage cases (S_3, S_5 and S_7), where the depth of damage was deeper than that of the second group (0.225 m). As was the case for Group 2, the characteristic peaks (see Figure 7-13 a) at the location of damage on a sensor line close to damage gradually disappeared as the length of damage increased in a direction parallel to a sensor line. As was seen for damage Group 2, the magnitude of the change in mode shape along lines more distant from damage also increased as the length of damage increased. However, the magnitude for damage Group 3 is generally twice the magnitude relative to damage Group 2. Results from the above three damage groups show that the magnitude of the

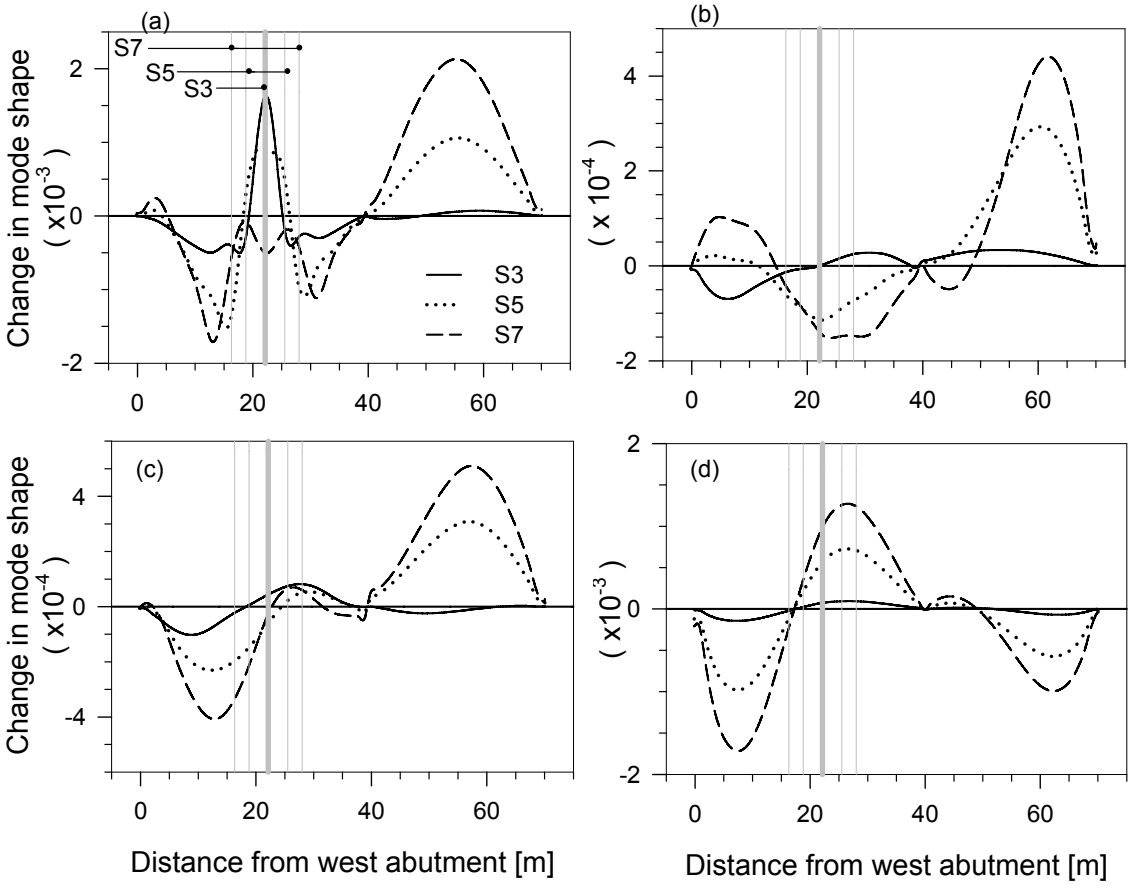

Figure 7-13. Change in mode shape distribution along longitudinal lines for damage cases S_3, S_5, S_7: (a) north edge of damage; (b) south barrier wall; (c) median; and (d) north barrier wall.

change in mode shape over the entire bridge deck increased as the size of damage increased. However, the characteristic peaks at the location of damage gradually disappeared as the length of damage decreased; therefore, the potential for Level II damage detection also decreased.

7.3.2 Effect of Damage Size on the Change in Flexibility

The effects of damage size on the change in flexibility parameter are demonstrated in Figure 7-14 through Figure 7-16. As with the change in mode shape, damage localization using change in flexibility becomes more challenging as the depth of damage decreases below a certain dimension while keeping the plan area of damage constant, and as the aspect ratio of the plan area of damage increases. While damage case S_3 in Figure 7-14 (a) shows a distinct positive peak at the location of damage, damage case S_1 in the same figure actually shows two inverted peaks near the damage. However, in an enlarged plot, these inverted peaks are still discernable, as was demonstrated in Section 7.2. Plots of VBDD parameters for change in flexibility along the more distant sensor lines are characterized by a broad hump on each span with unequal amplitudes. As was the case with the change in mode shape method, the change in flexibility along the sensor line along north barrier wall (farthest from damage) appeared to be less sensitive to the damage depth since the plots for damage cases S_1 to S_3 were nearly coincident. The change in flexibility along the median and south barrier wall, though, was sensitive to the depth of damage. The magnitude for damage cases S_1 and S_2 on the median and south barrier wall were very close, while damage case S_3 produced higher changes in flexibility, as seen in Figure 7-14 (b) and (c).

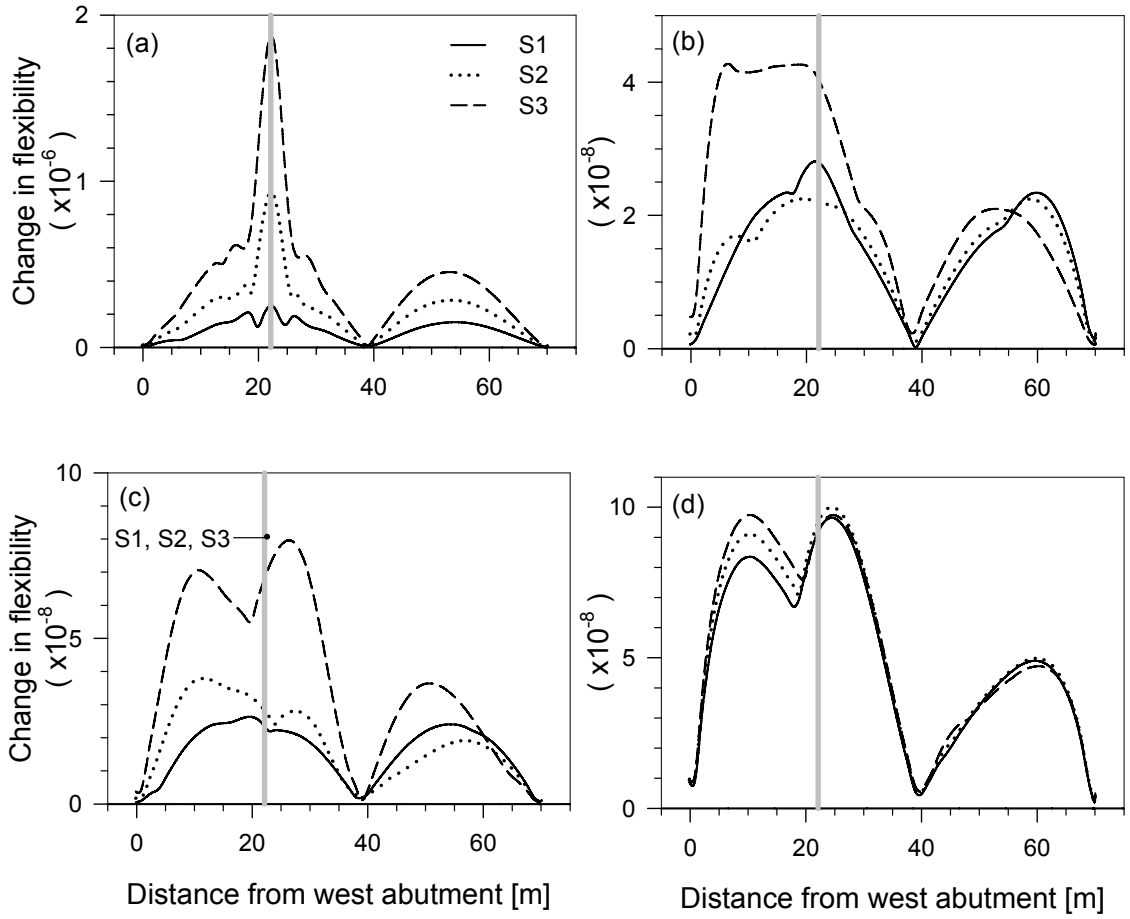

Figure 7-14. Change in flexibility distribution along longitudinal lines for damage cases S_1, S_2, S_3: (a) north edge of damage; (b) south barrier wall; (c) median; and (d) north barrier wall.

The influence of the aspect ratio of damage plan area on the change in flexibility is shown in Figure 7-15, where results for damage Group 2 are plotted along selected longitudinal sensor lines. Along lines distant from the damage location, (barrier walls and median) the change in flexibility parameter can be characterized, in general, by a positive hump on each span of the bridge. The magnitude of the change in flexibility parameter on all selected longitudinal sensor lines increased as the damage

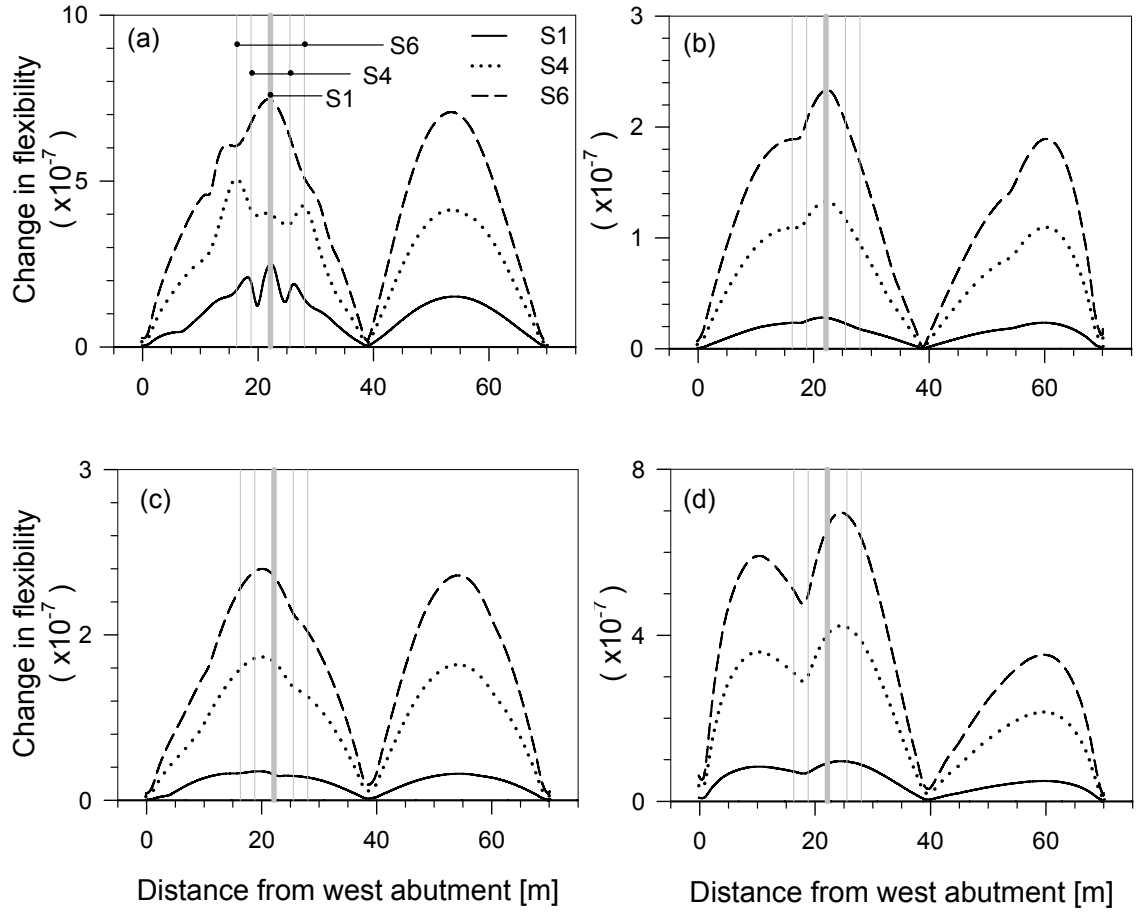

Figure 7-15. Change in flexibility distribution along longitudinal lines for damage cases S_1, S_4, S_6 :(a) north edge of damage; (b) south barrier wall; (c) median; and (d) north barrier wall.

size increased, which is beneficial for Level I damage detection. The characteristic peak on a line adjacent to the damage (which is beneficial for Level II damage detection), however, disappeared as the aspect ratio increased. Instead, it was replaced by a broader hump of higher magnitude as the length of damage increases from 1.7 m to 11.7 m.

The change in flexibility distributions for damage Group 3 (as shown in Figure 7-16) exhibited general trends that were similar to those for damage Group 2, but with

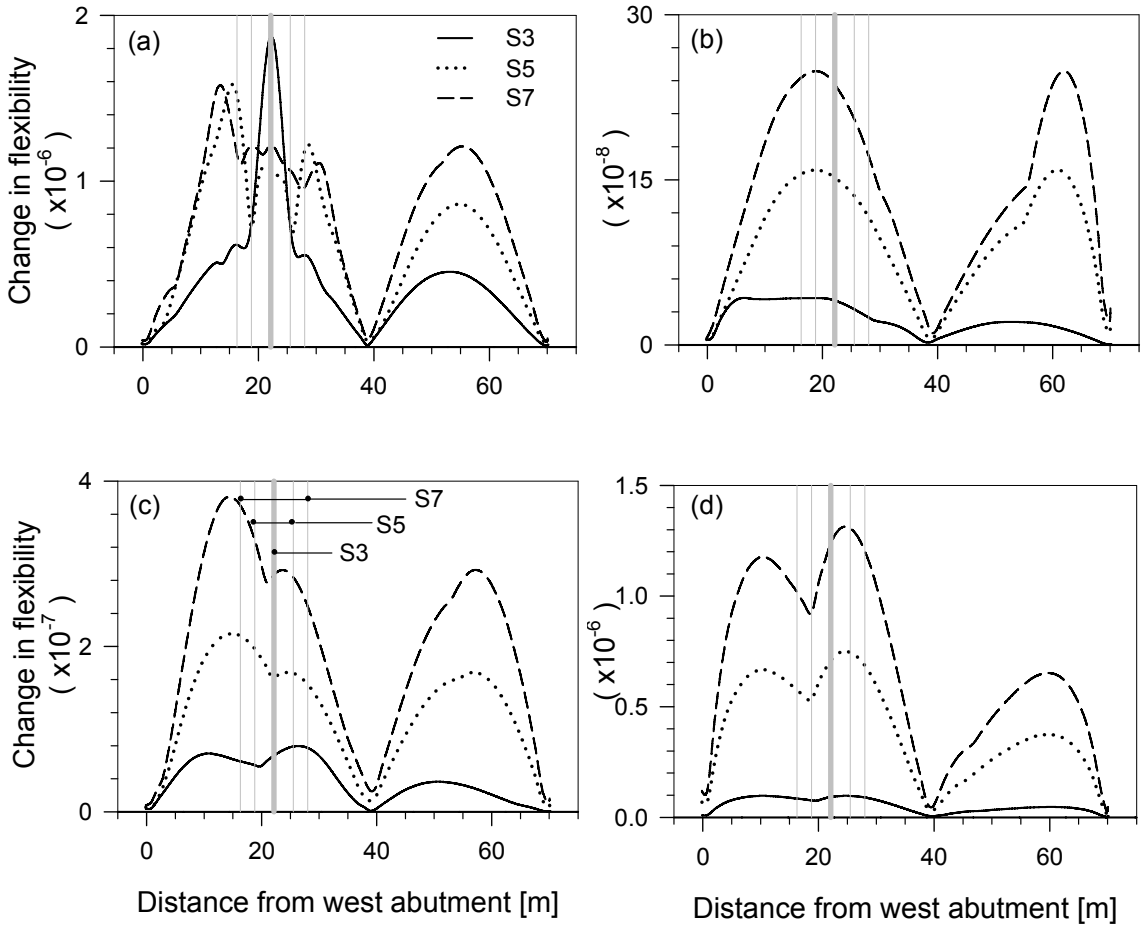

Figure 7-16. Change in flexibility distribution along longitudinal lines for damage cases S_3, S_5, S_7 :(a) north edge of damage; (b) south barrier wall; (c) median; and (d) north barrier wall.

higher magnitudes due to the increased depth of damage relative to Group 2. As seen in Figure 7-16 (a), the distinctive peak along a line adjacent to the damage location transformed to a characteristic fold centred on the damage location as the plan aspect ratio increased from 0.68:1 to 4.68:1, but it did not disappeared completely. However, it can be inferred from the observed trends from damage Group 2 that the characteristic fold will eventually disappear and become a positive hump for damage cases with higher plan aspect ratios.

7.3.3 Effect of Damage Size on Change in Mode Shape Curvature, Damage Index, and Change in Uniform Flexibility Curvature.

The influence of the damage size on the change in uniform flexibility curvature, damage index, and change in mode shape curvature parameters was very similar and is discussed together in this section. As mentioned in Section 7.2.3, the magnitudes of these parameters in regions distant from the damage location were very small (100 times smaller in general) in comparison to those in the vicinity of the damage location. However, the magnitude of these parameters in the distant regions were still found to be sensitive to the size of damage, increasing as the depth of damage or the plan aspect ratio of damage plan area increased.

Plots of the VBDD parameters for these three methods are presented in Figure 7-17 through Figure 7-19. To avoid repetition, only plots along a line adjacent to the damage and along the south barrier wall are provided. It is evident from all of these figures that the magnitude of the VBDD parameters on the south barrier wall increased as the size of damage increased. This was also true for the other distant sensor lines along the median and north barrier wall. The sensitivity of these parameters (using single line, unit-norm normalization) along the distant sensor lines may provide potential for Level I damage detection; however, the absence of any particular pattern on those distant sensor lines makes their use for damage detection quite challenging at this point.

The effects of damage depth on these three parameters along a line adjacent to the damage location are shown in Figure 7-17 (a), (c) and (e). As was seen with the change in mode shape and change in flexibility methods, the change in mode shape curvature parameter (see Figure 7-17 (a)) exhibited significant sensitivity to the depth of

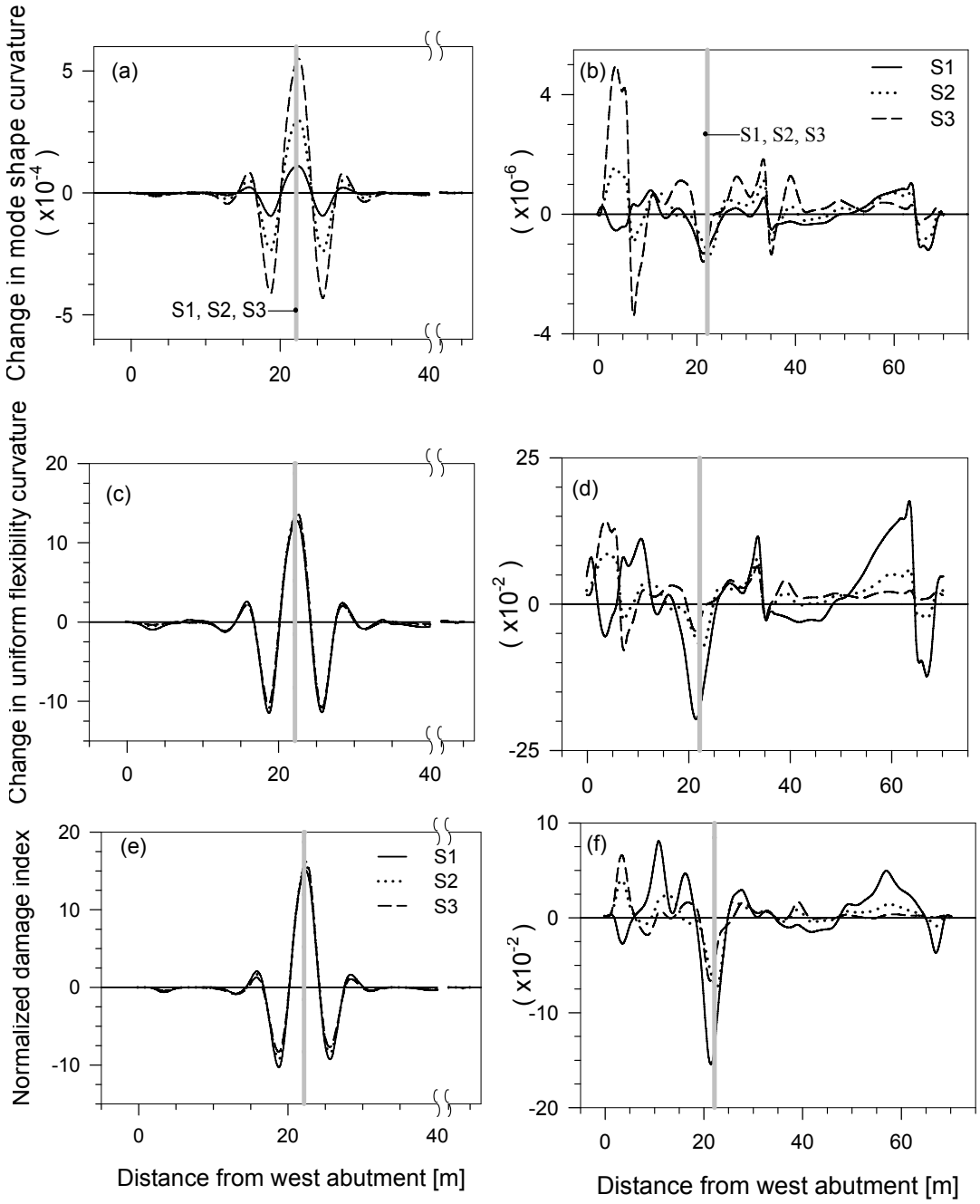

Figure 7-17. Distribution of VBDD parameters for Damage Case S_1, S_2 and S_3 for: change in mode shape curvature on: (a) north edge of damage and (b) south barrier wall; change in uniform flexibility curvature on: (c) north edge of damage and (d) south barrier wall; and normalized damage index on: (e) north edge of damage and (f) south barrier wall.

damage, with the magnitude decreasing as the depth of damage decreased. However, even the location of damage case S_1, which had the smallest depth (50 mm), could be identified unambiguously using the change in mode shape curvature method. On the other hand, the damage index and change in uniform flexibility curvature methods appeared to be less sensitive to the depth of damage (see Figure 7-17 (c) and (e)). Comparing the plots corresponding to damage cases S_3 and S_1 for the damage index and change in uniform flexibility curvature methods (see Figure 7-17 (c) and (e)), it is clear that the magnitude of the peak near the damage decreased only slightly as the damage depth decreased. Also the clarity of the peak was not diminished; instead, the peak was flanked by smaller negative peaks on either side for all the damage depths.

It should be recalled that the damage index and change in uniform flexibility curvature parameters were normalized to a unit standard deviation and zero mean over the entire bridge deck, assuming the parameters for these two methods had a normal distribution. This statistical normalization procedure makes these methods less sensitive to the damage depth, while, on the other hand, increasing their effectiveness to identify the location of damage (Level II).

The next focus is on the second and third groups of damage, where the length of damage increased from 1.7 m to 11.7 m (the aspect ratio of damage plan area increased from 0.68:1 to 4.68:1). As the length of the damaged area increased (comparing damage cases S_3 and S_7 in the third group and S_1 and S_6 in the second group), the single positive peak for these three methods was replaced by two, less dominant peaks at the extremities of the damaged areas (see Figure 7-18 and Figure 7-19). These peaks indicate that the curvature of the fundamental mode shape increased sharply at the

boundaries between damaged and undamaged regions, a feature which may prove beneficial for identifying the extent of damage. In addition to the appearances of these

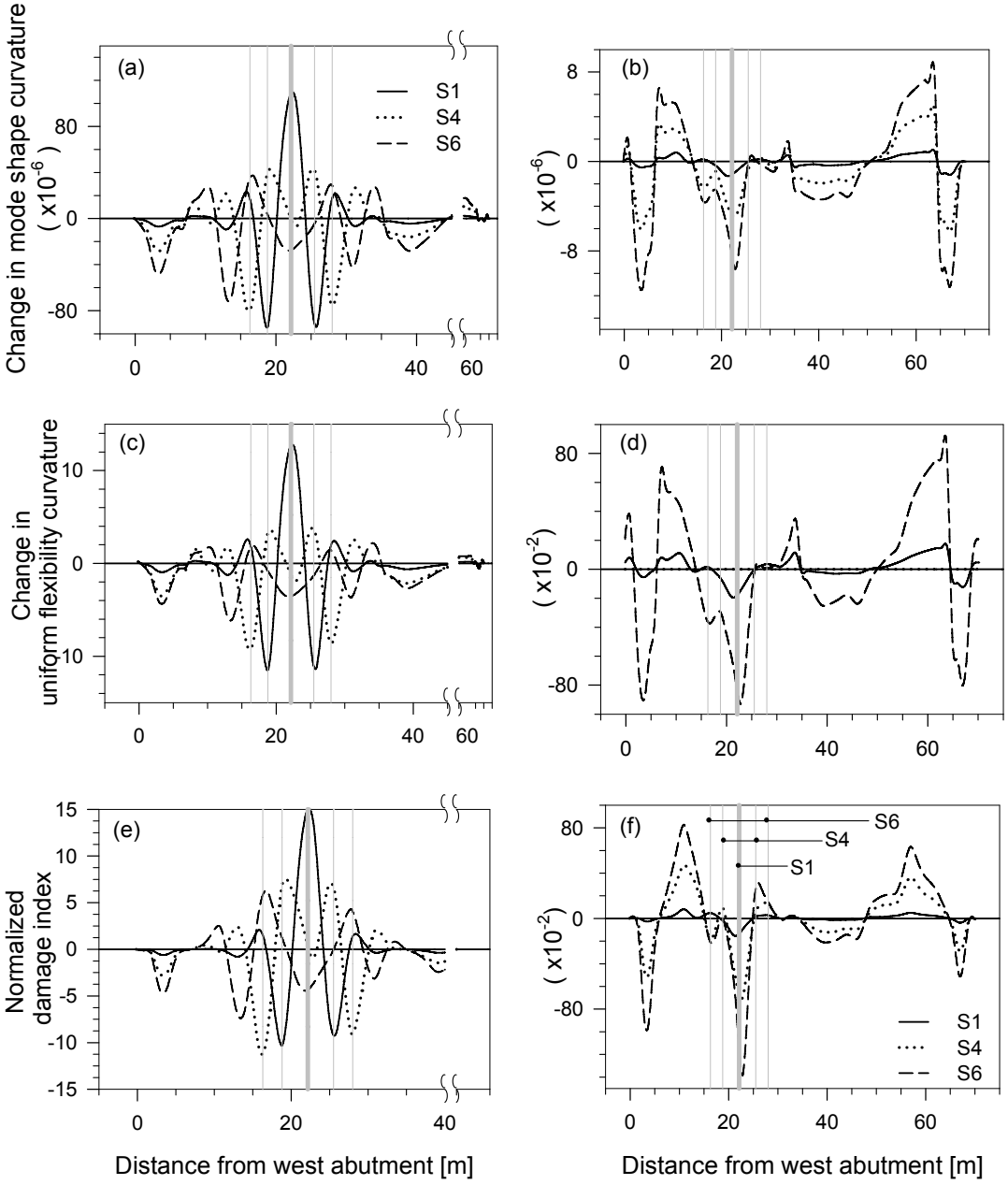

Figure 7-18. Distribution of VBDD parameters for damage Case S_1, S_4 and S_6 for: change in mode shape curvature on: (a) north edge of damage and (b) south barrier wall; change in uniform flexibility curvature on: (c) north edge of damage and (d) south barrier wall; and normalized damage index on: (e) north edge of damage and (f) south barrier wall.

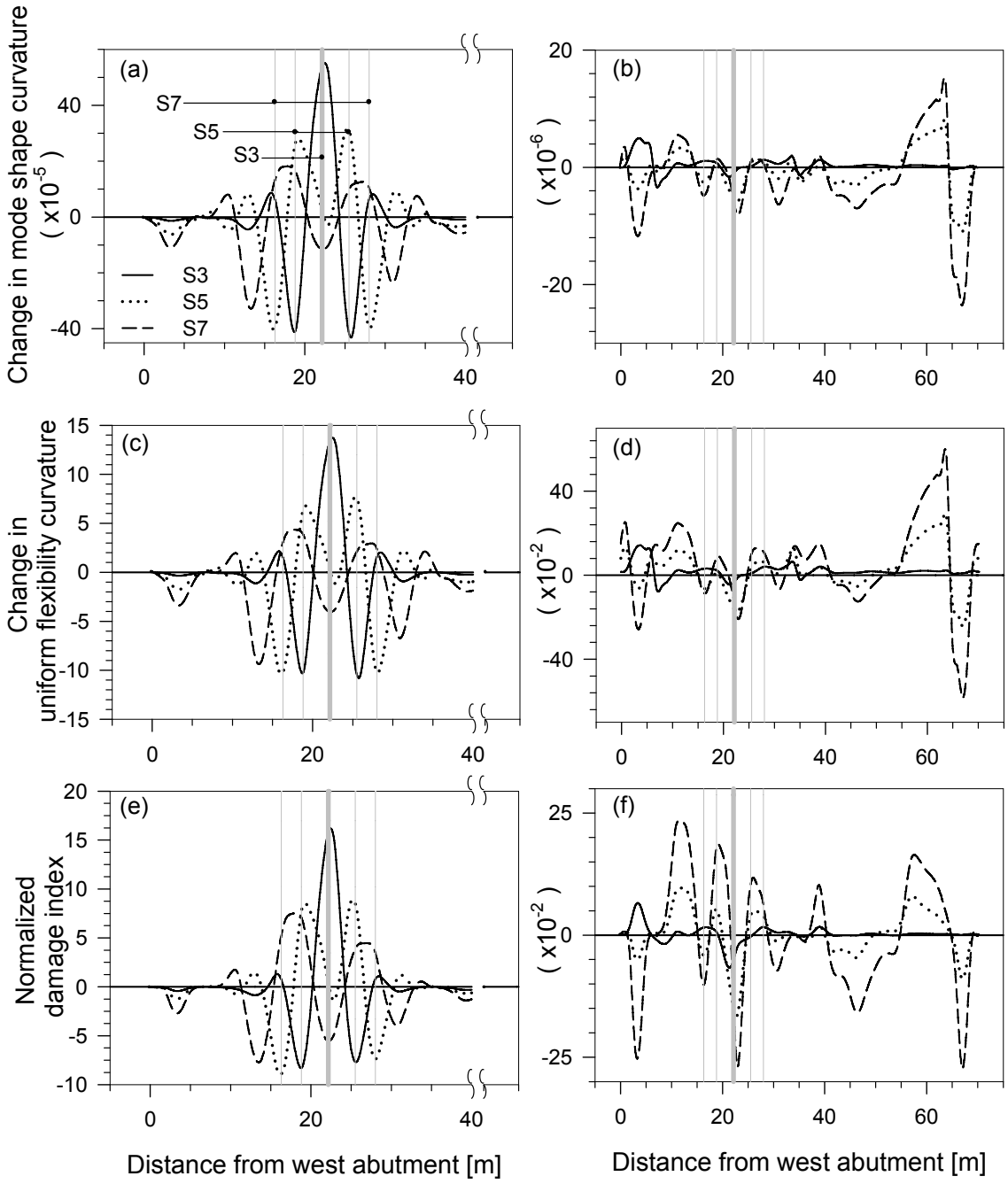

Figure 7-19. Distribution of VBDD parameters for Damage Case S_3, S_5 and S_7 for: change in mode shape curvature on (a) north edge of damage (b) south barrier wall, change in uniform flexibility curvature on (c) north edge of damage (d) south barrier wall, and normalized damage index on (e) north edge of damage (f) south barrier wall.

two peaks, the magnitude of the damage parameters increased in regions more distant from the damage location as the length of the damaged area increased, leading to the possibility of ambiguity in localizing the damage.

In summary, it was observed from the above examples that the magnitude of parameters for the five methods on any longitudinal sensor line spanning the entire bridge length depends on the size of damage as well as the distance of a sensor line from the location of damage. The magnitude of the VBDD parameters were found to increase as the size of damage increased. On the other hand, the magnitude of the parameters decreased as the distance of the sensor line from the damage location increased.

The presence of a characteristic peak at the location of damage in the plots of the five VBDD parameters along a longitudinal sensor line adjacent to the damage location provides potential for Level II damage detection. The distinctiveness of this peak appeared to depend on the aspect ratio of the plan area of damage and the depth of damage. A more identifiable peak could be expected at the damage location as the damage depth increased while the plan aspect ratio was kept constant. On the other hand, the peak gradually disappeared as the plan aspect ratio increased in a direction parallel to the sensor line.

The change in mode shape and change in flexibility parameters became less sensitive close to the damage location as the damage depth decreased. However, the smallest depth of induced damage used in this study (50 mm), which was relatively small in a practical sense, was successfully identified and localized using these two methods with sensors located along a line adjacent to the damage. Damage localization, though, became more challenging using these two methods as the aspect ratio of the

damage increased beyond certain limits (i.e., when the length of the damage increased) in a direction parallel to the sensor line. However, both of these methods still indicated the potential for Level II damage detection provided the aspect ratio of damage was within some limiting value. On the other hand, both of these methods could potentially perform Level I damage detection, regardless of the damage size, even using sensors located far from the damage.

Two of the curvature-based methods (the damage index and change in uniform flexibility curvature methods) were less sensitive to the damage depth, maintaining similar patterns and magnitudes close to the damage location regardless of the depth of damage, when plan area of damage was kept constant. The change in mode shape curvature method, in contrast to these methods, showed different magnitudes as the depth of damage changed. All of the three curvature-based methods exhibited a discernable peak at the location of damage, which is beneficial for Level II damage detection. However, the peak close to the damage location tended to diminish as the length of damage increased from 1.7 m to 11.7 m in the direction parallel to the sensor line. Finally, sharp changes (peaks) in mode shape curvature at the boundaries of damage appeared to provide a potential means of identifying the extent of damage.

7.4 INFLUENCE OF SENSOR SPACING ON THE ACCURACY OF DAMAGE DETECTION

In field monitoring of bridges, the number of locations at which mode shapes can be feasibly measured is limited by the availability of sensors, the capacity of data acquisition systems and time constraints, among other practical considerations. The significance of mode shape definition was demonstrated by Zhou et al. (2007), who

found that the accuracy with which small-scale damage could be located on a simple span bridge deck using VBDD methods decreased with increasing spacing between sensors used to measure the dynamic response.

In the present study, the effect of using relatively few measurement points was simulated by extracting eigenvector data from selected nodes only and using that subset of data as the basis for VBDD analyses. In this manner, the effectiveness of simulated sensors with various longitudinal spacing could be investigated. Since the location of the damage is also known to influence the accuracy of damage location, the analyses were repeated for 15 different damage cases distributed along the mid-width of the south-west quadrant of the bridge (damage cases R10C1 through R10C15, as shown in Figures 5.6 and 5.7).

To facilitate the comparison between results from different sensor spacings, mode shape amplitudes for all cases were generated at uniform 0.5 m intervals by fitting a cubic spline function between the extracted eigenvector data. Unit-norm, line normalized mode shape profiles along the north edge of all damage cases, were used in conjunction with VBDD methods to locate the damage in this part of the study.

Correlations between predicted and actual damage locations, relative to the west abutment, are illustrated in Figure 7-20 for simulated sensor spacings of 3.0 m, 5.0 m and 7.5 m. In each of these graphs, the accuracy of a given VBDD prediction is represented by the vertical distance between any given point and the dashed diagonal line. Points that have been plotted along the horizontal axes of the graphs indicate cases in which the VBDD method failed completely to locate the damage (i.e., a discernible peak was not present). Results from the change in mode shape curvature and uniform

flexibility curvature methods were found to be similar to those of the damage index method and so are not included here.

It is evident that all three VBDD methods provide reliable estimates of damage locations when the sensor spacing is 3.0 m. The accuracy of the predictions, though, is seen to deteriorate slightly near the abutment for the change in mode shape and change in flexibility methods (Figure 7-20 (a) and (b)), while no such degradation is apparent for the damage index method (Figure 7-20 (c)), which exhibits comparable accuracy levels at

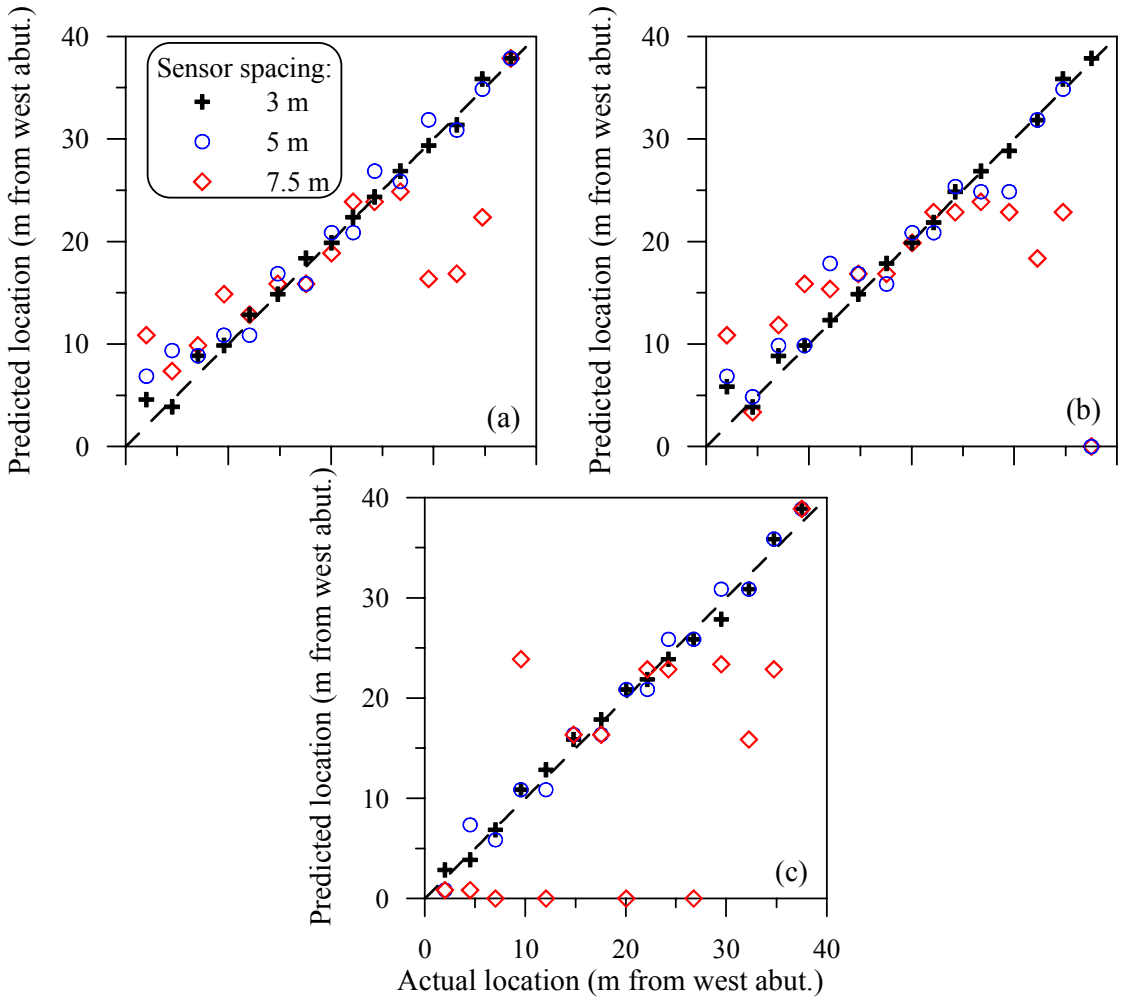

Figure 7-20. Correlations between the predicted and actual longitudinal location of damage, relative to the west abutment by: (a) change in mode shape; (b) change in flexibility; and (c) damage index method.

all locations. The accuracy of damage detection decreased with an increase in sensor spacing to 5.0 m, with the greatest decline in accuracy observed for the change in flexibility method. With a further increase in sensor spacing to 7.5 m (approximately 20% of the girder span length), significant errors appeared for all three VBDD methods. In fact, the damage index method failed to locate the damage at four of the 15 damage locations.

More quantitative assessments of damage localization predictions are provided in Table 7-1 for the change in mode shape and damage index methods. Here, the resolution of damage localization is defined as the algebraic difference between the predicted and actual damage locations. In comparing the two methods, the change in mode shape method is seen to provide a lower average error but a higher maximum error for the 3.0 m sensor spacing. This may be attributed to the fact that the change in mode shape method gave a consistently closer estimate of the true damage location except near the abutments, where its accuracy declined.

With a sensor spacing of 5.0 m, on the other hand, the damage index method produced a lower average and maximum error. For both methods, the resolution of damage detection deteriorated with increasing sensor spacing, as reflected in both the average and maximum error values. With a sensor spacing of 7.5 m, errors in the order of 15 m, roughly 40% of the girder span length, were observed; in addition, some locations could not be identified at all with the damage index method. Clearly, then, a sensor spacing of 7.5 m exceeds the upper permissible limit for the reliable application of VBDD methods to this particular bridge.

Table 7-1. The influence of sensor spacing on damage detection resolution.

	Resolution of damage detection (m)					
	Change in mode shape			Damage index		
Location[a] (m)	3 m Spacing	5 m Spacing	7.5 m Spacing	3 m Spacing	5 m Spacing	7.5 m Spacing
2.0	2.58	4.85	8.85	0.85	-1.15	-1.15
4.5	-0.65	4.85	2.85	-0.65	2.85	-3.65
7.0	1.83	1.83	2.83	-0.17	-1.17	–
9.6	0.30	1.30	5.30	1.30	1.30	14.30
12.1	0.80	-1.20	0.80	0.80	-1.20	–
14.8	0.05	2.05	1.05	1.05	1.55	1.55
17.6	0.80	-1.70	-1.70	0.30	-1.20	-1.20
20.1	-0.20	0.80	-1.20	0.80	0.80	–
22.2	0.20	-1.30	1.70	-0.30	-1.30	0.70
24.3	0.10	2.60	-0.40	-0.40	1.60	-1.40
26.8	0.10	-0.90	-1.90	-0.90	-0.90	–
29.5	-0.15	2.35	-13.15	-1.65	1.35	-6.15
32.3	-0.90	-1.40	-15.40	-1.40	-1.40	-16.40
34.8	1.10	0.10	-12.40	1.10	1.10	-11.90
37.5	0.35	0.35	0.35	1.35	1.35	1.35
Average[b]	**0.68**	**1.84**	**4.66**	**0.87**	**1.35**	**3.98**
Max. Error	**2.58**	**4.85**	**15.40**	**1.65**	**2.85**	**16.4**

[a]Longitudinal distance between center of damage and the west abutment.
[b]Average absolute value.
–Damage could not be detected

A quantitative comparison of the accuracy of the predicted damage location obtained by different VBDD methods can be made using the Mean Squared Error (MSE) value, defined as

$$\text{Mean Squared Error (MSE)} = \frac{\sum_{i=1}^{n}(\hat{\chi}_i - \chi_i)^2}{n}, \tag{7.1}$$

where $\hat{\chi}_i$, χ_i are the predicted and actual locations of the i^{th} damage case. In Table 7-2,

Table 7-2. Mean Squared Error value of the predication of damage location by VBDD methods.

Sensor spacing (m)	VBDD Methods		
	Change in mode shape	Change in flexibility	Damage Index
3	0.9	1.4	0.9
5	5	100	2
7.5	47	130	133

MSE values corresponding to the predicted damage locations obtained by the change in mode shape, change in flexibility and damage index methods for the three sensor spacings investigated (3m, 5m and 7.5m) are given. The MSE values for the change in mode shape curvature and change in uniform flexibility curvature methods were found to be similar to that of the damage index method, and are therefore not listed in this table. An MSE value of zero indicates perfect correlation between the predicted and actual damage locations. The MSE value increases as the error in the prediction increases. MSE values other than zero do not represent any particular meaning, but they can be used as a comparison tool for different methods. MSE values for the three VBDD methods were observed to be low (0.9 – 1.4) while the sensor spacing was 3m, and increased sharply when the sensor spacing increased to 7.5 m (47 – 133). This sharp increase in MSE values corresponds to the reduced accuracy in the prediction of damage location for the same spacing as shown in Figure 7-20. The MSE value for the change in flexibility method increased sharply (from 1.4 to100) as the sensor spacing increased from 3m to 5m, which indicates that the change in flexibility method was more sensitive to sensor spacing than were the other VBDD methods.

7.5 THE INFLUENCE OF UNCERTAINTY IN THE MEASURED MODE SHAPES

Up to this point, it has been assumed that the true damaged and undamaged mode shapes were known with perfect certainty. In practice, inaccuracies are introduced into the mode shape measurements through a number of sources, including instrumentation error, signal noise from nearby electrical fields, analog-to-digital discretisation error and signal processing routines (i.e., analog and digital filters, windowing functions, FFT's, etc.). In addition, the random nature of ambient traffic excitation adds considerable uncertainty into the interpretation of dynamic response results.

To study the effect of measurement uncertainty on damage detection analyses, simulated random uncertainty was superimposed on the numerically generated eigenvector results prior to the application of the VBDD methods. Normally distributed random errors with a mean value of zero and a uniform standard deviation were added to all extracted mode shape amplitudes of the damage induced model. Mode shapes corresponding to the pristine structural condition, generally used as a baseline for damage detection methods, were assumed to be extracted with sufficient accuracy. Therefore, uncertainty was not added to the mode shape of the undamaged structure for this study.

To match the variability observed in the mode shapes measured as part of the field study, the random errors were scaled to produce an average coefficient of variation (c.o.v.) of 2.61% in the resulting mode shape amplitudes. Details of the uncertainty simulation are given in Section 4.6 and Appendix D. Prior to the application of VBDD methods, mode shapes of the damaged finite element model, including uncertainty, were

interpolated using a cubic spline function to generate modal amplitudes at evenly spaced nodes (1 m). Unit-norm, single line normalization was then used to normalize the interpolated mode shape.

The change in mode shape curvature, damage index and change in uniform flexibility curvature methods exhibited similar results relating to the effects of measurement uncertainty. To avoid repetition, three methods (change in mode shape, change in flexibility and change in mode shape curvature) are presented here to explain the influence of uncertainty in mode shape measurements on damage detection using damage case R10C9.

Intuitively, the averaging of repeated random trials for the mode shape will tend to attenuate the uncertainty and improve the identification of damage using VBDD parameters. In this study, up to 10,000 trials were investigated to get a sense of how uncertainty in mode shape field measurements can be attenuated. To study the possibilities of false positive indications of damage (i.e., an indication of damage even though there is no damage) due to measurement uncertainty, VBDD parameters were also applied to undamaged model results that included simulated uncertainty. Results of this study are presented as spurious damage cases in the following figures.

Once again, VBDD parameter distributions were plotted for the entire bridge length along the barrier walls, the median and along a sensor line adjacent to the damage location. Averaged results for VBDD parameters based on 25, 100 and 5,000 random trials are shown in Figure 7-21 through Figure 7-23. The corresponding VBDD parameter plot for the same damage case with no measurement uncertainty is also

provided in each figure for comparison. In addition, Figure 7-24 shows averaged results for the VBDD parameters based on 25 random trials when no damage was present.

It is immediately obvious from parts a and b of Figure 7-21 through Figure 7-23, and comparison of these with Figure 7-24, that the inclusion of random uncertainty in the mode shape definition made it impossible to distinguish real damage from spurious peaks in the VBDD parameter plots, even when the results from 25 or 100 repeated trials were averaged. However, as indicated in part c of Figure 7-21 through Figure 7-23, in comparison with part d, the averaging of 5,000 repeated trials attenuated the

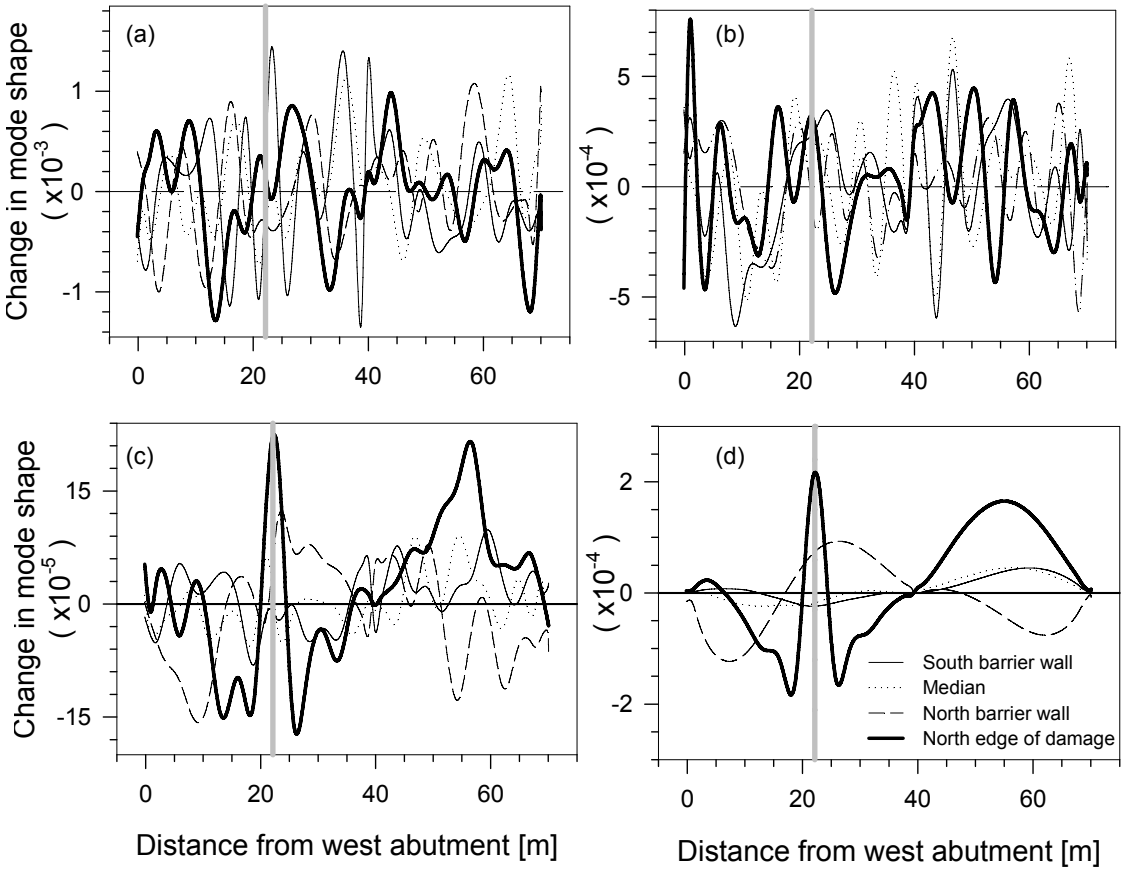

Figure 7-21. The distribution of change in mode shape along selected longitudinal lines (south barrier wall, median, north barrier wall and north edge of damage) for damage case R10C9, using an average of : a) 25 trials; b) 100 trials; c) 5,000 trials; and d) without any noise.

noise to the extent that damaged-induced peaks in the VBDD parameter plots could be reliably distinguished.

In the plots for change in flexibility (Figure 7-22), an underlying pattern, which featured a positive hump in each span, was apparent, even when the results of 25 trials were averaged. This feature may indicate that flexibility changes are more robust than other VBDD parameters for Level I damage detection in the presence of uncertainty. However, this underlying positive hump on each span was also apparent in Figure 7-24 (b) for the false damage case. This potential ambiguity could be alleviated if a larger

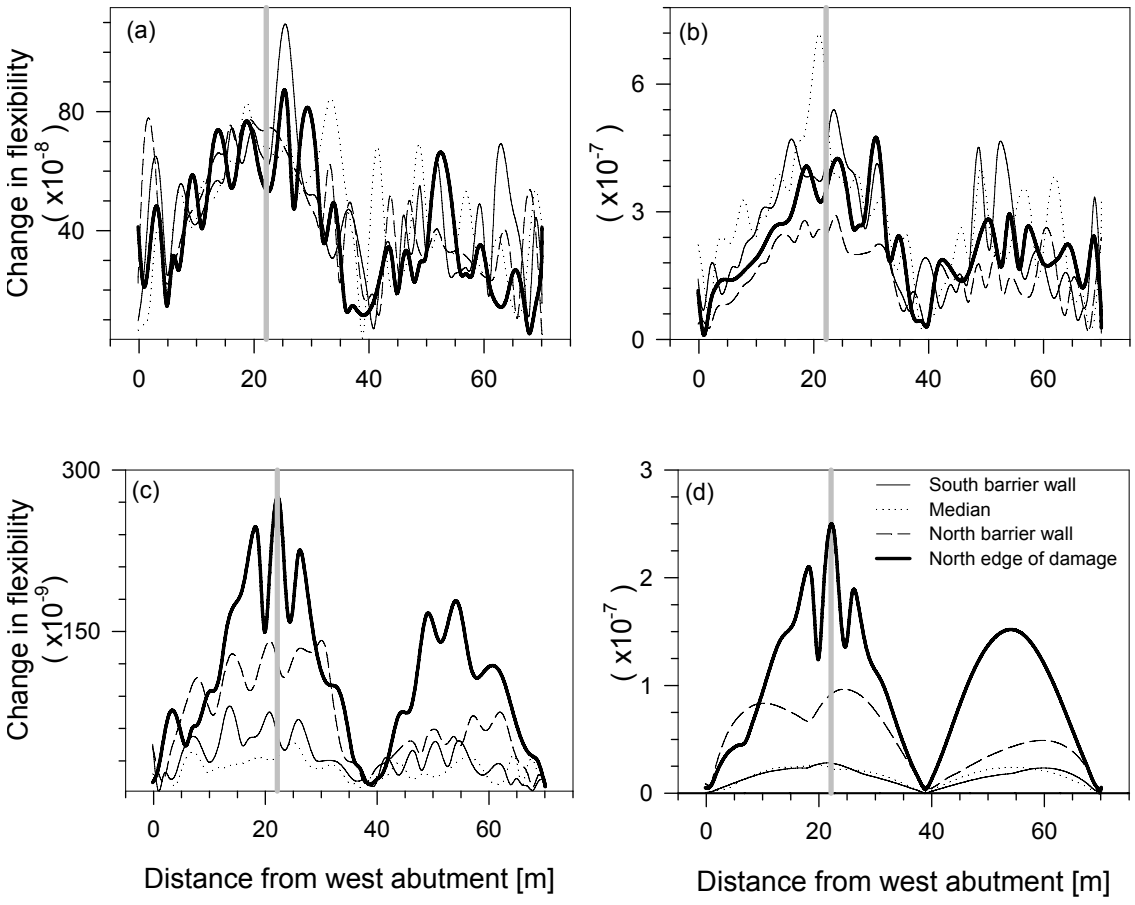

Figure 7-22. The distribution of change in flexibility along selected longitudinal lines (south barrier wall, median, north barrier wall and north edge of damage) for damage case R10C9, using an average of: a) 25 trials; b) 100 trials; c) 5,000 trials; and d) without any noise.

number of trials were used in the averaging process. The characteristic peaks centred at the location of damage clearly appeared when an averaging of 5,000 repeated trials was employed (see Figure 7-22 (c)).

To investigate the effect of damage size on the number of repeated trials required to attenuate the effects of uncertainty, a similar comparison using the VBDD parameters for change in mode shape was performed using a more severe damage case, S_3. Results are shown in Figure 7-25. By comparing Figure 7-25 (b) and Figure 7-25 (d),

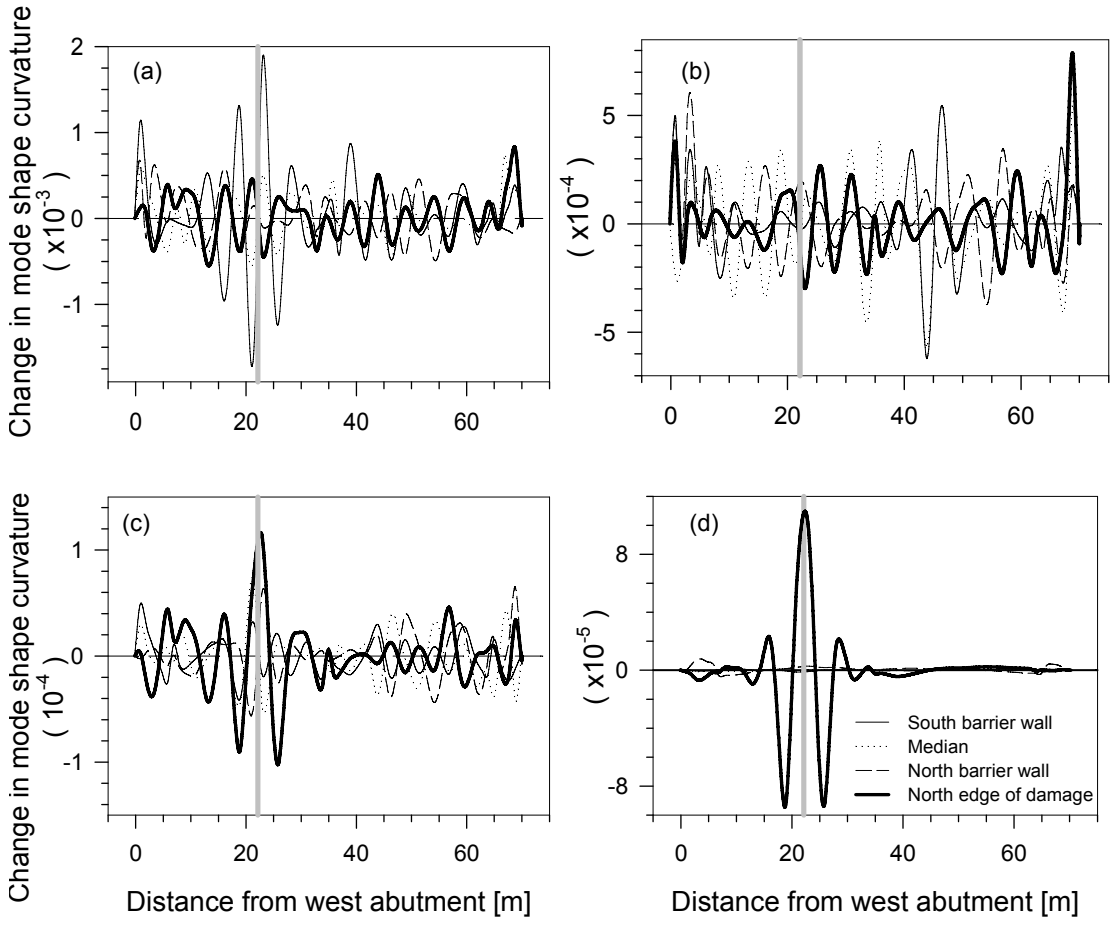

Figure 7-23. The distribution of VBDD parameter for change in mode shape curvature along selected longitudinal lines (south barrier wall, median, north barrier wall and north edge of damage) for damage case R10C9,using an average of : a) 25 trials; b) 100 trials; c) 5,000 trials; and d) without any noise.

It becomes evident that the location of damage can easily be identified using as few as 200 averaged trials, whereas roughly 5,000 repeated trials were required to identify the location of damage for a smaller damage case (i.e. R10C9). This study demonstrates that a relatively higher magnitude in mode shape change (1.5×10^{-3} for damage case S_3) reduces the required number of trials to attenuate the induced uncertainty (which produced a maximum amplitude of 1.5×10^{-3}). For damage case R10C9, on the other hand, the high level of uncertainty, which was approximately five times higher than the changes in mode shape (on the order of 0.3×10^{-3}), overshadowed the changes in mode shape. Therefore a larger number of repeated trials were required to identify the relatively small scale damage case. Alternatively, it is intuitive that a reduced level of uncertainty will also lessen the required number of repeated trials. Thus, the number of repeated trials required to attenuate the effects of noise depends on the level of noise as well as the severity of damage.

In summary, roughly 5,000 repeated trials were required to attenuate the effects of induced uncertainty in detecting the location of damage using the change in mode shape and damage index (as well as the change in mode shape curvature and change in uniform flexibility curvature methods). The change in flexibility, on the other hand, exhibited a false positive indication of damage for a smaller number of repeated trials. However, again, averaging roughly 5,000 repeated trials was seen to eliminate the possibility of a false positive indication of damage. The number of repeated trials required to attenuate the effects of uncertainty decreased as the severity of damage increases, or as the level of uncertainty decreased.

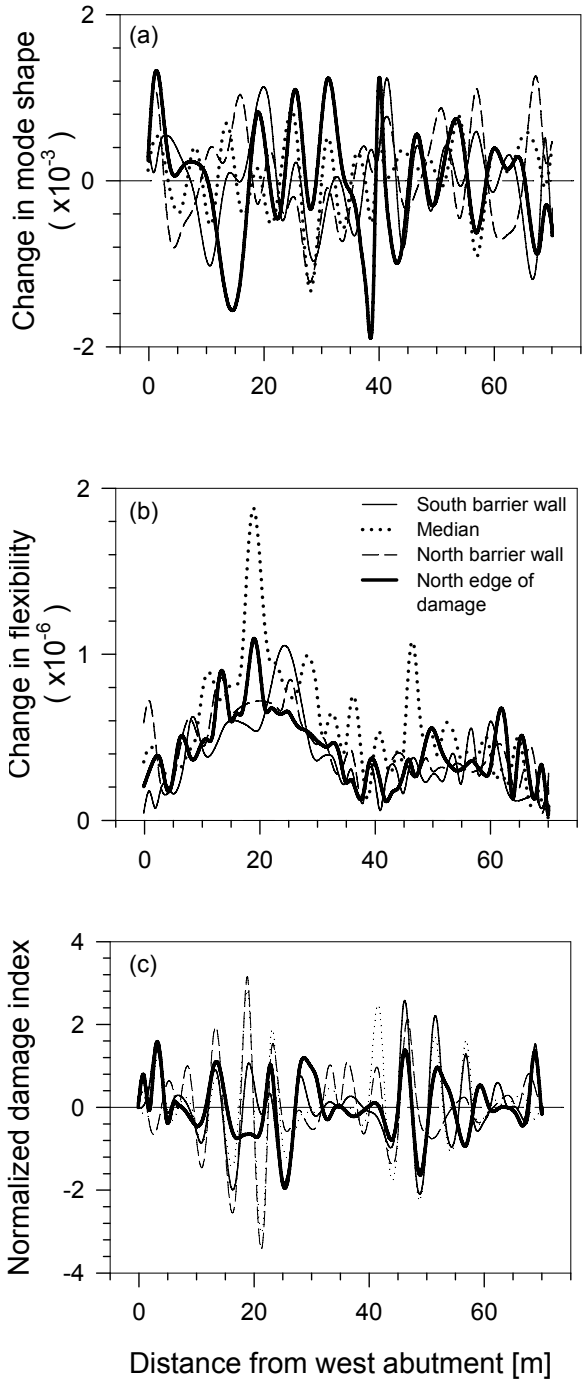

Figure 7-24. The distribution of VBDD parameters for: (a) change in mode shape ; (b) change in flexibility ; and (c) normalized damage index method along selected sensor lines for a spurious damage case (mode shape of the pristine condition with superimposed uncertainty) using an average of 25 trials.

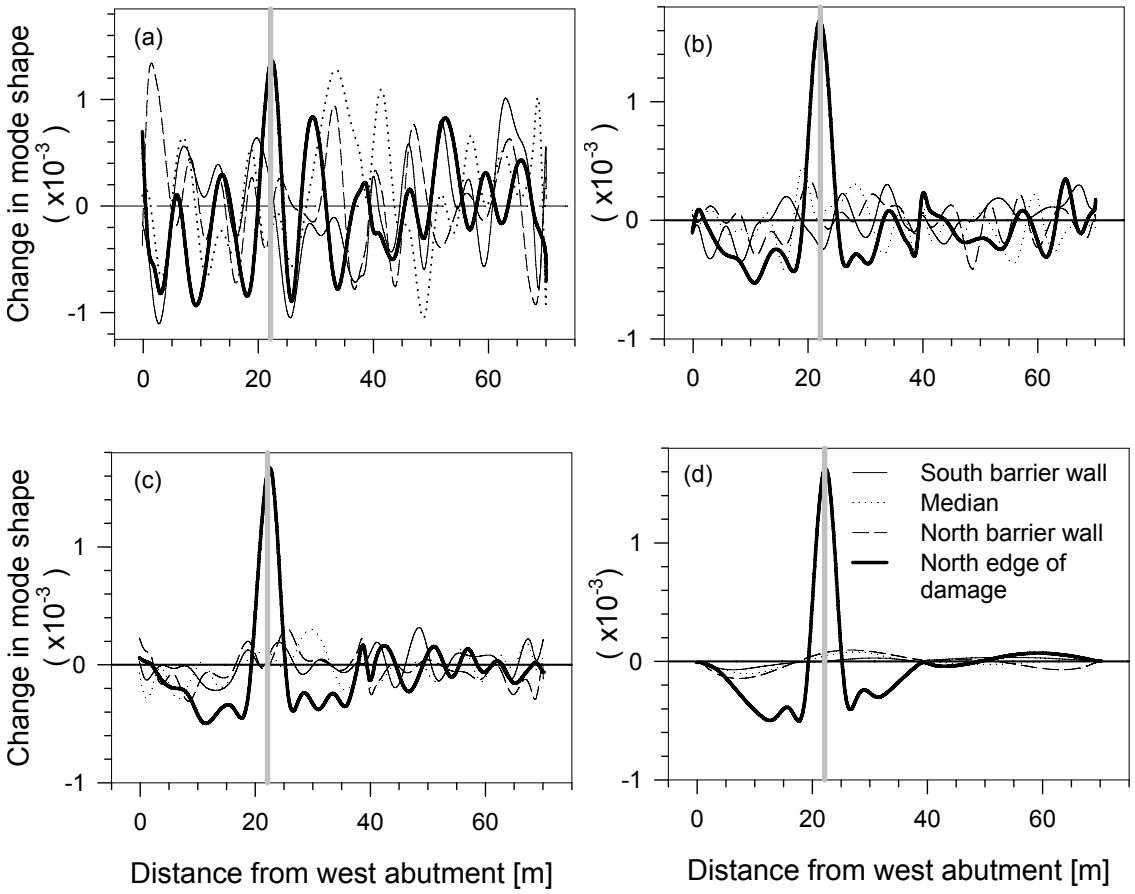

Figure 7-25. The distribution of change in mode shape along selected longitudinal lines, (south barrier wall, median, north barrier wall and north edge of damage) for damage case S_3 using an average of: a) 25 trials; b) 200 trials; c) 500 trials; and d) without any noise.

CHAPTER 8. DAMAGE DETECTION USING A SMALL NUMBER OF SENSORS

8.1 OVERVIEW

Results of the numerical study described in Chapter 7 suggest the applicability of VBDD for 'Level II' damage detection on a bridge structure, provided that a sufficient number of sensors are used and sensors are located in close proximity to the damaged areas. In practice, however, it is generally not feasible to provide the dense grid of sensors that would be required to meet these conditions. For example, sensors stationed within traffic lanes hinder the serviceability of the bridge unless they can be fixed to the underside of the bridge. However, underside sensor placement will also increase the expense of bridge monitoring, making it more difficult to achieve the goal of a low cost infrastructure management system. On the other hand, if sensors are placed on barrier walls or medians, the bridge can be monitored safely without interrupting the flow of traffic. The use of limited measurements to perform VBDD may serve the purpose of an economical preliminary assessment of the condition of a bridge prior to conducting a detailed damage detection investigation, if warranted.

In this chapter, the performance of VBDD parameters based on the change in mode shape, change in flexibility and change in mode shape curvature methods are presented, under the condition that sensor placement was restricted to the median and barrier walls of the Attridge Drive Overpass. The parameters for the change in uniform flexibility curvature method produced results similar to those of the change in mode shape curvature method; therefore, results for this method are not presented to avoid repetition. The damage index parameter, on the other hand, did not exhibit any

indication of damage at an appreciable distance away from the damage location and is, therefore, not considered in this chapter.

As was seen in Section 7.5, uncertainty in field measurements introduced some ambiguities in Level II damage detection when single line normalization was used. However, averaging repeatedly measured mode shapes helped to alleviate these ambiguities. The influence of uncertainty on the patterns of the VBDD parameter distributions (along selected longitudinal sensor lines) using the 3-line normalization procedure was investigated in this study and is presented in Section 8.5

8.2 VBDD USING CHANGE IN MODE SHAPE

It was shown in Section 7.2.1 that the change in mode shape produced on a sensor line located an appreciable distance from the damage became more prominent when 3-line, unit-norm normalization was used (as compared to single line normalization). A comparison of the influence of different normalization procedures on the change in mode shape was performed and is described in Section 8.2.1. Variations in the spatial patterns of the change in mode shape parameter as the location of damage changed were found to show potential for Level II damage detection. This aspect is presented in Section 8.2.2. The average intensity of the overall mode shape amplitude was also observed to vary with the location of damage. The potential of using this average intensity to locate damage is discussed in Section 8.2.3.

8.2.1 Influence of Normalization Procedure on VBDD Parameter for Change in Mode Shape

As described in Section 6.4, two general alternatives was considered for applying unit-norm normalization: (1) 3-line normalization, in which available data

along three lines of measurement were used for normalizing, and (2) single line normalization, in which mode shapes were normalized independently along individual longitudinal lines. The spatial extent of the mode shape segment considered in the normalization process was found to exert a significant influence on the resulting degree of correlation between the damaged and baseline mode shapes. In essence, the more limited the segment that was selected, the closer the general fit was over that segment, thereby emphasizing small, localized mode shape differences caused by damage. Results using both normalization alternatives are presented in this section. In the present context, since sensors were assumed to be limited to the barrier walls and median, 3-line normalization consisted of using the data from all sensors along these 3-lines, while single line normalization consisted of using different scaling factors along each of the three lines.

Mode shape changes based on the two normalization procedures are compared in Figure 8-1 for damage cases R10C1, R10C9 and R16C9 (see Figure 5-9 and Tables 5.4 for locations). In each case, mode shape changes are plotted along the two longitudinal edges of the bridge deck, as well as along the median. The longitudinal extent of the simulated damage is denoted on these plots by a shaded region.

The distribution of mode shape changes found using single line normalization, as shown in Figure 8-1 (on the left side), varied considerably depending on the location of the damage relative to the sensor lines. Although some general patterns were tentatively identified, attempts to locate the imposed damage, even in an approximate manner, based on these results would be overly speculative at the present time. The one

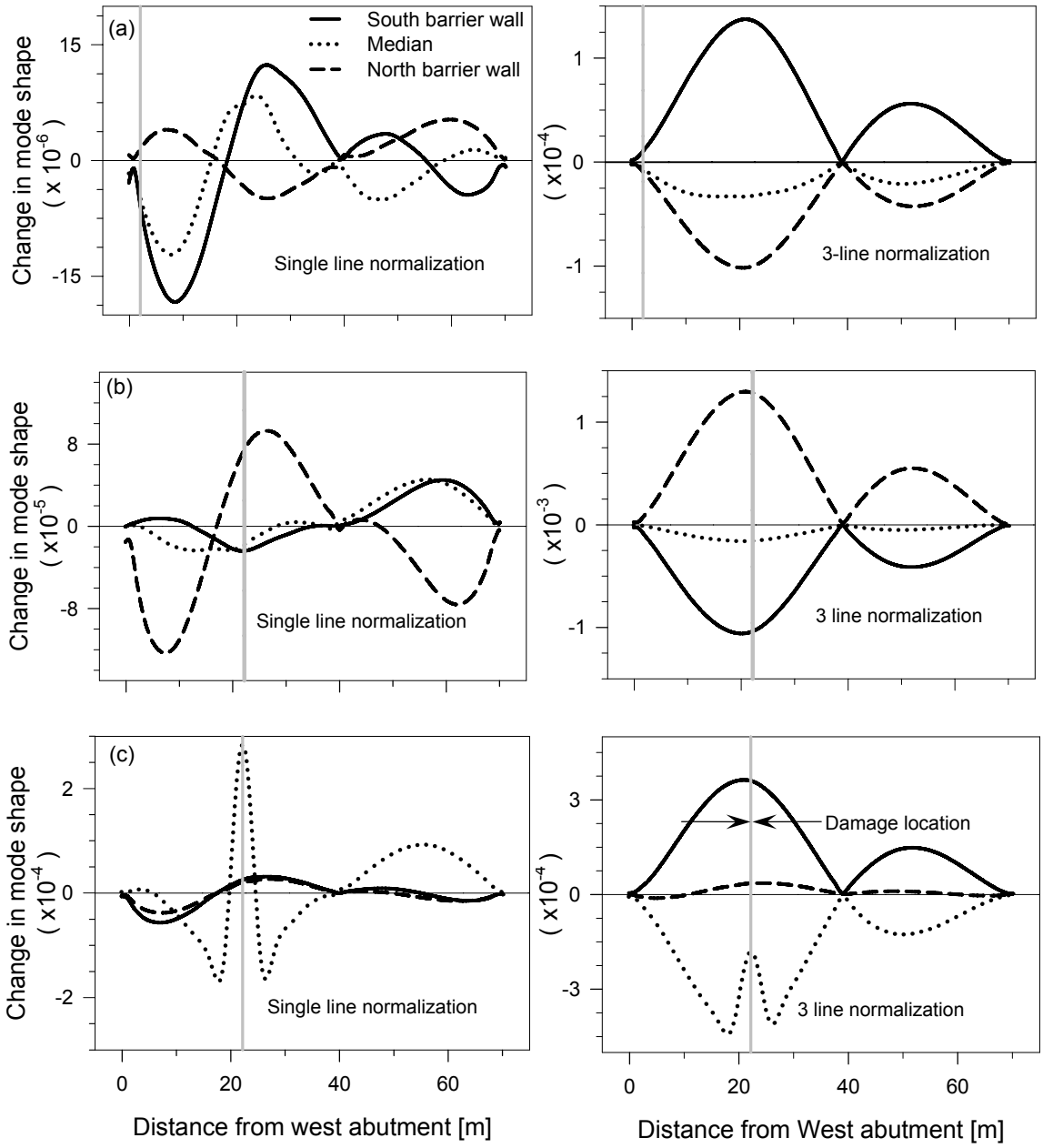

Figure 8-1. Comparison of change in mode shape based on single and 3-line normalization: (a) damage case R10C1; (b) damage case R10C9; and (c) damage case R16C9.

notable exception is seen in Figure 8-1c, where the change in mode shape curve plotted along the median features a distinctive positive peak indicative of damage that is centred

on the actual location of damage case R16C9; in this case, though, the damaged site is immediately adjacent to the sensor line.

As shown in Figure 8-1 (on the right side), 3-line normalization, on the other hand, produced change of mode shape plots whose general form appeared to be relatively insensitive to the damage location. In general, the curve representing each longitudinal sensor line featured a single, smooth hump across each span of the bridge, with the sign of the mode shape changes being the same in both spans. Only the magnitudes of the three plots varied in response to changes in the damage location. Once again, an exception is noted in the median line plot for damage case R16C9, where a small upward peak is centred on the damage location; however, this peak was not nearly as dominant as that produced by single line normalization, suggesting that single line normalization provides a more effective (less ambiguous) indication of the damage location (Level II detection) using sensors close to the damaged site (see Section 7.2). One trend that was observed in the 3-line normalization results was that the plots along the north and south edges of the bridge exhibited opposite signs except when the damage was located close to the mid-width of the bridge (i.e. near the median), in which case those two plots featured the same sign (Figure 8-1 c). Details of this trend will be presented in the next section.

One further consequence of the normalization procedure employed was the magnitudes of the resulting mode shape changes. Since normalizing along a single longitudinal line produced a closer fit between that segment of the damaged and baseline mode shapes, the algebraic difference between the normalized mode shapes was consistently lower than corresponding values obtained using 3-line normalization.

In fact, as is evident in Figure 8-1, the mode shape plots produced using 3-line normalization were, in general, an order of magnitude larger than corresponding plots generated using single line normalization. As discussed in the following section, the magnitude of measured mode shape changes was found to be significant when the effects of measurement uncertainty were introduced.

8.2.2 Patterns of VBDD Parameter Plot for Change in Mode Shape at Different Damage Locations

The general form of the change in mode shape plot using 3-line normalization was found to approximate a parabola on each span. As mentioned in Sections 7.2 and 8.2.1, this pattern was found to be apparently insensitive to the size and location of damage. However, the difference in the magnitudes and signs of the plots along the three sensor lines (south barrier wall, north barrier wall and median) appeared to be correlated to the damage location, based on a visual comparison. Even though sensor lines on the median and the barrier walls were the focus of this study, a spatial plot, which represents the mode shape changes over the entire bridge deck, were included here for a more comprehensive understanding of the patterns. It should be recalled that unit-norm, 3-line normalization of the mode shape over the entire bridge deck was performed using a single scaling factor determined from the data at vertical degrees of freedom located along the two barrier walls (north and south) and median only. A total of 133 damage cases (see Section 5.4) located within the south-west quadrant of the bridge deck were investigated to identify possible patterns in the VBDD results.

Patterns of mode shape changes were divided into seven groups, based on the sign and magnitudes of the plot along the median compared to corresponding plots along the barrier walls. For all of these patterns, mode shape changes were taken as

positive when the absolute magnitude of the mode shape of the damaged bridge deck at any node was greater than the absolute magnitude of the mode shape at that node corresponding to the pristine condition. Similarly, a negative sign represents the case in which the mode shape representing pristine condition was higher than that of the damaged condition.

It was found that spatial plots of all these patterns could be described, in general, approximately as parabolic curves within each span and along each longitudinal sensor line. Amplitudes of the parabolic curve along a given sensor line depended on the location of damage and the lateral distance of that sensor line from the damage location. In each of the seven patterns identified, the sign of the change in mode shape plot along a longitudinal sensor line varied from positive to negative as the location of longitudinal sensor line changed from the south barrier wall to the north barrier wall. This implies that there may have been a line of near-zero amplitude changes somewhere between the two sensor lines where the signs of the change in mode shape parameter were opposite to each other. Fictitious lines were assumed, therefore, based on visual examination; these were designated as neutral sensor locations in order to characterize all of the patterns. These fictitious lines may also prove to be beneficial for automatic pattern recognition at some stage in the future. The seven patterns for the change in mode shape plots are described below.

Pattern I, shown in Figure 8-2, features a positive sign for change in mode shape along the north barrier wall and the median, while it is negative along the south barrier wall. The amplitude along the median is smaller than that on the north and south barrier walls. The amplitude of the parabolic curves along a given longitudinal sensor line

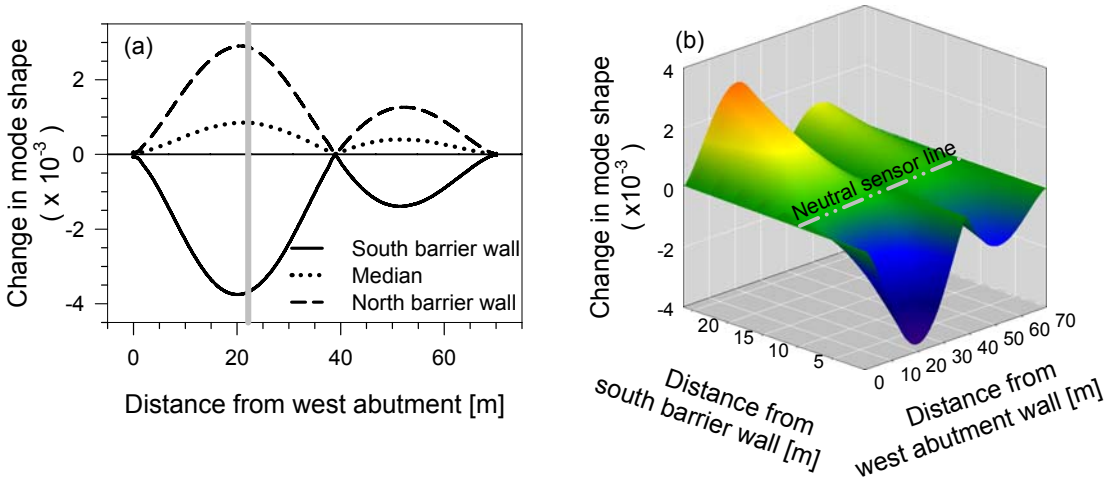

Figure 8-2. General Pattern I for change in mode shape (damage case R4C9): (a) longitudinal profile along three sensor lines; and (b) spatial plot.

decreased as the distance between a sensor line and the neutral sensor line decreased, as seen in the spatial plot of change in mode shape (see Figure 8-2 b). The neutral sensor line in this pattern was located close to the median, between the median and south barrier wall, as shown in Figure 8-2.

As with Pattern I, Pattern II (Figure 8-3) features positive values along the north barrier wall and negative values along the south barrier wall. However, the sign of the plot along the median is negative, which is opposite to that of Pattern I. The amplitude of mode shape changes along the median is still small compared to that along the barrier walls; however, it is also relatively smaller than that of Pattern I. Similar to Pattern I, the amplitude of the parabolic curves along individual longitudinal sensor lines decreased as the distance between the sensor line and neutral sensor line decreased. The location of the neutral sensor line also moved slightly towards the north barrier wall in Pattern II, placing it in close proximity to the median, and between the median and the north barrier wall.

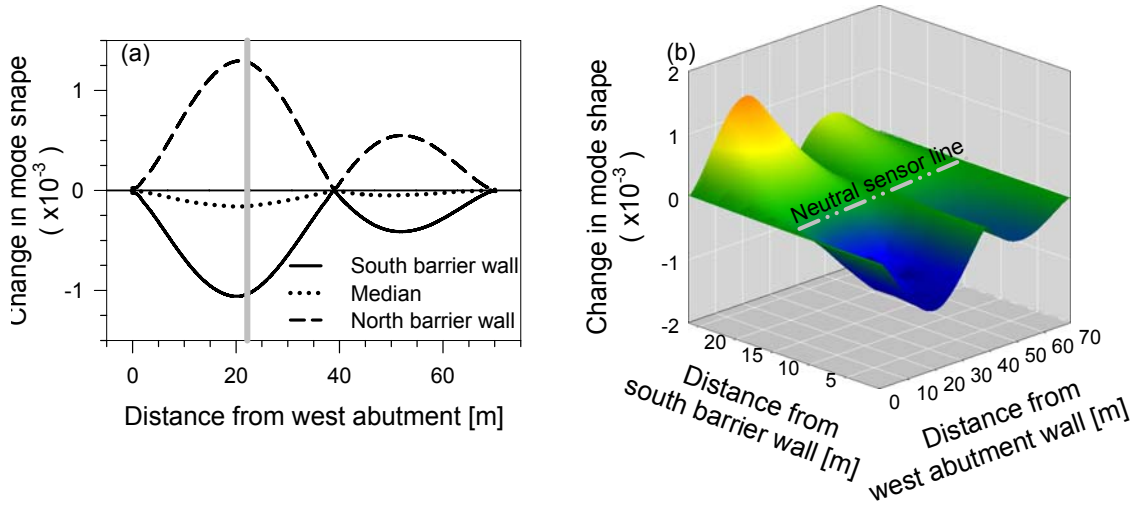

Figure 8-3. General Pattern II for change in mode shape (damage case R10C9): (a) longitudinal profile along three sensor lines; and (b) spatial plot.

As with Pattern II, Pattern III (see Figure 8-4) features negative changes in mode shape along the median and south barrier wall, while exhibiting positive changes along the north barrier wall. However, the amplitudes along the south barrier wall were the smallest among those on the three sensor lines. The neutral sensor line also moved slightly further north in comparison to its position for Pattern II, although still located between the median and north barrier wall. As with the previous two patterns, the amplitude of the parabolic curve along a given longitudinal sensor line decreased as the distance between that sensor line and the neutral sensor line increased.

In Pattern IV (see Figure 8-5 a and c), both the north and south barrier wall plots had positive values, although values between the two walls varied considerably, while the plot along the median exhibited a negative sign. Therefore, it was evident that two neutral sensor locations were required in Pattern IV, one between the median and each of the north and south barrier walls. Beyond these general characteristics variation of in the magnitudes along the north and south barrier walls depended on the location of the

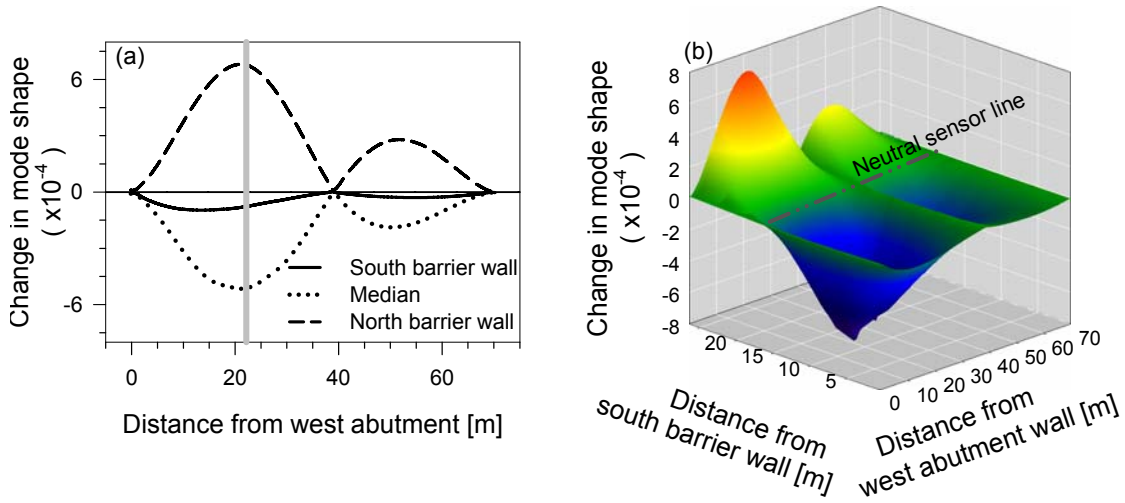

Figure 8-4. General Pattern III for change in mode shape (damage case R13C9): (a) longitudinal profile along three sensor lines; and (b) spatial plot.

damage. A characteristic peak in the plot along the median centred at the location of damage in Figure 8-5 b indicates the possibility for Level II damage detection; however, for cases in which such a peak was observed, the median happened to be located close to the damage location. A sensor line in close proximity to a damage location was found always to introduce the possibility of Level II damage detection, as described in Section 7.2.

In Pattern V (see Figure 8-6), change in mode shape values were positive along the south barrier wall, but negative on the median and north barrier wall. The magnitudes along the median were the smallest among the three sensor lines. Compared with Pattern I, the signs of the values on the selected sensor lines appeared to be opposite for Pattern V. Amplitudes of the parabolic curve along a given sensor line decreased as the distance between the sensor line and neutral sensor line decreased. In this case the neutral sensor line was located close to, and to the south of, the median.

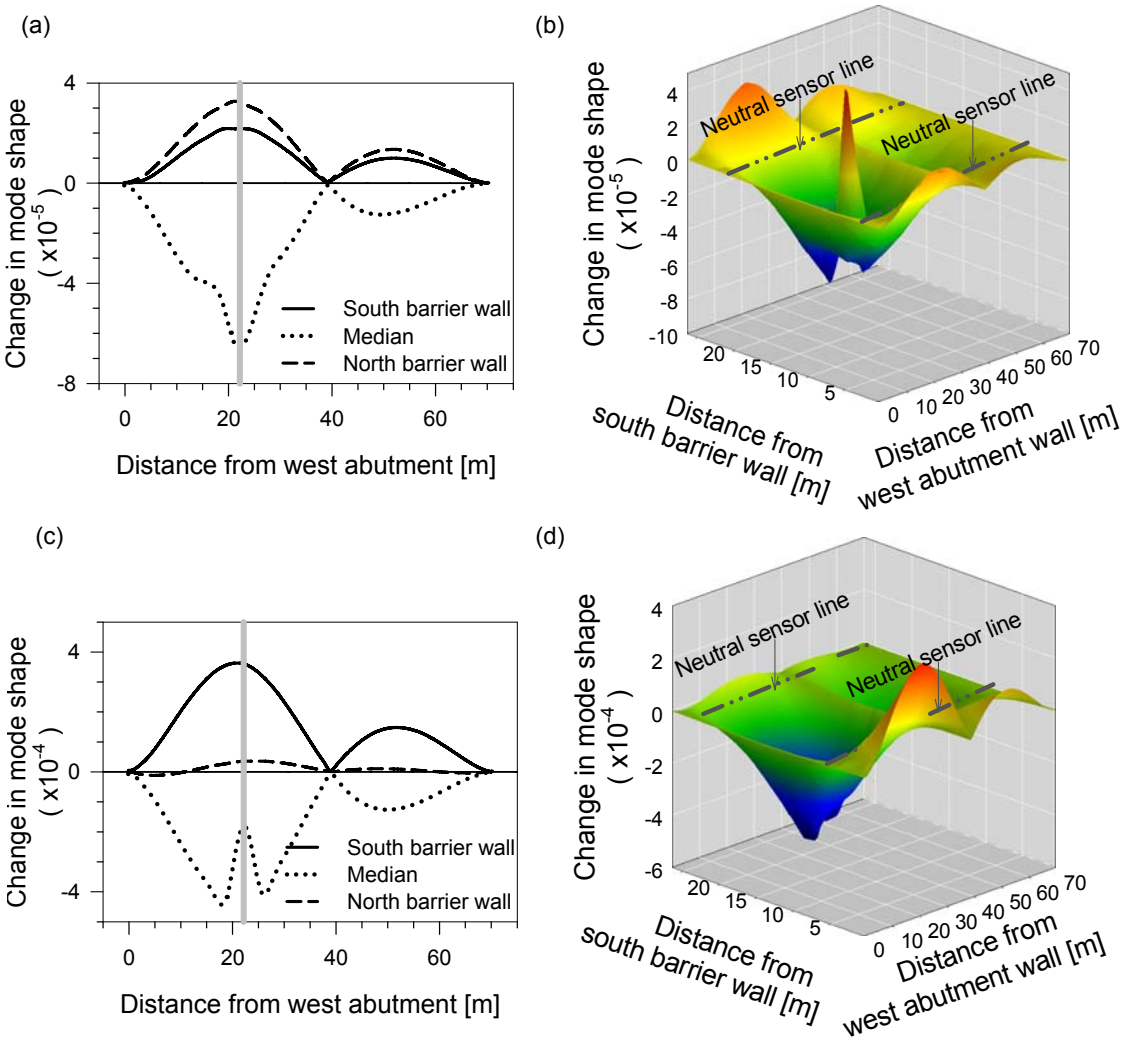

Figure 8-5. General Pattern IV for change in mode shape as seen for damage case R14C9: (a) longitudinal profile along three sensor lines; (b) spatial plot; and damage case R16C9: (c) longitudinal profile along three sensor lines; (d) spatial plot.

As with Pattern V, values of change in mode shape for Pattern VI were positive along the south barrier wall, but negative along the north barrier wall and median (see Figure 8-7). However, the highest magnitudes of the VBDD parameter among the three selected sensor lines appeared on the median for Pattern VI, while the highest changes appeared on the barrier walls for Pattern V. The neutral sensor line for Pattern VI was located slightly further south of the median compared to that of Pattern V.

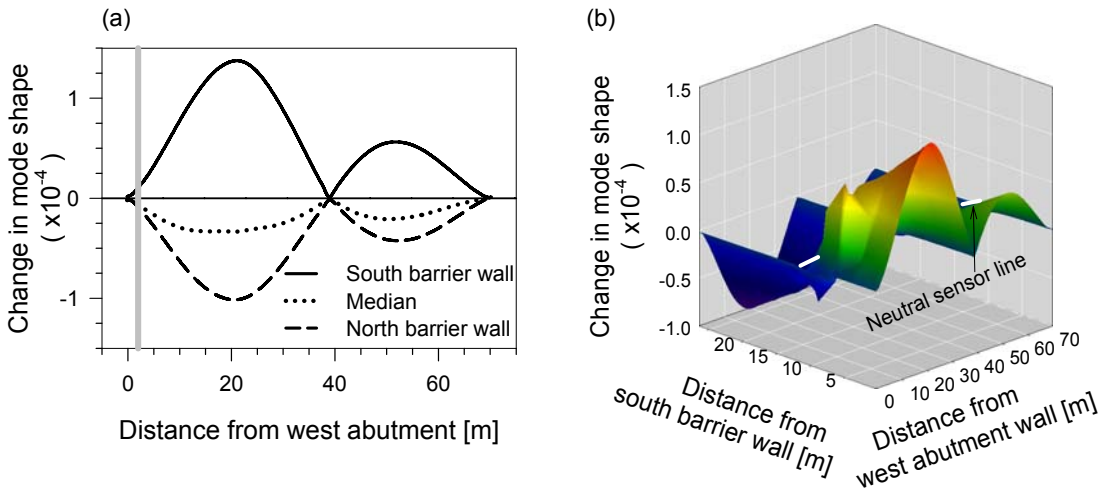

Figure 8-6. General Pattern V for change in mode shape (damage case R10C1): (a) longitudinal profile along three sensor lines; and (b) spatial plot.

Pattern VII was characterized by a localized peak centred at the location of damage along the median, which was a common feature when the sensor line was located close to the damage location (see Figure 8-8). As with Patterns V and VI, the values of change in mode shape along the south and north barrier walls were positive and negative, respectively. However, values along the median were positive, a characteristic opposite to that of Pattern V and VI. The neutral sensor line in Pattern VII was located on the north side of the median.

A summary of the sign of values along the three sensor lines and the magnitude among sensor lines for the seven patterns are given in Table 8-1. In this table, 'M>' indicates that the magnitude along the median was higher than that on the north or south barrier wall (NBW or SBW). On the other hand, 'M<' indicates that the magnitude along the median was lower than that on the sensor line indicated. The symbology 'M ≈' indicates that the magnitude on the median was very similar to that on the indicated sensor line.

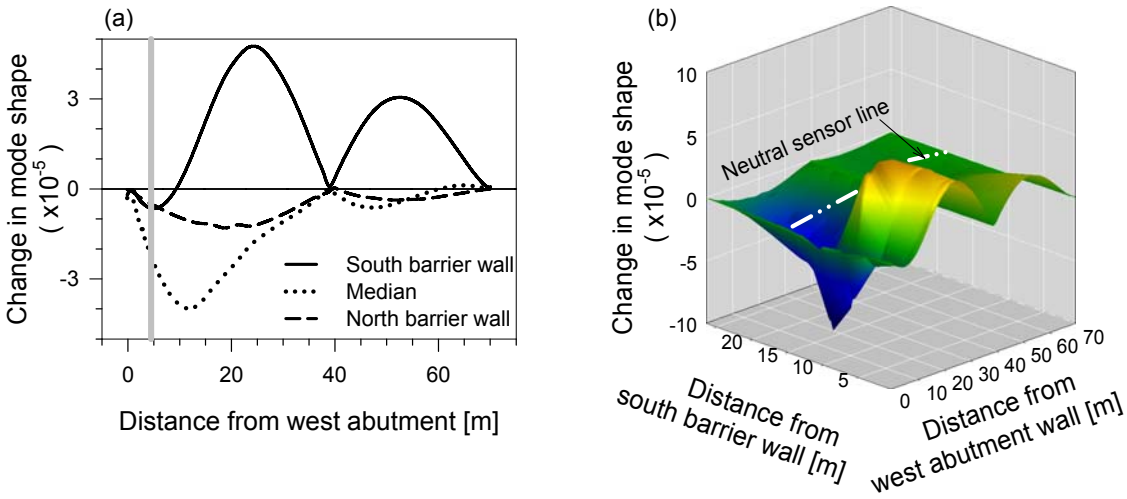

Figure 8-7. General Pattern VI for change in mode shape (damage case R10C2): (a) longitudinal profile along three sensor lines; and (b) spatial plot.

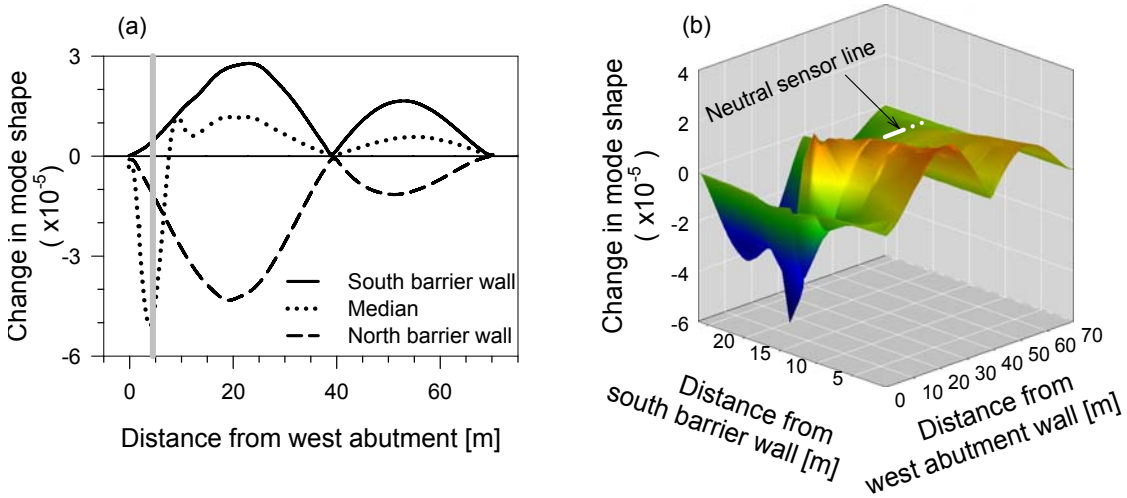

Figure 8-8. General Pattern VII for change in mode shape (damage case R16C2): (a) longitudinal profile along three sensor lines; and (b) spatial plot.

Positive and negative signs on the north and south barrier walls, respectively, were a common feature for Pattern I through Pattern III (in Figure 8-2 through Figure 8-4). The sign on the median changed from positive to negative as the damage location moved from the south barrier wall to the median (Pattern I to Pattern III).

Table 8-1. Signs of the change in mode shape values pertinent to seven patterns.

Pattern	Sign on south barrier wall	Sign on median	Sign on north barrier wall	Remarks	Representative Damage Cases
I	-	+	+	M< NBW & M< SBW	R4C9
II	-	-	+	M< SBW & M< NBW	R10C9
III	-	-	+	M≈NBW & M> SBW	R13C9
IV	+	-	+	M> SBW & M> NBW	R14C9 and R16C9
V	+	-	-	M< NBW & M< SBW	R10C1
VI	+	-	-	M> NBW & M≈SBW	R10C2
VII	+	+	-	M< SBW & M< NBW	R16C2

M = Magnitude along median, NBW= Magnitude along north barrier wall, SBW= Magnitude along south barrier wall

The magnitude along the median also increased as the damage location moved towards the median. The magnitude along the median in Pattern IV was the highest among those for the first four patterns, Pattern IV being the characteristic pattern when the damage was located in close proximity to the median. On the other hand, negative and positive signs on the north and south barrier walls, respectively, were a common feature for Pattern V through Pattern VII. For these patterns, the magnitudes along the median increased as the location of damage moved toward the median from the south barrier wall.

Each of the patterns described above may be correlated to a general location for damage on the bridge deck. A pattern map showing the damage locations on the bridge deck along with their corresponding patterns for change in mode shape is shown in Figure 8-9. Each pattern is represented by a different colour on the pattern map.

Patterns I through IV were the characteristic patterns for changes in mode shape when the damage was located in the middle region of south-west quadrant of bridge deck. It is observed in Figure 8-9 that the pattern varied from I through IV as the damage location moved towards the median from south barrier wall, provided that the damage was not located in close proximity to a support (abutment or pier), where the rigidity of bridge deck was relatively higher than that of the midspan region. Therefore, the midspan region of the south-west quadrant of the bridge deck could be subdivided into four general areas, each corresponding to one of the first four patterns. Pattern I was the characteristic pattern when the damage was located near the south barrier wall. Similarly, pattern IV was the characteristic pattern when the damage was located close to the median. Damage locations corresponding to Patterns II and III fell between these two general locations, as shown in Figure 8-9.

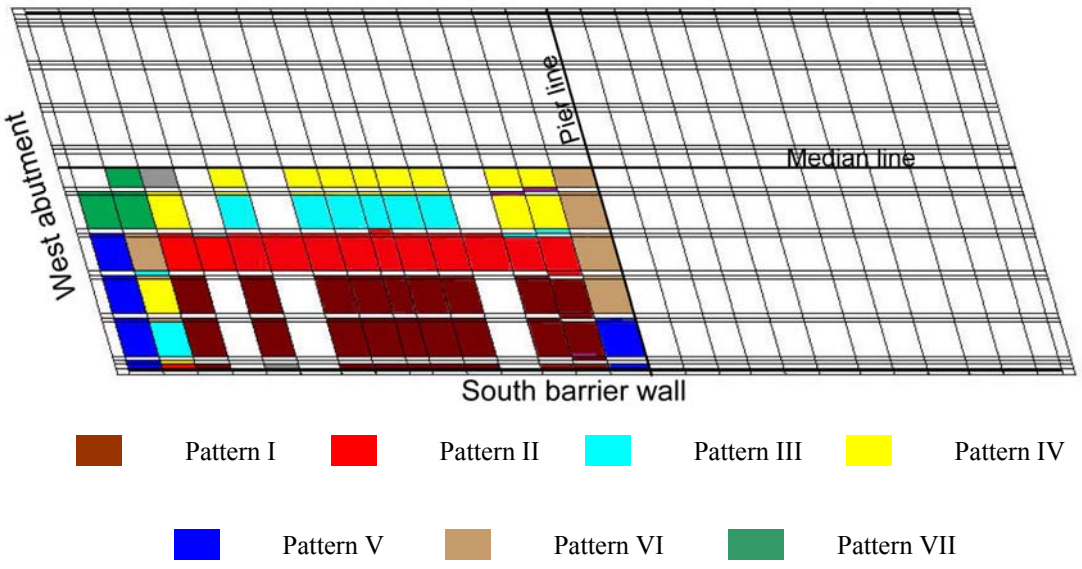

Figure 8-9. Plan of bridge deck showing zones pertinent to various patterns of VBDD parameter plots for change in mode shape (Pattern I through Pattern VII) on selected sensor lines.

The patterns observed for damage adjacent to supports were Pattern V through Pattern VII. Generally, patterns corresponding to damage located close to the supports (regions of high rigidity) were observed to produce plots with signs that were opposite to those for damage located in mid-span regions (regions of low rigidity). There appeared to be a zone that extended roughly 3 m in width and was located approximately 3 m east of west abutment wall, where Patterns II, III, IV, VI and VII were distributed in an apparently random fashion. This zone was located between the midspan region and the support region next to the west abutment wall, and appeared to be a transitional zone between the zones of relatively high and low rigidity.

In addition to the general localization of damage based on the pattern of the resulting change in mode shape plots, the magnitude of the overall changes in mode shape over the entire bridge deck was observed to vary as the location of damage changed. Damage cases R10C1 and R10C9 were similar in size, but the overall magnitude of changes in mode shape for damage case R10C9 (in Figure 8-3) is approximately 10 times higher than that for damage case R10C1 (in Figure 8-8). Therefore, the location of damage had an influence on the overall magnitude of changes in mode shape, a result that may be correlated to the level of rigidity for those respective regions. The variation of overall magnitude of the change in mode shape with the change of damage location is discussed in Section 8.2.3.

In summary, mapping of change in mode shape patterns showed that each pattern could potentially be correlated to damage located within a general region on the bridge deck. Therefore, the change in mode shape (using 3-line, unit-norm normalization) on selected longitudinal sensor lines (barrier walls and median) not only

permitted Level I damage detection, but also showed potential for Level II damage detection in a general sense.

8.2.3 Influence of Damage Location on the Magnitude of Mode Shape Changes

The magnitude of mode shape changes was found to be influenced, not only by the severity of the damage (Section 7.3), but also by its location on the bridge deck (Section 8.2.3). To investigate the effect of damage location on the likelihood of successfully applying VBDD methods, a series of damage cases of approximately equal size (2.5 m long X 3 m wide X 50 mm deep) were induced into the FE model. A quantitative indicator of the resultant intensity of mode shape changes, $I_{\Delta\phi}$, was the defined as

$$I_{\Delta\phi} = \frac{\sum_{i=1}^{n}(\phi_i^* - \phi_i)^2}{\sqrt{\sum_{i=1}^{n}\phi_i^{*2}\sum_{i=1}^{n}\phi_i{}^2}}, \tag{8.1}$$

where n is the total number of elements (simulated measurement points) along all three longitudinal measurements lines used in this study. The mode shapes vector $\boldsymbol{\phi}^*$ and $\boldsymbol{\phi}$ were scaled using the 3-line normalization approach.

Mode shape change intensity results for various damage locations in the south-west quadrant of the bridge are shown in Figure 8-10. Mode shape changes are greatest when the damage is located longitudinally near mid span between the abutment and the pier, where the bridge structure is most flexible.

The large variation in the intensity of mode shape changes, $I_{\Delta\phi}$, adds additional complexity to the assessment of VBDD results. In the scenario being considered here, where the severity is known to be similar for all damage cases, $I_{\Delta\phi}$values can be used to provide some additional indication as to the approximate damage location. In practice,

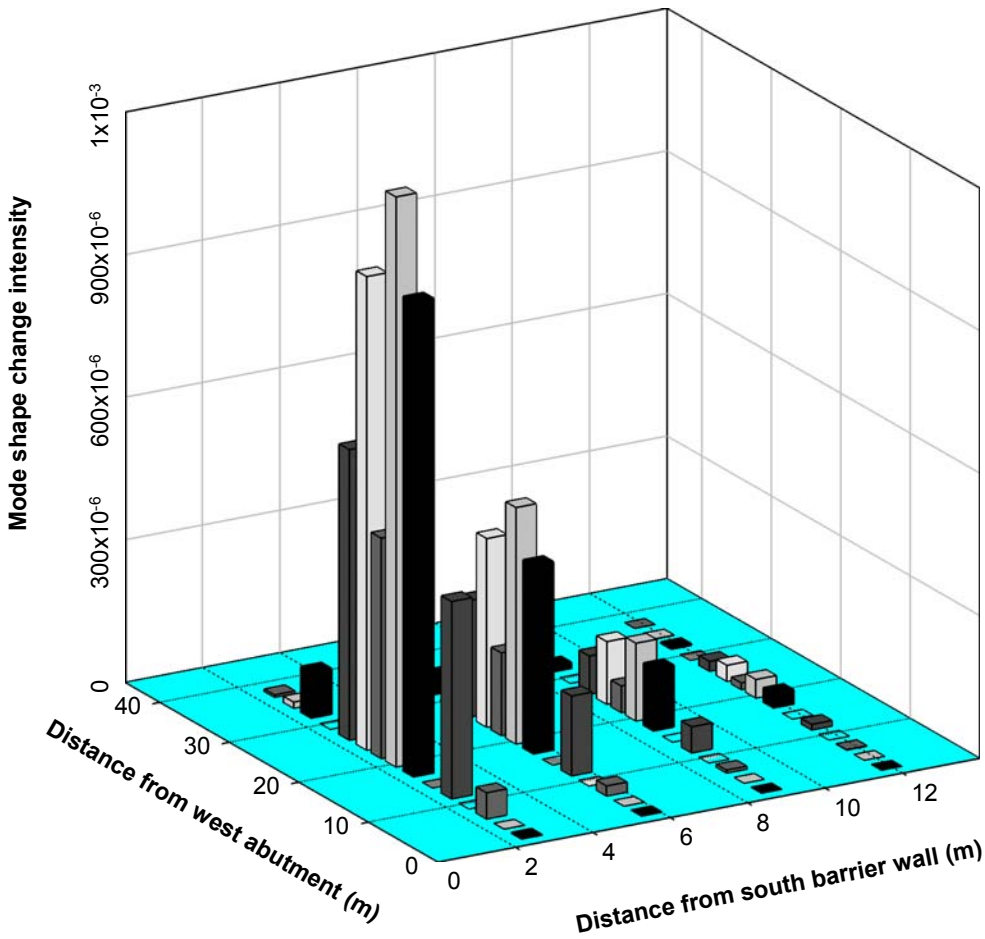

Figure 8-10. Mode shape change intensity for damage at varying locations on the deck, based on 3-line mode shape normalization.

however, the influence of damage location on the magnitude of measured mode shape changes cannot be distinguished from that of damage size, a fact which poses a challenge for performing Level II damage detection.

It is apparent from Sections 8.2.2 and 8.2.3 that damage localization capabilities using the change in mode shape parameter are somewhat limited and subject to uncertainty. However, the limited ability to correlate patterns to a particular damage location strictly by visual means suggests that there may be some potential for the successful application of automated pattern recognition algorithms.

8.3 VBDD USING CHANGE IN FLEXIBILITY

As was shown in Section 7.2, the change in flexibility parameter along the barrier walls and median typically indicated the presence of damage (Level I), regardless of the normalization procedures used. Also, 3-line normalization produced a more prominent indication of the presence of damage using sensor lines along barrier walls and median than that produced by single line normalization. However, the characteristic peak at the location of damage, as seen for single line normalization, disappeared when 3-line normalization was used. A comparison of the influence of normalization procedure on the change in flexibility is presented in Section 8.3.1. Changes in flexibility along barrier walls and median were also observed to vary as the location of damage changed. The potential of using the resulting patterns for Level II damage detection is discussed in Section 8.3.2.

8.3.1 Influence of Normalization Procedure on VBDD Parameter for Change in Flexibility

The influence of the two normalization procedures discussed in Section 6.4 on the change in flexibility is discussed in this section. The objective of this work was to ascertain the influence of the normalization procedure on the degree of precision with which damage detection can be performed using the change in flexibility method in conjunction with a limited number of sensors.

Flexibility changes based on both single line and 3-line normalization using limited sensors are compared in Figure 8-11. Regardless of the normalization procedure, or the location of damage, the general pattern of the change in flexibility plots along a longitudinal sensor line can be described as having a positive hump on each span. However, 3-line normalization was observed to transform the shape of the plot to being

approximately parabolic on each span, while an irregularly shaped positive hump was produced by single line normalization.

The change in flexibility along the barrier walls and median generally did not indicate the location of damage, unless the damage happened to be located in close proximity to any of these sensor lines. As seen in Figure 8-11 c, single line normalization produced a distinct peak along the median at the damage location, which happened to lie close to the median. This distinct peak can be interpreted as an abrupt change in flexibility corresponding to a damage location. However, this distinct peak at the location of damage was replaced by a small negative hump when 3-line normalization was used.

In general, 3-line normalization also increased the magnitude of the change in flexibility compared to that produced by single line normalization. However, as seen in Figure 8-11, the amount of this increase was observed to vary depending on the location of damage.

In summary, the prominent changes in flexibility along the barrier walls and median produced by 3-line normalization could potentially be used to identify the presence of damage (Level I). A detail discussion on this aspect is presented in the following section.

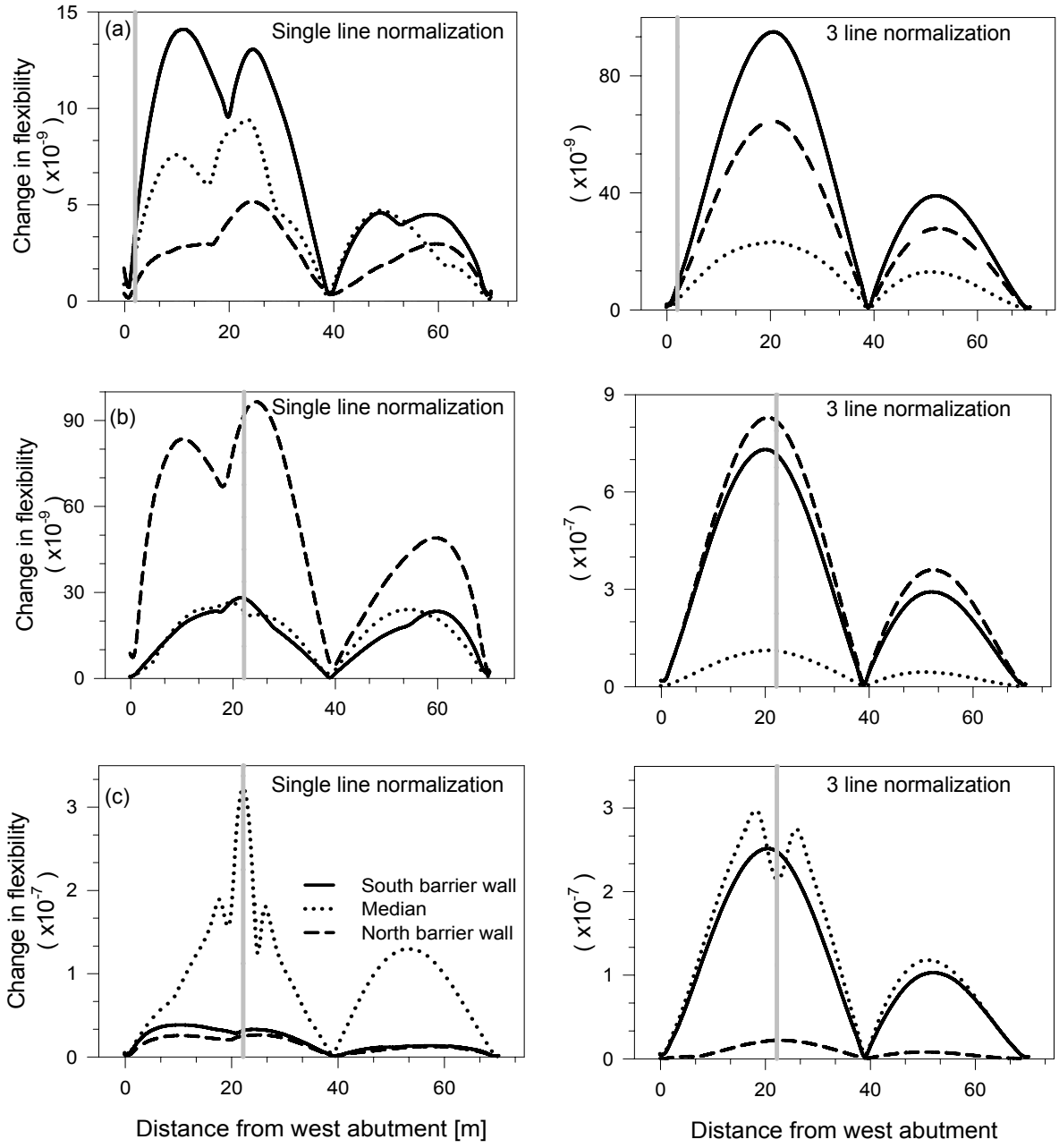

Figure 8-11. Comparison of change in flexibility based on single line and 3-line normalization: (a) damage case R10C1; (b) damage case R10C9; and (c) damage case R16C9.

8.3.2 Patterns of VBDD Parameter Plot for Change in Flexibility at Different Damage Locations

As mentioned in the previous section, observable changes in flexibility (using 3-line normalization) along three selected sensor lines appear to provide the potential for identifying the presence of damage (Level I), regardless of the damage location to the sensor lines. It was also found that the relative difference in magnitude among the three sensor lines may potentially be correlated to some general damage locations, thereby providing some potential for Level II damage detection.

Damage cases, as described in Section 5.4, were investigated to identify characteristic patterns of change in flexibility plots and to correlate them to some general damage locations. A total of six patterns were identified for damage located in the south-west quadrant of bridge deck; these patterns are presented in Figure 8-12 and Figure 8-13. Although longitudinal sensor lines along barrier walls and median are the focus of this study, a spatial plot of each pattern is also added to provide a sense of overall changes in the parameter over the entire bridge deck. Each pattern is described below.

In Pattern I (Figure 8-12 (a)), the largest magnitudes appeared along the south barrier wall, followed by those along the north barrier wall and then the median, respectively. Changes over the entire bridge deck are shown in Figure 8-12 (b). The magnitude was observed to decrease gradually as the location of the sensor line moved from the outer edges, toward the centre of the bridge deck. Therefore, the longitudinal sensor line with lowest amplitude was likely to be located somewhere between the north and south barrier walls.

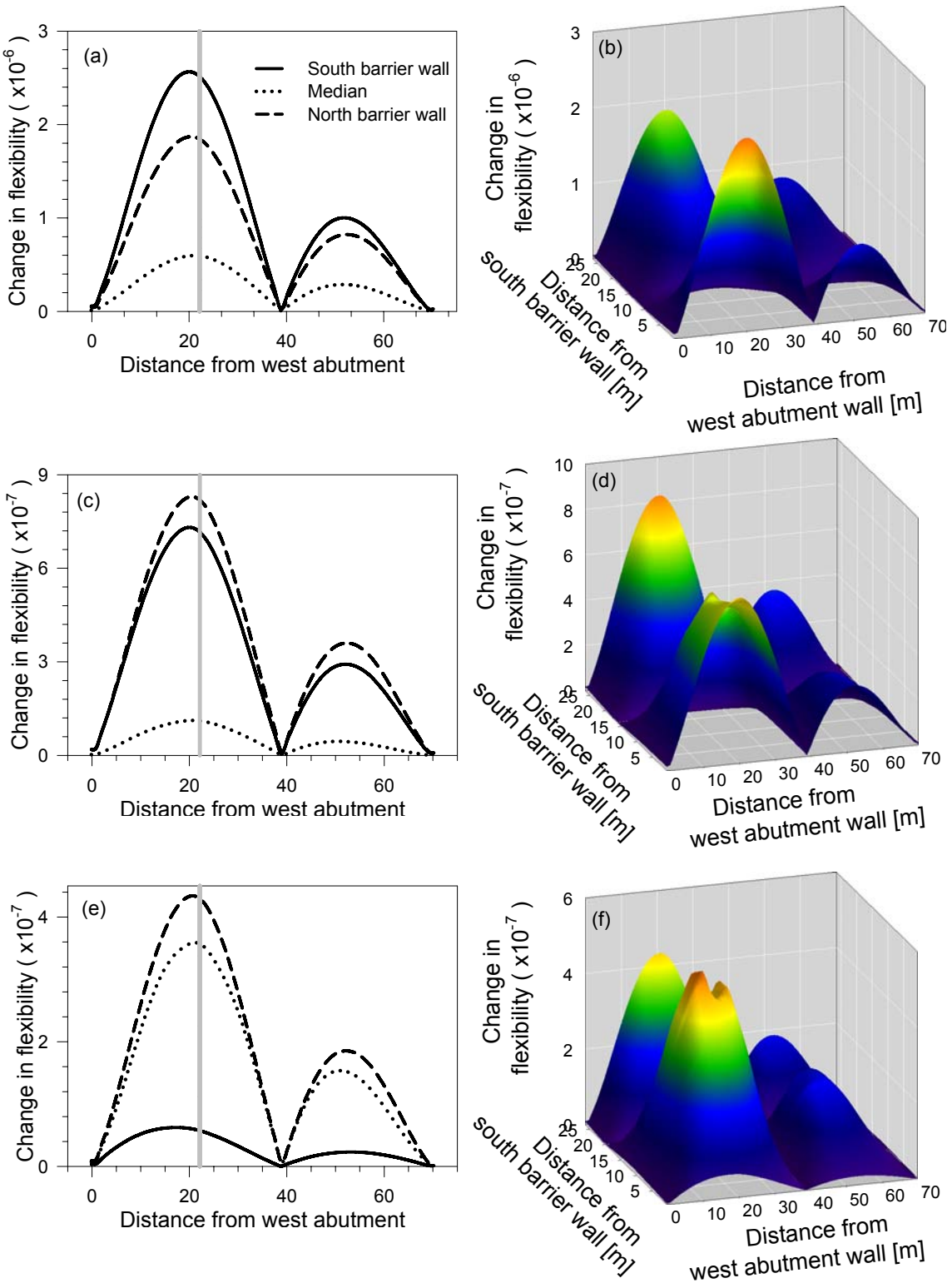

Figure 8-12. Longitudinal and spatial distributions of change in flexibility based on 3-line normalization:(a, b) Pattern I for damage case R4C9; (c, d) Pattern II for damage case R10C9 ; and(e, f) Pattern III for damage case R13C9.

In Pattern II (Figure 8-12 (b)), the largest magnitudes appeared on the north barrier wall, followed by those along the south barrier wall and the median, respectively. As with the Pattern I, the longitudinal sensor line with the lowest magnitude of changes was located somewhere between the north and south barrier wall.

As with Pattern II, the largest magnitude of changes appeared along the north barrier wall in Pattern III (Figure 8-12 (c)). However, the second and third largest magnitudes appeared along the median and south barrier wall, respectively. The longitudinal sensor line with the lowest magnitude was located somewhere between the median and north barrier wall.

In Pattern IV (Figure 8-13 (a)), the largest amplitude changes occurred along the median, followed by those along the north and south barrier walls, respectively. It was evident from the spatial plot (in Figure 8-13 (b)) that there were possibly two longitudinal sensor lines where the magnitudes were the lowest, one between each barrier wall and the median.

As with the Pattern IV, the largest amplitude changes occurred along the median in Pattern V (Figure 8-13 (b)). However, the second and third largest magnitudes appeared along the south and north barrier walls, respectively. A small negative hump at the location of damage along the median indicated the location of damage (Level II); however, the median happened to be the closest sensor line to this damage location. The location of the longitudinal sensor line with the lowest amplitude changes was located between the median and south barrier wall.

In Pattern VI (Figure 8-13 (c)), the largest amplitude changes occurred along the south barrier wall, followed by those along the median and north barrier wall, respectiv-

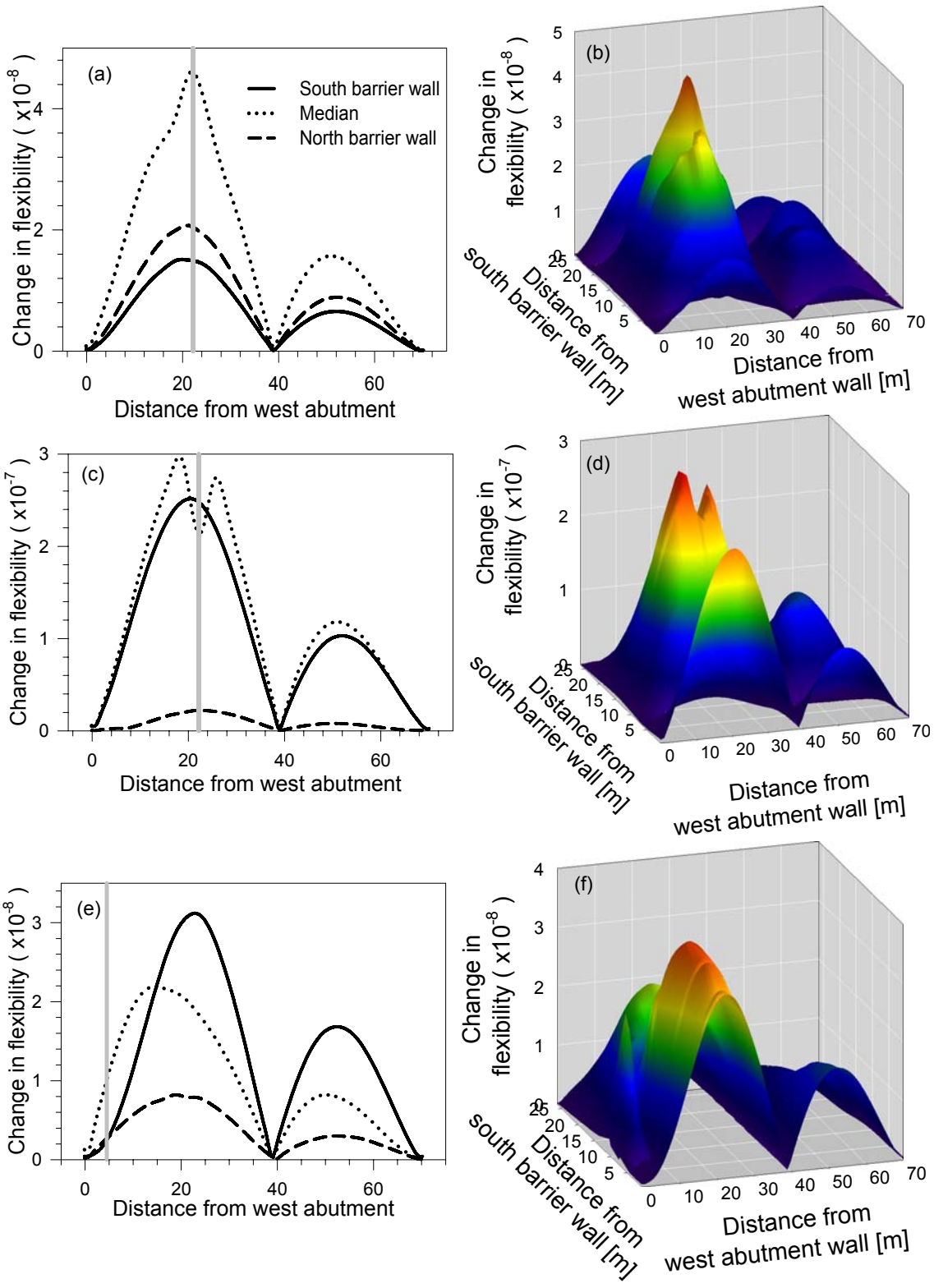

Figure 8-13. Longitudinal and spatial distributions of change in flexibility based on 3-line normalization: (a, b) Pattern IV for damage case R14C9; (c, d) Pattern V for damage case R16C9; and (e, f) Pattern VI for damage case R10C2.

-ely. The location of the longitudinal sensor line with the lowest amplitude changes was located close to the median for this pattern. A comparison of the magnitudes along these three sensor lines for each pattern is summarized in Table 8-2.

Each of the above mentioned patterns can be correlated to a general damage location on the south-west quadrant of the bridge deck. The general location related to each pattern is marked by a separate colour in the pattern map in Figure 8-14. A general trend that was apparent in the midspan region of south-west quadrant of bridge deck was that the pattern changed from I through IV as the location of damage moved from south barrier wall to the median. However, this trend was not followed when damage was located close to supports, which featured relatively high rigidity in comparison to the midspan region.

The midspan region can be discretized into four general damage locations depending on the first four patterns corresponding to the damage located in a particular general location. Pattern I, featuring the highest magnitude changes along the south barrier wall, was associated with a lower stiffness zone extending roughly 7.3 m from the south barrier wall. Patterns II and III, featuring the highest magnitude of changes along the north barrier wall, was associated with a region extending from approximately

Table 8-2. Different patterns of change in flexibility.

	Sensor line with largest magnitude of amplitude		
	1st Largest	2nd Largest	3rd Largest
Pattern I	South Barrier Wall	North Barrier Wall	Median
Pattern II	North Barrier Wall	South Barrier Wall	Median
Pattern III	North Barrier Wall	Median	South Barrier Wall
Pattern IV	Median	North Barrier Wall	South Barrier Wall
Pattern V	Median	South Barrier Wall	North Barrier Wall
Pattern VI	South Barrier Wall	Median	North Barrier Wall

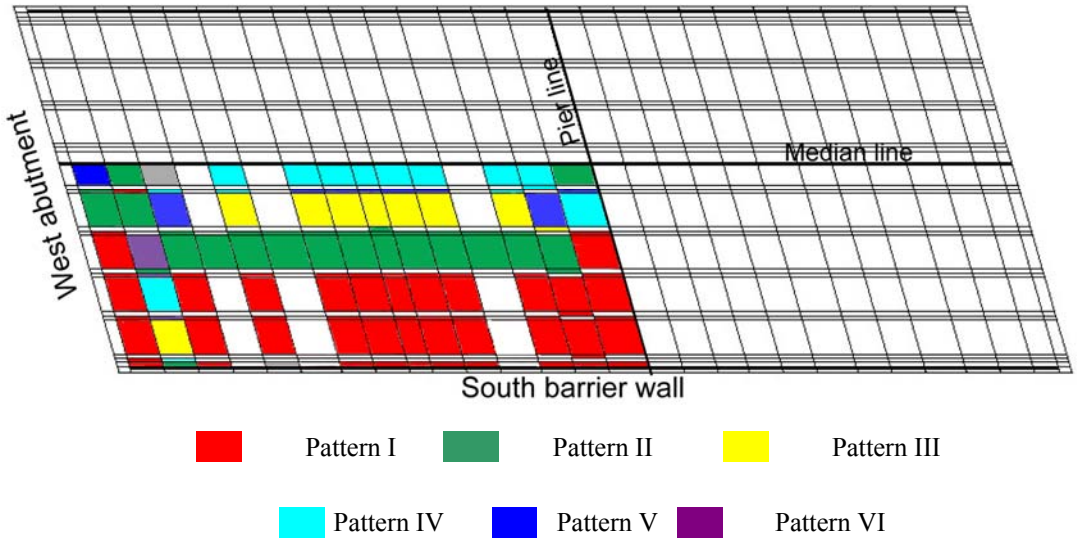

Figure 8-14. Plan view of bridge deck showing damage locations associated with different patterns for change in flexibility

7.6 m to 13.2 m from the south barrier wall. Pattern IV, which featured the highest magnitude changes along the median, was associated with a region extending from approximately 13.2 m to 15.3 m from the south barrier wall. On the other hand, regions close to the supports (abutment and pier) exhibited an irregular and inconsistent distribution of Pattern I through Pattern VI.

In summary, the change in flexibility method using 3-line normalization shows potential for Level I damage detection when sensors are placed along the barrier walls and median. Level II damage detection (i.e., localization to some general areas) based on pattern recognition can potentially be implemented with some limitations. It is recognized that the patterns identified here may be unique to this particular bridge. However, this discussion does suggest that patterns of changes in specific VBDD parameters may be useful in categorizing small-scale damage.

8.4 VBDD USING CHANGE IN MODE SHAPE CURVATURE, CHANGE IN UNIFORM FLEXIBILITY CURVATURE AND DAMAGE INDEX

As described in Section 7.2, curvature-based VBDD parameters calculated using single line normalization did not exhibit any observable indication of damage along sensor lines located an appreciable distance from the damage location. However, 3-line normalization produced some observable changes along these more distant sensor lines. A comparison of the influence of normalization procedures on the curvature-based VBDD parameters is presented in 8.4.1. It was found that the damage index parameter did not exhibit any identifiable pattern associated with the location of damage. However, the other two methods exhibited some identifiable patterns that could be associated with the location of damage. Both the change in uniform flexibility curvature and change in mode shape curvature methods exhibited similar results. Therefore, to avoid repetition, only patterns identified for the change in mode shape curvature are presented in Section 8.4.2.

8.4.1 Influence of Normalization Procedure on the VBDD Parameter for Change in Mode Shape Curvature, Change in Uniform Flexibility Curvature and Damage Index

The influence of the two normalization procedures, as described in Section 6.2, on the change in mode shape curvature, change in uniform flexibility curvature and damage index parameters is discussed in this section. Parameter plots for these three methods using single line and 3-line normalization for Damage Case R10C9 are given in Figure 8-15. Highly irregular patterns were produced when single line normalization was used, although identification of those patterns and associating them with specific damage locations would be too speculative at this point. On the other hand, 3-line normalization produced some observable patterns in the change in mode shape

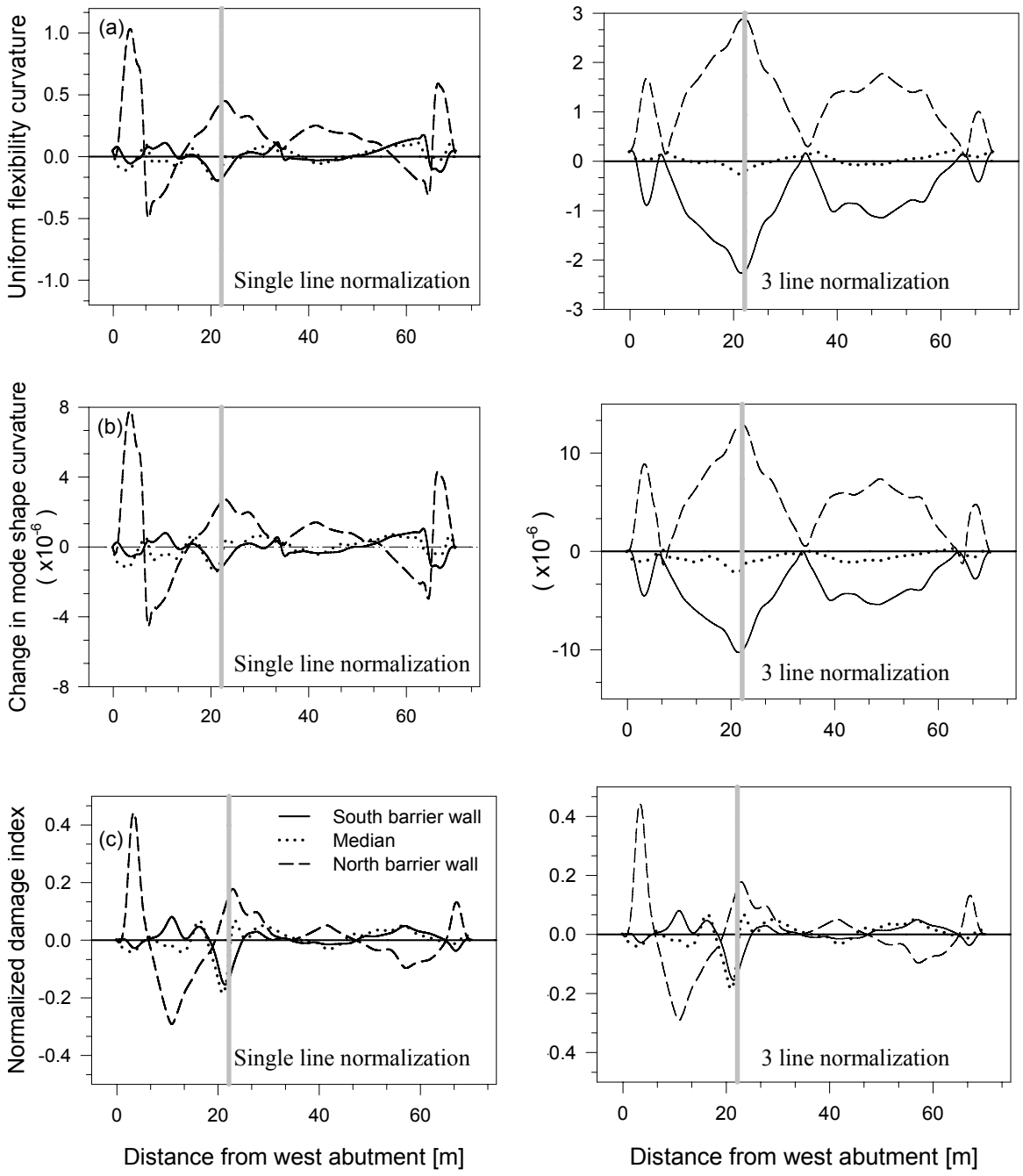

Figure 8-15. Comparison among the curvature- based VBDD parameters using both single and 3-line normalization for damage case R10C9: (a) change in uniform flexibility curvature; (b) change in mode shape curvature; and (c) damage index.

curvature and change in uniform flexibility curvature plots (Figure 8-15 (b) and (d)). Similar trends were also observed for all other damage cases. The damage index method

did not exhibit any distinctive indication of damage regardless of whether it was normalized by either single line or 3-line normalization procedure, unless a sensor line happened to be located close to the damage (Figure 8-15 (c) and (d)). Therefore, only results for the change in mode shape curvature are described in the subsequent discussion to illustrate the change in response patterns with damage location.

The changes in mode shape curvature calculated for damage cases R10C1, R10C9 and R16C9, using both single line and 3-line normalization, are presented in Figure 8-16. These plots illustrate the influence of the normalization procedure on the pattern of the VBDD parameter plot at different damage locations. As with all previous plots, the vertical shaded line represents the longitudinal extent of the damage.

The distributions of change in mode shape curvature using single line normalization along selected sensor lines are shown on the left side of Figure 8-16. Some general patterns can be identified when single line normalization was used; however, correlating these patterns with the general location of damage would be challenging at this point. The damage case that happened to be located in close proximity to a sensor line provided an unambiguous indication of the damage location (i.e., damage case R16C9 in Figure 8-16 (e)).

On the other hand, results obtained using 3-line normalization exhibited a general pattern along the barrier walls, featuring two unequal and uneven humps on each span, with the signs of the plot being the same on both spans. The general shape of plot was found to be relatively insensitive to the change of damage location. The distribution of change in mode shape curvature along the median did not exhibit any consistent pattern that could be used for damage identification at any level. Damage locations in

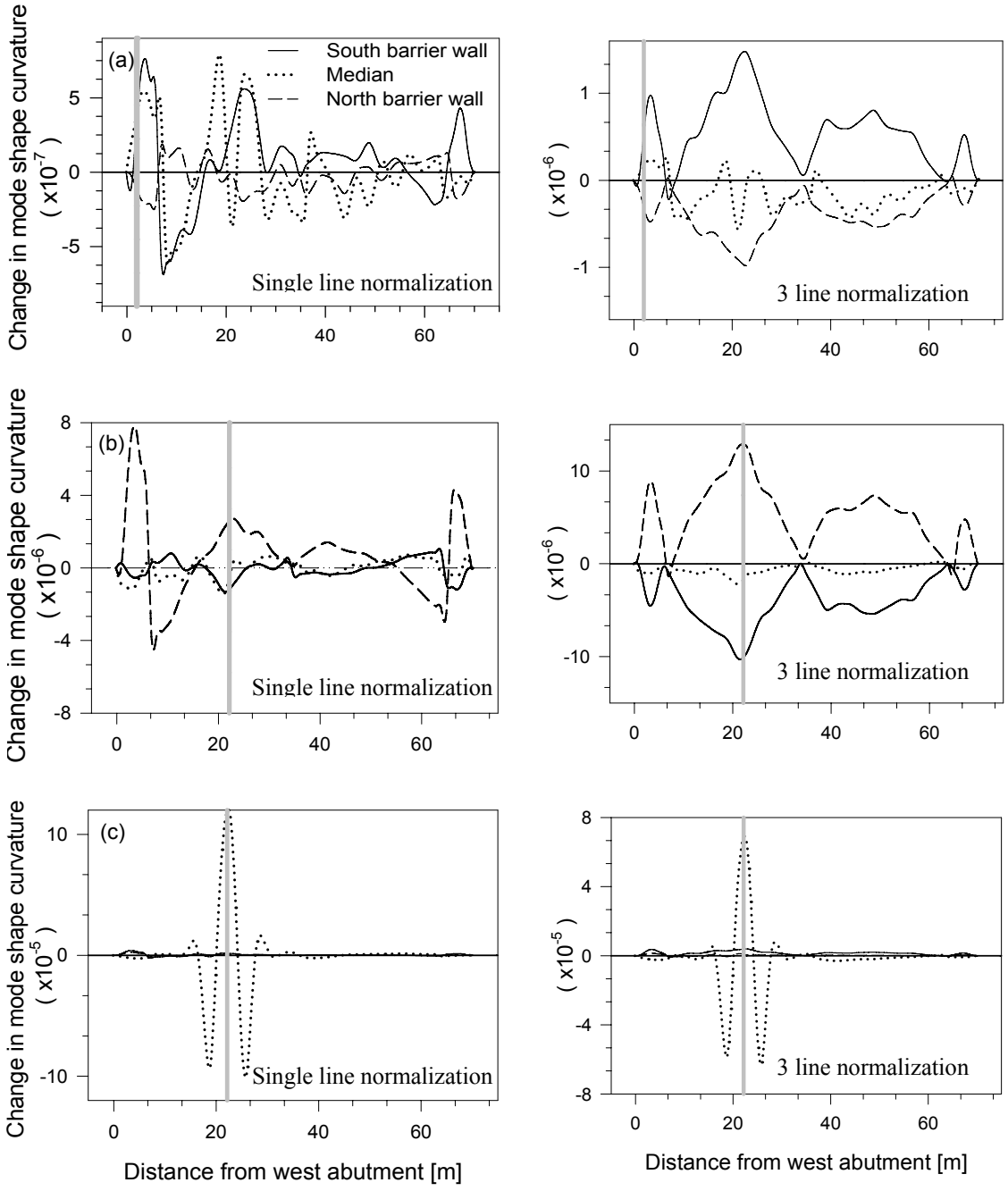

Figure 8-16. Comparison of VBDD parameter plot for change in mode shape curvature based on single line and 3-line normalization for: (a) damage case R10C1; (b) damage case R10C9; and (c) damage case R16C9.

close proximity to sensor lines did show an unambiguous indication of the presence and location of damage, as was the case for single line normalization. The potential of these patterns to localize damage is discussed in Section 8.4.2.

8.4.2 Patterns of VBDD Parameter Plot for Change in Mode Shape Curvature

In general, the plots for change in mode shape curvature along the barrier walls exhibited two unequal and uneven humps on each span. The sign of the plot varied as the damage location changed. A total of five patterns for change in mode shape curvature were identified for damage located on the south-west quadrant of the bridge deck. Distributions along the barrier walls, median and over the entire bridge deck for each pattern are given in Figure 8-17 and Figure 8-18.

Pattern I (Figure 8-17 (a)) featured positive and negative values along the south and north barrier walls, respectively. A spatial plot of Pattern I (Figure 8-17 (b)) exhibited very insignificant changes along the barrier walls; however, an enlarged plot along the barrier walls revealed the typical pattern illustrated in Figure 8-17 (a). The plot along the median for this pattern was difficult to identify with any certainty.

Pattern II (Figure 8-17 (c) and (d)) featured negative and positive values along the south and north barrier walls, respectively. The sign of plots in Pattern II were opposite to those in Pattern I.

In Pattern III, values for change in mode shape curvature were positive along the north barrier wall and negative along the median (Figure 8-17 e). In this pattern, the plot along the median had a number of peaks in the south span instead of a hump. The plot along the south barrier wall was found to be complex and inconsistent. As with Pattern I, an enlarged plot along the barrier walls revealed some potential patterns, even though

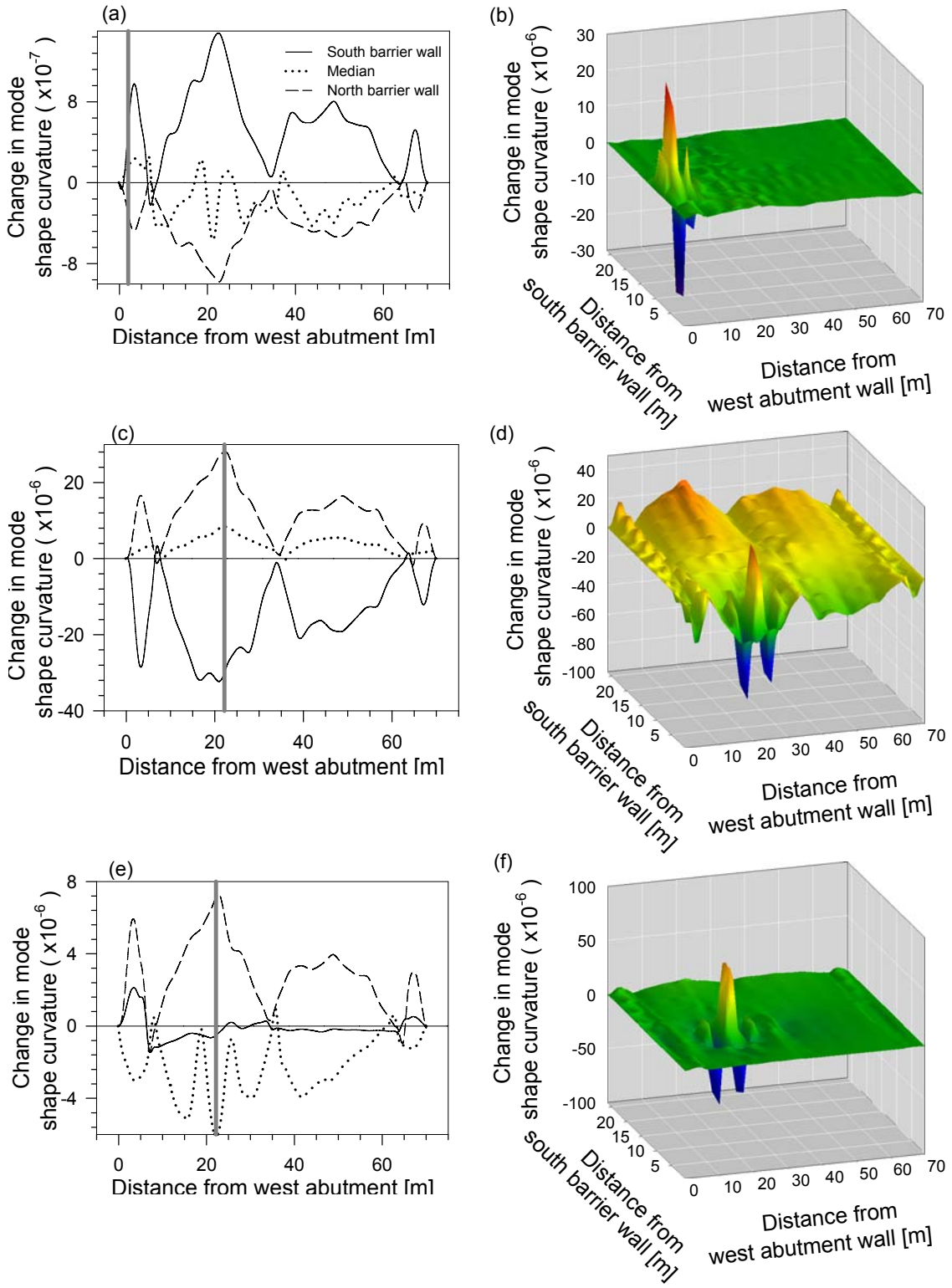

Figure 8-17. Longitudinal and spatial distributions of change in mode shape curvature based on 3-line normalization: (a, b) Pattern I for damage case R10C1; (c, d) Pattern II for damage case R4C9; and (e, f) Pattern III for damage case R13C9.

spatial plot did not show any significant changes along barrier walls in comparison to the region close to the damage location.

Pattern IV (Figure 8-18 (a)) featured a positive peak at the damage location, accompanied by an adjacent negative peak on each side. This was found to be a typical pattern for all curvature-based VBDD parameter plots along a sensor line close to the

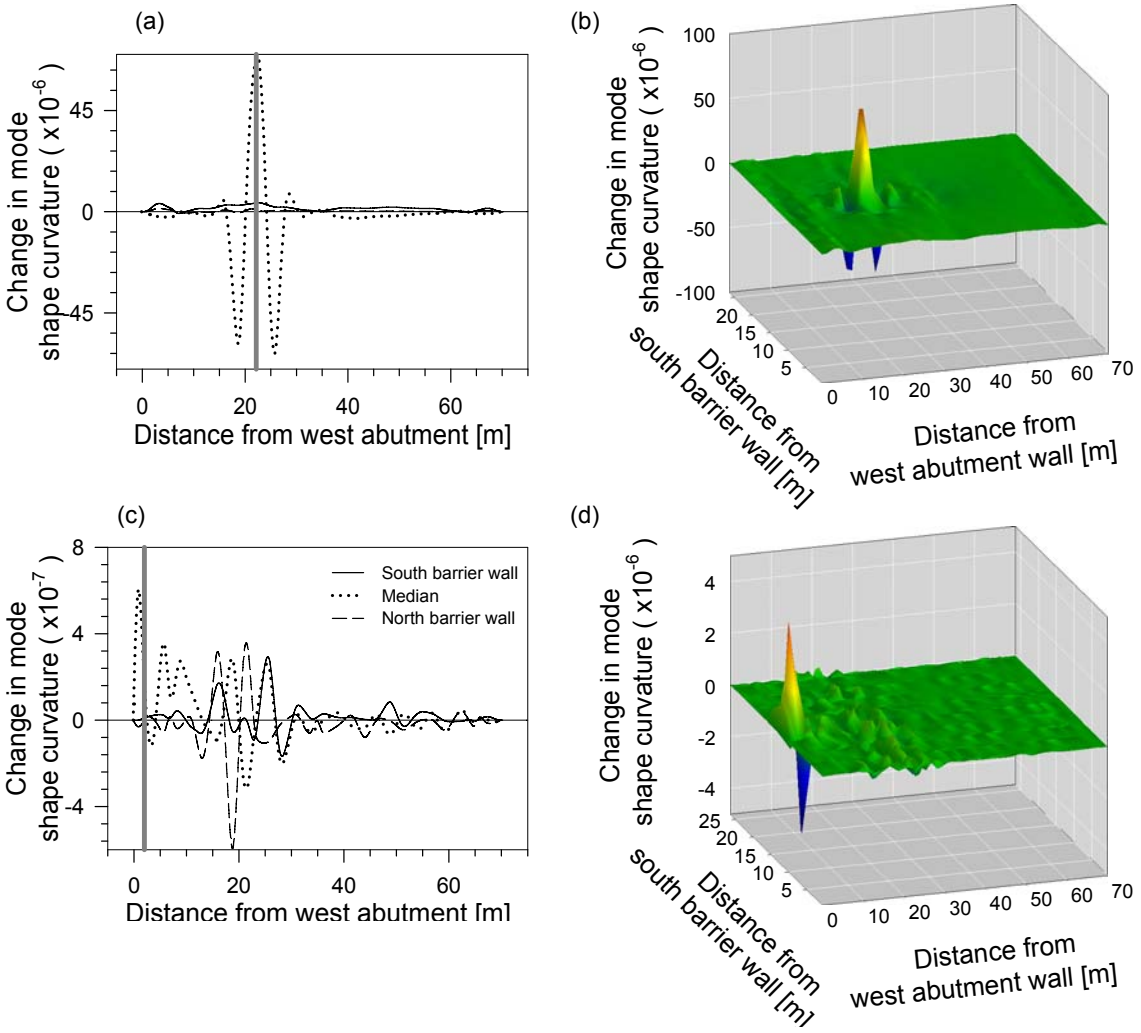

Figure 8-18. Longitudinal and spatial distributions of change in mode shape curvature based on 3-line normalization: (a) Pattern IV for damage case R16C9; and (b) Pattern V for damage case R14C1.

damage location. Pattern V (Figure 8-18 c) was characterized by random peaks along all of three sensor lines. This pattern was found to exist only for a few locations of damage.

All of these patterns were associated with some general damage locations on the bridge deck as shown in Figure 8-19. Each pattern was marked by a different colour in Figure 8-19. As seen in this figure, Pattern I was associated with a few locations in close proximity to either the west abutment wall or the pier support. On the other hand, Pattern II was associated with damage located in the midspan region of the south-west quadrant of the bridge deck. This pattern was appeared as the most dominant pattern on the south-west quadrant of bridge deck. Pattern IV was associated with the damage located in close proximity to either the south barrier wall or the median. The characteristic peaks at the location of damage could appear on any of these two sensor lines depending on which sensor line was close to the damage location. Pattern III was associated with a general area located adjacent to that associated with Pattern II and on

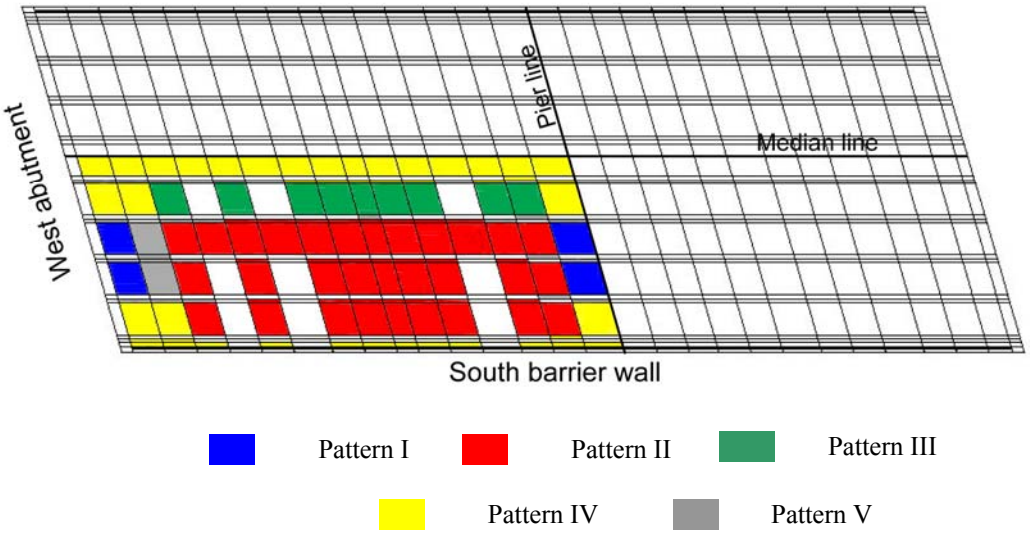

Figure 8-19. Plan view of the bridge deck showing damage locations corresponding to identified patterns of the change in mode shape curvature parameter.

the south side of the median. Pattern V is associated with a small area next to that for Pattern I and close to the west abutment wall.

In summary, the change in mode shape curvature exhibited some promise for Level I damage detection, with some limitations. Different patterns (unique to this particular bridge) associated with some general locations on the bridge deck suggested that pattern recognition could be a potential means for Level II damage detection. It should be noted, though, that pattern recognition in the presence of measurement uncertainty may be difficult using this VBDD parameter, given the low magnitudes often observed.

8.5 INFLUENCE OF UNCERTAINTY USING A SMALL NUMBER OF SENSORS

To ascertain the influence of measurement uncertainty on the performance of the VBDD methods when sensor placement is restricted to the barrier walls and median, simulated random noise was superimposed on the numerically generated eigenvector results in a manner similar to that described in Section 7.5, and at a similar magnitude.

Averaged plots of change in mode shape curvature and change in uniform flexibility curvature using 5000 repeated trials are presented in Figure 8-20. It is quite challenging to identify the presence of any damage using these noise modified plots. Since the averaging of 5000 repeated trials did not help to attenuate the effects of uncertainty for the change in mode shape curvature or change in uniform flexibility curvature methods, results for only the change in mode shape and change in flexibility methods are discussed in the following sections. As with Section 7.5, only damage case R10C9 is included here, as results for this case are considered sufficient to illustrate the

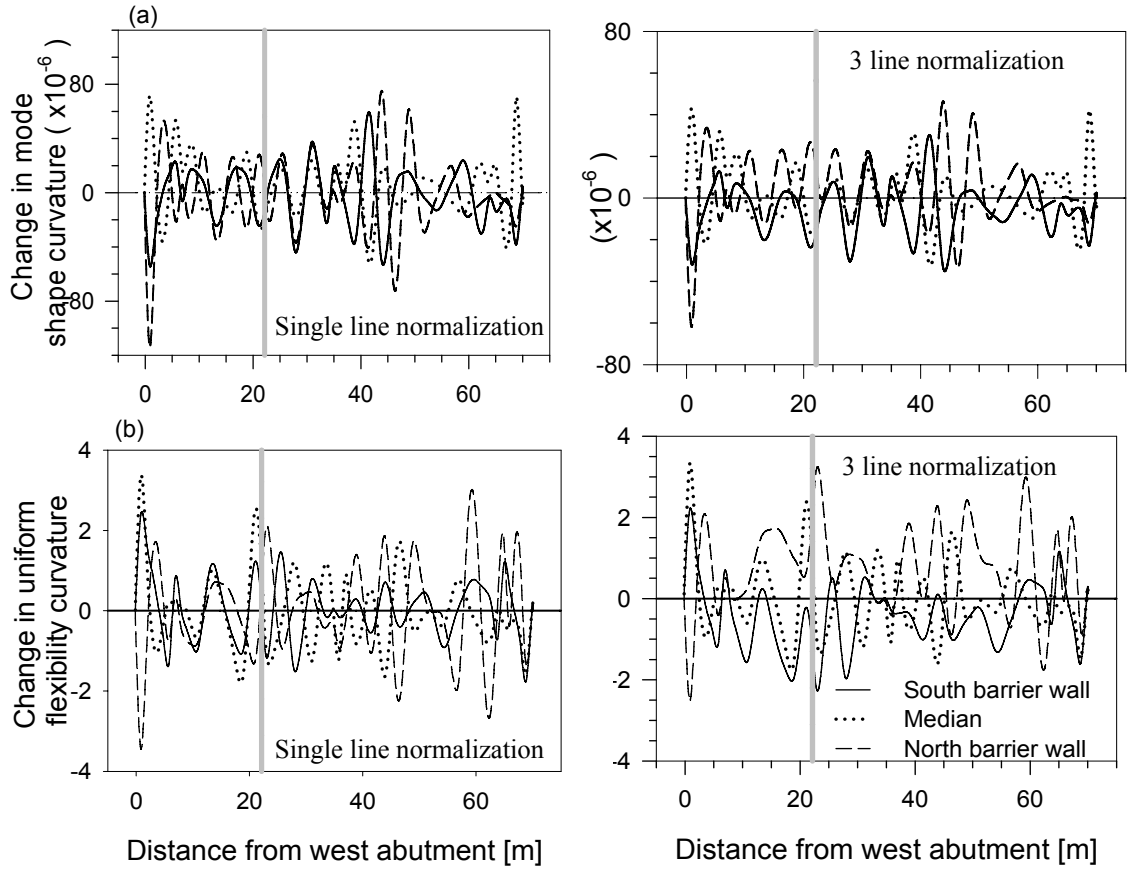

Figure 8-20. Effects of simulated measurement uncertainty using averaged plots for 5000 trials for damage case R10C9: (a) change in mode shape curvature; and (b) change in uniform flexibility curvature.

salient features.

Comparisons of single line and 3-line normalization results using the change in mode shape method are shown in Figure 8-21, based on the averaged results of 25, 100 and 500 random trials. For comparison, the corresponding plots without measurement uncertainty are reproduced in Figure 8-22. Mode shape changes resulting from the damage are completely masked by the measurement noise when the single line normalization approach is used, even for the case considering averaged results from 500 random trials. On the other hand, the underlying changes in mode shape patterns using

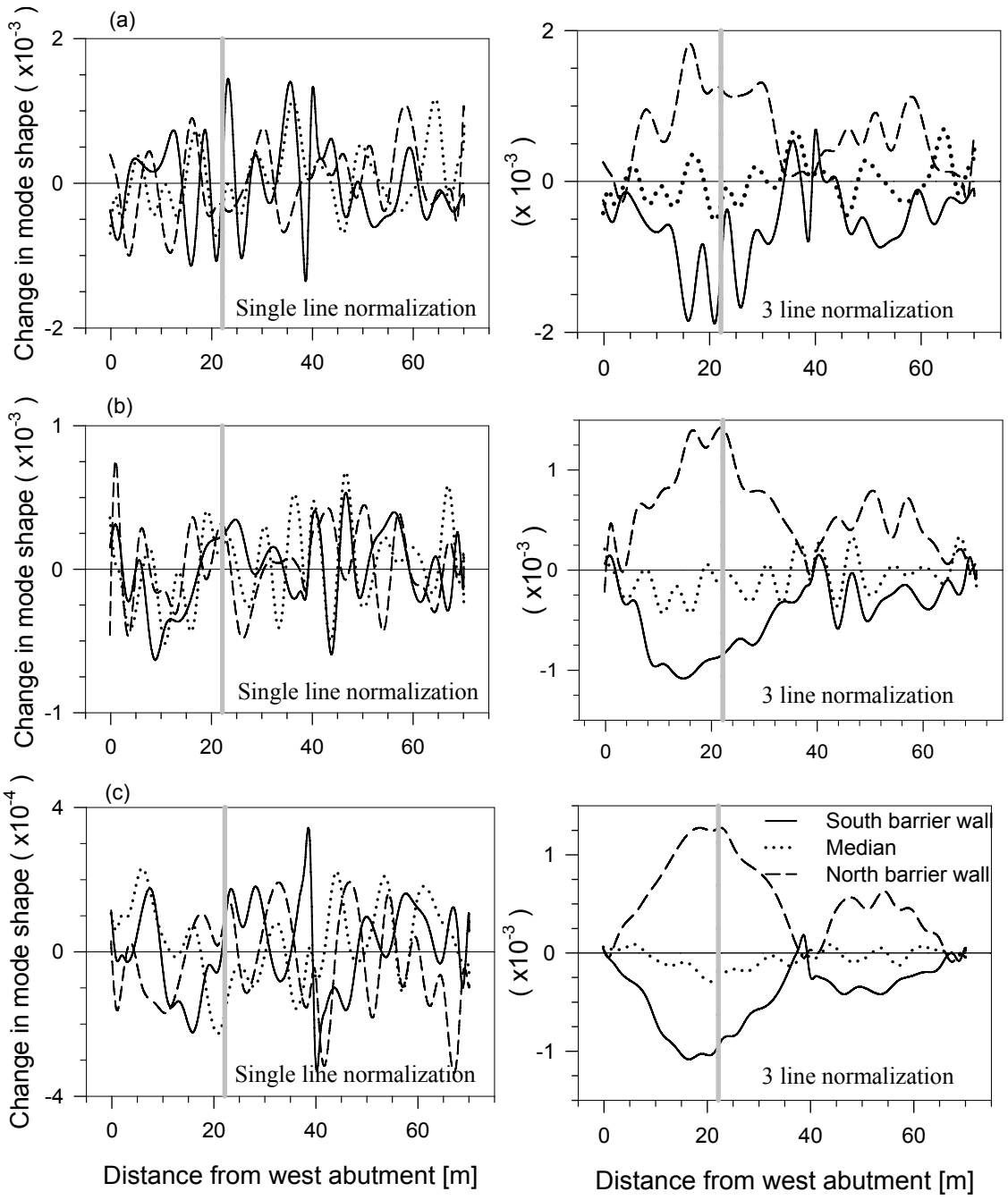

Figure 8-21. Averaged change in mode shape for damage case R10C9 in the presence of random measurement noise: (a) 25 trials; (b) 100 trials; and (c) 500 trials.

3-line normalization results are evident using averaged data from as few as 25 random trials, and are well established in the averaged results from 100 or 500 random trials.

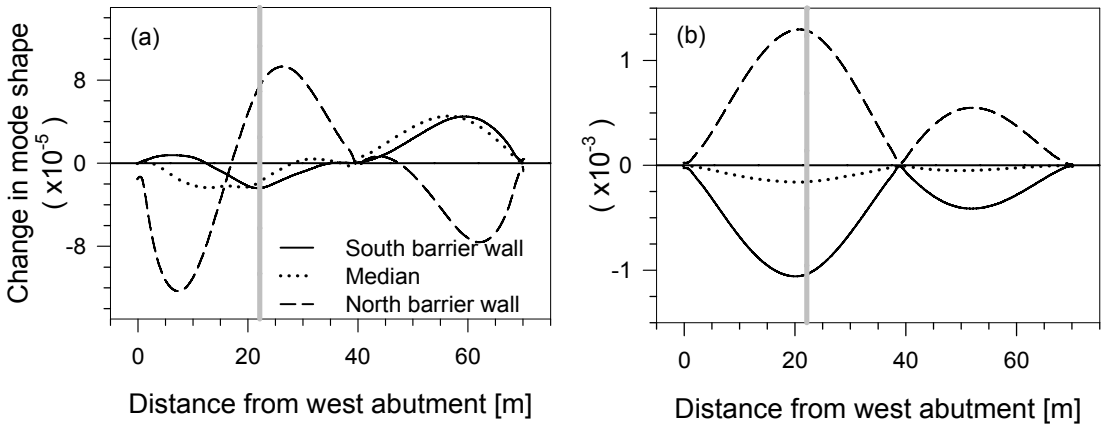

Figure 8-22. Change in mode shape for damage case R10C9 without measurement uncertainty: (a) single line normalization; and (b) 3-line normalization.

Averaged plots for change in flexibility for 25, 100 and 500 trials using both single line and 3-line normalization are presented in Figure 8-23. For comparison, the corresponding plots without the influence of uncertainty are given in Figure 8-24. For change in flexibility method, both single line and 3-line normalization allow the underlying patterns to become apparent, using averaged data from as few as 25 trials. Once again, the 3-line normalization approach is more effective than single line normalization in revealing the underlying pattern. In general, change in flexibility results were found to be robust in detecting damage when field uncertainty was incorporated into the mode shapes.

In order to determine whether the presence of uncertainty could lead to false positive indications of damage (i.e., the conclusion that damage is present when, in fact, it is not), random noise was superimposed on the undamaged mode shape. The average of 500 repeated trials was then used to calculate the change in mode shape and change in flexibility parameters. The baseline mode shape used for comparison was the eigenvector without any superimposed noise.

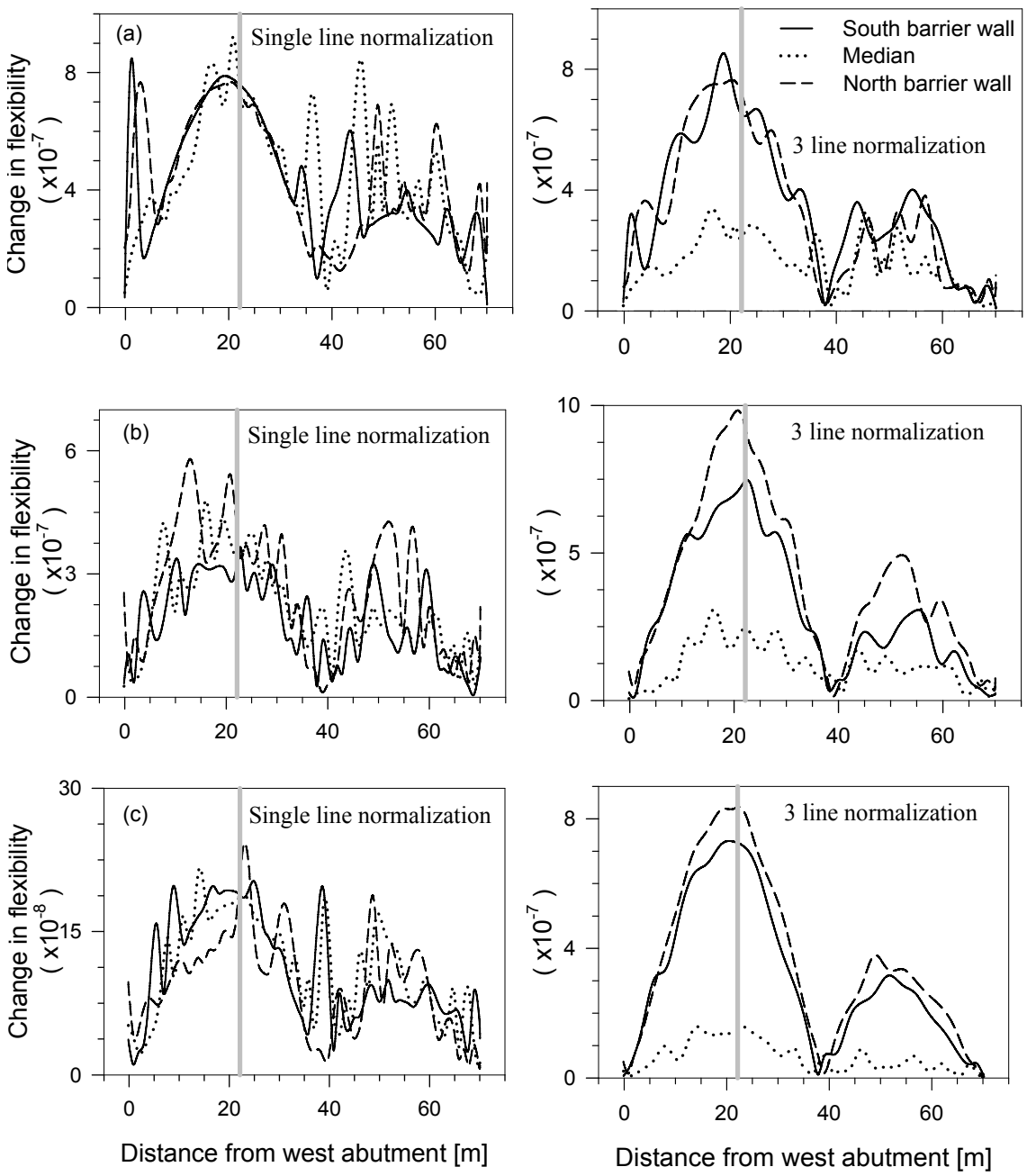

Figure 8-23. Averaged VBDD parameter plot for change in flexibility for damage case R10C9 in the presence of random measurement noise: (a) 25 trials; (b) 100 trials; and (c) 500 trials.

Figure 8-25 shows the resulting distributions. The change in mode shape (Figure 8-25 (c)) did not exhibit a discernable pattern in the distributions for a spurious damage case, so that a false positive result was unlikely in this case. Only 3-line normalization

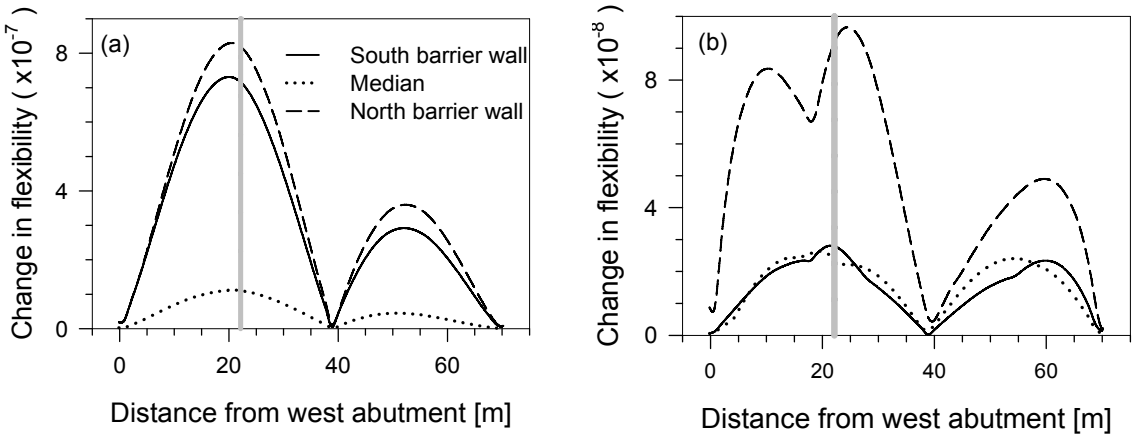

Figure 8-24. VBDD parameter plot for change in flexibility for damage case R10C9 without measurement uncertainty: (a) single line normalization (b) 3-line normalization.

for change in mode shape is presented here since both the single line and 3-line normalization exhibited similar results. However, the change in flexibility method results did imply an apparent pattern similar to those seen for actual damage cases, which could lead to the false conclusion that damage was present.

It is evident from the above discussion that the change in mode shape can potentially be used for Level I damage detection using a limited number of sensors, even with superimposed measurement uncertainty. In addition, the change in mode shape does not appear prone to providing false positive results when field measurement uncertainty is incorporated.

On the other hand, the change in flexibility method also provided promising indications of Level I damage detection while limited sensors were used, but also appeared to be prone to false positive results caused by measurement uncertainty. It was shown that flexibility change patterns apparently typical of damaged states were observed even for undamaged conditions when uncertainty was present. Measurement uncertainty was found to complicate the interpretation of flexibility changes for the purpose of damage detection, even though the method seems to be very promising for

detecting actual damage using as few as 25 trials. However, averaging as many as 500 trials using 3-line normalization (Figure 8-23 (c)) produced a smoother plot when actual damage was present that may help to distinguish the pattern related to a real damage case from that of a spurious damage case, which exhibited a very irregular plot even for 500 averaged trials (Figure 8-25 (b)).

Meaningful interpretations of VBDD results are, therefore, contingent upon ensuring that the magnitude of the mode shape change is sufficiently larger than the

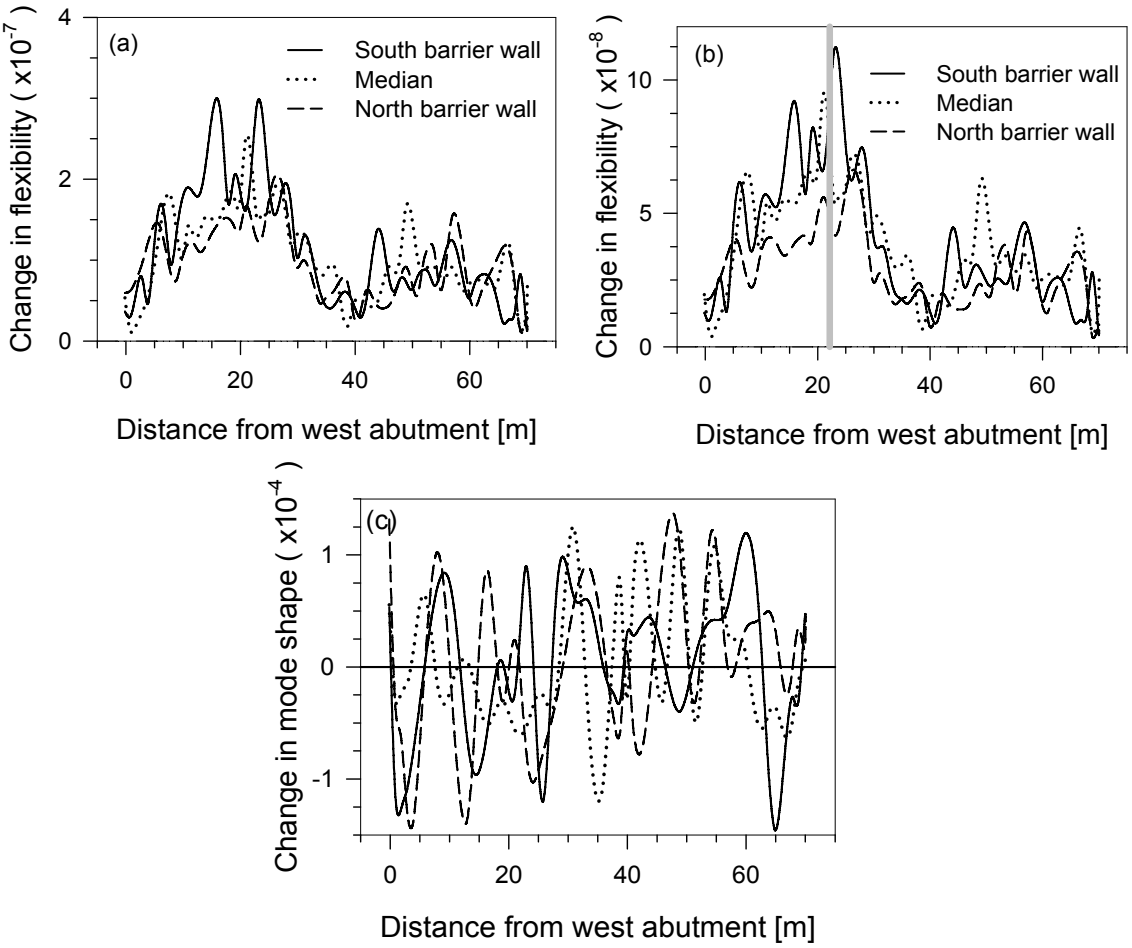

Figure 8-25. Averaged VBDD parameter plots of 500 trials for a spurious damage case for: a) change in flexibility using single line normalization ;b) change in flexibility using 3-line normalization; and c) change in mode shape using 3-line normalization.

level of noise caused by measurement uncertainty. Since all of the VBDD parameters considered in this study are based, in some manner, upon mode shapes, mode shape extraction with an adequate accuracy is an a priori requirement for all VBDD methods. Since the 3-line normalization procedure in this study generated significantly higher change in mode shape values than the single line approach, it was found to provide a more robust indication of the presence of damage (Level I detection) in the presence of measurement uncertainty. This enhanced reliability of Level I damage detection, though, was achieved at the cost of a loss in sensitivity with regard to localization of the damage (Level II detection). It may be surmised, therefore, that the appropriate mode shape normalization procedure will depend upon the objectives of the structural assessment (Level I or II), as well as on other factors, including the level of uncertainty in the mode shape measurements and the density of the sensor grid. Furthermore, the normalization method may well have to be varied depending on the stage of the assessment, changing from a broader-based normalization at the initial stage to ascertain the existence of damage to a more local normalization during more intensive investigations to localize the damage.

CHAPTER 9. CONCLUSIONS AND RECOMMENDATIONS

9.1 CONCLUSIONS

This thesis has presented the results of a study to investigate a number of issues related to the potential use of vibration-based damage detection (VBDD) algorithms to detect small-scale damage on the deck of an integral abutment bridge in Saskatoon, Canada, using both field data and a calibrated finite element model. In general, it was found that, conceptually, any of the five VBDD methods considered could successfully detect and locate localised deterioration in the top concrete cover of the deck, subject to a number of significant limitations. However, significant challenges remain regarding the practical application of these methods to full-scale structures in the field. More specific findings of the study are listed below.

The first three natural frequencies and mode shapes of the Attridge Drive Overpass were identified in four temperature ranges (-12°C to -5°C, -9°C to -7°C, 20°C to 26°C and 30°C to 40°C). The mode shapes and natural frequencies in the temperature range of 20°C to 26°C were used as baseline dynamic properties to calibrate the finite element model.

The lowest three measured natural frequencies of the bridge decreased by 8.3% to 12.84% as the ambient temperature increased from -12°C to 40°C. Corresponding changes due to damage, as determined numerically, were much lower (in the order of 10^{-4} Hz), suggesting that natural frequencies are not a sufficiently sensitive indicator of small-scale damage in the presence of ambient temperature variations.

Mode shapes for first three modes, measured experimentally, were found to be apparently insensitive to temperature changes. Averaged mode shapes measured at different temperatures were compared using the Modal Assurance Criteria (MAC); MAC values comparing mode shapes obtained at different temperatures varied from 0.987 to 0.998, indicating that measured mode shapes were very similar for all temperature ranges. Despite the MAC comparisons, however, some small changes in the first three mode shapes due to changes of ambient temperature were noted based on visual examinations; an alternative approach was therefore used to identify those changes.

Another important aspect for VBDD reliability is the uncertainty in measured mode shapes. Uncertainty, as represented by the coefficient of variation of modal amplitudes, was found to vary from 0.839% to 30.2%, with a mean value of 11% for the first mode shape, using all available data throughout a temperature range of -12°C to 40°C. Coefficient of variation of the second and third mode shapes varied from 0.16% to 32.8%.

The normalization procedure used to scale mode shapes had a significant influence on the resulting VBDD parameter distributions. Unit-norm normalization was found to be near optimal in terms of making the damaged and undamaged mode shapes as similar as possible in an averaged sense. The percent relative difference (PRD) value, an index used to compare unit-norm normalization with the optimal normalization, varied from 0.0012% to 0.4%, depending upon the amount of data in the subset considered in normalization and the orientation of sensor lines considered for the subset. It was found that unit-norm normalization using a subset of numerical data along an

individual longitudinal sensor line spanning the entire bridge length (single line normalization), produced the most discernible indication of damage location in the VBDD parameters distributions, provided that the damage case was in close proximity to the sensor line. Single line normalization was found to reduce the average differences between mode shapes derived from damaged and pristine conditions to a minimum level (percent relative difference value 0.00126%), thereby highlighting small differences and increasing the precision of Level II damage localization. On the other hand, 3-line normalization (percent relative difference value 0.35%), which included all available data along three selected longitudinal lines (two barrier walls and the median) when performing unit-norm normalization, did not reduce the average mode shape differences to the same degree as single line normalization, resulting in a reduction in the precision of Level II damage detection. However, 3-line normalization proved to be beneficial when uncertainty in the measurements was considered.

All five VBDD methods considered in this study could successfully locate small-scale damage as long as a sufficiently dense grid (a 3m x 3m grid) of sensors was used to measure the mode shapes and simulated measurements were error free. The reliability of the predicted damage location tended to improve if more than one method was applied, as the relative accuracy of the various VBDD methods varied for damage located in different regions of the bridge deck. The precision of damage localization was also found to depend on sensor spacing. A minimum longitudinal sensor spacing of 3 m proved to be sufficient to successfully locate small scale damage, while a sensor spacing of 7.5 m made the VBDD parameters incapable of locating small scale damage.

Increasing sensor spacing was found to make the VBDD parameters less precise, especially in locating damage close to support region.

At an intuitive level, the VBDD parameters seem to be more reliable at detecting and locating damage as the damage size increases. However, the aspect ratio of the damage, as well as the orientation of a rectangular damage area relative to the sensor line, had an influence on the performance of the VBDD parameters. It was found that a slender rectangular-shaped damage area would be located less precisely than a square shaped damage area, when the longer dimension was aligned with the sensor line. VBDD parameters appeared to produce ambiguous results when a 13.5 m long damage case was used; such large-scale deterioration, though, would likely be visually noticeable without the need for VBDD. However, more detailed study is required to explore the effects of plan aspect ratio of damage on VBDD parameters.

This study revealed that the distribution and magnitude of different damage detection parameters varied with damage size and location. This variation presumably increases as the complexity of the structural system increases.

With the introduction of uncertainty into the measured mode shapes, the averaged results from numerous (up to 5,000) repeated trials were required to distinguish actual damage from spurious peaks in the VBDD parameter plots. Since the number of required trials was proportional to the level of uncertainty in the measured mode shapes, using well-controlled excitation sources (for example, forced harmonic vibration rather than random traffic excitation) may greatly facilitate VBDD efforts, although such excitation was not considered in the present study.

Damage detection using a smaller number of sensors placed along the barrier walls and median (so as not to interfere with traffic flow) was shown to be possible if a 3-line normalization technique, including data from all three sensor lines, was used during unit-norm normalization. Under these conditions, the change in mode shape, change in mode shape curvature, change in flexibility methods and change in uniform flexibility curvature appeared to offer the greatest potential for detecting the presence of damage (Level I damage detection) and the location of damage (Level II damage detection) in a general sense, since these showed significant values even in regions far from the damage location. Damage index parameters were not able to identify the presence of damage when a small number of sensors was used, unless the damage happened to be located near one of the sensor lines.

When uncertainty was introduced, while sensor placement was limited, the method of normalization was found to become very important. Patterns indicating the presence of damage were completely masked when single line normalization was used, but became apparent when 3-line normalization was used in conjunction with the average of repeated trials. As few as 25 repeated trials were required for the underlying patterns to become apparent. The change in flexibility was found to be prone to producing false positive results when a small number of trials were used for averaging, even though the change in flexibility appeared to be a robust method when a dense grid of sensors was used. The distribution of change in flexibility using 3-line normalization was free from unevenness (peaks about an underlying pattern or ragged pattern) when damage was actually present, provided a sufficient number of trials were used to

attenuate the uncertainty. This was not the case when false positive conditions were encountered, presenting a possible method of eliminating false positive results.

9.2 SCOPE OF FUTURE RESEARCH

Further field study is required to investigate the temperature effects on the Attridge Drive Overpass, notably around the freezing point (0°C). Instead of measuring air temperature, thermocouples could be used to understand the correlation between specific structural responses and the actual structure's temperature. This would also help to accurately consider temperature changes using finite element modelling to understand the underlying mechanisms.

This study was mainly focused on single damage states. Multiple damage states could also be investigated to see if the detection methods are as successful in these cases.

Forced excitation can be tried both numerically and experimentally to investigate whether forced harmonic excitation yields lower levels of error in experimentally measured mode shapes.

An experimental study should be performed using a real structure to investigate the effects of the normalization procedure on VBDD parameters.

Future research should focus on the use of automated pattern recognition to provide more objective and accurate correlation between VBDD parameters and damage location. Neural networks, for example, could possibly be used to detect, localize and quantify the damage using these patterns, potentially permitting Level III damage detection. Data required to train the network could be generated from calibrated finite element models for damage of different sizes, states and at different locations.

REFERENCES

ADINA 2002. ADINA Version 7.5, ADINA R&D, Inc., Watertown, MA

Alampalli, S. 1998. Influence of in-service environment on modal parameters. Proceedings of the IMAC 16 conference, Santa Barbara, California, February 1998, pp 111–116.

Askegaard, V., and Mossing, P. 1988. Long term observations of RC-bridge using changes in natural frequency. Nordic Concrete Research, **7**: 20–27.

Bakht, B. and Csagoly, P.F. 1980. Diagnostic testing of a bridge. Journal of the Structural Division, ASCE, **106**(7): 1515-1529.

Beck, J.L., and Katafygiotis, L.S. 1992a. Probabilistic system identification and health monitoring of structures. Proceedings of the 10th World Conference on Earthquake Engineering, Madrid, Spain, 19-24 July 1992. Sponsored by International Association for Earthquake Engineering. A.A. Balkema, Rotterdam, The Netherlands. pp. 3721-3726.

Beck, J.L., and Katafygiotis, L.S. 1992b. Updating dynamic models and their associated uncertainties for structural systems. Proceedings of the 9th ASCE Conference on Engineering mechanics, College Station, Tex., 24-27 May 1992. Edited by L.D. Lutes and J.M. Niedzsecki. American Society of Civil Engineers, New York. pp-681-684.

Begg, R.D., Mackenzie, A.C., Dodds, C.J., and Loland, O. 1976. Structural integrity monitoring using digital processing of vibration signals. Proceedings of the 8th Annual Offshore Technology Conference, Houston, TX, 305-311.

Bendat, J.S. and Piersol, A.G. 1993. Engineering Applications of Correlation and Spectral Analysis. 2nd edition, John Wiley & Sons, New York, NY

Biswas, M., Pandey, A.K., and Samman, M.M. 1990. Diagnostic experimental spectral/ modal analysis of a highway bridge. Modal Analysis: The International Journal of Analytical and Experimental Modal Analysis, **5**: 33–42.

Brincker, R., Zhang, L., and Andersen, P. 2001. Modal identification of output-only systems using frequency domain decomposition. Smart Materials and Structures, **10**:441–445.

Brownlee, K. 2007. Many municipal bridges not inspected: SARM. The StarPhoenix, August 14, Saskatoon, SK, pp. A7.

CAC 2006. Concrete Design Hand Book. Cement Association of Canada, Ottawa, ON.

Casas, J.R., and Aparicio, A.C. 1994. Structural damage identification from dynamic-test data. Journal of Structural Engineering, ASCE, **120**(8): 2437-2450.

Catbas, F.N. and Aktan, A.E. 2002. Condition and damage assessment: Issues and some promising indices. Journal of Structural Engineering, ASCE, 128(8): 1026-1036.

Cawley, P., and Adams, R.D. 1979. The location of defects in structures from measurements of natural frequencies. Journal of Strain Analysis, **14**(2): 49-57.

Choi, M.Y., and Kwon, I.B. 2000. Damage detection system of a real steel truss bridge by neural networks. Smart structures and materials 2000: Smart Systems for bridges, Structures, and highways, Proceedings of SPIE, 3(988), Newport Beach, California, pp. 295–306.

Clough, R. W., & Penzien, J. 1975. Dynamics of Structures. McGraw Hill, New York.

Doebling, S. W., Farrar, C. R., and Prime, M. B. 1998. A summary review of vibration-based damage identification methods. The Shock and Vibration Digest, **30**(2): 91-105.

Doebling, S.W., Farrar, C.R., Prime, M.B., and Shevitz, D.W. 1996. Damage identification and health monitoring of structural and mechanical systems from changes in their vibration characteristics: A literature review, Report No. LA 13070-MS, Los Alamos National Laboratory, Los Alamos, NM.

Doebling, S.W., Farrar,C.R., and Cornwall, P.J. 1997. Diamond: A graphical user interface toolbox for comparative modal analysis and damage identification. Proceedings of the 6th International Conference on Recent Advances in Structural Dynamics, Southampton, UK, July 1997, pp-399-412.

Duggan, D.M., Wallace,E.R., and Caldwell, S.R. 1980. Measured and predicted vibrational behaviour of Gulf of Mexico platforms. Proceedings of the 12th Annual Offshore Technology Conference, 92-100.

Ewins, D.J. 2000. Modal testing: Theory, Practice and Application, 2nd ed. Research Studies Press Ltd., Hertfordshire, England.

Farrar, C. R., and Doebling, S. W. 1997. An overview of modal-based damage identification methods. EUROMECH 365 international workshop: DAMAS 97, Structural Damage Assessment Using Advanced Signal Processing Procedures, Sheffield, U.K

Farrar, C. R., Doebling, S. W., Cornwell, P. J., and Straser, E. G. 1997. Variability of modal parameters measured on the Alamosa Canyon Bridge. Proceedings of the

IMAC 15 Conference, Orlando, FL, February 1997, pp 257–263.

Farrar, C.R, Baker, W.E., Bell, T.M., Cone, K.M., Darling, T.W., Duffey, T.A., Eklund, A., and Migliori, A. 1994. Dynamic characterization and damage detection in the I-40 bridge over the Rio Grande, Rep. No. LA 12767-MS, Los Alamos National Laboratory, Los Alamos, NM.

Farrar, C.R. and Doebling, S.W. 1999. Damage detection II: field applications to large structures in modal analysis and Testing, J. M. M. Silva and N. M. M. Maia, edts., Nato Science Series, Kluwer Academic Publishers, Dordrecht, Netherlands.

Farrar, C.R. and Duffey, T.A. 1999. Vibration-based damage detection in rotating machinery. Key Engineering Materials, **167-168**: 224-235.

Felber, A. J. 1993. Development of a hybrid bridge evaluation system. Ph. D. Thesis, Department of Civil Engineering, University of British Columbia, B.C., Canada.

FHWA 2001. Reliability of visual inspection. Federal Highway Administration, Report. Nos. FHWA-RD-01-020 and FHWA-RD-01-021, Washington, DC.

Fox, C.H.J. 1992. The location of defects in structures: a comparison of the use of natural frequency and mode shape data. Proceedings of the 10th International Modal Analysis Conference, San Diego, California, 3-7 February1992. Society for Experimental Mechanics, Bethel, Conn, pp.522-528.

Galvín, P., and Domínguez, J. 2007. Dynamic analysis of a cable-stayed deck steel arch bridge. Journal of Constructional Steel Research, **63**:1024-1035.

Grygier, M.S., Gaspar, J., West, W., and Wilson, B. 1994. SMIS analysis report. Report No. OV-102 Control Surfaces, Johnson Space Center Test Branch Report.

Hajela, P., and Soeiro, F.J. 1990. Recent developments in damage detection based on system identification methods. Structural Optimization, **2**(1): 1-10.

Hu, N., Wang, X., Fukunaga, H., Yao, Z.H., Zhang, H.X., and Wu, Z.S. 2001. Damage assessment of structures using modal test data. International Journal of Solids and Structures, **38**(18):3111-3126.

Humar, J. L. 1990. Linearized eigenvalue problem and its properties. Dynamics of Structure, Princeton-Hall, Inc. Englewood Cliffs, New Jersey 07632, Chapter. 10,422-424.

Hunt, D.L., Weiss, S.P., West, W.M., Dunlap, T.A., and Freemeyer, S.R. 1990. Development and implementation of a shuttle modal inspection system. Sound and Vibration, **24**(8): 34-42.

Jauregui, D.V. and Farrar, C.R. 1996. Comparison of damage identification algorithms on experimental modal data from a bridge. Proceedings of the 14th International Modal Analysis Conference, Society of Experimental Mechanics, Bethel, CT, pp. 1423-1429.

Jenkins, C.H., Kjerengtroen, L., and Oestensen, H. 1997. Sensitivity of parameter changes in structural damage detection. Shock and Vibration, **4**(1): 27-37.

Kenley, R.M., and Dodds, C.J. 1980. West soles WE platform: Detection of damage by structural response measurements. Proceedings of the 12th Annual Offshore Technology Conference, 111-118.

Kim, J.T. and Stubbs, N. 2003. Nondestructive crack detection algorithm for full-scale bridges. Journal of Structural Engineering, ASCE, **129**(10): 1358-1366.

Kim, J.T., and Stubbs, N. 1995. Model uncertainty impact and damage detection accuracy in plate girder. Journal of Structural Engineering, ASCE, **121**(10): 1409-1417.

Kim, J.T., Park, J.H., and Lee, B.J. 2007. Vibration-based damage monitoring in model plate-girder bridges under certain temperature conditions. Engineering Structures, **29**:1354-1365.

Kim, K., and Paik, S.H. 1997. Optical fibre monitoring system of bridges in Korea. Structural Health Monitoring: Current Status and Perspectives, Stanford University, Palo Alto, California, pp. 555–563.

Kobayashi A. S. 1993. Non-destructive evaluation. Hand book on Experimental Mechanics, VCH, New York, N.Y., and SEM, Bethel, CT, USA.

LabView. 2000. LabView™, version 6i, National Instruments Corporation, Austin, Tex.

Loland, O., and Dodds, J.C. 1976. Experience in developing and operating integrity monitoring system in the North Sea. Proceedings of the 8th Annual Offshore Technology Conference, 313-319.

Maeck, J., and De Roeck, G. 1999. Damage detection on a prestressed concrete bridge and RC beams using dynamic system identification. Proceedings of the International Conference on Damage Assessment of Structures (DAMAS 99), Dublin, Ireland, pp. 320–327.

Masri, S.F., Nakamura, M., Chassiakos, A.G., and Caughey, T.K. 1996. Neural network approach to detection of changes in structural parameters. Journal of Engineering Mechanics, ASCE, **122**(4): 350-360.

MATLAB® 7.0.1, The MathWorks, Inc. Natick MA

Mirza, M. S., and Haider, M. 2003. The state of infrastructure in Canada: Implications for infrastructure planning and policy. Infrastructure Canada Report.

Nataraja, R. 1983. Structural integrity monitoring in real seas. Proceedings of the 15th Annual Offshore Technology Conference, 221-228.

Ni, Y.Q., Hua, X.G., Fan, K.Q., and Ko, J.M. 2005. Correlating modal properties with temperature using ling-term monitoring data and support vector machine technique. Engineering Structures, **27**: 1762-1773.

Pandey, A.K. and Biswas, M. 1994. Damage detection in structures using changes in flexibility. Journal of Sound and Vibration, **169**(1): 3-17.

Pandey, A.K., Biswas, M., and Samman, M.M. 1991. Damage detection from changes in curvature mode shapes. Journal of Sound and Vibration, **145**(2): 321-332.

Pearson, S.R., Owen, J.S., and Choo, B.S. 2001. The use of vibration signatures to detect flexural cracking in reinforced concrete bridge decks. Key Engineering Materials, **204-205**, pp. 17-26.

Peeters, B. 2000. System identification and damage detection in civil engineering. Ph.D. thesis, Department of Civil Engineering, Katholieke Universiteit, Leuven, Belgium

Peeters, B. and De Roeck, G. 2000. Reference based stochastic subspace identification in civil engineering. Inverse Problems in Engineering, **8**(1): 47-74

Peeters, B., Maeck, J. and Roeck G. D. 2001. Vibration-based damage detection in civil engineering: excitation sources and temperature effects. Smart Materials and

Structures, **10**: 518–527.

Peeters, J.M.B., Maeck, J., and De Roeck, G. 2000. Excitation sources and dynamic system identification in Civil Engineering. Proceedings of the European COST F3 Conference on System Identification and Structural Health Monitoring, Madrid, Spain, pp. 341–350.

Phares, B. M., Wipf, T. J., Greimann, L. F., and Lee, Y.S. 2005. Health monitoring of bridge structures and components using smart-structure technology volume 1. Wisconsin Highway Research Program Report No. 0092-04-14, Wisconsin Department of Transportation, Madison, Wisconsin.

Poudel, U.P., Fu, G., and Ye, J. 2005. Structural damage detection using digital video imaging technique and wavelet transformation. Journal of Sound and Vibration, **286**(2005):869-895.

Ramirez, R. 1985. The FFT: Fundamentals and Concepts, Prentice-Hall, Englewood Cliffs, N.J.

Roberts, G. P., and Pearson, A. J. 1998. Health monitoring of structures—Towards a stethoscope for bridges. Proceedings of the ISMA 23, Int. Conf. on Noise and Vibration Engineering, Leuven, Belgium, September 1998.

Rohrmann, R. G., Baessler, M., Said, S., Schmid, W., and Rücker, W. F. 2000. Structural causes of temperature affected modal data of civil structures obtained by long time monitoring. Proceedings of the IMAC 18 Conference, San Antonio, TX, 2000, pp 1–7.

Rytter, A. 1993.Vibration based inspection of Civil Engineering structures. Ph. D.

Dissertation, Dept. of Building Technology and Structural Eng., Aalborg University, Denmark.

Salane, H.J., Baldwin, J.W., and Duffield, R.C. 1981. Dynamics approach for monitoring bridge Deterioration. Transportation Research Record, **832**: 21–28.

Salawu, O.S. 1997. Detection of structural damage through changes in frequency: A review. Engineering Structures, **19**(9): 718-723.

Salawu, O.S., and Williams, C. 1994. Damage location using vibration mode shapes. Proceedings of the 12th International Modal Analysis Conference, Honolulu, Hawaii, 31 January-3 February. Society for Experimental Mechanics, Bethel, Conn. pp.933-939.

Schulz, J.L., Command, B., Goble, G.G. and Frangopol, D.M. 1995. Efficient field testing and load rating of short- and medium-span bridges. Structural Engineering Review, **7**(3): 181-194.

Shih, C.Y., Tsuei, Y.G., Allemang, R.J., and Brown, D.L. 1988. Complex mode indication function and its application to spatial domain parameter estimation. Mechanical Systems and Signal Processing, **2**(4): 367-377.

Shives, T.R. and Mertaugh, L.J. (Editors). 1986. Detection, diagnosis and prognosis of rotating machinery to improve reliability, maintainability, and readiness through the application of new and innovative techniques. Cambridge University Press, Cambridge, UK.

Sohn, H., and Farrar, C.R. 2001. Damage diagnosis using time series analysis of vibration signals. Smart Materials and Structure, **10**(2001): 1-6.

Sohn, H., Farrar, C.R., Hemez, F.M., Shunk, D.D., Stinemates, D.W., Nadler, B.R.

2003. A review of structural health monitoring literature: 1996-2001. Report No. LA-13976-MS, Los Alamos National Laboratory, Los Alamos, N.Mexico.

Srinivasan, M.G., and Kot, C.A. 1992. Effects of damage on the modal parameters of a cylindrical shell. Proceedings of the 10th International Modal Analysis Conference, San Diego, California, 3-7 February 1992. Society for Experimental Mechanics, Bethel, Conn. pp. 529-535.

Stubbs, N. and Osegueda, R. 1990. Global damage detection in solids–experimental verification. Modal Analysis: The International Journal of Analytical and Experimental Modal Analysis, **5**(2): 81–97.

Stubbs, N., and Kim, Y.I. 1995. Field verification of a non-destructive damage localization and severity estimation algorithm. Proceedings of the 13th International Modal Analysis Conference, Nashville, Tenn., 13-16 February 1995. Society of Experimental Mechanics, Bethel, Conn. pp. 210-218.

Stubbs, N., Sikorsky, C., Park, S.C., and Bolton, R. 1999. Verification of a methodology to non-destructively evaluate the structural properties of bridges. Structural Health Monitoring 2000, Stanford University, Palo Alto, California, pp. 440–449.

Tang, J.P., and Leu, K.M. 1991. Vibration tests and damage detection of P/C bridges. Journal of the Chinese Institute of Engineers, **14**: 531-536.

Todd, M., Johnson, G., and Vohra, S. 2000. Progress towards deployment of bragg grating-based fibre optic systems in structural monitoring applications. Proceedings of the European COST F3 Conference on System Identification and Structural Health

Monitoring, Madrid, Spain, pp. 521–530.

Toksoy, T. and Aktan, A.E. 1994. Bridge-condition assessment by modal flexibility. Experimental Mechanics, **34**(3): 271-278.

Vandiver, J.K. 1975. Detection of structural failure on fixed platforms by measurement of dynamic response. Proceedings of the 7th Annual Offshore Technology Conference, 243-252.

Vandiver, J.K. 1977. Detection of structural failure on fixed platforms by measurement of dynamic response. Journal of Petroleum Technology, March, 305-310.

Ventura, C.E., Brincker, R., Andersen, P., and Cantieni, R. 2002. Identification and damage detection studies of the Z24 highway bridge in Switzerland. Proceedings of the 6th International Conference on Short and Medium-span Bridges, Canadian Society for Civil Engineering, Montreal, Canada, pp. 851-858.

Wang, M.L., Satpathi, D., and Heo, G. 1997. Damage detection of a model bridge using modal testing. Structural Health Monitoring, Current Status and Perspectives, Stanford University, Palo Alto, California, pp. 589–600.

Wegner, L.D., Zhou, Z., Alwash, M., Siddique, A.B., and Sparling, B.F. 2004. Vibration-based damage detection on bridge superstructures. Proceedings of the Second International Workshop on Structural Health Monitoring of Innovative Civil Engineering Structures, ISIS Canada, Winnipeg, MB, Sept. 22-23, pp. 429-439.

West, W.M. 1984. Illustration of the use of modal assurance criterion to Detect structural changes in an orbiter test specimen. Proceedings of Air Force Conference on Aircraft Structural Integrity, 1-6.

West, W.M. Jr. 1982. Single point random model test technology application to failure detection. Shock and Vibration Bulletin, **52**(4): 25-31.

Whittome, T.R., and Dodds, C.J. 1983. Monitoring offshore structures by vibration techniques. Proceedings of the Design in Offshore Structures Conference, 93-100.

Wilson, J.C. 1988. Stiffness of non-skew monolithic bridge abutments for seismic analysis. Journal of Earthquake Engineering and Structural Dynamics Vol. 16.

Wojnarowski, M.E., Stiansen, S.G., and Reddy, N.E. 1977. Structural integrity evaluation of a fixed platform using vibration criteria. Proceedings of the 9th Annual Offshore Technology Conference, 247-256

Wu, X., Ghaboussi, J., and Garrettt, J.H., Jr. 1992. Use of neural networks in detection of structural damage. Computers and Structures, **42**(4): 649-659.

Xia, Y., Hao, H., Zanardo, G., and Deeks, A. 2006. Long term vibration monitoring of an RC slab: Temperature and humidity effect. Engineering Structures, **28**:441-452.

Zak, A., Krawczuk, M., and Ostachowicz, W. 1999. Vibration of a laminated composite plate with closing delamination. Structural damage assessment using advanced signal processing procedures, Proceedings of the DAMAS 99, University College, Dublin, Ireland, pp. 17–26.

Zhang, Q.W. 2007. Statistical damage identification for bridges using ambient vibration data. Computers and Structures, **85**: 476-485.

Zhang, Z. and Aktan, A.E. 1998. Application of modal flexibility and its derivatives in structural identification. Research in Nondestructive Evaluation, **10**(1): 43-61

Zhang, Z., and Atkan, A.E. 1995. The damage indices for constructed facilities. Proceedings of the 13th International Modal Analysis Conference, Nashville, Tenn., 13-16 February 1995. Society for Experimental Mechanics, Bethel, Conn. pp. 1520-1529.

Zhou, Z., Wegner, L., and Sparling, B. 2004. Vibration-based damage Detection on a prestressed concrete girder. Proceedings of 5th Structural Specialty Conference of the Canadian Society for Civil Engineering, Saskatoon, Canada.

Zhou, Z., Wegner, L.D., and Sparling, B.F. 2007. Vibration-based detection of small-scale damage on a bridge deck, ASCE Journal of Structural Engineering, **133**(9): 1257-1267.

Zimmerman, D.C. 1999. Looking into the crystal ball: The continued need for multiple viewpoints in damage detection. Damage assessment of structures, Proceedings of the International Conference on Damage Assessment of Structures (DAMAS 99), Dublin, Ireland, pp. 76–90.

Zimmerman, D.C., and Kaouk, M. 1994. Structural damage detection using a minimum rank update theory. Journal of Vibrations and Acoustics, ASME, **116** (2): 222-231.

APPENDIX A. MODAL PROPERTIES OF ATTRIDGE DRIVE OVERPASS

Natural frequencies and mode shapes of the Attridge Drive Overpass determined from the dynamic response (acceleration) measurements at different temperature ranges are given in the following sections.

A.1 NATURAL FREQUENCIES OF ATTRIDGE DRIVE OVERPASS

Natural frequencies of Attridge Drive Overpass were identified from the averaged normalized response acceleration spectra (see Section 3.4). Natural frequencies at different temperature ranges are summarized in Table A-1 through Table A-3. Averaged normalized response spectra of each quadrant in three temperature ranges are illustrated in Figure A-1 through Figure A-3.

Table A-1. Frequencies (Hz) corresponding to first three peaks (-9°C to -7°C).

	Frequency in Hz (Number of average spectra)			
	North–West Quadrant	North–East Quadrant	South–West Quadrant	South–East Quadrant
First peak	3.30 (6)	3.37 (6)	3.30 (6)	3.30 (6)
Second Peak	3.57 (6)	3.59 (6)	3.55 (6)	3.57 (6)
Third Peak	4.30 (6)	4.38 (6)	4.30 (6)	4.30 (6)

Table A-2. Frequencies (Hz) corresponding to first three peaks (-12°C to -5°C).

	Frequency in Hz (Number of average spectra)			
	North–West Quadrant	North–East Quadrant	South–West Quadrant	South–East Quadrant
First peak	3.35 (6)	3.35 (6)	3.35 (6)	3.31 (6)
Second Peak	3.68 (6)	3.66 (6)	3.64 (6)	3.68 (6)
Third Peak	4.34 (6)	4.36 (6)	4.36 (6)	4.36 (6)

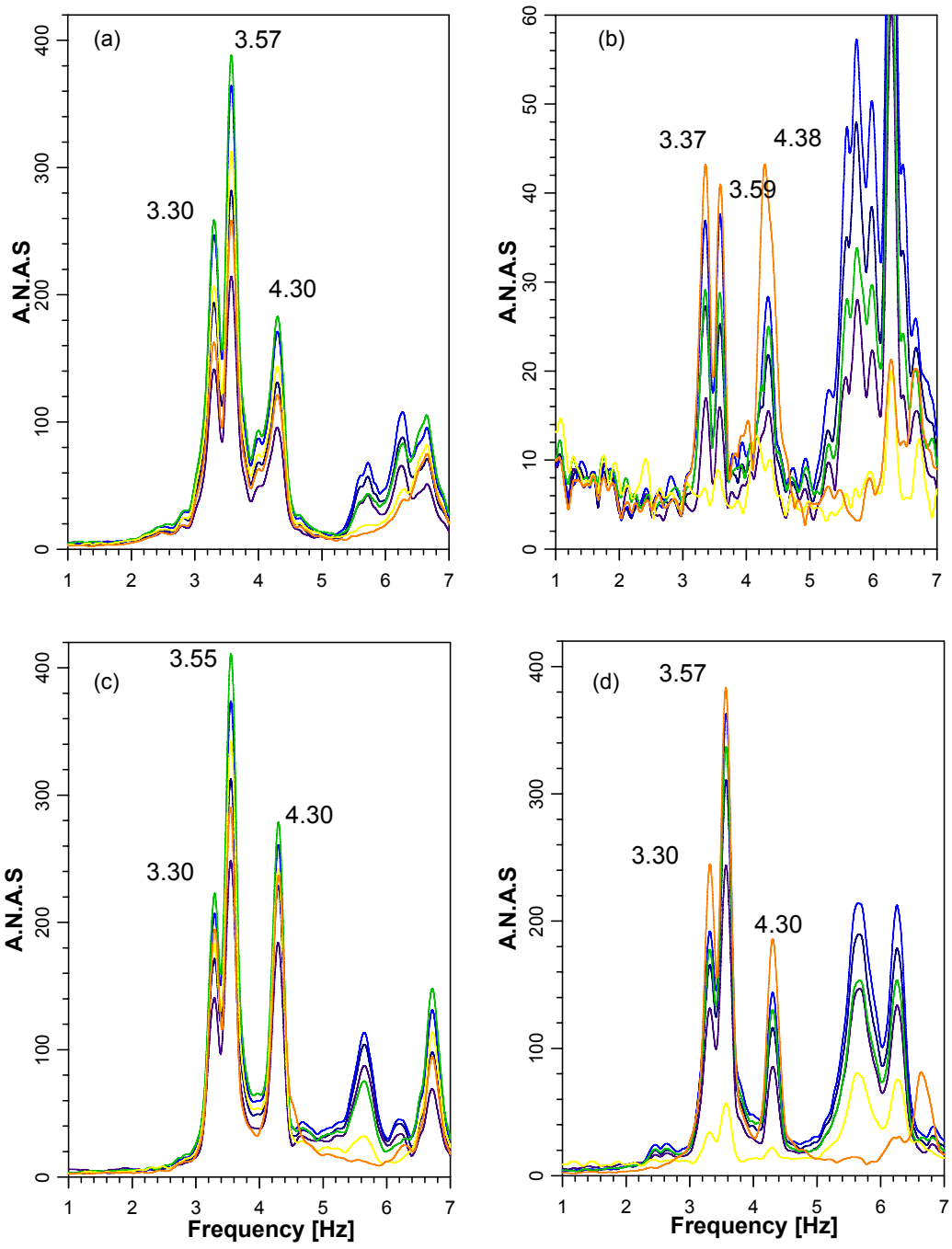

Figure A-1. Averaged normalized acceleration spectra from six accelerometers (each line represents a single accelerometer) in the temperature range -9°C – 7°C in: (a) north-west quadrant; (b) north-east quadrant; (c) south-west quadrant; and (d) south-east quadrant.

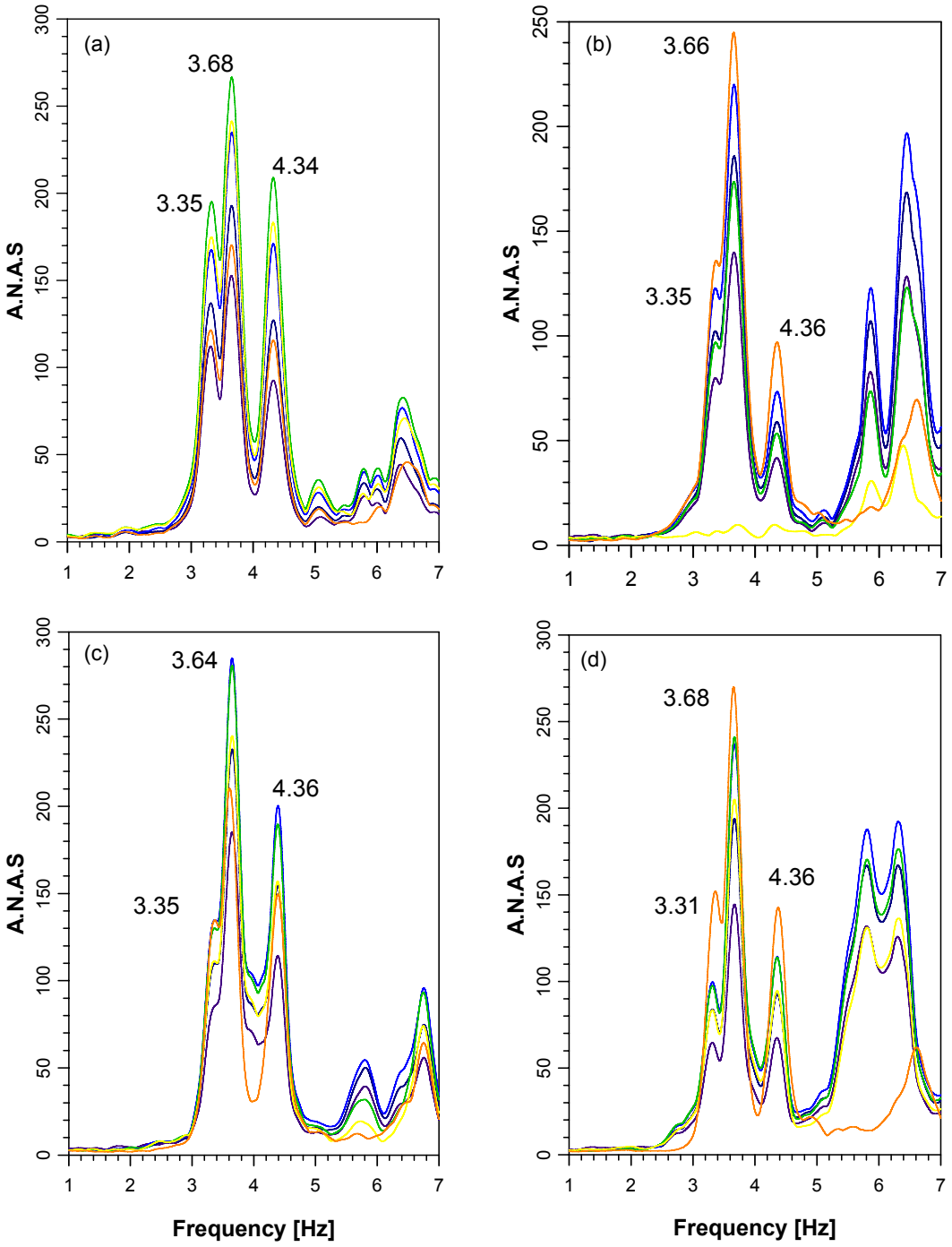

Figure A-2. Averaged normalized acceleration spectra from six accelerometers (each line represents a single accelerometer) in the temperature range -12°C – -5°C in: (a) north-west quadrant; (b) north-east quadrant; (c) south-west quadrant; and (d) south-east quadrant.

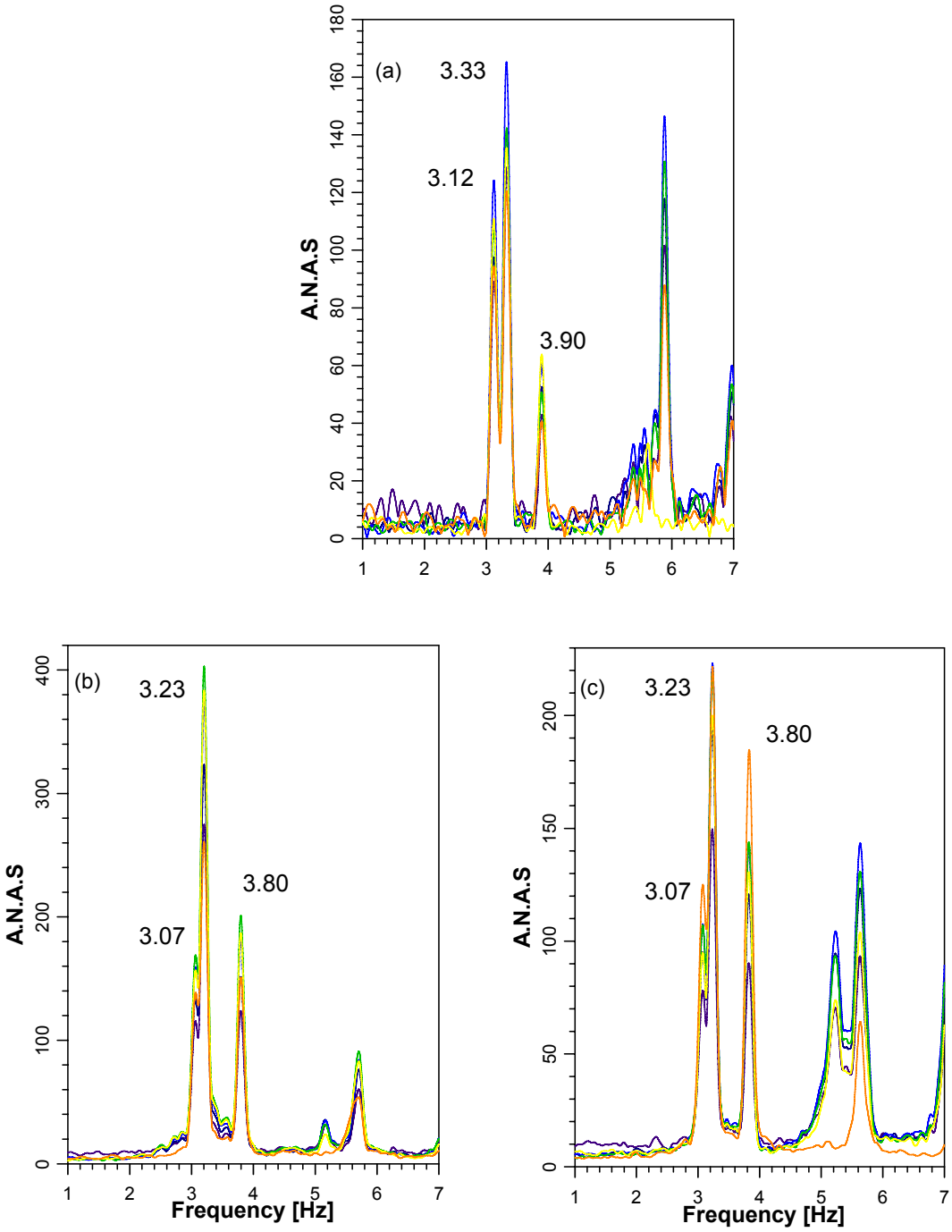

Figure A-3. Averaged normalized acceleration spectra from six accelerometers (each line represents a single accelerometer) in the temperature range 30°C – 40°C in: (a) north-east quadrant; (b) south-west quadrant; and (c) south-east quadrant.

Table A-3. Frequencies (Hz) corresponding to first three peaks (30°C to 40°C).

	Frequency in Hz (Number of average spectra)			
	North–West Quadrant	North–East Quadrant	South–West Quadrant	South–East Quadrant
First peak	N/A	3.12 (6)	3.07 (6)	3.07 (6)
Second Peak	N/A	3.33 (6)	3.23 (6)	3.23 (6)
Third Peak	N/A	3.9 (6)	3.80 (6)	3.80 (6)

A.2 MODE SHAPES OF ATTRIDGE DRIVE OVERPASS

Average modal amplitudes at every sensor location are given in Table A-4 through Table A-7. Average mode shapes for every temperature range are also illustrated in Figure A-4 through Figure A-7 by the solid line.

A.3 UNCERTAINTY IN MODE SHAPE MEASUREMENTS

Mode shape measurements in this study have some degree of uncertainty, which is quantified by standard deviation at each sensor location. Coefficients of variation at each sensor location were also determined to provide a common basis to compare the uncertainty at different locations.

Uncertainties (standard deviations and coefficients of variation of modal amplitudes at each sensor location) in mode shape measurement at different temperature ranges are summarized in Table A-4 through Table A-7. Average mode shapes along with coefficients of variation (of modal amplitudes) at each sensor location are illustrated in Figure A-4 through Figure A-7.

Table A-4. Uncertainty of mode shape at -12°C to -5°C.

			Sensor Location from West Abutment (meter)									
			5	10	15	20	25	44.3	49.3	54.3	59.3	64.3
1st Mode Shape	South Side	Avg	0.35	0.82	1.18	N/A	1.18	-0.69	N/A	-0.7	-0.55	-0.27
		SD	0.093	0.21	0.28	N/A	0.32	0.14	N/A	0.16	0.11	0.08
		COV	26.32	25.47	24.17	N/A	27.24	-20.2	N/A	22.5	19.97	30.2
	North Side	Avg	0.521	1.107	1.618	N/A	1.85	-0.43	N/A	-0.68	-0.52	-0.25
		SD	0.035	0.060	0.068	N/A	0.076	0.031	N/A	0.050	0.035	0.019
		COV	6.66	5.44	4.17	N/A	4.13	-7.04	N/A	7.33	6.87	7.67
2nd Mode Shape	South Side	Avg	0.52	1.135	1.633	N/A	1.665	-0.81	N/A	-0.82	-0.61	-0.3
		SD	0.052	0.099	0.127	N/A	0.14	0.095	N/A	0.08	0.08	0.05
		COV	10.01	8.75	7.796	N/A	8.36	-11.8	N/A	9.5	13.2	16.8
	North Side	Avg	-0.5	-1.08	-1.56	N/A	-1.76	0.4	N/A	0.63	0.47	0.22
		SD	0.066	0.043	0.053	N/A	0.061	0.042	N/A	0.052	0.042	0.044
		COV	-13.2	-4.02	-3.36	N/A	-3.47	10.62	N/A	8.25	8.96	20.52
3rd Mode Shape	South Side	Avg	0.480	1.056	1.53	N/A	1.554	-0.62	N/A	-0.66	-0.47	-0.24
		SD	0.035	0.077	0.071	N/A	0.108	0.060	N/A	0.065	0.075	0.05
		COV	7.224	7.304	4.67	N/A	6.969	-9.78	N/A	-9.92	-15.8	-20.3
	North Side	Avg	0.459	1.059	1.56	N/A	1.779	-0.35	N/A	-0.59	-0.44	-0.19
		SD	0.047	0.055	0.055	N/A	0.062	0.056	N/A	0.08	0.07	0.036
		COV	10.32	5.234	3.53	N/A	3.468	15.9	N/A	14	16.6	18.9

Avg = Average; SD= Standard Deviation; COV= Coefficient of Variation

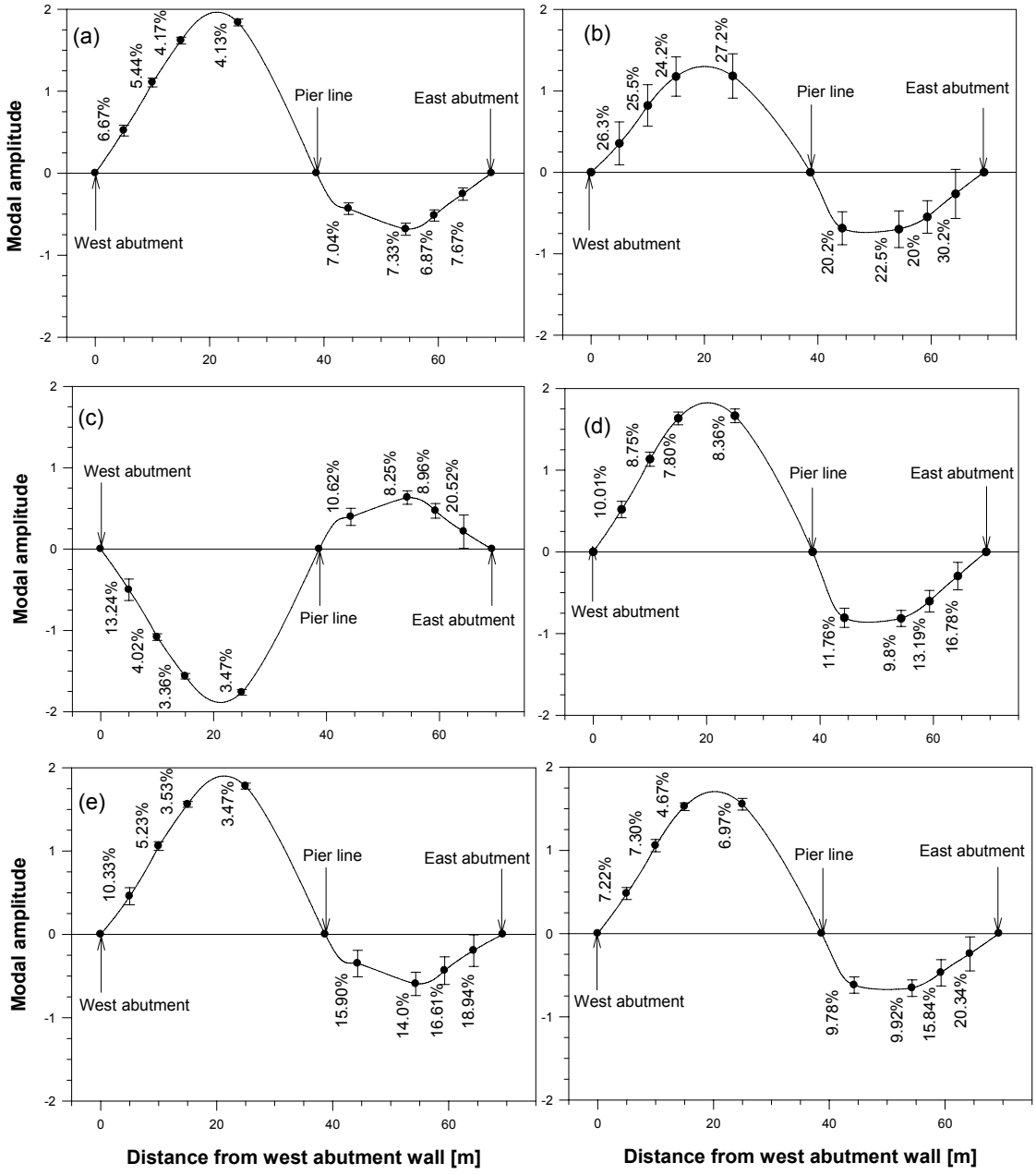

Figure A-4. Coefficients of variation of sensor responses at -12°C to -5°C for : a) 1st mode north; b) 1st mode south; c) 2nd mode north; d) 2nd mode south; e) 3rd mode north; and f) 3rd mode south.

Table A-5. Uncertainty of mode shape at -9°C to -7°C.

			Sensor Location from West Abutment (meter)									
			5	10	15	20	25	44.3	49.3	54.3	59.3	64.3
1st Mode Shape	South Side	Avg	0.474	1.088	1.586	N/A	1.718	-0.46	N/A	-0.67	-0.49	-0.24
		SD	0.078	0.187	0.276	N/A	0.297	0.073	N/A	0.120	0.075	0.039
		COV	16.39	17.19	17.37	N/A	17.31	15.8	N/A	18	15.2	16.3
	North Side	Avg	0.504	1.120	1.659	N/A	1.802	-0.56	N/A	-0.82	-0.61	-0.33
		SD	0.023	0.027	0.044	N/A	0.038	0.071	N/A	0.050	0.053	0.05
		COV	4.485	2.442	2.657	N/A	2.132	12.7	N/A	6.14	8.65	15.0
2nd Mode Shape	South Side	Avg	0.516	1.206	1.78	N/A	1.958	-0.59	N/A	-0.84	-0.61	-0.28
		SD	0.051	0.121	0.169	N/A	0.174	0.085	N/A	0.086	0.062	0.025
		COV	9.97	10.05	9.55	N/A	8.901	14.5	N/A	10.3	10.1	8.97
	North Side	Avg	-0.47	-1.04	-1.58	N/A	-1.73	0.448	N/A	0.75	0.519	0.305
		SD	0.017	0.031	0.039	N/A	0.033	0.064	N/A	0.045	0.048	0.071
		COV	-3.73	3.01	2.47	N/A	1.9	14.36	N/A	6.02	9.29	23.13
3rd Mode Shape	South Side	Avg	0.395	0.979	1.441	N/A	1.60	-0.41	N/A	-0.58	-0.41	-0.19
		SD	0.037	0.082	0.107	N/A	0.12	0.053	N/A	0.112	0.079	0.04
		COV	9.400	8.428	7.430	N/A	7.43	13.1	N/A	19.1	19.2	20.5
	North Side	Avg	0.469	1.035	1.550	N/A	1.68	-0.43	N/A	-0.59	-0.43	-0.23
		SD	0.038	0.044	0.064	N/A	0.042	0.058	N/A	0.066	0.025	0.041
		COV	8.059	4.29	4.16	N/A	2.50	-13.25	N/A	11.1	5.77	18.3

Avg = Average; SD= Standard Deviation; COV= Coefficient of Variation

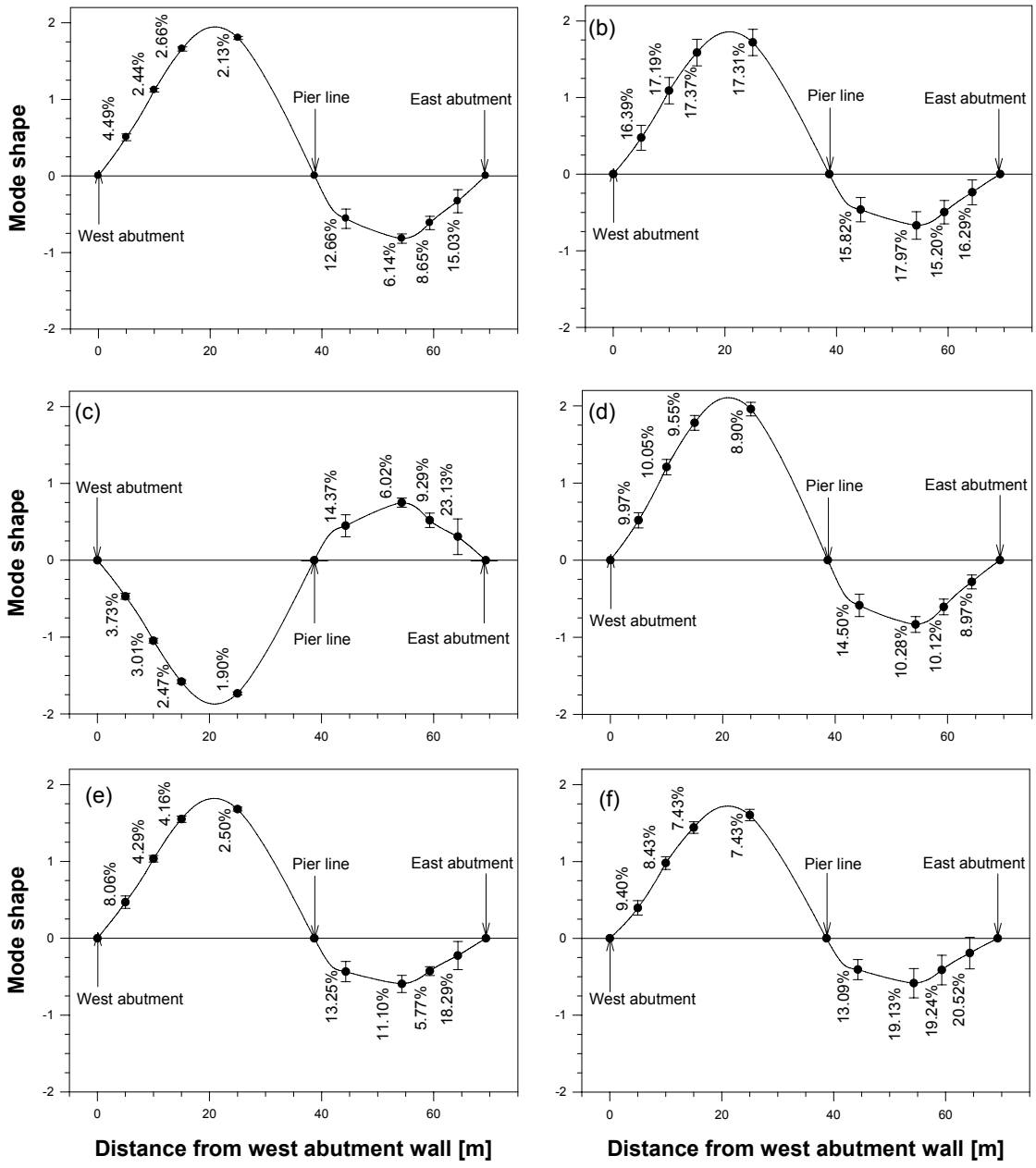

Figure A-5. Coefficients of variation of sensor responses at -9°C to -7°C for : a) 1st mode north; b) 1st mode south; c) 2nd mode north; d) 2nd mode south; e) 3rd mode north; and f) 3rd mode south.

Table A-6. Uncertainty of mode shape at 20°C to 26°C.

			Sensor Location from West Abutment (meter)									
			5	10	15	20	25	44.3	49.3	54.3	59.3	64.3
1st Mode Shape	South Side	Avg	0.429	0.826	1.202	1.366	1.283	-0.43	-0.65	-0.62	-0.48	-0.24
		SD	0.020	0.018	0.037	0.051	0.027	0.041	0.045	0.047	0.032	0.024
		COV	4.634	2.175	3.043	3.709	2.066	-9.44	-7.01	-7.66	-6.56	-9.79
	North Side	Avg	0.496	1.111	1.632	1.797	1.704	-0.41	-0.69	-0.71	-0.59	-0.28
		SD	0.032	0.058	0.103	0.087	0.068	0.037	0.067	0.041	0.056	0.050
		COV	6.389	5.207	6.310	4.859	4.014	-8.98	-9.69	-5.77	-9.39	-17.8
2nd Mode Shape	South Side	Avg	0.558	1.226	1.792	2.044	1.866	-0.51	-0.76	-0.71	-0.53	-0.24
		SD	0.015	0.036	0.060	0.073	0.067	0.035	0.056	0.059	0.017	0.011
		COV	2.726	2.930	3.358	3.575	3.591	6.912	7.412	8.378	3.287	4.612
	North Side	Avg	-0.46	-1.04	-1.5	-1.71	-1.64	0.391	0.650	0.657	0.520	0.231
		SD	0.032	0.041	0.045	0.083	0.048	0.042	0.046	0.070	0.037	0.032
		COV	7.038	3.997	2.980	4.822	2.943	10.72	7.080	10.64	7.153	13.76
3rd Mode Shape	South Side	Avg	0.343	0.883	1.207	1.439	1.289	-0.42	-0.61	-0.59	-0.43	-0.19
		SD	0.014	0.014	0.030	0.024	0.027	0.040	0.043	0.032	0.025	0.026
		COV	3.982	1.561	2.487	1.680	2.086	9.576	7.030	5.439	5.750	13.62
	North Side	Avg	0.430	1.021	1.486	1.694	1.644	-0.35	-0.57	-0.58	-0.43	-0.2
		SD	0.028	0.036	0.040	0.069	0.051	0.023	0.035	0.028	0.017	0.012
		COV	6.550	3.543	2.712	4.101	3.105	6.521	6.097	4.817	3.980	5.860

Avg = Average; SD= Standard Deviation; COV= Coefficient of Variation

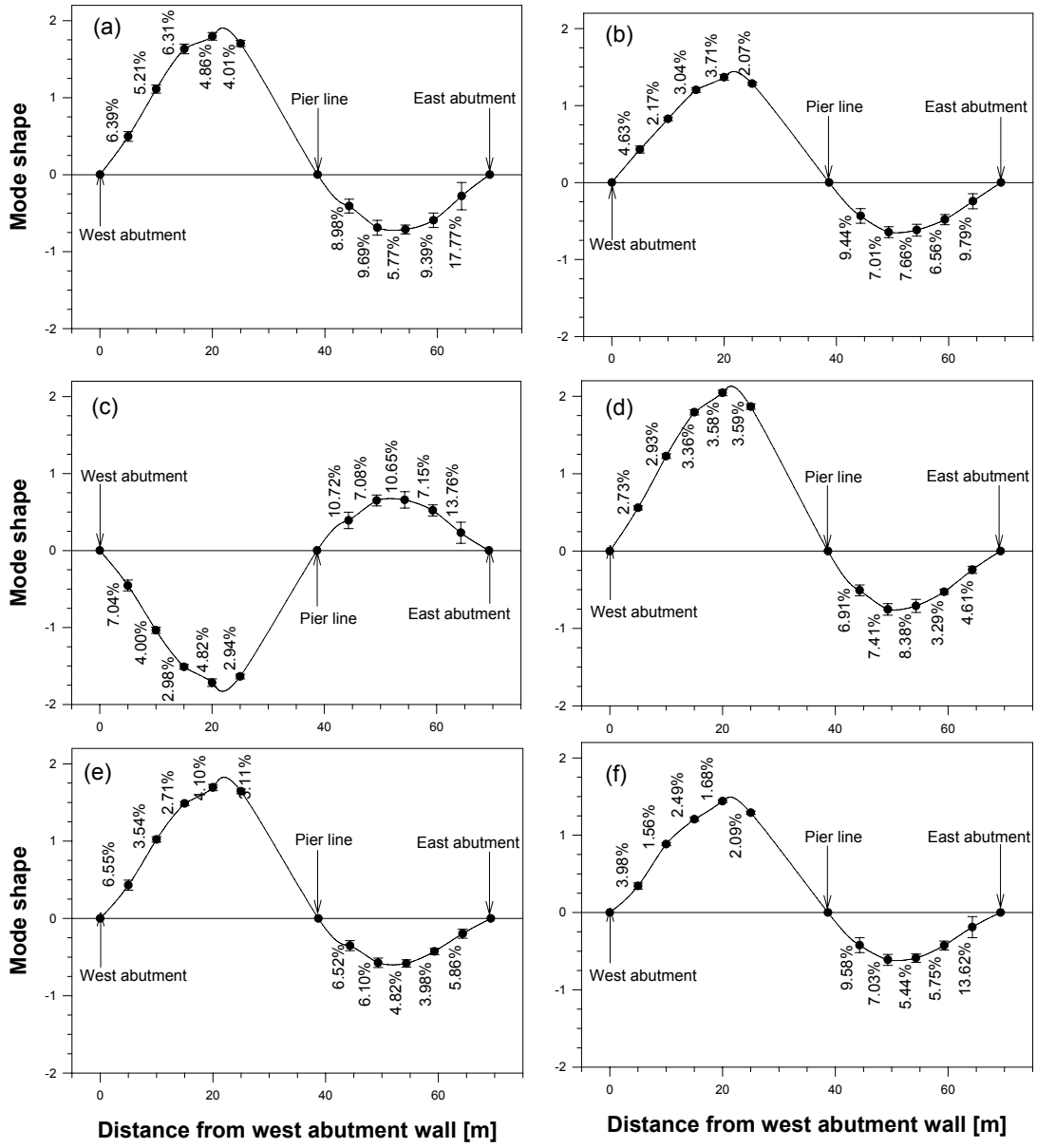

Figure A-6. Coefficients of variation of sensor responses at 20°C to 26°C for : a) 1st mode north; b) 1st mode south; c) 2nd mode north; d) 2nd mode south; e) 3rd mode north; and f) 3rd mode south.

Table A-7. Uncertainty of mode shape at 30°C to 40°C.

			Sensor Location from West Abutment (meter)									
			5	10	15	20	25	44.3	49.3	54.3	59.3	64.3
1st Mode Shape	South Side	Avg	0.399	0.869	1.225	1.373	1.225	-0.45	-0.67	-0.68	-0.52	-0.23
		SD	0.105	0.161	0.186	0.207	0.187	0.059	0.074	0.069	0.048	0.038
		COV	26.28	18.57	15.17	15.05	15.23	13.17	10.98	10.16	9.264	16.30
	North Side	Avg	N/A	N/A	N/A	N/A	N/A	-2.17	-1.5	-1.65	-1.33	-0.71
		SD	N/A	N/A	N/A	N/A	N/A	0.061	0.086	0.014	0.093	0.037
		COV	N/A	N/A	N/A	N/A	N/A	2.803	5.727	0.839	6.960	5.199
2nd Mode Shape	South Side	Avg	0.609	1.329	1.963	2.238	2.052	-0.54	-0.70	-0.70	-0.51	-0.23
		SD	0.092	0.188	0.226	0.277	0.259	0.040	0.073	0.045	0.062	0.042
		COV	15.14	14.15	11.52	12.37	12.61	7.507	10.33	6.427	12.16	18.28
	North Side	Avg	N/A	N/A	N/A	N/A	N/A	2.473	1.940	1.561	0.943	0.693
		SD	N/A	N/A	N/A	N/A	N/A	0.021	0.395	0.218	0.515	0.05
		COV	N/A	N/A	N/A	N/A	N/A	0.849	20.35	13.95	54.56	7.139
3rd Mode Shape	South Side	Avg	0.410	0.983	1.443	1.677	1.549	-0.42	-0.66	-0.65	-0.45	-0.21
		SD	0.043	0.079	0.134	0.152	0.131	0.029	0.039	0.025	0.043	0.015
		COV	10.36	7.999	9.295	9.050	8.455	6.574	5.888	3.888	9.480	7.416
	North Side	Avg	N/A	N/A	N/A	N/A	N/A	-3.48	-1.77	-1.93	-1.6	-0.85
		SD	N/A	N/A	N/A	N/A	N/A	0.637	0.144	0.146	0.234	0.277
		COV	N/A	N/A	N/A	N/A	N/A	-18.3	-8.13	-7.56	-14.5	-32.8

Avg = Average; SD= Standard Deviation; COV= Coefficient of Variation

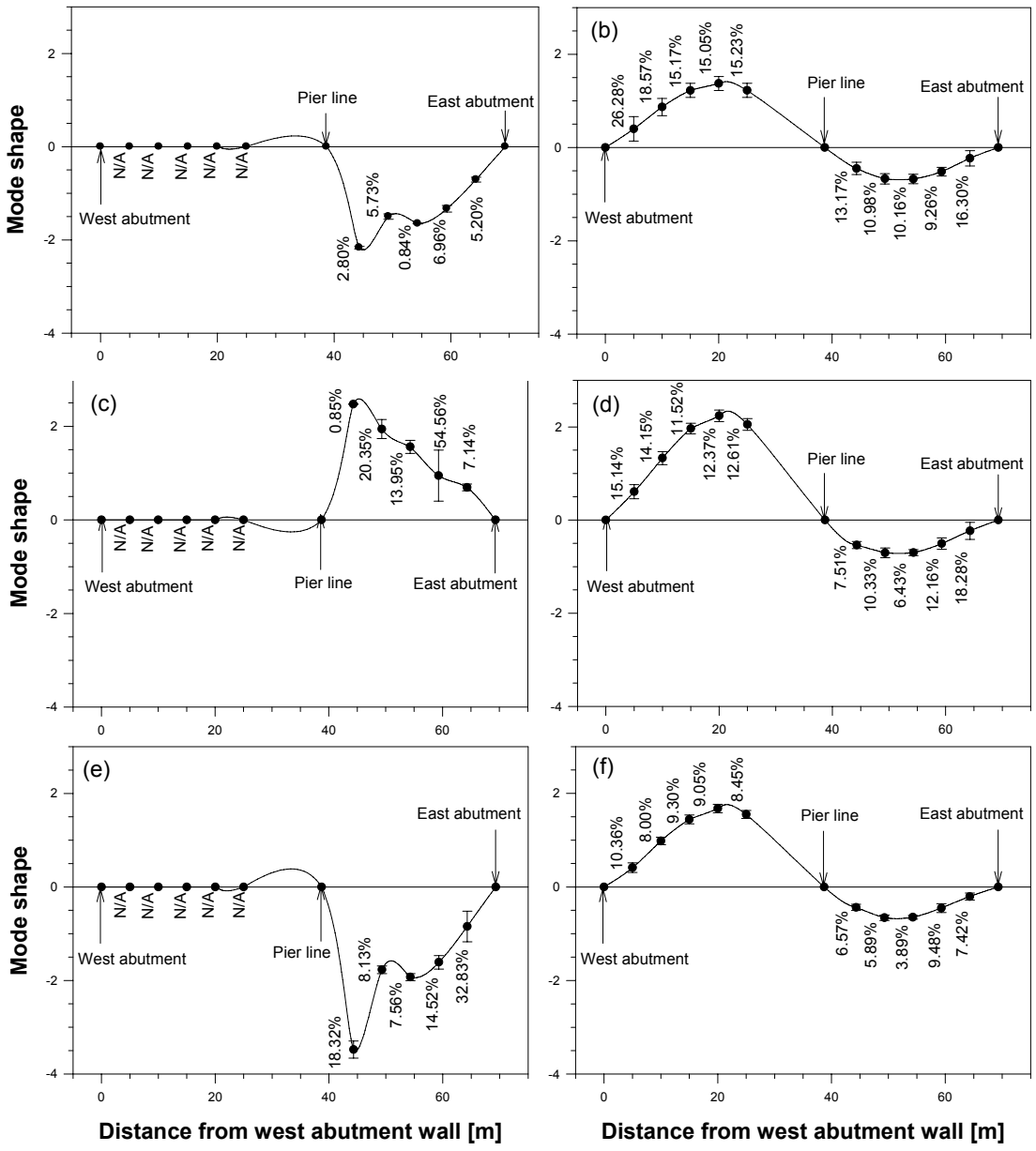

Figure A-7. Coefficients of variation of sensor responses at 30°C to 40°C for : a) 1st mode north; b) 1st mode south; c) 2nd mode north; d) 2nd mode south; e) 3rd mode north; and f) 3rd mode south.

APPENDIX B. DESCRIPTION OF BOUNDARY CONDITIONS USED IN THE FINITE ELEMENT MODEL

Attridge Drive Overpass is supported on deep foundations (concrete piles). Both the abutment walls at the two ends and pier in the mid span are supported on piles. In the FE model, support at the pier line was modelled using hinges with translational fixity in the transverse and vertical direction of the overpass structure. The remainder of the rotational (about the longitudinal, transverse and vertical directions with respect to bridge structure) and translational (along the longitudinal direction with respect to bridge structure) degrees of freedom at the pier line hinges were not constrained. Piles below the abutment walls were modelled using springs with rotational and translational stiffness. Detail of stiffness calculations for the concrete piles below abutment walls are given in Section B.1.

Backfill resistance on the abutment walls were modelled using springs with translational stiffness along the longitudinal direction of bridge structure. Details of the spring stiffness calculations for backfill resistance are given in Section B.2.

B.1 ROTATIONAL STIFFNESS OF PILE

The concrete piles supporting the abutment walls of Attridge Drive Overpass have a diameter of 950 mm. For simplicity, the concrete piles were replaced with springs having rotational and translational stiffness in the FE model of Attridge Drive Overpass.

Each pile was simplified as a beam fixed at one end and free on the other end. Embedment of the pile in the ground soil produces a support condition very close to a

fixed support. Rotational and translational stiffness of a pile (Fixed-Free beam) are therefore determined using Equations B.1 and B.2, respectively.

$$K_\theta = \frac{2E_c I}{L} \quad , \tag{B.1}$$

$$K_\Delta = \frac{3E_c I}{L^3} \quad , \tag{B.2}$$

$$\text{where} \qquad E_c = 4500 \times \sqrt{f_c^{'}} \quad \text{[CAC 2006]} \tag{B.3}$$

$f_c^{'}$ = strength of concrete
= 45 MPa

E_c = modulus of elasticity
= 30 GPa

I = second moment of inertia of pile cross-section
= 0.04 m^4

L = length of effective pile length based on calibration
= 5.5 m

therefore;

K_θ = rotational stiffness of pile
= $960 \ \frac{N.m}{Unit \quad rotation}$

K_Δ = translational stiffness of pile
= $47.6 \ \frac{N}{m}$

Each abutment wall is supported on 6 piles; therefore, both the rotational and translational stiffness of the 6 piles were distributed equally on 64 nodes (in FE model) at the bottom of each abutment wall.

B.2 BACKFILL PRESSURE

The linear stiffness for translational springs due to backfill resistance was estimated using Wilson Equation (Wilson 1988) as given below:

$$K_{spring} = \frac{E_{soil} \times L}{(1-\upsilon^2) \times I} \quad , \tag{B.4}$$

$$\text{where} \qquad I = 1.2136 \times \log_{10}\left(\frac{L}{B}\right) + 0.84 \tag{B.5}$$

L = length of abutment along skew as shown in Figure B-1.
= 28 m

B = height of abutment wall.
= 8 m

I = shape factor for soil contact area.
= 1.5

E_{soil} = Young's modulus of either in situ or compacted soil at spring location.
= 47.88 MPa

υ_s = Poisson's ratio of soil at spring location
= 0.35

therefore; total translational stiffness of backfill soil for each abutment wall,

K_{spring} = $1.018 \times 10^9 \ \frac{N}{m}$

The stiffness of each abutment wall was distributed among 224 nodes. Stiffness of pile and backfill pressure as assigned on each node is given Table B-1.

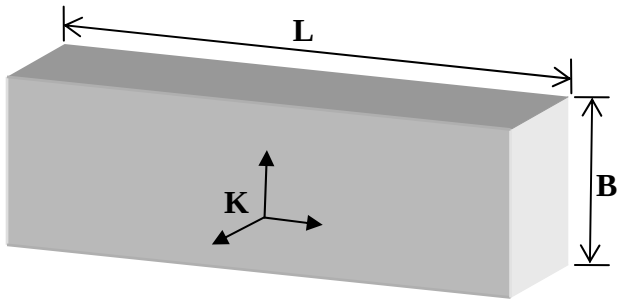

Figure B-1. Length and height of a typical abutment wall.

Table B-1. Stiffness of spring elements used in place of pile and backfill.

Actual structural/support feature	Stiffness	Direction	Magnitude at each node	
Pile	Rotational	About the longitudinal and transverse directions of bridge structure	90	$\frac{N.m}{Unit \quad rotation}$
Pile	Translational	Along the longitudinal and transverse directions of bridge structure	4.46	$\frac{N}{m}$
Translational	Translational	Along the longitudinal direction of bridge structure	$4.5X10^6$	$\frac{N}{m}$

APPENDIX C. DESCRIPTION OF MODIFIED CONCRETE STIFFNESS ADJUSTED TO THE DIRECTIONAL CRACKING

The concrete bridge deck of the Attridge Drive Overpass is supported on nine steel girders. Also, the entire composite bridge deck (concrete deck and steel girders) is supported on abutment walls at the ends and piers at midspan. Due to these support conditions, the concrete deck suffers more cracking in the longitudinal direction; however, the stiffness in the lateral direction is also reduced by cracking in that direction. To consider the cracking of the concrete deck, an orthotropic material model was used for deck definition in the finite element model.

A simple equivalent stiffness of cracked concrete approach was used instead of a non-linear analysis. Two limiting stiffness values were determined using the moment of inertia of the gross effective section (upper bound) and the moment of inertia of a fully cracked section (lower bound).

Effective modulus of rigidity values in each direction were determined using modulus of elasticity and Poisson's ratio, where Poisson's ratio values were adjusted to make the stress-strain constitutive matrix of finite element model positive definite as well as to correlate with the natural frequencies and mode shapes of the FE model to the field measured properties.

C.1 EFFECTIVE AREA MOMENT OF INERTIA

Effective modulus of elasticity values in the lateral direction with respect to bridge structure was determined using the Equation C.1 (CAC 2006).

$$E_{effective} = E_c \times \frac{I_e}{I_g} \quad , \tag{C.1}$$

where

$E_{effective}$ = effective modulus of elasticity of cracked section

E_c = modulus of elasticity of non-cracked concrete.

= $4500\sqrt{f_c^{'}}$

I_e = effective area moment of inertia

I_g = gross area moment of inertia determined using Equation.

The effective area moment of inertia I_e was determined using Equation C.2 (CAC. 2006).

$$I_e = \left(\frac{M_{cr}}{M_a}\right)^3 I_g + \left[1 - \left(\frac{M_{cr}}{M_a}\right)^3\right] I_{cr} \quad , \tag{C.2}$$

where $$M_{cr} = \frac{f_r I_g}{y_t} \tag{C.3}$$

$$I_g = \frac{1}{12} bh^3 \tag{C.4}$$

$$y_t = \frac{h}{2} \tag{C.5}$$

M_a = moment due load under consideration.

M_{cr} = moment which will initiate crack at the extreme fibre of the cross section determined using Equation C.3.

I_{cr} = moment of inertia of cracked transformed section

f_r = tensile strength of concrete.

= $0.6\lambda\sqrt{f_c^{'}}$;

λ = unit value for normal density concrete.

$f_c^{'}$ = ultimate strength of concrete in MPa

b = width of concrete section as shown in Figure C-1a

h = height of concrete section as shown in Figure C-1a

The area moment of inertia of a cracked transformed section was determined using Equations C.6, C.7 and C.8 (CAC 2006).

$$I_{cr} = \frac{1}{3}b(kd)^3 + nA_s d^2(1-k)^2 + (n-1)A_s^{'}(kd-d^{'})^2 \quad , \tag{C.6}$$

$$k = \frac{\left[\sqrt{2dB\left(1+\frac{rd^{'}}{d}\right)+(1+r)^2}-(1+r)\right]}{B} \quad , \tag{C.7}$$

$$B = \frac{b}{nA_s} \quad , \quad r = \frac{(n^{'}-1)A_s^{'}}{nA_s} \quad \text{and} \quad n = n^{'} = \frac{E_s}{E_c} \tag{C.8}$$

where

A_s = area of steel provided in the tensile zone.

$A_s^{'}$ = area of steel provided in the tensile zone.

E_s = modulus of elasticity of steel.

d , $d^{'}$ and kd are illustrated in Figure C-1.

In the present study, a one meter strip of concrete deck supported on nine steel girders was considered to determine the modulus of elasticity of cracked concrete. Assuming the strip to be a continuous beam on nine hinge supports (steel girders), maximum negative moment at the two ends of each span were determined using Equation C.9 and Equation C.10 (CAC 2006).

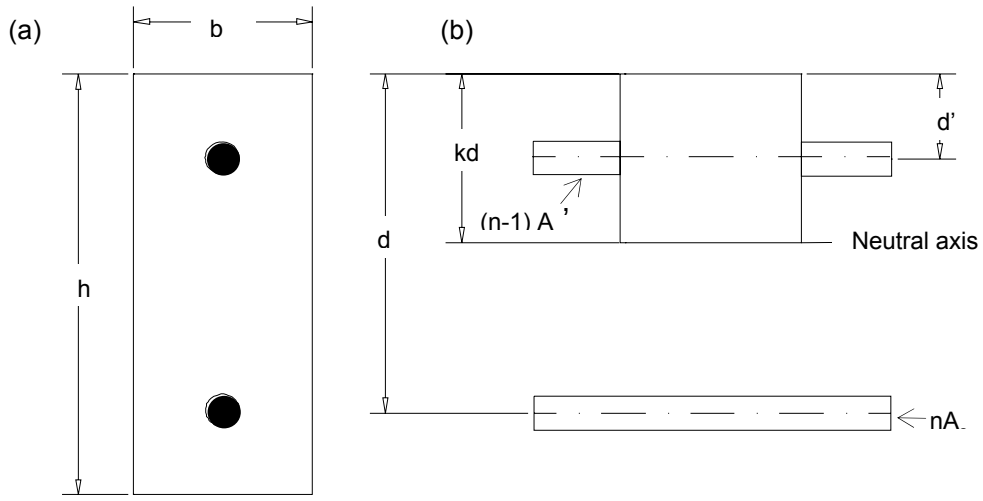

Figure C-1. Typical notations used for: (a) a reinforced concrete section; and (b) a transformed concrete section.

$$M_{aend1} = 0.107\omega l^2 \quad \text{(C.9)}$$

$$M_{aend2} = 0.071\omega l^2 \quad \text{(C.10)}$$

The maximum positive moment at midspan between two adjacent girders was determined using Equation C.11 (CAC 2006).

$$M_{amidspan} = 0.0361\omega l^2 \ , \quad \text{(C.11)}$$

where ω is the distributed load consisting of the concrete deck, wearing surface and live load, and l is the clear span in between two adjacent steel girders . The effective area moments of inertia at two ends (I_{eend1}, I_{eend2}) and in the midspan ($I_{emidspan}$) were determined using Equation C.2. The averaged effective area moment of inertia was determined using the Equation C.12 (CAC 2006).

$$I_{eavg} = 0.15I_{eend1} + 0.7I_{emidspan} + 0.15I_{eend2} \quad \text{(C.12)}$$

The effective modulus of elasticity of concrete was then determined using Equation C.1, where I_{eavg} was used in place of I_e. All parameter values used to determine the effective modulus of elasticity are given in Table C-1.

C.2 EQUIVALENT MODULUS OF ELASTICITY OF A FULLY CRACKED SECTION

The equivalent modulus of elasticity values of a fully cracked section was determined using the Equation C.13 (CAC 2006).

$$E_{fully-cracked} = E_c \times \frac{I_{cr}}{I_g} \quad , \tag{C.13}$$

where

$E_{fully-cracked}$ = modified modulus of elasticity of a fully cracked section.

E_c, I_{cr} and I_g are explained in Section C.1.

Poisson's ratio values in the lateral, longitudinal and vertical directions were estimated based on trials ensuring that stress-strain constitutive matrix in the eigenvalue analysis was positive definite in each trial. Modulus of rigidity were then determined using Equation C.14.

$$G = \frac{1}{2(1+\nu)} E \tag{C.14}$$

This equation determines the modulus of rigidity in each direction proportionately for an orthotropic material model using isotropic material equation in each direction. Final material properties for an orthotropic model used in the FE model are given in Table 5.1.

Table C-1. Different parameter values used to determine effective modulus of elasticity of concrete.

Notation	Description	Magnitude
b	Width of concrete strip	1 m
h	Depth of concrete deck	0.225 m
l	Span in between two adjacent steel girders	3.1 m
$f_c^{'}$	Ultimate strength of concrete	45 MPa
E_s	Modulus of elasticity of steel	200 GPa
ω	Unit load due to dead load (225 mm deck at 2400 $\frac{kg}{m^3}$ and 90 mm asphalt concrete at 2300 $\frac{kg}{m^3}$)	7.32 $\frac{N}{m}$
A_s and $A_s^{'}$	Area of reinforcing steel for both compression and tension (15M bars @ 300 o/c, Top and bottom, Each way)	666.67 $\frac{mm^2}{m}$

The effective modulus of elasticity, modulus of elasticity of a fully cracked section and the modulus of elasticity used in the calibrated FE model in three material directions are given in Table C-2. As it is very challenging to estimate the actual crack pattern in the field, the concrete stiffness was varied arbitrarily to fit the dynamic response of the FE model to that of the field study, while ensuring that the concrete stiffness did not go below the equivalent stiffness of a fully cracked section.

Table C-2. Spring stiffness values at corresponding nodes for pile and backfill soil.

Properties	E used in the calibrated model (GPa)	$E_{effective}$ (GPa)	$E_{fully-cracked}$ (GPa)	Without Crack (GPa)
Modulus of elasticity in longitudinal direction	13	-	3.231	30
Modulus of elasticity in lateral direction	4.1	4.7×10^4	3.231	30
Modulus of elasticity in vertical direction	13	30	-	30

APPENDIX D. SIMULATION OF FIELD UNCERTAINTY IN THE NUMERICAL MODEL

D.1 BACKGROUND

Mode shapes extracted from the vibration response (acceleration) of Attridge Drive Overpass varied with the data sample measured in the field. The uncertainty at each sensor location was quantified by the standard deviation of modal amplitudes at that sensor location. To ascertain how uncertainty in mode shape measurements impairs VBDD, a numerical simulation of field uncertainty was performed in the present study. A description of that numerical simulation is given in the following sections.

D.2 METHODOLOGY

The finite element (FE) model of Attridge Drive Overpass was calibrated to the modal properties (first three mode shapes and natural frequencies) of the real structure in the temperature range of 20°C to 26°C. The fundamental (first) mode shape of the calibrated model was used to investigate different VBDD methods. Therefore, uncertainty in the first (fundamental) mode shape as extracted from field data in the temperature range of 20°C to 26°C was simulated numerically to investigate the effects of uncertainty on VBDD parameters. There were different steps involved in the simulation process as shown in Figure D-1.

The uncertainty in the field measurements was quantified by the standard deviation of modal amplitudes at each sensor location. There were 20 sensor locations on the bridge deck to record the vibration response (acceleration) in the temperature range of 20°C to 26°C. The first mode shape of the overpass in the temperature range of

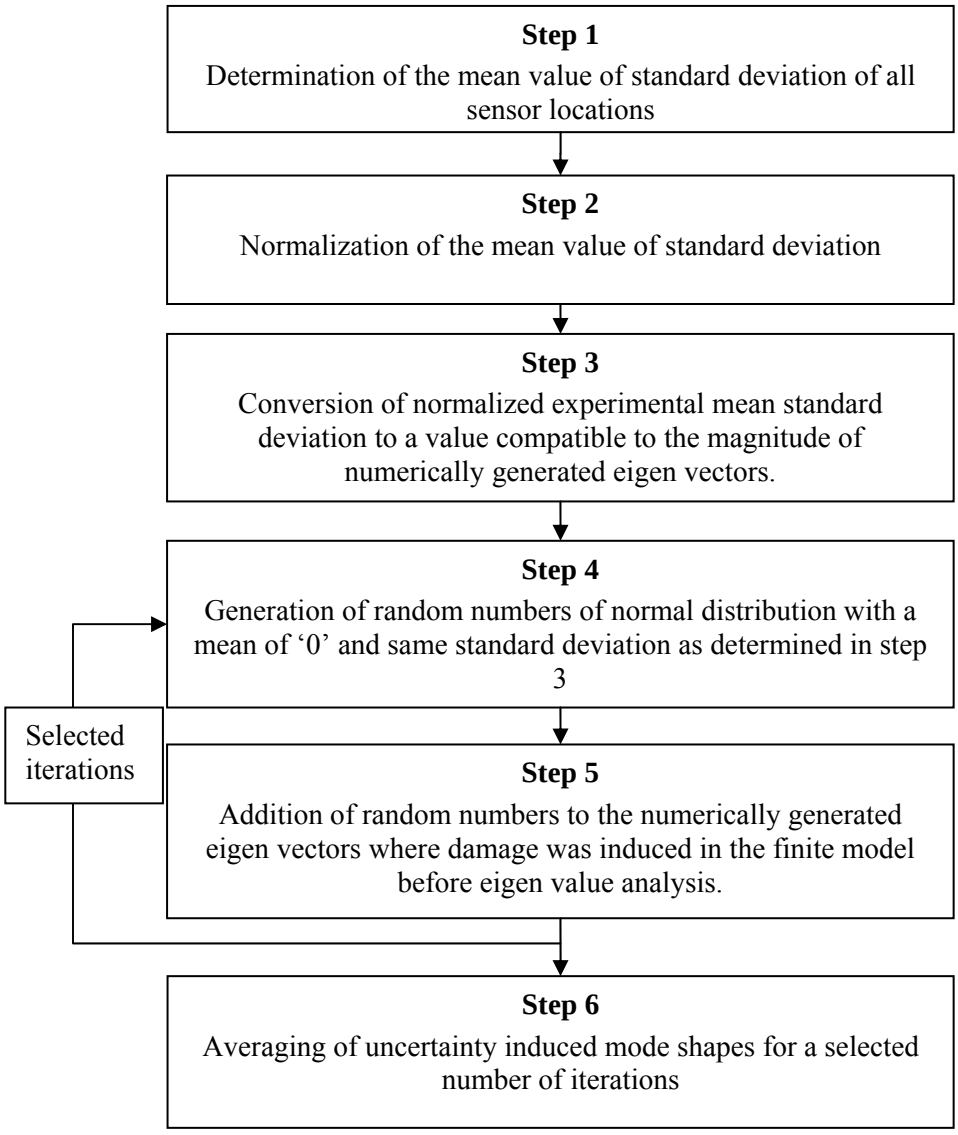

Figure D-1. Flow chart of generating uncertainty induced mode shapes.

20°C to 26°C was defined by the average value of all extracted modal amplitudes at each sensor location. The standard deviation of modal amplitudes at each sensor location was found to be different than that of other sensor locations. Therefore, a mean value for the standard deviation at all of these sensor locations was determined first. The standard deviation of modal amplitudes for the first mode shape in the temperature

range of 20°C to 26°C are given Table A-6; and the mean value of standard deviation at all sensor locations was 0.04705.

Mode shape amplitudes are indeterminate by definition. Relative magnitude of modal amplitudes as extracted from the field data were different than those extracted from finite element model. Therefore, in step 2 (Figure D-1), the mean value of the standard deviation, as determined in the first step, was normalized by dividing it by the magnitude of average modal amplitude of a given reference sensor in the same temperature range. The reference sensor was located on the north barrier wall, 20 m away from the west abutment wall. The average modal amplitude on the reference sensor location in the temperature range of 20°C to 26°C was 1.797. Therefore,

$$Normalized\ Mean\ Value\ of\ Standard\ Deviation$$

$$= \frac{Mean\ Value\ of\ Standard\ Deviation}{Average\ Modal\ Amplitude\ of\ the\ Reference\ Sensor}$$

$$= \frac{0.04705}{1.797}$$

$$= 0.0261$$

In Step 3, a standard deviation value was generated using Equation (D.1), which is compatible to the magnitude of numerically generated mode shape

$$Standrad\ Devivation\ for\ numerical\ model = C_1 \times \emptyset_{ref} \times Normalized\ Mean\ Standard\ Deviation\ \ , \tag{D.1}$$

where $C_1 = \frac{1}{2}$; a coefficient determined by trials to make the spatial distribution of numerically generated uncertainty very close to those as measured in the field. Uncertainties as measured in the field are compared with those generated numerically in Table D-1 using coefficienst of variation of modal amplitudes at each sensor location.

Here, $\emptyset_{ref}$ is the reference vertical eigenvector of a node located in the same location of the reference sensor in the field. As there is no node (on the bridge deck of finite element model) at exactly 20 m east from the centreline of west abutment wall, a cubic spline was fit to the eigenvectors at the actual nodes located along the north barrier wall to determine an approximate reference eigenvector.

In Step 4, random numbers were generated using a Matlab® function 'normrnd', where random numbers were chosen from a normal distribution with a mean value of zero and a standard deviation value as determined in Step 3. A single standard deviation value was used to generate random number for all the nodes on the bridge deck.

In Step 5, generated random numbers for each node as determined in Step 4, were superimposed on the eigenvector at that respective node to induce uncertainty in the mode shape of a damage induced model. The sign of random number was kept

Table D-1. Comparison of uncertainty determined from field measurement and numerical model.

South Side				North Side			
Field Measurement		Numerical Model		Field Measurement		Numerical Model	
Distance from west abutment (m)	C.O.V.[1]	Distance from west abutment (m)	C.O.V.[1]	Distance from west abutment (m)	C.O.V.[1]	Distance from west abutment (m)	C.O.V.[1]
5	4.6	5.76	8.1	5	6.4	5.76	8.8
10	2.2	10.81	4.1	10	5.2	10.81	4.5
15	3.0	16.31	3.1	15	6.3	16.31	3.3
20	3.7	21.31	2.9	20	4.9	21.31	3.1
25	2.1	25.51	3.4	25	4.0	25.51	3.5
44.3	9.4	44.00	11.7	44.3	9.0	44.00	12.0
49.3	7.0	48.81	7.6	49.3	9.7	48.81	7.6
54.3	7.7	54.31	7.2	54.3	5.8	54.31	7.1
59.3	6.6	59.31	9.3	59.3	9.4	59.31	8.9
64.3	9.8	64.81	20.1	64.3	17.8	64.81	18.9

[1] C.O.V. = Coefficient of variation

similar to that of the corresponding eigenvector while superimposing the uncertainty on the average modal amplitudes.

For a selected number of iterations, Step 4 and 5 were repeated to generate an uncertainty induced mode shape for each iteration. Mode shapes from a selected number of repeated iterations were averaged in Step 6 to attenuate the effect of uncertainty. Interpolation of average mode shapes (as determined in Step 6) using a cubic spline function was performed prior to the application of unit-norm normalization process. Unit-norm normalized, uncertainty induced, average mode shape were then used for further VBDD investigation.